



Using Gravitational Waves to Study Neutron Stars in General Relativity and Alternative Theories of Gravity

Von der QUEST-Leibniz-Forschungsschule
der Gottfried Wilhelm Leibniz Universität Hannover

zur Erlangung des Grades
Doktorin der Naturwissenschaften
(Dr. rer. nat.)

genehmigte Dissertation
von
Stephanie M. Brown

2023

Referent:

Prof. Dr. Bruce Allen
Max Planck Institute for Gravitational Physics (Albert Einstein Institute)
Leibniz Universität Hannover

Korreferenten:

Prof. Dr. Badri Krishnan
Institute for Mathematics, Astrophysics and Particle Physics, Radboud University

Prof. Dr. Luciano Rezzolla
Institute for Theoretical Physics, Goethe University

Prof. Dr. Anna Watts
Anton Pannekoek Institute for Astronomy, University of Amsterdam

Tag der Promotion:

09 February 2023

“I have no special talents. I am only passionately curious.”

Albert Einstein

Throughout this work, $G = c = 1$ units are used unless otherwise specified. The metric signature $(-,+,+,+)$ is also used.

Notation

G_*	gravitational coupling constant
$g_{\mu\nu}$	metric tensor
$R_{\mu\nu}$	Ricci tensor
R	Ricci scalar
$T^{\mu\nu}$	stress energy tensor
$T \equiv g^{\mu\nu}T_{\mu\nu}$	trace of the stress-energy tensor
d_μ	partial derivative with respect to μ
∇_μ	covariant derivative with respect to μ
$\square = g^{\mu\nu}\nabla_\mu\nabla_\nu$	D'Alembertian operator

Acronyms

EOS	equation of state
JFBD	Jordan-Fierz-Brans-Dicke
MCMC	Markov chain Monte Carlo
TOV	Tolman-Oppenheimer-Volkoff equation
EFT	effective field theory

Abstract

LIGO's detection of gravitational waves emitted by a binary black hole merger in 2015 opened a new window into our universe. The era of multi-messenger astronomy began in 2017 with the detection of binary neutron star merger GW170817 and its electromagnetic counterpart GRB170817A. Gravitational wave observations have become a valuable tool for studying diverse areas of physics. Gravitational waves are particularly suited to tests of general relativity in the strong field regime and to studies of nuclear matter in extreme conditions. The work presented in this thesis uses gravitational wave data to contribute to our understanding of neutron stars, nuclear matter, and general relativity, explore the capabilities of current and future detectors, and provide a foundation for future studies of alternate theories of gravity.

Binary neutron star merger GW170817 offered new insights into nuclear physics, astrophysics, gravitational physics, and many other disciplines. The first study in this thesis combines the multi-messenger signals from GW170817 with state-of-the-art nuclear theory to place tight constraints on neutron star radii and tidal deformabilities, improving the radius measurement by a factor of 2. This study also constrains the nuclear equation of state and predicts that future neutron star-black hole mergers are unlikely to be disrupted and thus unlikely to have an electromagnetic counterparts.

The second study in this thesis builds upon the first and focuses on the capabilities of aLIGO-Virgo, LIGO A+, LIGO Voyager, the Einstein Telescope, and Cosmic Explorer to study neutron star-black hole mergers without electromagnetic counterparts. The results demonstrate that neither the present LIGO-Virgo detector network nor its near-term upgrades are likely to distinguish between neutron star-black hole and binary black hole mergers. Third-generation instruments such as Cosmic Explorer may be able to make the distinction given an event with favorable parameters. This result emphasizes the need for third-generation detectors.

The third study widens the scope of this thesis and analyzes data from all gravitational wave events detected to date to test for birefringence. Birefringence occurs when a wave's left- and right-handed polarizations propagate along different equations of motion. Bayesian inference was performed on the 4th-Open Gravitational-wave Catalog (4-OGC) using a parity-violating waveform. The vast majority of events show no deviation from general relativity, but the two most massive events (GW190521 and GW191109) support the birefringence hypothesis. Excluding these two events, the constraint on the parity-violating energy scale is an improvement over previous results by a factor of five. Future detections of massive binary black hole mergers will help shed light on the origin of this apparent birefringence.

The final study in this thesis provides a foundation that will improve future tests of general relativity using neutron stars. Any gravitational waveform for a system with a neutron star must include tidal effects. Even though tidal deformabilities in alternative theories can differ from their general relativistic counterparts, tests of general relativity seldom take this into account. The tidal deformabilities for static neutron stars in scalar-tensor theories with a focus on spontaneous scalarization are derived. The results demonstrate that tidal deformabilities can differ significantly between theories. Future analyses can apply these results alone or combine them with the parameter estimation methods developed in the first part of this thesis for more accurate tests of scalar modes in gravitational waves from neutron star mergers.

neutron stars · gravitational waves · alternative theories of gravity

Contents

1	Introduction	6
1.1	General Relativity	6
1.1.1	Gravitational Waves	8
1.1.2	Gravitational Wave Detectors	13
1.2	Data Analysis and Bayesian Inference	17
1.2.1	Data	19
1.2.2	Parameter Estimation	20
1.2.3	Model Selection	22
1.3	Neutron Stars and Tidal Deformability	24
1.3.1	Equation of State	25
1.3.2	Neutron Star Structure	27
1.3.3	Tidal Deformability	29
1.4	Alternate Theories of Gravity and Tests of General Relativity	30
1.4.1	Birefringence	32
1.4.2	Scalar-Tensor Theory	34
1.5	Clarifications of Contributions	36
1.5.1	Chapter 2	36
1.5.2	Chapter 3	37
1.5.3	Chapter 4	38
1.5.4	Chapter 5	38
2	Stringent Constraints on Neutron Star Radii From Multimessenger Observations and Nuclear Theory	40
2.1	Abstract	40
2.2	Introduction	40
2.3	Methods	46
2.3.1	Nuclear Equations of State From Chiral Effective Field Theory	46
2.3.2	Gravitational Wave Parameter Estimation	48
2.3.3	Constraints on Neutron Star Radii From Multimessenger Observations	49
2.3.4	Conditions for Neutron Star Tidal Disruption	50
2.3.5	Prospects for Tighter Constraints On Neutron Star Radii	51
2.4	Data Availability	52
2.5	Code Availability	52
2.6	Acknowledgments	54

2.7	Supplementary Material	56
2.7.1	Comparison to Previous Multimessenger Constraints	56
3	Using Gravitational Waves to Distinguish Between Neutron Stars and Black Holes in Compact Binary Mergers	58
3.1	Introduction	58
3.2	Methods	60
3.3	Results	63
3.4	Discussion	66
	Appendices	69
3.A	Data Tables	69
4	Tests of Gravitational Wave Birefringence With the Open Gravitational Wave Catalog	73
4.1	Introduction	73
4.2	Waveform Templates for Gravitational Wave Birefringence	75
4.3	Bayesian Inference	76
4.4	Results	77
4.4.1	GW190521 and GW191109	78
4.5	Discussion and Conclusion	79
	Appendices	81
4.A	Investigation of Data Quality Systematics by General Relativity Injection	81
5	Tidal Deformability of Neutron Stars in Scalar-Tensor Theory	84
5.1	Introduction and Motivation	84
5.2	Neutron Stars in Scalar-Tensor Theory	86
5.3	Stationary Perturbations	88
5.4	Neutron Star Tidal Deformability	89
5.4.1	Electric Type Love Numbers	90
5.4.2	Magnetic Type Love numbers	92
5.5	Results	95
5.5.1	Electric Love Numbers	95
5.5.2	Magnetic Love Numbers	98
5.6	Discussion	100
	Appendices	102
5.A	Numerical Methods	102
5.A.1	Background Configuration	102
5.A.2	Tidal Deformability	104
5.B	Perturbation Equations	105
5.B.1	Perturbed Energy-Momentum Tensor	105
5.B.2	Equations for Even Parity	106
5.B.3	Equations for Odd Parity	107
5.C	Conformal Transformations	108
5.C.1	Magnetic	108
5.C.2	Electric	109
5.D	Higher Order Love numbers	110

6	Conclusion and Outlook	112
7	Acknowledgements	134

1 | Introduction

LIGO detected gravitational waves from a pair of merging black holes for the first time in 2015 and opened up a new window to the universe [1]. The detection of binary neutron star merger GW170817 [2] along with its electromagnetic counterpart GRB170817A [3] in 2017 began the era of multi-messenger astronomy. LIGO has since announced nearly one-hundred confident gravitational wave events [4–7]. These observations have led to new techniques for studying compact objects and testing Einstein’s theory of general relativity in the strong field regime. Our knowledge of neutron stars and the nuclear equation of state (EOS) have greatly improved, and increasingly strong constraints have been placed on any possible deviations from general relativity.

This thesis aims to study neutron stars with gravitational waves, explore the capabilities of current and future gravitational wave detectors to detect neutron stars, test existing gravitational wave data for birefringence, and explore the behavior of neutron stars outside of general relativity.

This chapter briefly summarizes any necessary background information. The basics of general relativity and gravitational waves are presented in Section 1.1. Section 1.2 focuses on the basics of Bayesian inference and the data analysis methods used in this thesis. Section 1.3 discusses relevant aspects of neutron stars. Theories of gravity beyond general relativity are discussed in Section 1.4.

The following three chapters of this thesis contain material that has been published in or accepted to scientific journals. Section 1.5 outlines the significance of each chapter and details the contributions of the author. Chapter 2 was initially published in *Nature Astronomy* as Capano et al. [8]. Chapter 3 is accepted for publication in the *Astrophysical Journal* as Brown et al. [9] and available as a preprint [9]. Chapter 4 has been published in *Physical Review D* as Wang, Y. et al. [10]. Chapter 5 is adapted from two papers currently in preparation.

Lastly, Chapter 6 gives a summary of the results of this thesis along with an outlook for possible future research.

1.1 General Relativity

Einstein revolutionized the world’s understanding of gravity in 1915 with his theory of general relativity. Both the concept of relativity and the idea of gravity as geometry were fundamental shifts in how gravity was understood. John Wheeler once eloquently explained the idea underlying general relativity as “Spacetime tells matter how to move; matter tells spacetime how to curve” [11].

Spacetime is a 4-dimensional manifold that connects space and time and is described by the metric tensor $g_{\mu\nu}$. While the mathematics of general relativity is complex, Einstein’s theory can be

expressed in a single line

$$G_{\mu\nu} = 8\pi T_{\mu\nu} . \quad (1.1)$$

The left-hand side expresses the geometry of spacetime or ‘how it curves’ and contains the Einstein tensor $G_{\mu\nu}$. The right-hand side of the equation contains the stress-energy tensor $T_{\mu\nu}$, which includes all matter-energy source terms.

This equation, and all equations in this introduction, are written in geometric units where G is the gravitational constant, c is the speed of light in vacuum, and both are set to one ($G = c = 1$). When necessary $\hbar = 1$ as well. We will also use Einstein notation, which means a set of matching raised and lowered indices (i.e. X^μ_μ) are summed over. As is conventional, Greek indices are for 4D spacetime and take on the values 0,1,2,3, and Latin indices are for spacial coordinates and run over 1,2,3. Finally, we will assume that the spacetime metric has the $(-,+,+,+)$ signature.

Taking a closer look at the Einstein equation, we start by explicitly defining the Einstein tensor;

$$G_{\mu\nu} = R_{\mu\nu} - \frac{1}{2}Rg_{\mu\nu} , \quad (1.2)$$

where the Ricci curvature tensor $R_{\mu\nu}$ and the Ricci curvature scalar ($R = R^\mu_\mu$) contain information about the curvature of spacetime. They are both contractions of the Riemann curvature tensor $R_{\alpha\beta\mu\nu}$, which is the most common way to describe the curvature of Riemannian or pseudo-Riemannian manifolds such as spacetime. The Riemann curvature tensor, and thus the Ricci tensor and Ricci scalar, depend only on the metric tensor and its derivatives

$$R_{\beta\mu\nu}^\alpha = \partial_\mu \Gamma_{\nu\beta}^\alpha - \partial_\nu \Gamma_{\mu\beta}^\alpha + \Gamma_{\mu\gamma}^\alpha \Gamma_{\nu\beta}^\gamma - \Gamma_{\gamma\nu}^\alpha \Gamma_{\mu\beta}^\gamma , \quad (1.3)$$

where $\Gamma_{\mu\nu}^\alpha$ is the Christoffel Symbol:

$$\Gamma_{\mu\nu}^\alpha = \frac{1}{2}g^{\alpha\beta} (\partial_\mu g_{\beta\nu} + \partial_\nu g_{\beta\mu} - \partial_\beta g_{\mu\nu}) , \quad (1.4)$$

and ∂_μ are ordinary derivatives taken with respect to a coordinate x^μ .

The right-hand side of the equation contains the matter terms in the form of the stress-energy tensor $T_{\mu\nu}$, which describes the density and flux of energy and momentum through spacetime. The stress-energy tensor used throughout this paper is that of a perfect fluid:

$$T_{\mu\nu} = (\rho + p)u_\mu u_\nu + pg_{\mu\nu} , \quad (1.5)$$

where u_μ , ρ , and p are the four-velocity, density, and pressure respectively. The four velocity is defined as

$$u^\mu = dx^\mu / d\tau , \quad (1.6)$$

where τ is the proper time.

The idea of curvature is intrinsic to general relativity, but it is not necessarily intuitive. We typically consider a 2D surface, such as the surface of a ball, to be curved because of how it is embedded in a higher (3D) space. This is an extrinsic definition of curvature. There is no proof that spacetime is embedded in a higher dimensional (5D) manifold, and so an intrinsic idea of curvature is necessary. The concept of intrinsic curvature depends on parallel transport. Consider a flat 2D plane such as the one in Fig. 1.1; a vector that is transported along a closed loop on the plane while kept ‘as straight as possible’ will point in the same direction at the end as at the

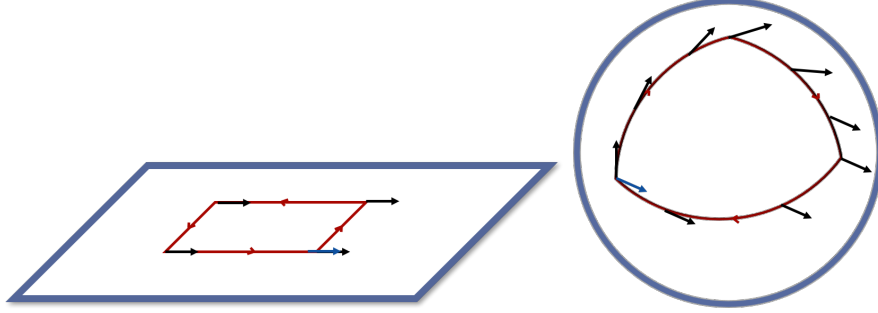


Figure 1.1: A flat plane (left) and a sphere (right) with vectors parallel transported around a closed loop on the surface. The plane is flat (has no curvature), so any vector parallel transported around a loop on the surface will be parallel to the starting vector. The sphere is curved, and the vectors before and after parallel transport along a closed loop are not parallel.

beginning. If the process is repeated on the surface of a sphere, the vector at the end will no longer be parallel to the original vector. This idea is the basis of using parallel transport to define curvature [12].

Objects move along paths that curve as little as possible in general relativity. On a flat plane, an object moves along a straight line, but on a curved surface, the object moves along a curve. These ‘straightest possible paths’ are known as geodesics. A particle moving along geodesics without any influence from non-gravitational forces is said to be in free fall [13].

Another way to think of geodesics in general relativity is to consider that they extremize the proper time (τ) between two points. In flat spacetime, a line is the shortest distance between two points, and that geodesic is governed by the following equation:

$$\frac{d^2 x^\alpha}{d\tau^2} = 0 . \quad (1.7)$$

Extending this idea to curved spaces gives the following equation of motion for geodesics

$$\frac{d^2 x^\alpha}{d\tau^2} = -\Gamma_{\mu\nu}^\alpha \frac{dx^\mu}{d\tau} \frac{dx^\nu}{d\tau} . \quad (1.8)$$

The Einstein field equations are a coupled system of non-linear partial differential equations for the metric tensor $g_{\mu\nu}$, which is commonly written either as a rank two tensor or in the form of a line element $ds^2 = g_{\mu\nu} dx^\mu dx^\nu$. These equations do not have analytical solutions except for in a handful of simple cases and must be solved using numerical methods. A few known solutions include the Minkowski metric, the Schwarzschild metric, and the Kerr metric. Schwarzschild’s famous metric describes the vacuum solution around a static black hole [14], and the Kerr metric describes the vacuum solution around a rotating black hole [15]. The simplest solution is the Minkowski metric, which describes flat spacetime:

$$ds^2 = -dt^2 + dx^2 + dy^2 + dz^2 . \quad (1.9)$$

1.1.1 Gravitational Waves

Gravitational waves are one of the fundamental predictions of general relativity; they were first proposed by Einstein in 1916 and are ripples in the fabric of spacetime itself [16]. The first gravita-

tional waves were not detected by LIGO [1] until 2015, nearly a hundred years after their proposal.

Gravitational waves are generated by the non-uniform, non-spherically symmetric motion of massive objects. There are many possible sources of gravitational waves, but all gravitational waves detected thus far come from compact binary coalescences. As two massive objects orbit each other, they emit gravitational waves, which carry away energy, shrinking their orbit until they collide. The emitted gravitational waves travel radially away from the source and have two polarizations perpendicular to the direction of propagation. As they propagate, they distort spacetime, and their passing can be detected by a change in the relative position of two test masses. The amplitude of gravitational waves is minuscule, and so the measurable change in position of the test masses is also very small, which makes them difficult to detect here on earth.

Gravitational waves that are far from their source can be considered as a small perturbation $h_{\mu\nu}$ on an otherwise flat or Minkowski spacetime $\eta_{\mu\nu}$. The metric has the form:

$$g_{\mu\nu} = \eta_{\mu\nu} + h_{\mu\nu} , \quad (1.10)$$

where $|h_{\mu\nu}| \ll 1$ everywhere. In this regime, we can work with linearized gravity to solve the Einstein equation. Linearized gravity is an approximation that applies to spacetimes where any changes $h_{\mu\nu}$ are small enough that terms of $\mathcal{O}(h_{\mu\nu}^2)$ or higher can be neglected.

Combining the approaches of Refs. [12, 13], we define ∂_μ to be the derivative operator associated with flat space $\eta_{\mu\nu}$. Indices are raised and lowered with $\eta_{\mu\nu}$ rather than the complete metric $g_{\mu\nu}$. The exception to this is $g^{\mu\nu}$, which is the inverse metric of $g_{\mu\nu}$.

The first step to constructing the Einstein equation in linearized gravity is substituting the metric Eq. (1.10) into the definition of the Christoffel symbol Eq. (1.4) and keeping linear order terms:

$$\Gamma_{\mu\nu}^\alpha = \frac{1}{2}\eta^{\alpha\beta}(\partial_\mu h_{\beta\nu} + \partial_\nu h_{\beta\mu} - \partial_\beta h_{\mu\nu}) . \quad (1.11)$$

To linear order in $h_{\mu\nu}$, the Ricci tensor is

$$\begin{aligned} R_{\mu\nu} &= R_{\mu\gamma\nu}^\gamma = \partial_\gamma \Gamma_{\mu\nu}^\gamma - \partial_\mu \Gamma_{\gamma\nu}^\gamma \\ &= \frac{1}{2}(-\square h_{\mu\nu} + \partial_\mu V_\nu + \partial_\nu V_\mu) , \end{aligned} \quad (1.12)$$

where $h = h^\mu{}_\mu$, the \square operator is the flat spacetime wave operator, also known as the D'Alembertian,

$$\square \equiv \eta^{\mu\nu} \partial_\mu \partial_\nu = -\frac{\partial^2}{\partial t^2} + \vec{\nabla}^2 , \quad (1.13)$$

and V_μ is

$$V_\mu = \partial_\gamma h_\mu^\gamma - \frac{1}{2} \partial_\mu h^\gamma{}_\gamma . \quad (1.14)$$

We will proceed to focus on waves that are a vacuum solution to the Einstein equations and perturbations on a flat spacetime. Gravitational waves also occur near a source where $T_{\mu\nu} \neq 0$, but working with the vacuum solution simplifies the Einstein equation to $R_{\mu\nu} = 0$. In making this choice, the wave solution can be discussed without delving into more complex mathematics.

Gravitational waves that are vacuum solutions and perturbations on a flat spacetime are solutions to the simplified equation

$$R_{\mu\nu} = \frac{1}{2}(-\square h_{\mu\nu} + \partial_\mu V_\nu + \partial_\nu V_\mu) = 0 . \quad (1.15)$$

In general relativity, there is the freedom to choose the gauge. Choosing the correct gauge can often simplify the problem greatly. So far, it was assumed that $\eta_{\mu\nu} = \text{diag}(-1, 1, 1, 1)$ and $h_{\mu\nu}$ is some small, unknown, perturbation; while $\eta_{\mu\nu}$ is fixed, $h_{\mu\nu}$ is not. Changes of $h_{\mu\nu}$ can still be made so long as Eq. (1.10) remains unchanged. Such coordinate changes have a specific form

$$x'^{\mu} = x^{\mu} + \xi^{\mu}(x) \quad (1.16)$$

where $\xi^{\mu}(x)$ are four arbitrary functions of the coordinates x^{μ} . $\xi^{\mu}(x)$ are of the same magnitude as $h_{\mu\nu}$. In other words, $\xi^{\alpha}(x) \ll 1$. Under a generic change of coordinates, the metric transforms in the following way

$$g'_{\mu\nu}(x') = \frac{\partial x^{\gamma}}{\partial x'^{\mu}} \frac{\partial x^{\delta}}{\partial x'^{\nu}} g_{\gamma\delta}(x) \quad (1.17)$$

Combining Eqs. (1.16) and (1.17), a new metric perturbation $h'_{\mu\nu}$ that satisfies Eq. (1.10) can be defined:

$$h'_{\mu\nu} = h_{\mu\nu} - \partial_{\mu}\xi_{\nu} - \partial_{\nu}\xi_{\mu} . \quad (1.18)$$

As ξ_{ν} is arbitrary, but small, it can be chosen so that Eq. (1.15) takes on a simpler form. Specifically, it is chosen to ensure that $V'_{\alpha} = 0$. Eq. (1.15) reduces to the gravitational wave equation in this case:

$$\square h_{\mu\nu}(x) = 0 , \quad (1.19)$$

where we have dropped the prime. The wave equation is valid as long as the gauge conditions hold:

$$V_{\mu} = \partial_{\gamma} h_{\mu}^{\gamma} - \frac{1}{2} \partial_{\mu} h^{\gamma}_{\gamma} = 0 . \quad (1.20)$$

The wave equation appears throughout physics, and its solutions are well known. To solve the gravitational wave equation, we start by searching for a solution with the familiar form of a plane wave

$$h_{\mu\nu} = a_{\mu\nu} e^{i\mathbf{k}\cdot\mathbf{x}} , \quad (1.21)$$

where $\mathbf{k} = (\omega_k, \vec{k})$, is a definite wave 4-vector and $a_{\mu\nu}$ is a tensor whose components are the wave amplitudes.

The amplitudes of $a_{\mu\nu}$ are not arbitrary and are constrained by the wave equation and the gauge conditions. To properly define the new metric, it is necessary to choose the vectors ξ^{μ} that do not violate the gauge conditions. Inserting Eq. (1.18) into Eq. (1.20), we find that ξ^{μ} must satisfy the following relation

$$\square \xi_{\mu} = 0 . \quad (1.22)$$

Since both $h_{\mu\nu}$ and ξ^{μ} satisfy the wave equation, the transformation can be used to make any four components of $h_{\mu\nu}$ vanish. Traditionally, the following choices are made

$$h_{tj} = 0 \quad (1.23a)$$

$$h^{\gamma}_{\gamma} = 0 \quad (1.23b)$$

It follows from these choices that $a_{t\mu} = a^{\gamma}_{\gamma} = 0$. Combining these conditions with the gauge constraint (Eq. (1.20)), yields

$$V_t = \frac{\partial h_t^t}{\partial t} = i\omega_k a_{tt} e^{i\mathbf{k}\cdot\mathbf{x}} = 0 \quad (1.24a)$$

$$V_i = \frac{\partial h_i^j}{\partial j} = ik^j a_{ji} e^{ik \cdot x} = 0. \quad (1.24b)$$

This implies that

$$a_{tt} = 0 \quad (1.25a)$$

$$k^i a_{ij} = 0. \quad (1.25b)$$

The $k^i a_{ij} = 0$ condition ensures that gravitation waves, similar to electromagnetic waves, are transverse waves.

From the original ten free coefficients $\alpha_{\mu\nu}$, only two degrees of freedom remain. The four time components vanish because of Eqs. (1.23a) and (1.25a). The combination of Eqs. (1.23b) and (1.25b) leads to four further constraints, leaving only two independent values in $a_{\mu\nu}$. By orienting the coordinates such that the wave propagates in the \hat{z} direction, we can write the tensor $a_{\mu\nu}$ explicitly. All a_{iz} components vanish because the waves are transverse. This leaves a single symmetric 2×2 matrix whose trace must vanish (Eq. (1.23b)). We have the most general solution to the linearized Einstein equation with a definite wave number expressed in Cartesian coordinates:

$$h_{\mu\nu}(x) = \begin{pmatrix} 0 & 0 & 0 & 0 \\ 0 & A_+ & A_\times & 0 \\ 0 & A_\times & -A_+ & 0 \\ 0 & 0 & 0 & 0 \end{pmatrix} e^{i\omega(z-t)}. \quad (1.26)$$

This choice of gauge, where the transverse and traceless conditions are written out explicitly, is known as the transverse-traceless gauge and is often denoted $h_{\mu\nu}^{TT}$. The two amplitudes A_+ and A_\times represent the two gravitational wave polarizations generally referred to as ‘plus’ and ‘cross’.

The general equation for a plane wave moving in the \hat{z} is a linear combination of both the plus and cross modes:

$$(h^{\mu\nu})^{TT}(t, z) = h_+(t, z)e_+^{ij} + h_\times(t, z)e_\times^{ij} \quad (1.27)$$

where e_+^{ij} and e_\times^{ij} are the necessary combinations of the unit basis vectors e_x^i and e_y^i , and

$$h_+(t, z) = A_+ \cos(\omega_k(t - z) - \phi_+) \quad (1.28)$$

$$h_\times(t, z) = A_\times \cos(\omega_k(t - z) - \phi_\times) \quad (1.29)$$

where $\phi_{+, \times}$ are phase angles.

A completely generic waveform is a superposition of waves with the form in Eq. (1.26) with different values of ω , A_+ , A_\times , and different directions of propagation.

There are many predicted astrophysical sources of gravitational waves; supernovae, compact binary coalescences, and rotating non-axisymmetric neutron stars are a few candidates [17]. So far, we have only detected mergers of compact objects, such as black holes and neutron stars [1, 2, 18], and it is these systems that are the focus of this thesis.

The gravitational wave signals emitted by compact binary coalescences have three parts: inspiral, merger, and ringdown [19, 20]. The inspiral phase occurs as the two objects orbit each other. As they orbit, they emit gravitational waves, which radiate away energy and cause the orbit to shrink and the velocities to increase. In turn, this causes the amplitude and frequency of the emitted gravitational waves to grow and accelerates the inspiral process. While the inspiral phase is the vast majority of the life span of any binary, only the end of the inspiral phase, where the

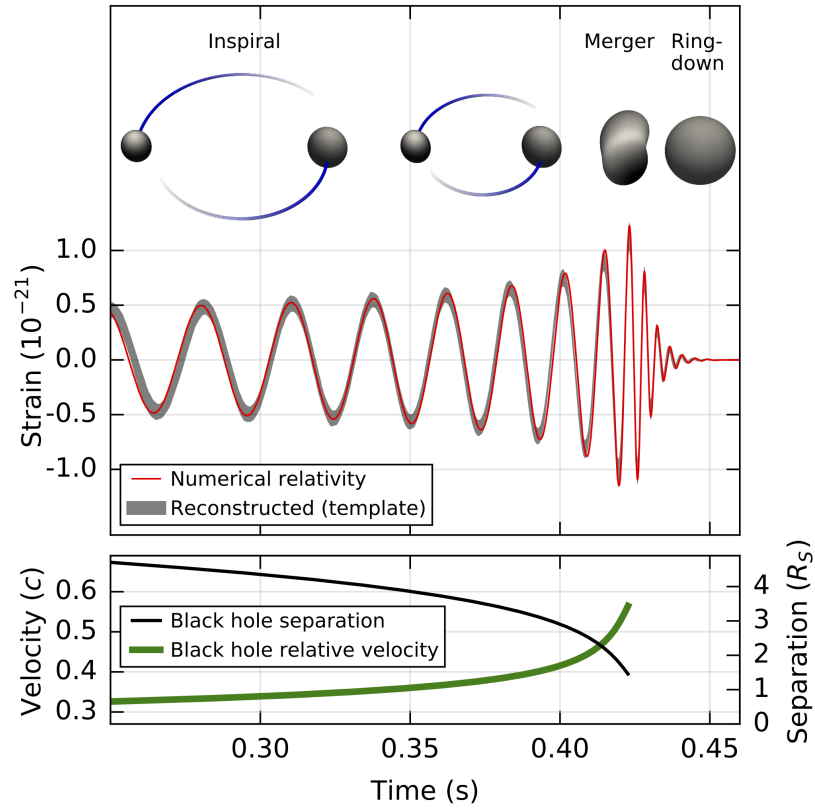


Figure 1.2: Figure 2 in the LIGO paper on the first ever detected gravitational wave event: GW150914 [1]. The upper panel shows a schematic of the three stages of a compact binary coalescence: inspiral, merger, ringdown. It also shows two gravitational waves (detected dimensionless strain as a function of time) that are constructed to be as close to the observed signal of GW150914 as possible. The lower panel shows how the binary velocity and separation evolves over time as the system coalesces.

gravitational waves are strongest, is detectable on Earth. This inspiral phase can be modeled by a post-Newtonian expansion [21, 22] or the effective-one-body formalism [23], and can be calculated without full numerical solutions to the Einstein equations.

When the objects are close enough together, the merger phase begins. Two compact objects merging while moving close to the speed of light is a fully relativistic event, dependent on the Einstein equations. The approximations used to model the inspiral fail in this regime, and numerical relativity is needed to solve the Einstein equations [24–26].

During the ringdown phase, the merger remnant settles down from its highly perturbed state to its final one. The remnant can be either a black hole or a neutron star. Only a pair of low mass neutron stars merging can create a stable neutron star remnant [27, 28]. The ringdown phase for a merger with a neutron star merger is highly complex and can only be modelled with relativistic hydrodynamics. The ringdown phase for black hole remnants is modeled as perturbations of the Kerr spacetime, which are radiated away. The solution to these perturbation equations is a superposition of exponentially damped sinusoids [29, 30].

1.1.2 Gravitational Wave Detectors

The first gravitational waves were first detected in 2015 [1] almost one hundred years after they were proposed by Einstein [16]. While detecting gravitational waves is conceptually straightforward, it presents a serious technical difficulty because the gravitational wave strain is $\mathcal{O}(10^{-20})$ [1].

To understand how gravitational waves can be detected, first consider a pair of test masses at rest in flat spacetime. As a gravitational wave passed through, the spacetime between them expands and contracts, changing the proper distance between the two even though they remain at rest, or equivalently, in free fall [13].

Take two particles A and B that are at rest in the coordinate frame (t, x, y, z) . Then, choose the spacial coordinates such that A is at the origin $x_A^i = (0, 0, 0)$ and B is at some arbitrary position $x_B^i = (x_B, y_B, z_B)$. As both A and B are at rest, the only non-vanishing component of their 4-velocities is the time component i.e.

$$u_A^\mu = u_B^\mu = (1, 0, 0, 0) . \quad (1.30)$$

When the gravitational wave passes through, the change in spacetime will cause a change in the proper distance between A and B . We need to solve the geodesic equation (Eq. (1.8)) in order to follow the change in position of the test masses. Since we defined gravitational waves to be small $|h_{\mu\nu}| \ll 1$, the changes in positions of the particles (δx_A^i and δx_B^i) are also small, and terms second order or higher in $\delta x_{A,B}^i$ can be neglected. Writing Eq. (1.8) in terms of δx^i , which can be either δx_B^i or δx_A^i , and using the fact that $\Gamma_{\mu\nu}^i = 0$ in flat spacetime, we have

$$\frac{d^2 \delta x^i}{d\tau^2} = -\delta\Gamma_{\mu\nu}^i u^\mu u^\nu = -\delta\Gamma_{tt}^i \quad (1.31)$$

where $u^{\mu,\nu}$ are the unperturbed four-velocities from Eq. (1.30) and $\delta\Gamma_{\mu\nu}^i$ are first order changes to $\Gamma_{\mu\nu}^i$. $\delta\Gamma_{tt}^i$, which is calculated using the gravitational wave metric Eq. (1.26) and Eq. (1.11), vanishes, and Eq. (1.31) becomes

$$\frac{d^2 \delta x^i}{d\tau^2} = 0 . \quad (1.32)$$

Since the two test masses were at rest initially, both $\delta x^i = 0$ and $d(\delta x^i)/d\tau = 0$ at $\tau = 0$, the above equation implies that

$$\delta x_{A,B}^i(\tau) = 0. \quad (1.33)$$

The coordinate positions of the test masses remains unchanged, and their spacial coordinate separation is similarly unchanged. This does not mean that their proper distance is unaffected [12, 13, 31].

The change in proper distance δL between two points is different from the coordinate separation. The proper distance between two points is [31]

$$\delta L = \int |ds^2|^{1/2} \quad (1.34)$$

Consider the same two test masses. A remains at the origin, but B is now on the x -axis some distance L from A . A gravitational wave passes through, propagating along the z -axis. The proper length $L(t)$ measured along the x -axis as the gravitational wave passes through is

$$L(t) = \int_{x_A}^{x_B} |g_{\mu\nu} dx^\mu dx^\nu|^{1/2} \quad (1.35)$$

$$= \int_A^B |g_{xx}|^{1/2} dx \quad (1.36)$$

$$= \int_A^B |(\eta_{xx} + h_{xx}^{TT})|^{1/2} dx \quad (1.37)$$

$$\approx L[1 + \frac{1}{2}h_{xx}^{TT}(t, 0)]. \quad (1.38)$$

To obtain the last line, it is necessary that the scale on which h_{xx}^{TT} varies must be much greater than the length from A to B so that h_{xx}^{TT} can be assumed to be approximately constant over the distance L . The change in distance δL is then given by

$$\frac{\delta L}{L} = \frac{1}{2}h_{xx}^{TT}(t, 0). \quad (1.39)$$

Since $h_{xx}^{TT}(t)$ is generally not zero, the change in proper length is nonzero as well. Furthermore, the proper distance between the two test masses changes with time, just like h_{xx}^{TT} . $\delta L/L$ is known as the dimensionless strain, and, in this example, it oscillates with half the amplitude of the gravitational wave:

$$\frac{\delta L}{L} = \frac{1}{2}A_+ \cos(\omega_k(t - z) - \phi_+) \quad (1.40)$$

This example assumed that the test mass was along the x -axis, but the test mass B could be anywhere in space. Repeating this calculation along the y - and z -axes yields a similar expression for the \hat{y} direction but not in the \hat{z} direction because \hat{z} is the direction of propagation. The gravitational wave strain along the y -axis takes the form

$$\frac{\delta L}{L} = -\frac{1}{2}A_+ \cos(\omega_k(t - z) - \phi_+). \quad (1.41)$$

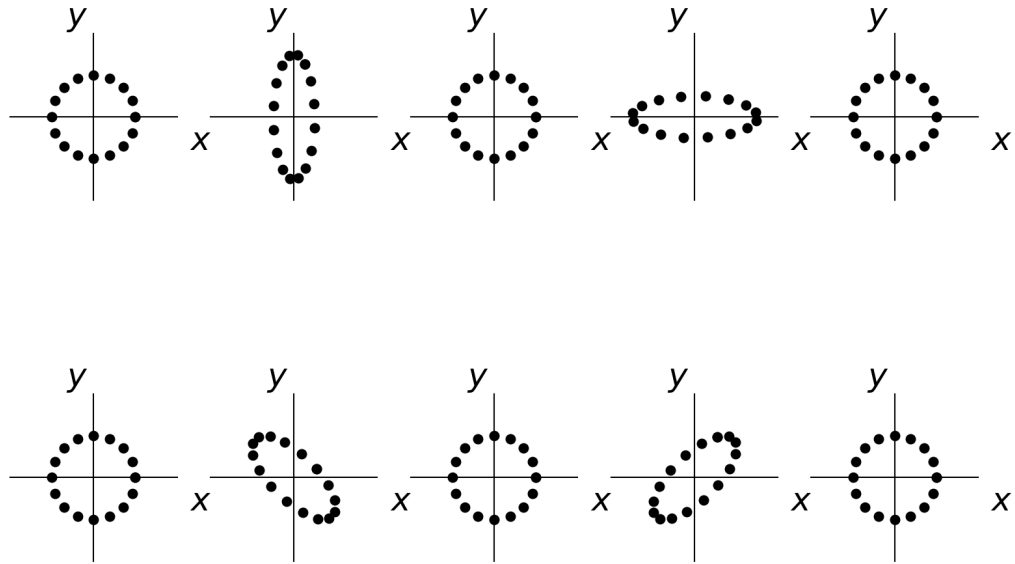


Figure 1.3: The effect of a passing gravitational wave on a ring of particles in free fall. Each subplot shows a ring of free falling particles in the xy -plane as they encounter a gravitational wave traveling in the \hat{z} direction. The top row depicts the plus h_+ polarization, and the bottom row shows the cross h_\times polarization. The plus polarization first stretches spacetime the \hat{y} direction and compresses it in the \hat{x} direction. Then it compresses in the \hat{y} direction and stretches in the \hat{x} direction. This causes the particles to move in a rough plus shape, hence the name of the polarization mode. The cross polarization mode has the same effect except on a 45° angle.

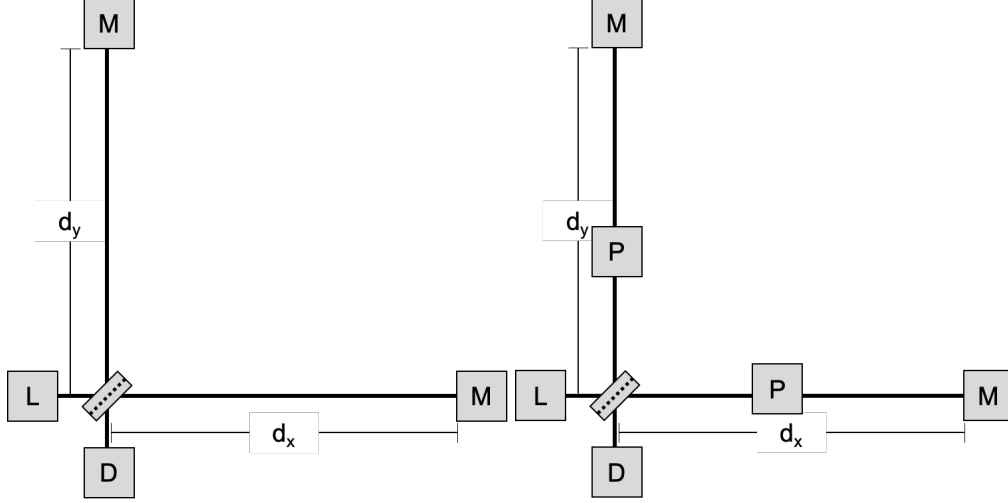


Figure 1.4: A schematic of (right) a Michelson interferometer and (left) a Michelson interferometer with a power recycling mirror.

The two equations for $\delta L/L$ give us an idea of how a ring of test masses in the xy -plane would behave. Repeating the process with the cross-polarization $h_{xy} = h_{yx}$, we can completely determine the behavior of free-falling particles in the path of a gravitational wave [13, 31].

This principle has been applied to gravitational wave detectors around the world [32–34]. The first two of these detectors to observe gravitational waves were the two advanced Laser Interferometer Gravitational Wave Observatory (LIGO) detectors in the US [1]. Since then, the Italian Virgo detector began taking data [35]. This thesis uses data from all of these detectors [36]. The Japanese KAGRA detector has recently entered its first data-taking phase and is expected to join LIGO and Virgo or the fourth scheduled observing run [32].

The change in proper distance between two free-falling test masses is miniscule $\delta L/L \lesssim \mathcal{O}(10^{-20})$. The gravitational wave strain is measured with Michelson interferometers shown in Fig. 1.4. Interferometers take advantage of laser interference patterns to measure the tiny changes in proper distance between two test masses.

The test particles in these detectors are two mirrors (M), one at the end of each interferometer’s arm, and a beam splitter. Light is emitted from a laser (L), split by the beam splitter, travels along two perpendicular arms, reflected by the mirror test masses back to the beam splitter, and recombined before traveling to the detector. The laser light travels a distance through each arm (d_x and d_y) that is some multiple of its wavelength λ i.e. $d_x = n_x \lambda$ where n is not necessarily an integer. Destructive interference occurs when they differ by an odd number of half wavelengths, and constructive interference occurs when two waves differ by an integral number of wavelengths.

$$\Delta L_{constructive} = d_x - d_y = n\lambda \quad n = 0, 1, 2, \dots \quad (1.42a)$$

$$\Delta L_{destructive} = d_x - d_y = \left(n + \frac{1}{2}\right) \lambda \quad n = 0, 1, 2, \dots \quad (1.42b)$$

As the δL increases with arm length, a power recycling mirror (P) is added to each arm. Then the beam bounces back and forth between the mirrors, increasing the effective arm length and thus the detectable change. The beams are tuned to be out of phase when they reach the detector.

When a gravitational wave passes through, it changes the arm lengths d_x and d_y causing the interference pattern to change. ΔL changes over time between varying levels of constructive and destructive interference as the gravitational wave passes through, and the detector picks up this light pattern.

Consider a gravitational wave moving perpendicular to the detector along the z -axis with some frequency ω . If the x - and y -axes are oriented along the two detector arms, both arms will contract and expand in and out of phase:

$$\frac{\delta d_x}{d_x} = +\frac{1}{2}a \sin(\omega t) \quad (1.43a)$$

$$\frac{\delta d_y}{d_y} = -\frac{1}{2}a \sin(\omega t) \quad (1.43b)$$

Combining Eq. (1.42) and Eq. (1.43), we can calculate ΔL and see that it varies with time as the gravitational wave passes through:

$$\Delta L = (1 + \delta d_x)d_x - (1 + \delta d_y)d_y \quad (1.44)$$

This equation assumes that the detector's arm length $d_x = d_y = d$ is much less than the wavelength of the passing gravitational wave ($d \ll \lambda_{GW}$), which ensures that the metric tensor is approximately constant for the time it takes for the laser light to travel through the detector.

A gravitational wave source could be anywhere in the sky, in which case some combination of the plus and cross modes ($h_{+,\times}$) are detected [37]. This strain $h(t)$ will depend on the location of the source with respect to the detector:

$$h(t) = F_+(\theta, \phi, \Psi)h_+ + F_\times(\theta, \phi, \Psi)h_\times \quad (1.45)$$

where θ and ϕ are the spherical angular coordinates of the source in the frame of the detector, and Ψ is a polarization angle that relates the detector frame and the radiation frame.

The two response functions are

$$F_+(\theta, \phi, \Psi) = \frac{1}{2}(1 + \cos^2 \theta) \cos(2\phi) \cos(2\psi) - \cos(\theta) \sin(2\phi) \sin(2\Psi) \quad (1.46a)$$

$$F_\times(\theta, \phi, \Psi) = \frac{1}{2}(1 + \cos^2 \theta) \sin(2\phi) \cos(2\psi) - \cos(\theta) \sin(2\phi) \sin(2\Psi) \quad (1.46b)$$

Due to the rotation of the earth, these are functions of time as well.

This is the basic concept for gravitational wave detectors. In practice there are a great many technical challenges. As detected dimensionless strains are $\mathcal{O}(10^{-21})$, the detector must be extremely sensitive. For a more technical discussion of the design of existing detectors see [33, 34].

1.2 Data Analysis and Bayesian Inference

Parts of this thesis include analysis of real or simulated data from gravitational wave detectors such as LIGO. The goal of the analysis is to either learn about the properties of the source or to determine what models best fit the data. This analysis uses Bayesian inference, and this section lays out the basics of the techniques used. The basis of Bayesian inference is Bayes theorem, which can be derived from the basic laws of probabilities.

Assuming that we have two statements A and B , it is possible to derive the following relation from the product rule:

$$p(A, B) = p(A|B)p(B) = p(B|A)p(A), \quad (1.47)$$

where $p(A, B)$ is the probability that both A and B are true and $p(A|B)$ is the probability that A is true given B is true. If both A and B are assumed to be true given some third statement C , then the above equation becomes

$$p(A, B|C) = p(A|B, C)p(B|C) = p(B|A, C)p(A|C). \quad (1.48)$$

This can be rearranged into Bayes theorem, which is the basis of Bayesian inference [38]

$$p(A|B, C) = \frac{p(B|A, C)p(A|C)}{p(B|C)}. \quad (1.49)$$

This work is interested in the relationship between some parameters $\vec{\vartheta}$, the data d , and a gravitational wave model or waveform h .

The data $d = d_i(t)$ is the sum of time series data from a network of gravitational wave detectors i . The data depends linearly on the detector noise $n_i(t)$ and any signal present $h_i(t, \vec{\theta})$:

$$d_i(t) = n_i(t) + h_i(t, \vec{\theta}). \quad (1.50)$$

$\vec{\vartheta}$ is a set of fourteen parameters that define gravitational waveform. Fig. 1.5 displays the intrinsic and extrinsic parameters. The parameters intrinsic to the binary determine the phase and amplitude evolution of the gravitational waves emitted. These are the individual masses $m_{1,2}$, three-dimensional spin vectors $\chi_{1,2}$, dimensionless tidal deformabilities $\Lambda_{1,2}$, and the binary's eccentricity e . In the case of a black hole, the tidal deformability is zero. The extrinsic parameters, which affect only the amplitude, fix the location of the source in relation to the detectors or visa-versa. The five necessary angles are typically expressed as sky location (right ascension α and declination δ), inclination of the binary ι , polarization ψ , and reference phase ϕ . The final parameters are the luminosity distance to the source d_L and the coalescence time t_c . The extrinsic parameters are important because the detected gravitational wave strain is a combination of the plus and cross polarization and depends on the extrinsic parameters (see Sec. 1.1.1 for more details).

$$h(t) = F_+(t; \alpha, \delta, \psi)h_+ + F_\times(t; \alpha, \delta, \psi)h_\times \quad (1.51)$$

where $F_{+, \times}$ are functions of the angles defining the location of the source.

The large number of parameters and the fact that many of the signal's parameters are correlated make Bayesian inference of gravitational wave signals difficult and computationally expensive. Extensive work by the community has made gravitational wave inference possible [39, 40]. Despite this, simplifications are often necessary in Bayesian inference of gravitational waves. For instance, it is assumed initial eccentricity has been radiated away by the time the binary enters the detectors' sensitivity bands is standard. Analyses also typically assume that the black hole spin vectors align with the binary's angular momentum. Based on electromagnetic observations of binary neutron stars, the spins of neutron stars are often assumed to be negligible.

Substituting the values of interest, we re-express Bayes theorem as [40, 41]

$$p(\vec{\vartheta}|\vec{d}(t), h) = \frac{p(\vec{d}(t)|\vec{\vartheta}, h)p(\vec{\vartheta}|h)}{p(\vec{d}(t)|h)}. \quad (1.52)$$

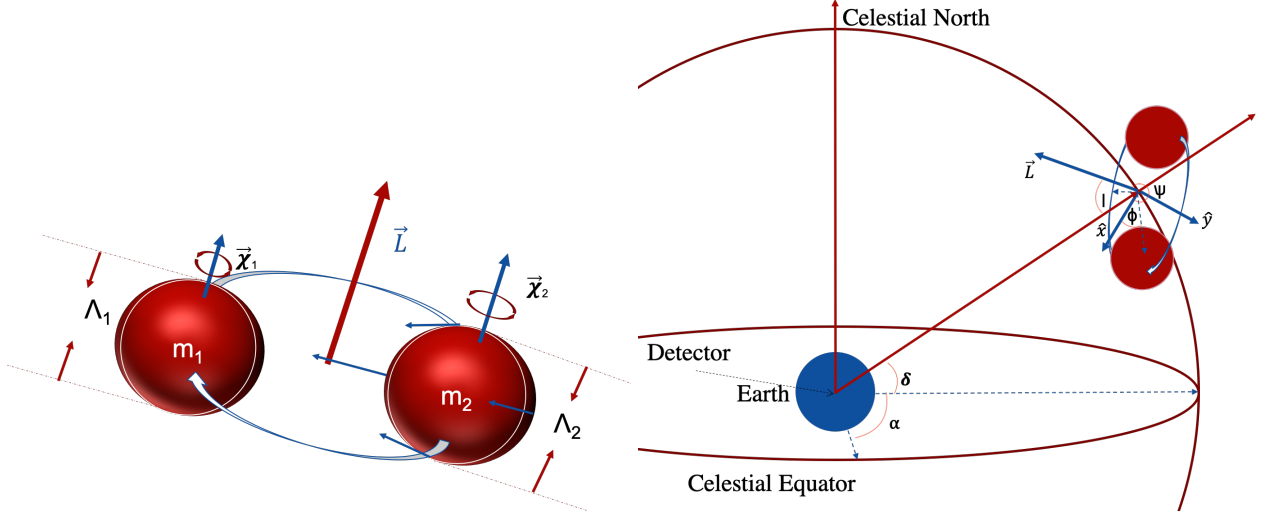


Figure 1.5: The intrinsic (left) and extrinsic parameters (right) of a compact binary coalescence. Intrinsic parameters are component mass $m_{1,2}$, spin $\vec{\chi}_{1,2}$, and dimensionless tidal deformability $\Lambda_{1,2}$. The orbital momentum \vec{L} is labeled for reference to the extrinsic parameters. The extrinsic parameters are sky location (right ascension α and declination δ), distance d_L , inclination i , polarization ψ , and phase ϕ .

The posterior probability distribution or simply posterior $p(\vec{\vartheta}|\vec{d}(t), h)$ gives the probability distribution of the parameters given the data and the hypothesis and is the end goal in Bayesian parameter estimation. The likelihood $\mathcal{L} = p(\vec{d}(t)|\vec{\vartheta}, h)$ indicates how likely the data is given the hypothesis and specific parameter ϑ_i . Calculating the likelihood requires that the model h is generative, i.e., that the model allows us to predict the data given the parameters. The prior probability distribution or prior contains any a priori information on the parameters: for instance, neutron star masses M_{NS} are constrained to be between one and three solar masses ($1M_\odot < M_{NS} < 3M_\odot$). Lastly, the evidence $\mathcal{Z} = p(\vec{d}(t)|h)$ is also known as the marginalized likelihood. It is the likelihood \mathcal{L} marginalized, or integrated, over all variables, and so it is independent of them i.e.

$$p(\vec{d}(t)|h) = \int p(\vec{\vartheta}|d, h) d\vartheta_1 \dots d\vartheta_n . \quad (1.53)$$

Probability density functions are continuous distributions, and they describe the probability over a finite interval rather than at a single point. Therefore, the results are presented not as a single number but in a credible interval. The $x\%$ credible interval is the interval in which the true value of the parameter lies with $x\%$ probability. In this work, we typically use the 90% credible interval and write it as A_{-C}^{+B} where A is the median value and $A - C$ and $A + B$ are the lower and upper boundaries of the x -th percentile credible interval [40].

1.2.1 Data

There are two types of data used in this work: gravitational wave data from the LIGO-Virgo (LVC) data release [36] and simulated gravitational wave data using detector sensitivity curves

from LIGO-Virgo, LIGO A+, LIGO Voyager, the Einstein Telescope, or Cosmic Explorer 1 and 2 [42–44].

As was written in Eq. (1.50), we assume that the data $d_i(t)$ is a combination of detector noise $n_i(t)$ and a possible signal $h_i(t, \vec{\vartheta})$. The signal $h_i(t, \vec{\vartheta})$ in each detector is different because it depends on the location and orientation of the detector. The noise is assumed to be stationary and Gaussian. These assumptions are essential to parameter estimation, which is discussed in the next section. When analyzing LIGO-Virgo Collaboration (LVC) data, an examination of the noise near the signal can validate these assumptions.

Simulated gravitational wave data is generated using a gravitational waveform approximant and a detector’s noise sensitivity curve. Stationary, white Gaussian noise is generated and then colored by the power spectral density representative of the desired detector. The noise is then added to waveform $h(t, \vec{\vartheta})$ with parameters $\vec{\vartheta}$.

Nearly all waveform approximants used in this analysis combine the inspiral, merger, and ring-down signals and are calibrated against numerical relativity data. There are several types of waveform approximants constructed using different methods. They include analytical Post-Newtonian, semi-analytical effective-one-body, and numerical relativity surrogate models. As Bayesian inference evaluates waveforms $\mathcal{O}(10^9)$ times per analysis, waveforms need to be fast and efficient. Waveforms from numerical relativity, which are slow and require significant computational resources, are prohibitively expensive.

There are numerous waveform approximants for binary black hole mergers (IMRPhenomX-PHM [45], IMRPhenomPv3HM [46], NRSur7dq4 [47]), binary neutron star mergers (TaylorF2 [48–53], IMRPhenomD_NRTidal [54–57]), and neutron star-black hole mergers (IMRPhenomNSBH [54, 56–58], SEOBNRv4_ROM_NRTidalv2_NSBH [59]). As an inspiral-only model, TaylorF2 has limited application, but it suffices for GW170817 as the portion of the signal picked up by the detectors came from the inspiral phase.

1.2.2 Parameter Estimation

The goal of Bayesian parameter estimation is to determine posterior distributions $p(\vec{\vartheta}|\vec{d}(t), h)$ from data using Bayes theorem. The goal of parameter estimation in this work is to determine the properties of the gravitational wave source, e.g., masses, spins, tidal deformabilities, sky location, and distance.

From Bayes theorem, defined in Eq. (1.52), we can see that

$$p(\vec{\vartheta}|\vec{d}(t), h) \propto p(\vec{d}(t)|\vec{\vartheta}, h)p(\vec{\vartheta}|h). \quad (1.54)$$

The posterior depends only on the likelihood \mathcal{L} and the prior. The evidence $\mathcal{Z} = p(\vec{d}(t)|h)$ is independent of the parameters $\vec{\vartheta}$ and acts only as a normalization factor that is the same for all parameters. Therefore, it can be neglected during parameter estimation.

Often, only a subset of the full parameter space is of interest. In this case, the posterior probability is marginalized over the unwanted parameters by integrating $p(\vec{d}(t)|\vec{\vartheta}, H)p(\vec{\vartheta}|H)$ over them.

As discussed briefly above, the prior contains any information known about the parameter ϑ before considering the data. Since the posterior depends on the prior, it is important to choose a prior carefully. Generally, one chooses the priors in a way that reduces any bias, but choosing an appropriate prior distribution can decrease computation time and prevent non-physical results.

An example of a prior choice is choosing declination δ and right ascension α to be uniform over the entire sky. This limits the analysis to considering only sky locations that make physical sense without favoring any specific region of the sky and skewing the results. While the choice of prior is important, in the end, it is a specific choice based on considerations specific to each project. We leave the discussion of specific prior choices to the individual chapters.

The observed data enters Bayes theorem through the likelihood \mathcal{L} , which is the probability of obtaining the data given a hypothesis or waveform and a specific set of parameters. `PyCBC Inference` assumes that the noise is stationary, Gaussian, and not correlated between detectors when calculating the likelihood. Gaussian noise, which is generated from stochastic processes, follows the familiar Gaussian distribution [60]:

$$f(x) = \frac{1}{\sqrt{2\pi}\sigma} e^{-\frac{1}{2}\left(\frac{x-\mu}{\sigma}\right)^2} \quad (1.55)$$

Here we assume that the mean $\mu = 0$ and the standard deviation $\sigma > 0$ is known. The noise is also assumed to be stationary i.e., σ does not evolve with time.

The likelihood of a system with Gaussian noise $n(t)$ is well known:

$$p(\vec{d}(t)|\vec{\vartheta}, H) = \exp\left(-\frac{1}{2}\sum_{i=1}^N \langle \tilde{n}_i(f)|\tilde{n}_i(f)\rangle\right) \quad (1.56)$$

where N is the number of detectors in the network and $\tilde{n}(f)$ is the frequency-domain representation of $n(t)$, which is obtained through a Fourier transform [61]. The inner product $\langle \tilde{a}_i(f)|\tilde{b}_i(f)\rangle$ is defined to be

$$\langle \tilde{a}_i(f)|\tilde{b}_i(f)\rangle = 4\mathbb{R} \int_0^\infty \frac{\tilde{a}_i(f)\tilde{b}_i(f)}{S_n^{(i)}(f)} \quad (1.57)$$

where $S_n^{(i)}(f)$ is the power spectral density of the i -th detector's noise.

From the definition of the data (Eq. (1.50)), the noise can be written as a function of the data itself $d(t)$ and the waveform model $h_i(t, \vec{\vartheta})$, both of which are known:

$$n_i(t) = d_i(t) - h_i(t, \vec{\vartheta}) \quad (1.58)$$

By substituting the above into Eq. (1.56), the definition of the likelihood can be rewritten into a more useful form [61]:

$$p(\vec{d}(t)|\vec{\vartheta}, H) \propto \exp\left(-\frac{1}{2}\sum_{i=1}^N \langle \tilde{d}_i(f) - \tilde{h}_i(f, \vec{\vartheta})|\tilde{d}_i(f) - \tilde{h}_i(f, \vec{\vartheta})\rangle\right). \quad (1.59)$$

A stochastic sampler such as a Markov chain Monte Carlo (MCMC) sampler can then construct the posterior distribution. An ensemble MCMC sampler selects a set of n samples $\vec{\vartheta}_n$ from the prior distributions, approximating a random selection of points in prior space. From this random distribution, the MCMC chain evolves with each iteration l . For each set of parameters $\vec{\vartheta}_l^{(k)}$, the sampler proposes a ‘jump’ or new set of parameters $\vec{\vartheta}_l^{\prime(k)}$ from a proposal distribution Q . This new point $\vec{\vartheta}_l^{\prime(k)}$ only depends on $\vec{\vartheta}_l^{(k)}$ and no previous points. Based on a given acceptance probability, the

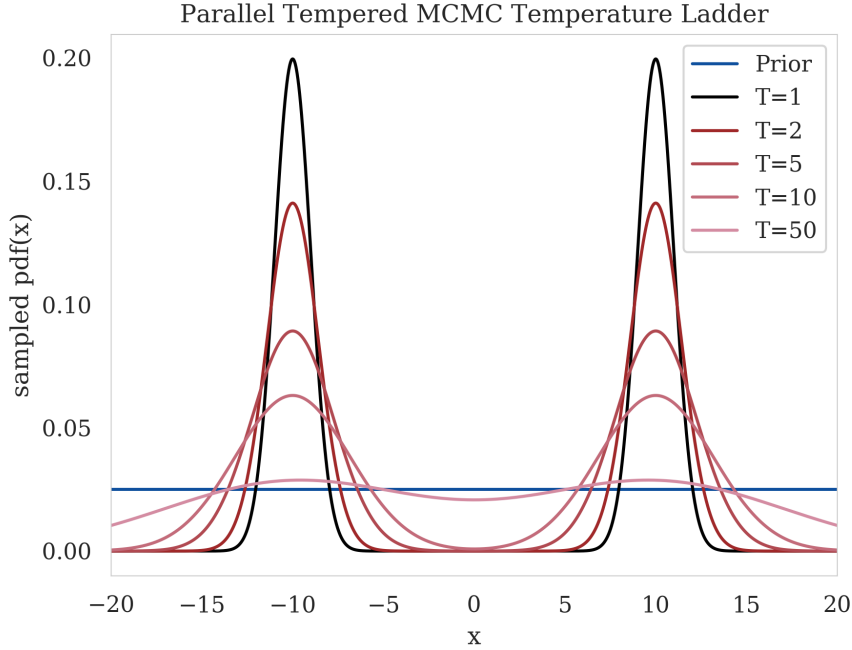


Figure 1.6: A one-dimensional posterior distribution with two Gaussian peaks, both with $\sigma = 1$ and with $\mu = \pm 10$. The prior is uniform between $[-20, 20]$. The prior distribution is uniform and plotted in blue. The target distributions for a temperature ladder $T = (1, 2, 5, 10, 50)$ are shown.

new point is either rejected and $\vec{v}_{l+1}^{(k)} = \vec{v}_l^{(k)}$ or accepted and $\vec{v}_{l+1}^{(k)} = \vec{v}_l^{(k)}$. After enough iterations, the ensemble converges to a distribution proportional to the posterior probability distribution.

There are two samplers used in this thesis: a parallel tempered MCMC sampler called `emcee_pt` [62, 63] and a dynamic nested sampling algorithm `dynesty` [64, 65]. In this work, `emcee_pt` is primarily used in parameter estimation, and `dynesty` is primarily used in model selection. `dynesty` is discussed in depth in the next section.

The `emcee_pt` sampler combines an MCMC sampler with a process called parallel-tempering. Parallel-tempering involves multiple chains evolving at different ‘temperatures’ T . The likelihood evaluated for each chain is raised to the power of $1/T$. As $T \rightarrow \infty$, the posterior distribution being sampled approaches the prior [62]. Fig. 1.6 demonstrates the effect of the temperature ladder. High-temperature chains can move about the prior volume without becoming trapped in regions of high density, and low-temperature chains explore high-density regions more effectively. Exchanges between chains at different temperatures allow colder chains to move between widespread modes. Parallel tempered MCMC samplers are particularly suited to posterior distributions with well-separated modes[62].

1.2.3 Model Selection

The second use of Bayes Theorem in this paper is model selection. As the name suggests, Bayesian model selection aims to determine to what extent the data favors one model over the other.

The basis of model selection is what is known as the Bayes factor \mathcal{B} , which gives a numerical

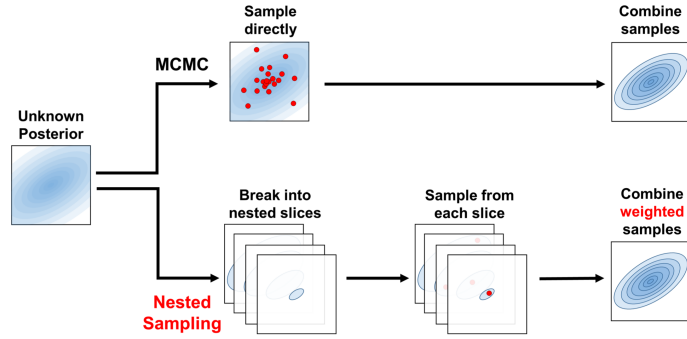


Figure 1.7: Figure 1 from the 2020 `dynesty` paper [64]. It contains a schematic representation of the difference between a traditional MCMC sampler to a nested sampler. The MCMC sampler samples the posterior directly, but the nested sampler breaks the posterior up into nested slices and samples those before combining the slices together at the end.

indication of how much the data supports one hypothesis H_A over another H_B . When $\mathcal{B} > 1$, H_A is favored over H_B , and the larger \mathcal{B} is, the more H_A is favored.

Mathematically, the Bayes factor is the ratio of the evidences for two different models:

$$\mathcal{B} = \frac{p(\vec{d}(t)|H_A)}{p(\vec{d}(t)|H_B)} = \frac{\mathcal{Z}_A}{\mathcal{Z}_B}, \quad (1.60)$$

and the evidence is defined in Eq. (1.53).

Throughout this thesis, the evidences are calculated using a dynamic nested sampler called `dynesty` [64, 65] accessed through the `PyCBC Inference Toolkit` [40]. Nested sampling algorithms differ from MCMC approaches because they estimate the evidence instead of the posterior. This makes nested samplers particularly suited to model selection.

Nested samplers break down the problem of sampling the posterior into three parts:

1. slicing the posterior into many simpler distributions
2. sampling each of the smaller distributions
3. combining the results from each slice to form a single posterior.

The algorithm begins by selecting N points, referred to as ‘live’ points, uniformly throughout the prior. For each iteration i , the point $\vec{\vartheta}_i^n$ with the lowest likelihood is saved to a list of ‘dead’ points along with a weight w_i . This weight is an estimation of how much of the prior mass lies between the likelihood hypersurfaces defined by the new dead point and the one before it. A new point $\vec{\vartheta}_{i+1}^n$ is chosen by an MCMC sampler, and is only accepted if the likelihood of $\vec{\vartheta}_{i+1}^n$ is greater than that of the saved point $\vec{\vartheta}_i^n$. This creates nested slices of likelihood [66]. Because `dynesty` is a dynamic sampling algorithm, it will dynamically adjust the number of points in each likelihood slice to maximize accuracy. The process is repeated until some cut-off criterion is met, and then the weighted samples are then combined to reconstruct the prior.

The natural cut-off point for a method that calculates the evidence is one where the dead points encompass the vast majority of the posterior [66]. In other words, the algorithm will stop when

the estimated remaining evidence is smaller than some cutoff threshold. While the total evidence is not known, a rough upper bound can be placed on the remaining evidence $\Delta\mathcal{Z}$. Intuitively, we know that the maximum remaining evidence would occur if the entire remaining prior volume X_i had the maximum likelihood value \mathcal{L}_{max} . The remaining evidence would be

$$\Delta\mathcal{Z} \leq \mathcal{L}_{max}X_i . \quad (1.61)$$

However, \mathcal{L}_{max} and X_i aren't known exactly; they can only be estimated from the calculated distribution. This means that the strict inequality becomes an approximate one:

$$\Delta\mathcal{Z} \lesssim \mathcal{L}_{max}X_i . \quad (1.62)$$

The final set of weighted samples $\{\vec{\vartheta}_1 \dots \vec{\vartheta}_N\}$, can then be used to estimate the 1-D evidence integral using standard numerical techniques. `dynesty` uses the 2nd-order trapezoid rule to minimize integration errors. Thus, the evidence can be calculated using the following relation

$$\mathcal{Z} = \sum_{i=1}^{N+K} \frac{1}{2} \left[\mathcal{L}(\vec{\vartheta}_{i-1}) + \mathcal{L}(\vec{\vartheta}_i) \right] \times [X_{i-1} - X_i] , \quad (1.63)$$

where K is the number of iterations [66].

1.3 Neutron Stars and Tidal Deformability

Neutron stars are the ultra-dense remnants of massive stars that have gone supernova. They were first proposed in 1933 by Baade and Zwicky [67] only two years after the discovery of the neutron by Chadwick [68]. They remained undetected until 1968, when graduate student Jocelyn Bell noted the presence of a persistent periodic source in the data from the Mullard Radio Astronomy Observatory just outside Cambridge [69]. This type of spinning neutron star with consistent pulsating emission profiles became known as pulsars, and thousands have now been observed.

Neutron stars are one of the most interesting astrophysical objects in the era of multi-messenger astronomy. Gravitational waves, electromagnetic waves, and neutrinos are all emitted by neutron stars at various stages of their lives. They are important for studying ultra-dense matter and testing gravity in the strong field regime because they are one of the most compact objects ever observed, second only to black holes. The internal densities of neutron stars can reach densities many times nuclear saturation density and far exceed anything that we can create in a laboratory on Earth. This makes them critical to understanding the EOS of ultra-dense matter.

Neutron stars were originally thought to be supported entirely by neutron star degeneracy pressure, but the star's core densities are too high to be counterbalanced by neutron star degeneracy pressure alone. Theories of ultra-dense matter with different compositions abound. Hyperons, quark matter, and Bose condensates are a few possible candidates [70]. Improved observations of neutron stars are needed to constrain these theories. The EOS is related to the mass and radius of the neutron star by the Tolman-Oppenheimer-Volkoff (TOV) equations. Measurements of neutron star mass and radii came from electromagnetic observations until the detection of GW170817 in 2017. Measurements confirmed theoretical predictions that neutron star masses are $1.1M_{\odot} < M_{ns} \lesssim 2.1M_{\odot}$. It is possible to measure mass and radius with X-ray observation,

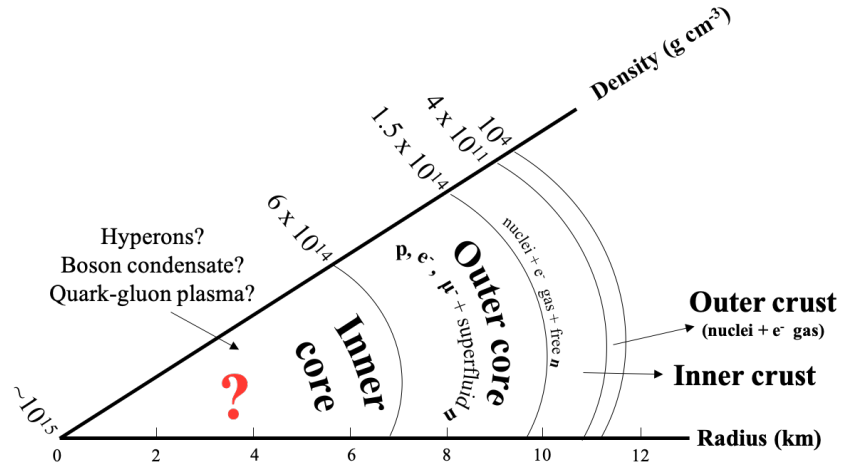


Figure 1.8: The generic structure of a neutron star that shows four distinct regions: outer crust, inner crust, outer core, inner core. The x -axis shows increasing radii and the axis at 45° is the matter density.

but the radii were poorly constrained and heavily model dependent [71, 72]. Gravitational wave event GW170817 [2] and its electromagnetic counterpart GRB170817A [3, 73] led to significantly improved constraints on neutron star radii [8, 74–76], see Chapter 2 for details.

1.3.1 Equation of State

The EOS defines the relationship between the thermodynamic properties of matter: pressure, mass density, and temperature. Neutron stars are remnants of a dead star and so generate none of their own energy. They rapidly cool through neutrino emission [77–84]. For this reason, EOSs assume that the temperature of the neutron star is negligible, and relates only the internal pressure p and density ρ .

While the exact EOS inside of a neutron star is still unknown, the states of matter inside a neutron star are not entirely mysterious [70, 85]. Neutron stars have four main layers: the outer crust, the inner crust, the outer core, and the inner core [77]. Fig. 1.8 shows this layered structure.

The outer crust has the lowest densities with $\times 10^{14} \text{g/cm}^3 \lesssim \rho \lesssim 4 \times 10^{11} \text{g/cm}^3$. This layer is formed primarily out of a lattice of nucleons that cluster into neutron rich nuclei and a degenerate electron gas that permeates the lattice [86, 87]. The transition to inner crust occurs at densities around $4 \times 10^{11} \text{g/cm}^3$ when the neutrons begin to ‘drip’ out of the nuclei and the nuclei can deform away from spherical. The inner crust is made of a lattice of positively charged nuclei surrounded by a gas of free neutrons and a background electron gas that maintains the overall neutral charge [86–88]. The outer and inner crust are thin but important to understanding phenomena such as neutron star glitches. The core is often broken into an inner and outer core. Densities in the core are greater than $\sim 1.5 \times 10^{14} \text{g/cm}^3$ and can be as large as ~ 10 times the nuclear saturation density $n_{\text{sat}} \approx 2.5 \times 10^{14} \text{g/cm}^3$. Near the nuclear saturation density, matter becomes a homogeneous neutron fluid with some fraction of protons, electrons, and muons [77, 86]. This region is sometimes referred to as the outer core. It is unknown exactly what happens at the higher densities of the inner core, but

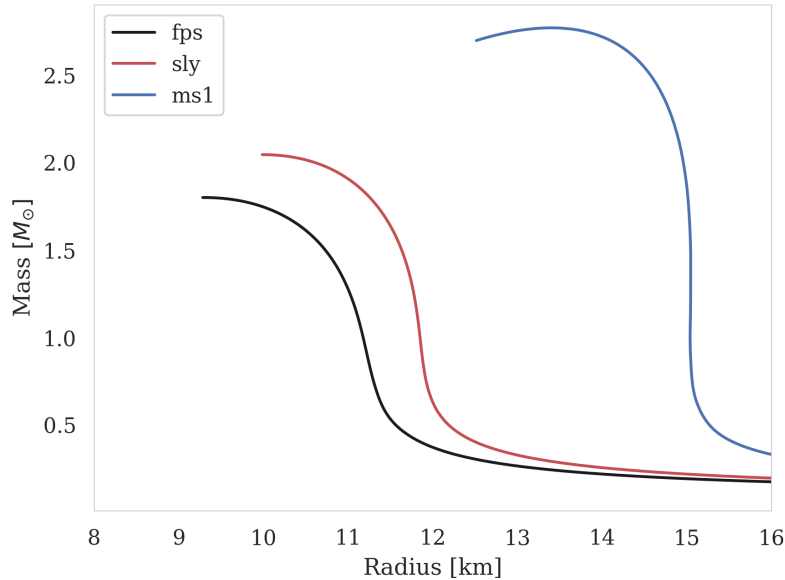


Figure 1.9: Mass-radius curves for three realistic EOSs.

popular theories propose that core may include hyperons, quark matter, or Bose condensates [70]. Due to the extreme nature of this matter, it cannot yet be studied in a laboratory on Earth [77, 89].

When studying neutron stars, it is necessary to relate the EOS describing the internal physics to the astrophysical observables: mass, radius, and tidal deformability. When integrated together with the structure equations discussed in Section 1.3.2, they define mass-radius relations such as the ones shown in Fig. 1.9.

Any EOS can only support a limited mass M_{max} ; above this mass, it the star collapses down to a black hole. This mass is generally around $\sim 2M_{\odot}$, but pulsar observations require $M_{max} \geq 2.16M_{\odot}$ [90]. The exact value of M_{max} depends on the EOS, which means that by detecting massive neutron stars it is possible to constrain the nuclear EOS. The EOS can also be constrained by simultaneous measurements of the mass and radius.

There are many published EOSs; they have different underlying assumptions and have been constructed using various methods. In this thesis, we limit the discussion to a specific family of EOSs, which are defined by chiral effective field theory (EFT) and are used in Chapters 2 and 3. For a more extensive discussion of the nuclear EOSs, see [70, 77, 85].

This work uses two sets of EOSs defined by chiral EFT. Chiral EFT is an EFT that describes the strong force. It expands the interactions in power of momenta, describes interactions in terms of nucleons and pions, and includes all operators consistent with the underlying chiral symmetries of strong interactions [91–95]. This expansion defines a systematic order-by-order scheme that can be truncated at a given order and, most importantly, enables reliable theoretical estimates of the uncertainty from neglected contributions. The uncertainties in the EOS grow rapidly over nuclear saturation, growing from $\sim 30\%$ at nuclear saturation to a factor of ~ 2 at twice nuclear saturation density [96]. Since this theory breaks down at higher densities, the EOSs used in this thesis are only defined by chiral EFT up to either once or twice nuclear saturation density [96, 97]. Above

these densities, the EOSs are constrained only to have a speed of sound less than the speed of light and to be able to support a two-solar-mass neutron star [98]. For each of the two families, 2000 individual EOSs distributed so that the radius of a $1.4 M_{\odot}$ neutron star is approximately uniform are generated.

1.3.2 Neutron Star Structure

Neutron stars are fully relativistic objects, and must be considered in full general relativity. Understanding their structure begins by understanding their effect on spacetime.

This section will focus on static, spherically symmetric stars for simplicity purposes. The geometry exterior to a neutron star can be described by the well-known Schwarzschild metric [14]:

$$ds^2 = - \left(1 - \frac{2M}{r}\right) dt^2 + \left(1 - \frac{2M}{r}\right)^{-1} dr^2 + r^2 d\theta^2 + r^2 \sin^2(\theta) d\phi^2, \quad (1.64)$$

where M is the total mass of the star. This only applies exterior to the star. A metric that describes the internal spacetime is also necessary. It is possible to construct a generic spherically symmetric, time-independent metric:

$$ds^2 = -e^{\nu(r)} dt^2 + e^{\lambda(r)} dr^2 + r^2 d\theta^2 + r^2 \sin^2(\theta) d\phi^2, \quad (1.65)$$

where both $\nu(r)$ and $\lambda(r)$ are functions of r only [99, 100].

Additionally, we assume that a neutron star's stress-energy tensor is that of a perfect fluid (Eq. (1.5)) and depends only on pressure p , density ρ , and the fluid's 4-velocity u^{μ} . Since the matter in the neutron star is static, the spacial components of the 4-velocity vanish:

$$u^{\mu} = (e^{-\nu/2}, 0, 0, 0). \quad (1.66)$$

The stress-energy tensor then has the form $T_{\nu}^{\mu} = \text{diag}(-\rho, p, p, p)$ where pressure and density are connected by some EOS $p = p(\rho)$, which is discussed in more in the previous section: Section 1.3.1. This leaves three unknown functions ($\nu(r)$, $\lambda(r)$, $p(r)$) to be determined by solving the the Einstein equation. Starting with the tt component of the Einstein equation i.e. $G_{00} = 8\pi T_{00}$, it is possible to write out an equation for $e^{\lambda(r)}$

$$\frac{1}{r^2} \frac{d}{dr} [r(1 - e^{-\lambda(r)})] = 8\pi\rho, \quad (1.67)$$

which can be solved for $e^{\lambda(r)}$.

$$e^{\lambda(r)} = \left(1 - \frac{2m(r)}{r}\right), \quad (1.68)$$

where

$$m(r) = 4\pi \int_0^r \rho(r') r'^2 dr' \quad (1.69)$$

m is not the proper mass m_p because it is not integrated over the entire volume element $4\pi e^{\lambda/2} r^2 \sin^2 \theta dr d\theta d\phi$, and differs from the proper mass m_p by the binding energy E_B (i.e., $m_p = m + E_B$).

An equation for $\nu(r)$ can be determined in a similar manner from the rr component of the Einstein equation. By substituting the definition of $\lambda(r)$ and $\nu'(r)$ into the $\theta\theta$ component of the

Einstein equations, one can retrieve an equation for the last unknown $\tilde{p}(r)$. The equation for $\tilde{p}(r)$ is known as the TOV equation.

Written together, the structure equations for a spherical star in general relativity are

$$\frac{dm}{dr} = 4\pi\rho r^2, \quad (1.70a)$$

$$\frac{d\nu}{dr} = \frac{m(r) + 4\pi r^3 p}{r(r - 2m(r))}, \quad (1.70b)$$

$$\frac{dp}{dr} = -(p + \rho) \frac{m(r) + 4\pi r^3 p}{r(r - 2m(r))}. \quad (1.70c)$$

These three differential equations together with an EOS define the neutron star's structure [13, 101].

The structure equations can be combined with the EOS to learn about the neutron star's physical properties such as mass and radius. They also place constraints on the maximum and minimum mass of a neutron star. While the exact maximum mass varies between EOSs, it is possible to demonstrate that neutron stars do have a maximum mass with a few basic assumptions [13]

1. $\rho > 0$
2. $p > 0$
3. $dp/d\rho > 0$
4. $(1 - 2m/r) > 0$

Assumption one is a general statement for matter, and assumptions two and three are related to microscopic stability. If either of these equations do not hold, it becomes energetically favorable for any small volume to collapse. The last condition comes from the Schwarzschild metric and is necessary to ensure that the neutron star does not collapse into a black hole.

According to the TOV equation (Eq. (1.70c)), the pressure decreases with increasing radius so long as the Schwarzschild condition holds. The density also decreases with radius because $dp/d\rho > 0$. The neutron star can be divided into a core, where $\rho > n_{\text{sat}}$, and an envelope, where $\rho \leq n_{\text{sat}}$, where n_{sat} is the nuclear saturation density. The nuclear saturation density is roughly the nuclear density for most nuclei all the way from helium to uranium [13].

Since the density decreases with radius, the mass of the core is constrained from the bottom:

$$M(r) = 4\pi \int_0^{r_0} \rho(r)r^2 dr \geq 4\pi \int_0^{r_c} \rho_c r^2 dr \quad (1.71)$$

where r_0 is the radius of the core. Solving for M , we find

$$M \geq \frac{4}{3}\pi r_0^3 \rho_0 \quad (1.72)$$

This constraint can be combined with the Schwarzschild constraint, which limits the maximum mass that can be supported without collapse to a black hole:

$$\frac{r_0}{2} > M. \quad (1.73)$$

Combining these two constraints gives

$$M \leq \frac{1}{2} \left(\frac{3}{8\pi\rho_0} \right)^{1/2}. \quad (1.74)$$

While more stringent constraints can be calculated using the structure equations and a specific EOS, this brief exercise gives a straightforward example of how the structure equations constrain the observable properties of a neutron star [13].

1.3.3 Tidal Deformability

Studying the nuclear EOS is a key part of modern astrophysics and one of the foci of this thesis. Gravitational waves from binary neutron star mergers are a promising method for studying the nuclear EOS; this is because the gravitational waveform depends on the finite size effects of the neutron star [102, 103]. The change in the gravitational wave signal from the internal structure of the neutron star in the inspiral phase depends on one parameter: tidal deformability λ . The tidal deformability measures the strength of a neutron star's response to an external field ($\mathcal{E}_{ij\dots k}$), and the resulting induced multipole moment $Q_{ij\dots k}$:

$$Q_{ij\dots k} = -\lambda \mathcal{E}_{ij\dots k}. \quad (1.75)$$

This is a tensor equation, but both $\mathcal{E}_{ij\dots k}$ and $Q_{ij\dots k}$ can be decomposed into tensor harmonics:

$$\mathcal{E}_{ij\dots k} = \sum_{m=-\ell}^{\ell} \mathcal{E}_m Y_{ij\dots k}^{\ell m}(\theta, \phi) \quad (1.76)$$

$$Q_{ij\dots k} = \sum_{m=-\ell}^{\ell} Q_m Y_{ij\dots k}^{\ell m}(\theta, \phi), \quad (1.77)$$

where $Y_{ij\dots k}^{\ell m}(\theta, \phi)$ are the even parity tensor spherical harmonics defined by [106]. The tensor relation in Eq. (1.75) can be expressed as a scalar relation

$$Q_m = -\lambda \mathcal{E}_m, \quad (1.78)$$

and λ can be calculated from a single non-vanishing \mathcal{E}_m [102]. The leading order quadrupolar tidal field $\mathcal{E}_{ij\dots k} = R_{i0j0}$

Much like the radius and mass, tidal deformability is an intrinsic property of a neutron star and depends on the nuclear EOS. As such, measurements of tidal deformability can constrain nuclear theory. The leading order ($\ell = 2$) electric tidal deformability enters the gravitational waveform at the 5th post-Newtonian order and can be measured directly in gravitational wave signals from binary neutron star mergers [2, 8]. The tidal deformability is intrinsically related to the tidal Love number k_2

$$k_2 = \frac{3}{2} GR^{-5}, \quad (1.79)$$

where R is the radius of the neutron star. Tidal Love numbers were initially developed in Newtonian physics [104, 105]. However, studying neutron stars requires a fully relativistic definition

of tidal deformability. The first published relativistic calculations were for the $\ell = 2$ electric tidal deformability [102]. The relativistic theory of tidal Love numbers was soon expanded to $\ell > 2$ and to the odd parity tidal deformabilities, which have no Newtonian analog [107, 108].

In general relativity, the external tidal field and the induced multipole moment affect spacetime in and around the neutron star. Exterior to the star, the behavior of the metric at large r can be expressed in terms of \mathcal{E}_{ij} and Q_{ij} . In the local asymptotic rest frame, the g_{tt} component of the metric for large r has the form [109]

$$g_{tt} = g_{tt}^0 + h_{tt} = -\left(1 - \frac{2\mu}{r}\right) + \frac{3Q_{ij}n^i n^j}{r^3} + \mathcal{O}(r^{-4}) - \mathcal{E}_{ij}n^i n^j r^2 + \mathcal{O}(r^3) \quad (1.80)$$

where n^i is the unit radial vector.

Gravitational measurements of neutron star properties (mass, radius, tidal deformability) began with the first observed binary neutron star merger, GW170817. Studies of GW170817, including the work presented in Chapter 2 of this thesis, have already improved our knowledge of the nuclear EOS and ruled out some EOSs entirely by measuring neutron mass and star tidal deformability [8, 74, 75, 110].

Gravitational waves can also be used to study physics beyond general relativity, and various studies have already used gravitational wave data to do so [111–117]. Regardless of the theory, any gravitational waves emitted by a binary neutron star system depend on matter effects. These matter effects may well differ between theories. Despite this, analyses of GW170817 outside of general relativity typically do not use modified tidal deformability [118–120]. Indeed, tidal deformabilities have only been calculated for a limited selection of alternative theories [121–124].

1.4 Alternate Theories of Gravity and Tests of General Relativity

Einstein’s general relativity has proven to be an incredibly successful theory of gravity. It not only resolved existing problems with Newtonian physics such as the perihelion of mercury, it also predicted phenomena such as gravitational lensing and gravitational waves. Despite its successes, general relativity there are reasons to look beyond it, and numerous alternative theories of gravity have been developed. None of these theories has proven to be as successful as general relativity.

Both theoretical and observational reasons exist to look beyond Einstein’s theory of general relativity. Astrophysical observations of large-scale structures has led to two theories: dark matter and dark energy. Assuming general relativity holds true, then observational evidence says that only $\sim 4\%$ of the universe is visible [125]. The rest is made up of dark matter and dark energy. Dark matter is matter that interacts with gravity but not with electromagnetic radiation, and dark energy is the vacuum energy driving the universe’s expansion. General relativity can explain these phenomena, but alternative theories of gravity have also been developed to explain them.

The theory of dark matter has a long history; the idea of matter that neither emits nor absorbs electromagnetic radiation was first presented in 1884 [126]. Nearly a century of observations beginning in the 1920s and 30s have shown that stars in galaxies, particularly those at the outer edge, orbit much faster than the observed luminous matter can explain. Fig. 1.10 displays the difference between the expected and observed velocities. The rotation curves of spiral galaxies

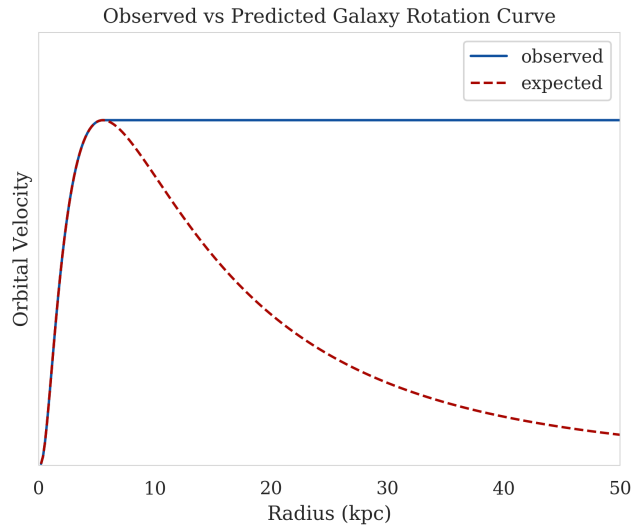


Figure 1.10: A schematic comparison of observed galactic rotation curves from spiral galaxies and the galactic rotation curves expected based on luminous mass measurements and Kepler’s law.

are expected to resemble that of the solar system with objects from the center orbiting slowly ($1/r$) because the bulk of the observable mass is in the galactic center. This idea is at odds with observations, which show that speed of stars is approximately constant away from the galactic center.

Dutch astronomers Oort and Kapteyn related the idea of dark matter to the unexpected stellar velocities they observed [127, 128] in the 1920s and 30s. Researchers including Vera Rubin and Kent Ford made detailed observations of twenty-one galaxies in the 1960s and 70s, confirming that the rotation curves of galaxies do not match the theoretical predictions based on observation of luminous matter [129, 130]. Gravitational lensing measurements also suggest the existence of more mass than the observed stars can account for and provides further proof for the existence of dark matter[131].

Common theories of dark matter include non-baryonic particles, macroscopic non-interacting objects, and modified theories of gravity. Weakly interacting massive particles (WIMPS), were the most popular theory of particle dark matter, but all laboratory experiments to date have failed to detect the existence of WIMPS [132]. There are other proposed particles, such as axions [133], but none of these have been detected. For details on the status of particle dark matter see e.g. [134]. Some theorists have proposed that dark macroscopic objects make up dark matter. These are called massive compact halo objects (MACHOS). MACHOS can be black holes, neutron stars, brown dwarves, or even something as yet unknown. However, observations have placed strong constraints on these theories, making it unlikely that MACHOS could solve the dark matter problem [135, 136].

There are observations that dark matter cannot explain. One example is the Tully-Fisher relation, which is an observational rule that connects the luminosity of a spiral galaxy to its radial velocity [137]. The Baryonic-Tully-Fisher relation, which relates observed baryonic mass from various wavelengths to the asymptotic radial velocity [138] has proven to be even more successful than the original relation. One would not expect any relation between luminous matter and radial

velocity if dark matter made up the vast majority of the mass of the galaxy.

Alternate theories of gravity have been proposed as solutions to this observational problem. Instead of assuming that our understanding of gravity is correct and our observations are missing the majority of the mass, these theories state that the observations of matter are correct but our understanding of gravity is incorrect at large galactic scales. There are three main alternative explanations to dark matter: modified Newtonian dynamics (MoND) [139], tensor-vector-scalar (TeVeS) gravity [140], and emergent gravity [141].

Another observational motivation for alternate theories of gravity is dark energy. Dark energy is an unknown form of energy that acts at the largest scales, countering the inward pull of gravity. Observations of supernovae in the 1990s showed that the universe was not static or shrinking but rather expanding at an accelerating rate [142]. Gravity is currently the only long range force among the fundamental forces. In general relativity, gravity is purely attractive; so the universe should be coming together, not moving apart.

Interestingly, the Einstein equation temporarily contained the cosmological constant Λ ; Λ counterbalanced the inward pull of gravity to ensure a static universe [143]:

$$G_{\mu\nu} + \Lambda g_{\mu\nu} = 8\pi T_{\mu\nu} , \quad (1.81)$$

Einstein later removed the cosmological constant from the equation. After the universe's accelerating expansion was discovered decades later, the idea of the cosmological constant was resurrected [144] as it is the simplest explanation for dark energy. Another model of dark energy, called quintessence, states that the acceleration comes from the potential energy of a new physical scalar field ϕ that weakly couples that matter and has some potential $V(\phi)$. This theory has more flexibility than the cosmological constant because the potential can vary in space and time [145–147]. Modified theories of gravity, including scalar-tensor theories, are another possibility to explain the observed acceleration.

There are also theoretical justifications for studying modified theories of gravity. One of the leading theoretical reasons for modifying or expanding general relativity is the attempt to unify gravity and the other fundamental forces. General relativity, as a classical theory, is incompatible with quantum mechanics. Kaluza-Klein theory was one of the earliest attempts to unify gravity and electromagnetism [148, 149]. This led to scalar-tensor theory [150]. Since then, the field of quantum gravity has grown significantly. Numerous theories, including string theory and loop quantum gravity, have been developed, but none of these have been entirely successful [151].

This thesis explores two different alternative theories of gravity.

We search for the birefringence effect in Chapter 4, which is discussed in depth in the next section Section 1.4.1. Birefringence arises from an EFT expansion of general relativity. Chapter 5 focuses on scalar-tensor theory, which is one of the oldest and most well-studied theories of modified gravity. Scalar-tensor theory is discussed in depth in Section 1.4.2.

1.4.1 Birefringence

Birefringence is a phenomenon in which a wave's left- and right-hand modes propagate along different geodesics. Birefringence has been observed in electromagnetic waves but not in gravitational waves. Gravitational waves detected by current detectors travel vast distances; gravitational waves from the most distant gravitational wave event, GW190521, travelled around 5,000 Megaparsecs before reaching the Earth. We need a metric that describes the curvature of the universe

on cosmological scales to adequately describe the propagation of these gravitational waves. The Friedmann–Robertson–Walker (FRW) metric is a cosmological solution to the Einstein equation. It assumes that spacetime is homogenous, isotropic, expanding, and path-connected [152–158]. Path-connected means that a continuous path can connect any two points in the space. The FRW metric is associated with the Λ CDM model and is often called the standard model in cosmology [159]. The metric takes the form

$$ds^2 = dt^2 - a^2(t) (dx^2 + dy^2 + dz^2) \quad (1.82)$$

where $a(t)$ is constrained by the Einstein equations.

As discussed in Sec. 1.1.1, linearized gravity is a valuable framework for studying gravitational waves and will be used here. The linearized Einstein-Hilbert action in the FRW universe is

$$S = \frac{1}{16\pi G} \int dt d^3x a^3 \left[\frac{1}{4} \dot{h}_{ij}^2 - \frac{1}{4a^2} (\partial_k h_{ij})^2 \right], \quad (1.83)$$

where a is the cosmic scale factor and h_{ij} is the small deviation from the universal metric ($|h_{ij}| \ll 1$). The equation of motion for the circular gravitational wave polarization modes h_A can be derived from this linearized action:

$$h''_A + 2\mathcal{H}h'_A + k^2 h_A = 0, \quad (1.84)$$

where \mathcal{H} is the Hubble parameter, k is the wave number, and a prime denotes the derivative with respect to the cosmic conformal time τ , and $A = L, R$ represents the right- or left-hand polarizations respectively. In general relativity, both left- and right-hand polarization follow the same equation of motion. In other words, there is no birefringence.

Birefringence can occur in theories of gravity beyond general relativity. It arises from the EFT extension of gravity. EFT is a non-theory-specific framework for constructing non-general relativistic actions. It includes action terms that purposely preserve or violate certain symmetries. It can also be mapped to specific theories by the correct choice of constants [160].

The leading order EFT terms are terms with three derivatives [160–162]:

$$\epsilon^{ijk} \dot{h}_{il} \partial_j \dot{h}_{kl} \quad (1.85a)$$

$$\epsilon^{ijk} \partial^2 h_{il} \partial_j h_{kl}, \quad (1.85b)$$

where $i, j, \dots = 1, 2, 3$ refer to spacial coordinates, ∂_j denotes spacial derivatives, dot denotes derivatives with respect to time, ∂^2 is the Laplacian, and ϵ^{ijk} is the antisymmetric symbol. These terms violate parity symmetry, which is the symmetry under inversion of spacial coordinates, because they are not symmetric in the spacial indices. We obtain the leading order EFT action by adding these terms to the linearized Einstein-Hilbert action

$$S = \frac{1}{16\pi G} \int dt d^3x a^3 \left[\frac{1}{4} \dot{h}_{ij}^2 - \frac{1}{4a^2} (\partial_k h_{ij})^2 + \frac{1}{4} \left(\frac{c_1}{a M_{\text{PV}}} \epsilon^{ijk} \dot{h}_{il} \partial_j \dot{h}_{kl} + \frac{c_2}{a^3 M_{\text{PV}}} \epsilon^{ijk} \partial^2 h_{il} \partial_j h_{kl} \right) \right], \quad (1.86)$$

where M_{PV} is the energy scale and $c_{1,2}$ are two undetermined functions of cosmic time. The reduced Planck's constant has been set to one along with G and c ($G = c = \hbar = 1$). c_1 and c_2 vary between theories and can be chosen to match any specific theory [163–172].

From this new action, new equations of motion can be derived. The equation of motion for the gravitational wave circular polarization modes h_A is

$$h_A'' + (2 + \nu_A)\mathcal{H}h_A' + (1 + \mu_A)k^2h_A = 0, \quad (1.87)$$

where μ_A and ν_A are the phase and amplitude birefringence parameters. They have the exact forms

$$\begin{aligned} \nu_A &= -[\rho_A c_1 k / (aM_{\text{PV}})]' / \mathcal{H}, \\ \mu_A &= \rho_A (c_1 - c_2) k / (aM_{\text{PV}}), \end{aligned} \quad (1.88)$$

and $\rho_A = \pm 1$ for left- and right-handed polarizations and represents broken parity symmetry. The two polarizations follow two different equations of motions because ν_A and μ_A have opposite signs for the left- and right-hand polarization modes. In other words, birefringence occurs. The general relativistic equation of motion (Eq. (1.84)) can be retrieved by setting $\mu_A = \nu_A = 0$ in Eq. (1.87).

To retrieve the modified left- and right- handed circular polarization modes, one needs to solve Eq. (1.87). The polarization modes take the form

$$h_L^{\text{PV}}(f) = (1 + \delta h)h_L^{\text{GR}}(f)e^{-i\delta\Psi(f)} \quad (1.89a)$$

$$h_R^{\text{PV}}(f) = (1 - \delta h)h_R^{\text{GR}}(f)e^{i\delta\Psi(f)}. \quad (1.89b)$$

Gravitational wave polarizations are typically expressed as plus (h_+) and cross (h_\times) modes rather than as circular modes; the waveform can be re-expressed as

$$h_+ = (h_L + h_R) / \sqrt{2} \quad (1.90a)$$

$$h_\times = (h_L - h_R) / (\sqrt{2}i). \quad (1.90b)$$

1.4.2 Scalar-Tensor Theory

One of the most straightforward and well-studied classes of alternative theories is scalar-tensor theories of gravity. In scalar-tensor theory, dynamical scalar field(s) are added to the Einstein-Hilbert action. Scalar-tensor theory was developed for Kaluza-Klein theories and the need for gravity in 5D [150]. Later work introduced scalar fields as an attempt to incorporate Mach's principle into gravity [173]. Today scalar-tensor theory is an alternative to dark energy. Scalar degrees of freedom are also critical for string theory, superstring theory, and other supergravity theories [174].

Scalar-tensor theory was first proposed by Jordan [150] and further developed by Jordan [175], Fierz [176], and Brans and Dicke [173]. The original theory, known as Jordan-Fierz-Brans-Dicke (JFBD) theory, is the simplest case of scalar-tensor theory, where the constant scalar field is defined by a single dimensionless parameter ω_{BD} . The modified action in JFBD theory has the form:

$$S = \frac{1}{16\pi} \int \sqrt{-\tilde{g}} \left(\phi \tilde{R} - \frac{\omega_{BD}}{\phi} \tilde{g}^{\mu\nu} \partial_\mu \phi \partial_\nu \phi \right) + S_m[\Psi_m] d^4x, \quad (1.91)$$

where ϕ is the scalar field, $\tilde{g}_{\mu\nu}$ is the metric, and \tilde{R} is the Ricci scalar. S_m denotes the action of the matter, which is a function of the matter fields Ψ_m .

The left-most term of Eq. (1.91), known as the non-minimal coupling term, depends on $\phi\tilde{R}$ and replaces the standard Einstein-Hilbert Lagrangian \mathcal{L}_{EH} :

$$\mathcal{L}_{EH} = \frac{1}{16\pi G} \sqrt{-g} R . \quad (1.92)$$

This means there is no longer a gravitational constant G but rather a gravitational function $\tilde{G} = G(\phi)$, which depends on the scalar field ϕ .

Later works generalized this action to include arbitrary functions of the scalar field $\omega(\phi)$. The $\omega(\phi)$ term allows for theories that deviate significantly from general relativity in high energy regimes while still passing solar system constraints that strongly limit the JFBD parameter [177–179]. An arbitrary potential $\lambda(\phi)$ can also be added to the action. This potential acts as a cosmological term, similar to Einstein’s cosmological constant [177, 179]. It is also possible to include multiple scalar fields [180], but this work will not explore these theories.

Taking all of this into account gives a more general Lagrangian of the form

$$S = \frac{1}{16\pi} \int \sqrt{-\tilde{g}} \left(\phi\tilde{R} - \frac{\omega(\phi)}{\phi} \tilde{g}^{\mu\nu} \partial_\mu \phi \partial_\nu \phi + 2\lambda(\phi) \right) + S_m[\Psi_m, \tilde{g}_{\mu\nu}] d^4x . \quad (1.93)$$

When working in scalar-tensor theory, it is necessary to choose a conformal frame. Two conformal frames are used extensively in the literature: the Jordan and the Einstein frames. Jordan originally wrote the action as it appears in Eq. (1.91), and this is now known as the Jordan frame. In this work, we denote Jordan frame values with a tilde. The correct choice of frame has been the subject of much debate historically [181]. Today it is generally agreed that non-Cavendish type experiments measure Jordan frame quantities, but the equations are more straightforward in the Einstein frame [124, 172, 182–184]. The matter fields couple to $\tilde{g}_{\mu\nu}$; this can be seen in Eq. (1.93). Using the conformal transformation

$$\tilde{g}_{\mu\nu} = A^2(\varphi) g_{\mu\nu} , \quad (1.94)$$

the action Eq. (1.93) can be rewritten to better resemble the Einstein-Hilbert action:

$$S = \frac{1}{16\pi} \int \sqrt{-g} \left(R - 2g^{\mu\nu} \partial_\mu \varphi \partial_\nu \varphi \right) + S_m(\psi_m; A^2(\varphi) g_{\mu\nu}) d^4x , \quad (1.95)$$

where φ is the scalar field in the Einstein frame. There is one free parameter: the coupling function $A(\varphi)$. In JFBD theory, $A(\varphi) = e^{\alpha_0 \varphi}$, and the Brans-Dicke parameter ω_{BD} and the coupling function are related by the following equation:

$$\alpha_0 \equiv (3 + 2\omega_{BD})^{1/2} . \quad (1.96)$$

By varying the Einstein frame action, the scalar-tensor field equations can be derived:

$$G_{\mu\nu} = 8\pi G_* T_{\mu\nu} + T_{\mu\nu}^{(\varphi)} \quad (1.97a)$$

$$\square_g \varphi = -4\pi G_* \alpha(\varphi) T \quad (1.97b)$$

$T_{\mu\nu}$ is the stress-energy tensor in the Einstein frame, and T is the contracted stress-energy tensor $T = T^\mu_\mu = g^{\mu\nu} T_{\mu\nu}$. This is related to the Jordan frame stress-energy tensor ($\tilde{T}_{\mu\nu}$) in the following manner

$$T_{\mu\nu} \equiv \frac{2}{\sqrt{|g|}} \frac{\delta S_m}{\delta g^{\mu\nu}} = A^2(\varphi) \tilde{T}_{\mu\nu} \quad (1.98)$$

The matter stress-energy tensor is defined in the physical frame and takes the same form as in general relativity (Eq. (1.5)). $T_{\mu\nu}^{(\varphi)}$ can be considered the stress-energy of the massless scalar field and has the form

$$T_{\mu\nu}^{(\varphi)} \equiv 2\partial_\mu\varphi\partial_\nu\varphi - g_{\mu\nu}g^{\alpha\beta}\partial_\alpha\varphi\partial_\beta\varphi. \quad (1.99)$$

Lastly $\alpha(\varphi) \equiv d \ln A(\varphi)/d\varphi$. When $\alpha(\varphi)$ is set to zero, the equations reduces to those of general relativity.

There are stringent constraints on the value of α_0 in JFBD theories from solar system experiments [185, 186]. Gravitational wave observations have also been used to put bounds on α_0 [117]. These constraints significantly limit the strong-field behavior as well as the weak-field behavior. Damour and Esposito-Ferès discovered the ‘spontaneous scalarization’ effect, which allows large deviations from general relativity in the strong field regime while still being consistent with the strict solar system constraints. They defined

$$A(\varphi) = e^{\left(\frac{1}{2}\beta\varphi^2\right)} \quad (1.100)$$

and found that scalarization occurs for $\beta \lesssim -4.5$ [187]. A follow-up study showed that scalarization occurs for $\beta \lesssim -4.35$ [188]. Further studies have shown that neutron stars may dynamically scalarize during the inspiral phase of binary neutron star mergers [182], which makes these theories especially interesting for studying binary neutron star mergers with general relativity.

1.5 Clarifications of Contributions

Chapters 2, 3, and 4 contain work which has previously been published or accepted for publication and was done in collaboration with several colleagues. This section lays out the contents of each chapter, clarifies the roles of all authors, and focuses on the work done by the author of this thesis.

1.5.1 Chapter 2

Chapter 2 contains work that was originally published as Capano, C.D., Tews, I., Brown, S.M. et al. *Stringent constraints on neutron-star radii from multimessenger observations and nuclear theory*. Nat Astron 4, 625–632 (2020). <https://doi.org/10.1038/s41550-020-1014-6> [8].

For the majority of the duration of this project, the author of this thesis was the lead author. As published in the original paper, the author’s roles were primarily in formal analysis, software development, validation of results, visualization, draft writing, and revision. The author contributed to the gravitational wave analysis portion of the paper along with D. A. Brown, C. D. Capano, S. De, B. Krishnan, and S. Kumar. Nuclear theory contributions were made by I. Tews and S. Reddy, and analysis of the electromagnetic counterparts was provided by B. Margalit.

While lead author of this project, the author of this thesis performed the bulk of the parameter estimation work with suggestions and assistance by S. Kumar, S. De, C. D. Capano, and D. A. Brown. The paper was written collaboratively by D. A. Brown, C. D. Capano, I. Tews, and the author before being reviewed and edited by all contributing authors. The authorship order was adjusted due to considerations of the software development, which was led by C. D. Capano and assisted by others, including the author of this thesis.

This work combines a Bayesian analysis of the GW170817 data with state-of-the-art nuclear theory and constraints from the electromagnetic counterpart to GW170817. This work constrained both the tidal deformability and radius of neutron stars. The novel parameter estimation method in this work is an improvement from previous methods because it uses realistic EOSs and ensures that both neutron stars have the same EOS. The radius of a $1.4M_{\odot}$ neutron star was constrained to be $11.0_{-0.6}^{+0.9}$ km at the 90th percentile credible interval. At the time of publication, this paper placed the strongest constrain up to that date on neutron star radii by a factor of ~ 2 . Furthermore, these results have implications for future results. We predicted that neutron star-black hole binaries are unlikely to be disrupted and thus unlikely to have electromagnetic counterparts. This prediction has important implications for future analyses of neutron star-black hole systems. Since the date of the publication, two neutron star-black hole mergers have been announced by the LIGO-Virgo collaboration, neither of which had an electromagnetic counterpart.

The EOSs are defined at low densities by chiral EFT and were generated by I. Tews. In order to use these EOSs, the `PyCBC Inference` sampler needed to draw neutron star mass, radius, tidal deformability from a file. This capability was added to the `PyCBC Inference Toolkit` by S. De. Furthermore, the method required sampling over many EOSs and opening the corresponding files to retrieve the mass-radius-tidal deformability relationship. This capability was added to the code by the author. Integration of the `dynesty` sampler into the `PyCBC Inference Toolkit` was done primarily by S. Kumar. In addition to providing assistance on these three things, C. D. Capano developed and improved much of the `PyCBC Inference Toolkit`, including but certainly not limited to the application of the parallel tempered MCMC sampler.

The parameter estimation results were then combined with information from the kilonova ejecta, which showed that there was a short lived remnant that was neither a stable neutron star nor a black hole formed by prompt collapse and placed a bound on the maximum mass of a neutron star. That analysis was done by B. Margalit and folded into the gravitational results by C. D. Capano and the author of this thesis.

1.5.2 Chapter 3

Material in chapter 3 was originally published under Brown, S.M., Capano, C.D., Krishnan, B. *Using Gravitational Waves to Distinguish Between Neutron Stars and Black Holes in Compact Binary Mergers*. *Astrophys J* (accepted 2022). <https://doi.org/10.48550/arXiv.2105.03485> [9]. This paper has been accepted for publication by the *Astrophysical Journal*. The author is the first author of this work, which is available on arXiv as a preprint.

All formal analysis and any and all verification of results in this chapter was performed by the author. It was written by the author under the guidance of C. Capano and B. Krishnan. C. Capano suggested verification methods and corrections, and comments by C. Capano and B. Krishnan were incorporated.

Chapter 3 contains a study of the capabilities of current and future gravitational wave detectors to distinguish neutron star-black hole binaries from binary black holes using gravitational waves alone. Neutron star-black hole systems are unlikely to have an electromagnetic counterpart (see Chapter 2). This means that evidence for the existence of a neutron star in the binary must come from gravitational waves. This evidence is especially important for objects that are in the mass gap between neutron stars and black holes such as the $2.6M_{\odot}$ object in GW190814 [18]. The results presented in this chapter show that current gravitational wave detectors and their near term up-

grades are unable to distinguish neutron stars from black holes in neutron star-black hole systems. It also demonstrates that 3G detectors can successfully make this measurement under certain conditions, which strengthens the arguments in favor of funding the Einstein Telescope and Cosmic Explorer 1 and 2.

In this work, Bayesian parameter estimation and model selection are carried out using the `PyCBC Inference Toolkit` [40]. The analysis was run on the ATLAS cluster [189].

1.5.3 Chapter 4

Material in chapter 4 was originally published as Wang, Y., Brown, S.M. et al. *Tests of Gravitational-Wave Birefringence with the Open Gravitational-Wave Catalog* Phys. Rev. D 106, 084005 2022. <https://link.aps.org/doi/10.1103/PhysRevD.106.084005> [10]. This work contains an analysis of gravitational wave events from 4-OGC [190] to search for evidence of birefringence in publicly available gravitational wave data [36].

Y. Wang led this project in collaboration with the author, L. Shao, and W. Zhao. The paper was put together by Y. Wang and the author and revised by all authors. L. Shao and W. Zhao provided their expertise in the EFT extension of general relativity as well as their understanding of the birefringence effect and its relation to alternative theories of gravity. Analysis of the gravitational wave data was done by Y. Wang and the author. Y. Wang modified existing waveforms to include birefringence. The parameter estimation was done jointly by Y. Wang and the author. Following the parameter estimation, we performed Bayesian model selection. Y. Wang performed the computation. Y. Wang and the author shared the responsibility for interpreting the results. In-depth studies of two events were necessary. This analysis included an injection study done by both Y. Wang and the author, employing the author's knowledge of injections from Chapter 3. Finally, Y. Wang, assisted by the author, led the additional statistical analysis.

Birefringence is a non-general relativistic effect that causes asymmetry between the left and right-hand propagation modes. It arises from the EFT extension of general relativity and is a feature of several theories of gravity, including Chern-Simons gravity [163, 165–168], Hořava-Lifshitz gravity [169–171], and ghost-free scalar-tensor gravity [172]. The chapter found that the two most massive events in the gravitational wave catalogue exhibited evidence of birefringence; none of the other events deviated significantly from general relativity. This is interesting but is not conclusive evidence for birefringence. Analysis of future gravitational wave events will be needed to make any definite statements about physics beyond general relativity.

1.5.4 Chapter 5

Chapter 5 is adapted from two manuscripts that are in preparation and have not yet been accepted to or published by any journal. The work was led by the author, and the author of this thesis is primary author on both papers. The first paper is available as a preprint on arXiv as Brown, S. *Tidal Deformability of Neutron Stars in Scalar-Tensor Theories of Gravity for Gravitational Wave Analysis* <https://arxiv.org/abs/2210.14025> and will be submitted to the Astrophysical Journal. The second is a letter for the Astrophysical Journal Letters titled *Tidal Deformability of Neutron Stars in Scalar-Tensor Theory*. This chapter details the derivations of the various tidal responses of neutron stars in scalar-tensor theory. It also discusses the numerical methods used to calculate the properties of neutron stars.

This work was lead by S. Brown under the guidance of B. Krishnan. All derivations contained therein (e.g., perturbations, tidal Love numbers, tidal deformabilities, and conformal transformations) were done by the author. S. Brown developed all code used and generated all visualizations. The paper was written by the author and revised by the author helpful with comments from S. Kumar, X. Jiménez Forteza, and B. Krishnan. The author would like to thank G. Creci, S. Kumar, S. Datta, X. Jiménez Forteza, P. Mourier, and B. Allen for their valuable discussion.

This chapter is designed to improve future tests of alternative theories of gravity using gravitational waves from binary neutron star mergers. Gravitational waves depend on the tidal deformabilities of the merging objects; tidal deformability is zero for black holes but strictly greater than zero for neutron stars. With current gravitational wave detectors, there is a large uncertainty on the tidal deformability. This uncertainty is similar to or larger than the expected deviations from general relativity. Understanding exactly how the tidal deformabilities in alternative theories differ from general relativity will help decouple the deviations from general relativity and the uncertainty in the tidal deformability measurements.

In order to use the tidal love numbers derived in this chapter for gravitational wave analysis, it is necessary to calculate the numerical relations between the mass, radius, and tidal deformability of neutron stars with different EOSs. The methods used for this are laid out in this chapter. Then results are shown for several realistic EOSs.

2 | Stringent Constraints on Neutron Star Radii From Multimessenger Observations and Nuclear Theory

This chapter contains material published as Capano, Collin D., Tews, Ingo, Brown, Stephanie M. et al. *Stringent constraints on neutron star radii from multimessenger observations and nuclear theory*. Nat Astron 4, 625–632 (2020). <https://doi.org/10.1038/s41550-020-1014-6>.

2.1 Abstract

The properties of neutron stars are determined by the nature of the matter that they contain. These properties can be constrained by measurements of the star’s size. We obtain stringent constraints on neutron star radii by combining multimessenger observations of the binary neutron star merger GW170817 with nuclear theory that best accounts for density-dependent uncertainties in the EOS. We construct EOSs constrained by chiral EFT and marginalize over these using the gravitational wave observations. Combining this with the electromagnetic observations of the merger remnant that imply the presence of a short-lived hyper-massive neutron star, we find that the radius of a $1.4 M_{\odot}$ neutron star is $R_{1.4 M_{\odot}} = 11.0^{+0.9}_{-0.6}$ km (90% credible interval). Using this constraint, we show that neutron stars are unlikely to be disrupted in neutron star black hole mergers, and subsequently, that such events will not produce observable electromagnetic emission.

2.2 Introduction

Neutron stars are arguably the most fascinating astrophysical objects in the multimessenger era. Gravitational waves, electromagnetic radiation, and neutrinos produced by various neutron star phenomena carry information about the mysterious dense matter in their cores. The nature of this matter contains important information needed to understand phases of matter encountered in Quantum Chromodynamics—the fundamental theory of strong interactions. Measuring a neutron star radius or compactness is critical to interpreting multimessenger observations of neutron stars and determining the EOS of dense matter [85]. Until recently, measurement of neutron star radii relied on X-ray observations of quiescent and accreting neutron stars. These analyses typically obtained radii in the range 10–14 km and had poorly understood systematics [71], although this situation is likely to improve with recent observations by NICER [191, 192]. The multimessenger observation

of the fortuitously close binary neutron star merger GW170817 [2] provides information that can independently and more accurately determine neutron star radii.

We combine state-of-the-art low-energy nuclear theory, constrained by experimental data, with multimessenger observations of the binary neutron star merger GW170817 [2] to measure the radii of neutron stars and constrain the nuclear EOS. Using conservative assumptions about nuclear physics and the properties of the electromagnetic counterpart, we obtain the most stringent constraints on neutron star radii to date. We find that the radius of a $1.4 M_{\odot}$ neutron star is $R_{1.4 M_{\odot}} = 11.0_{-0.6}^{+0.9}$ km.

Previous analyses of GW170817 have either neglected constraints on the EOS from nuclear physics or used a parameterization informed by a large number of nuclear physics models [2, 74, 75, 193, 194]. Neither approach properly accounts for the density-dependent theoretical uncertainties in our current understanding of dense matter. For the first time, we employ a strategy that allows us to overcome this deficiency. At low density, chiral EFT describes matter in terms of nucleons and pions in which interactions are expanded in powers of momenta and include all operators consistent with the underlying symmetries of strong interactions [91–95]. This expansion defines a systematic order-by-order scheme that can be truncated at a given order and, most importantly, enables reliable theoretical uncertainty estimates from neglected contributions. Quantum Monte Carlo techniques are then used to solve the many-body Schrödinger equation to obtain the EOS [195]. The resulting EOS is characterized by an uncertainty that grows with density in a manner that can be justified by fundamental theory. We extend the EOSs to higher densities, where the low-energy EFT expansion breaks down in a general way [96, 97], while ensuring that the speed of sound is less than the speed of light and that the EOSs support a two-solar-mass neutron star [98]. The multimessenger observations of GW170817 are then used to constrain these EOSs. This ensures that they are consistent with: (i) the detected gravitational waves during the inspiral; (ii) the production of a post-merger remnant that does not immediately collapse to a black hole (BH); and (iii) the constraints that the energetics of the gamma-ray burst and kilonova place on the maximum mass of neutron stars, M_{\max} .

In neutron matter, chiral EFT interactions are expected to provide a good description of the EOS up to $1 - 2 n_{\text{sat}}$ where $n_{\text{sat}} = 0.16 \text{ fm}^{-3}$ is the nuclear saturation density. Previous calculations show that uncertainties grow quickly with density, from roughly 30% in the energy at saturation density to a factor of 2 at twice saturation density [96]. To be conservative, we generate two collections of nuclear EOSs that differ in the density range restricted by *ab initio* calculations: chiral EFT constraints are either enforced up to nuclear saturation density or up to twice nuclear saturation density. These two sets of EOSs are extended to higher densities as described earlier and allow us to study the impact of the assumption that chiral EFT remains valid up to twice nuclear saturation density. For each of the two families, we generate 2000 individual EOSs distributed so that the radius of a $1.4 M_{\odot}$ neutron star is approximately uniform. The left-most panel of Fig. 2.1 shows the resulting prior on $R_{1.4 M_{\odot}}$. For each set of EOSs, we use stochastic samplers [40] to compute the posterior probabilities in such a way that the tidal deformability of GW170817 is consistent with a specific EOS. When generating model gravitational waveforms, the stochastic sampler randomly draws the neutron star masses from a uniform distribution between 1 and $2 M_{\odot}$, and then randomly draws a specific EOS to compute the tidal deformability of each star. The sky-position and luminosity distance of the source are fixed to those of the electromagnetic counterpart [3, 73]. This procedure allows us to constrain nuclear effective field theories from the gravitational wave observations directly and to compute marginalized posterior probabilities for the star’s radii using

a model-independent non-parametric approach.

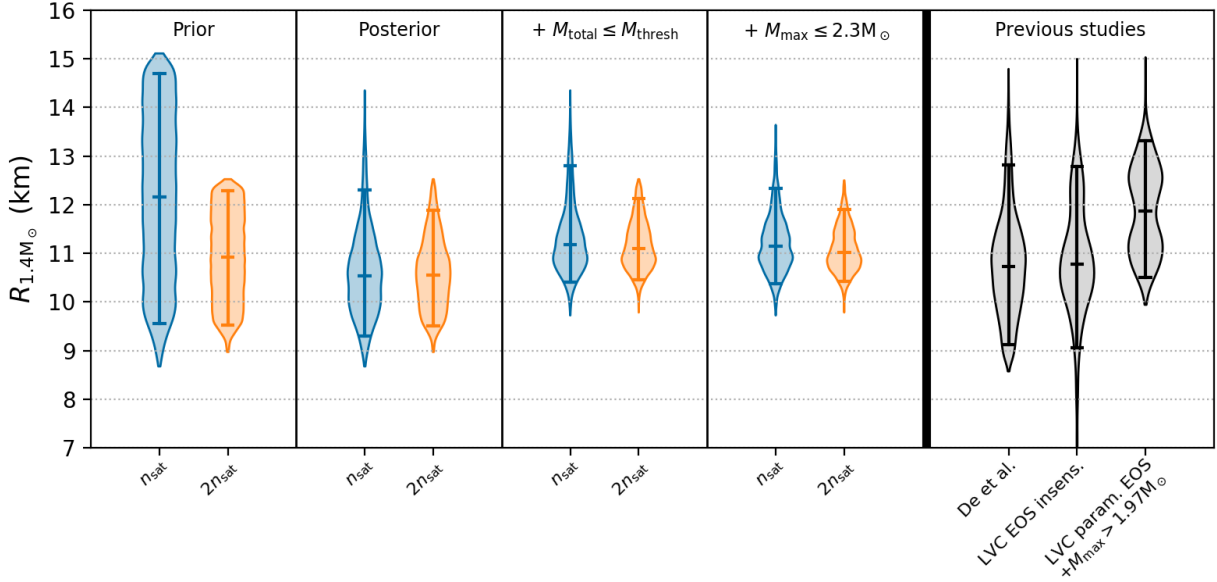


Figure 2.1: Comparison of the estimated radius of a $1.4 M_{\odot}$ neutron star, $R_{1.4 M_{\odot}}$, at different stages of our analysis. In all panels, 1D marginal distributions are indicated by the shaded regions, with the median and the plus/minus 95th and 5th percentiles indicated by the lines. The left panel shows the marginalized prior on $R_{1.4 M_{\odot}}$, assuming chiral EFT up to n_{sat} (blue) and $2n_{\text{sat}}$ (orange). Subsequent panels show the posterior on $R_{1.4 M_{\odot}}$ from the gravitational wave analysis alone, the posterior with the constraint that the estimated total mass M_{total} to be less than the threshold mass for prompt collapse M_{thresh} , and the posterior with the additional constraint that the maximum neutron star mass M_{max} supported by all EOSs $\leq 2.3 M_{\odot}$. The right panel shows posteriors on $R_{1.4 M_{\odot}}$ from De et al. [193], and $R_1 \approx R_{1.4 M_{\odot}}$ from the EOS-insensitive and parameterized EOS analyses reported by Abbott et al. [75] (labelled LVC). In all analyses, a uniform prior was used on the component masses.

The second panel of Fig. 2.1 shows the result of constraining nuclear theory with the gravitational wave observations. We find that the gravitational wave observation GW170817 constrains the maximum radius of neutron stars but is not informative at low radii, which is consistent with previous analyses [75, 193]. The lower limit on the radius is set by nuclear theory and the requirement that the EOS must support a neutron star of at least $1.9 M_{\odot}$ [98]. If one assumes that the chiral EFT description is valid only up to nuclear saturation density, it is possible to obtain large neutron stars inconsistent with the tidal deformability constraint from GW170817. In contrast, if a description in terms of nuclear degrees of freedom remains valid up to twice nuclear saturation density and the EFT approach can be applied, as suggested by earlier work [196], then nuclear theory predicts neutron star radii and tidal deformabilities that are consistent with GW170817. GW170817 excludes simpler phenomenological models for the EOS that are uninformed by nucleon-nucleon scattering data and which predict considerable stiffening of the EOS between n_{sat} and $2n_{\text{sat}}$.

The electromagnetic counterparts to GW17081 can provide additional constraints on the EOS.

Since modeling the counterparts is challenging, we use a conservative approach that relies only on qualitative inferences from the kilonova and gamma-ray burst observations. The properties of these counterparts are inconsistent with either direct collapse to a black hole or the existence of a long-lived neutron star remnant [28, 197]. This allows us to place two further constraints on the allowed EOSs.

First, we discard samples from the posterior in which the total gravitational mass of the binary exceeds the threshold for prompt collapse to a black hole. Several approaches have been taken to calculate this threshold mass [198, 199]. Here, for each EOS in our sample, we use relations calibrated to numerical relativity simulations of Ref. [198], including uncertainties. The third panel of Fig. 2.1 shows the effect of this constraint on the neutron star radius, which significantly constrains the lower limit on $R_{1.4M_\odot}$ [197]. Second, we apply an upper limit on the maximum mass of neutron stars implied by the inconsistency of the electromagnetic counterparts with a long-lived neutron star remnant [28]. We adopt a conservative estimate for this limit, $M_{\max} < 2.3 M_\odot$ [200], consistent also with the 68.3% credible interval of the recently reported $2.14^{+0.10}_{-0.09} M_\odot$ pulsar [201]. The fourth panel of Fig. 2.1 shows the result of applying this constraint.

When constraining the allowed EOSs to those for which the maximum neutron star mass is less than $2.3 M_\odot$, we find that the predicted range for $R_{1.4M_\odot}$ does not significantly change for any prior we investigated. This implies that there is no correlation between $R_{1.4M_\odot}$ and M_{\max} . Such a correlation is typically found for smooth EOSs, e.g., EOSs that assume a description in terms of nucleons to be valid in the whole neutron star. In this case, limiting M_{\max} would also constrain $R_{1.4M_\odot}$. However, the sets of EOSs used here include EOSs with phase transitions that generally break this correlation and effectively decouple the high-density EOS, which sets M_{\max} , from the low-density EOS, which determines $R_{1.4M_\odot}$ [96]. Consequently, we include EOSs that have both the largest possible $R_{1.4M_\odot}$ and a sufficiently small maximum mass. Thus, enforcing an upper limit on M_{\max} has a negligible impact on the predicted radius range. This decoupling highlights the importance of methods constraining the EOS in different density regimes.

The right-most panel of Fig. 2.1 compares our results to previous analyses [75, 193]. Our constraint of $R_{1.4M_\odot} = 11.0^{+0.9}_{-0.6}$ km is the most stringent bound on the neutron star radius to date by a factor of $\simeq 2$. Fig. 2.2 shows the resulting mass-radius relation for our two EOS sets and the marginalized posterior distributions of the component masses and radii for the two neutron stars in GW170817. Table 2.1 summarizes our findings for the radii, tidal deformabilities, and maximum neutron star masses for the two EOS sets. In addition, we present results for the maximum pressure explored in any neutron star, P_{\max} , and the pressure at four times nuclear saturation density, $P_{4n_{\text{sat}}}$.

Comparing the constraints summarized in Table 2.1 for both EOS sets, i.e., EOSs constrained by chiral EFT up to n_{sat} with those constrained up to $2n_{\text{sat}}$, indicates that both EFT-based predictions for the EOS are consistent with each other and with observations. These findings suggest that, in the absence of phase transitions in this density regime, the EFT description of neutron-rich matter remains useful and reliable up to $2n_{\text{sat}}$ and excludes a considerable stiffening of the EOS between $(1 - 2) n_{\text{sat}}$. Despite the larger uncertainties in the EOS at higher densities, the electromagnetic and gravitational wave observations are combined with EFT-based EOSs up to $2n_{\text{sat}}$ —for the first time—to improve the constraint on the neutron star radius significantly. This has important implications for dense-matter physics and astrophysics.

For dense-matter physics, we can derive robust constraints on the pressure of matter at moderate densities by combining our low-density EOSs with the lower bound on the neutron star radius derived from electromagnetic observations and the upper bound from gravitational wave observa-

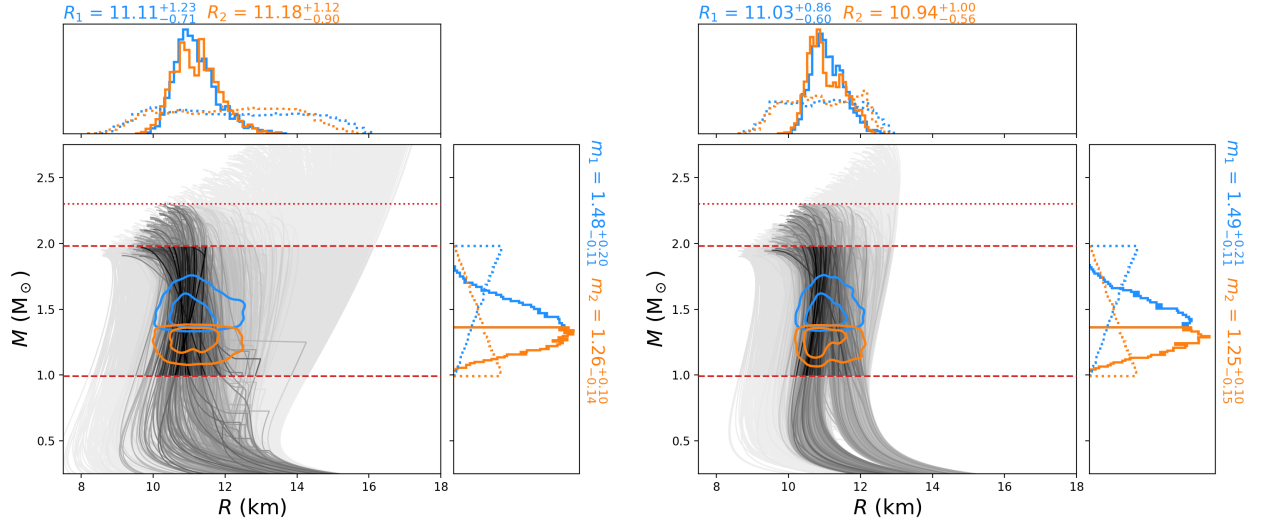


Figure 2.2: Neutron star mass-radius curves and marginalized posterior distributions of the source component masses $m_{1,2}$ and radii $R_{1,2}$, assuming a prior uniform in component masses, with chiral EFT enforced up to n_{sat} (left) and $2n_{\text{sat}}$ (right) and all additional observational constraints enforced. The dashed, horizontal red lines indicate the range of masses spanned by the prior. The top dotted red line indicates the maximum neutron star mass constraint. Any EOS that has support above that line is excised. Each gray-black line represents a single EOS, which we sample directly in our analysis. The shading of the lines is proportional to the marginalized posterior probability of the EOS; the darker the line, the more probable it is. The contours show the 50th and 90th percentile credible regions (blue for the more massive component, orange for the lighter component). The 1D marginal posteriors are shown in the top and side panels; the corresponding priors (without electromagnetic constraints) are represented by the dotted blue and orange lines. Quoted values are the median plus/minus 95th and 5th percentiles.

tions. The pressure at $4n_{\text{sat}}$ is found to be $P_{4n_{\text{sat}}} = 161_{-46}^{+58} \text{ MeV/fm}^3$. This, taken together with the lower pressures predicted by nuclear theory in the interval $(1 - 2) n_{\text{sat}}$, supports earlier claims that the speed of sound in massive neutron stars must exceed $c/\sqrt{3}$ [202], where c is the speed of light. We also provide improved estimates of the maximum pressure that can be realized inside neutron stars [203], $P_{\text{max}} \leq 890 \text{ MeV/fm}^3$.

Our constraints on the neutron star radius and deformability impact the ability of gravitational wave observations to distinguish between binary black hole mergers and mergers containing neutron stars [204]. The gravitational wave observations of GW170817 alone do not rule out the possibility that one or both objects in the merger were black holes [205]. If Advanced LIGO and Virgo were to observe a source at comparable distance to GW170817 once they reach design sensitivity its signal-to-noise ratio would be 100. Using simulated signals of this amplitude, we find that the gravitational waves could easily distinguish between a binary black hole merger and the merger of two neutron stars governed by the SLy or AP4 EOSs with a Bayes factor greater than 10^6 .

Detecting the presence of matter from the inspiral of the compact objects is more challenging for neutron star–black hole binaries. We simulated a neutron star–black hole binary containing $10 M_{\odot}$ black hole and a $1.4 M_{\odot}$ neutron star that has a dimensionless tidal deformability at the upper bounds of our 90% credible interval, $\Lambda = 370$. We place the source at the same distance as GW170817 and assume that the detectors are at design sensitivity [206]; this binary has a signal-to-noise ratio of 190. We calculate the Bayes factor comparing a neutron star–black hole model to a binary-black hole model (i.e. zero tidal deformability for both compact objects). Even at this extremely large signal-to-noise ratio, we find that the Bayes factor is ~ 1 meaning that the models are indistinguishable. The inspiral waveforms of binary black holes and neutron star–black hole mergers become less distinguishable as the neutron star mass increase, the deformability decreases, or the black hole mass increases, and any effect of matter becomes even harder to measure with gravitational waves alone. Electromagnetic counterparts or post-merger signatures will therefore be critical to distinguish between binary black hole, binary neutron star, and neutron star–black hole mergers observed by Advanced LIGO and Virgo [207].

The composition and amount of ejecta from binary neutron stars and neutron star–black hole binaries, which powers the electromagnetic emission, is sensitive to the neutron star radius [208–210]. Our limits have implications for electromagnetic signatures and their observability. This is especially true for mergers such as S190814bv, which was recently reported by the LIGO and Virgo collaborations [211]. A kilonova or gamma-ray burst counterpart is only expected if the neutron star is tidally disrupted before the merger; a condition which depends crucially on the neutron star radius. Fig. 2.3 summarizes the parameter space of neutron star–black hole mergers where a mass ejection (and a corresponding electromagnetic counterpart) is expected based on fits to numerical relativity simulations [212]. Our novel constraints on $R_{1.4 M_{\odot}}$ imply that $\sim 1.4 M_{\odot}$ neutron stars cannot be disrupted in such mergers by non-spinning black holes, unless the black hole mass is unusually low ($< 3.4 M_{\odot}$). More generally, our constraints on neutron star radii will be useful to predict and test correlations between electromagnetic and gravitational wave observations in the future [213].

Our improved constraints on the neutron star radius have implications for the interpretation of electromagnetic observations of neutron stars, in particular for X-ray observations of accreting neutron stars in low mass X-ray binaries (LMXBs). Recent observations suggest the presence of accretion-driven heating and cooling of the neutron star inner crust [214]. The interpretation of

the X-ray light curves in terms of the fundamental properties of the matter in the inner crust such as its thermal conductivity and specific heat is sensitive to the assumed neutron star radius [215]. Similarly, the radius is a key parameter in models of X-ray bursts and quiescent surface emission of neutron stars in LMXBs. In the past, this sensitivity has been exploited to place constraints on neutron star radii. Knowing the radius could shed light on other astrophysical aspects of these commonly observed X-ray phenomena [216].

Observations of neutron star mergers with higher signal-to-noise ratios will improve these constraints. Using a simulated signal at a signal-to-noise ratio of ~ 100 , we find that the gravitational wave signal alone would improve the constraint on $R_{1.4M_\odot}$ by a factor of 2 relative to our result that uses the multimessenger observations of GW170817. For a signal of this amplitude, we will be able to place a lower bound on the neutron star radius from the gravitational wave observation, independent of the electromagnetic counterpart. However, to realize this measurement in practice, improved waveforms will be needed so that modelling systematics do not bias the measurement [217, 218].

Over the next ten years, the LIGO and Virgo detectors are expected to gain an additional factor of ~ 3 in sensitivity [219]. In addition, the Japanese KAGRA detector and LIGO India are expected to be operational. With these improvements, we estimate the rate of binary neutron star mergers with a signal-to-noise ratio ≥ 100 to be one per 4_{-3}^{+36} years [4]. Constraints on $R_{1.4M_\odot}$ from gravitational wave observations alone will be dominated by these relatively rare, high signal-to-noise ratio events. In contrast, multimessenger methods of constraining the EOS can provide significant improvements even for low signal-to-noise events with detected electromagnetic counterparts [213]. These methods are thus extremely promising, however their susceptibility to systematics will need to be better understood.

We combined multimessenger observations of the binary neutron star merger GW170817 and the best current knowledge of the uncertainties associated with the EOS of dense matter to determine the neutron star radius. This also allows us to place stringent bounds on the pressure of matter at moderate density where theoretical calculations remain highly uncertain. Our robust upper bound on the neutron star radius of $R_{1.4M_\odot} = 11.0_{-0.6}^{+0.9}$ km is a significant improvement, with important implications for multimessenger astronomy and nuclear physics. To allow our results to be used by the community for further analysis we provide the EOSs used as our prior and the full posterior samples from our analysis as supplemental materials.

2.3 Methods

2.3.1 Nuclear Equations of State From Chiral Effective Field Theory

Nuclear EFT methods [94, 95] represent a consistent and efficient way of constructing models for nuclear interactions while incorporating symmetries of the fundamental theory for strong interactions, as well as low-energy constraints from nuclear experiments. This is especially useful when extrapolating nuclear interactions to regimes where experimental data is scarce or not available, in particular for neutron-rich systems. Among nuclear effective field theories, chiral EFT starts from the most general Lagrangian containing both pions and nucleons, consistent with all the fundamental symmetries for nuclear interactions. Since this Lagrangian has an infinite number of terms, the separation of scales between typical momenta in nuclear systems and all heavier degrees of free-

dom is used to expand the Lagrangian in powers of p/Λ_b . Here, p is the typical momentum scale of the system at hand $\Lambda_b \approx 600$ MeV [220] is the breakdown scale, which determines when heavier degrees of freedom become important and the EFT breaks down. This expansion defines a systematic order-by-order scheme for the interaction, that can be truncated at a given order and enables the estimation of reliable theoretical uncertainties from neglected contributions. Chiral EFT describes nuclear interactions in terms of explicitly included long-range pion-exchange interactions and parameterized short-range contact interactions. These short-range interactions depend on a set of unknown low-energy couplings, that absorb all unresolved high-energy degrees of freedom, and are adjusted to reproduce experimental data.

To generate our families of EOSs, we start from microscopic quantum Monte Carlo calculations of the neutron-matter EOS using two different nuclear Hamiltonians from chiral EFT up to $2n_{\text{sat}}$ [196]. The two Hamiltonians used in this work were fit to two-nucleon scattering data, the binding energy of the alpha particle, and the properties of neutron-alpha scattering, and reliably describe these systems [221]. They also have been benchmarked in calculations of nuclei up to ^{16}O with great success [222, 223]. In neutron matter, the limit of applicability of these EFT interactions has been estimated to be around twice nuclear saturation density [196]. Each of the two Hamiltonians we employ here has an associated theoretical uncertainty band stemming from the above-mentioned truncation of the chiral series at a finite order. These bands serve as an estimate for the uncertainty due to the limited description of nuclear interactions. The difference between the two Hamiltonians explores the remaining scheme and scale dependence of the chiral interactions. These two sources of uncertainty dominate the neutron-matter calculations.

From these neutron-matter calculations, we then construct the neutron star EOS by extending the pure neutron matter results to beta equilibrium and adding a crust [224]. This allows us to extend our neutron-matter uncertainties to the EOS of neutron stars up to $2n_{\text{sat}}$. At higher densities, chiral EFT breaks down because short-range details that are not resolved in the chiral EFT description become important. To be able to describe neutron stars up to the highest masses, we need to extend our calculations to higher densities in a general and unbiased fashion, i.e., without making assumptions about the properties of the EOS or its degrees of freedom. To achieve this, we use the results from our microscopic calculations where they remain reliable, up to a density n_{tr} which we choose to be either n_{sat} or $2n_{\text{sat}}$. We then compute the resulting speed of sound, c_S , in neutron star matter with its uncertainty band for the two Hamiltonians. For each Hamiltonian, we select a c_S curve up to n_{tr} from the uncertainty band, by sampling a factor $f_{\text{err}} \in [-1, 1]$ which interpolates between upper and lower uncertainty bound. At densities above n_{tr} , we sample a set of points $c_S^2(n)$ randomly distributed between n_{tr} and $12n_{\text{sat}}$, and connect these points by line segments. We only require the speed of sound to be positive and smaller than the speed of light, c , i.e., the resulting curve has to be stable and causal. For each such curve, we construct a related curve that includes a strong first-order phase transition, by replacing a segment with a random onset density and width with a segment with $c_S = 0$. We then reconstruct the EOS from the resulting curve in the c_S plane and solve the Tolman-Oppenheimer-Volkoff equations. We have explored the sensitivity of neutron star properties to the number of points in the c_S plane, and constructed extensions with 5-10 points. The differences between these different extensions have been found to be very small. For the EOSs explored here, we chose a 6-point extension. We repeat this procedure for equal numbers of EOSs of $\mathcal{O}(10,000)$ for the two microscopic Hamiltonians [225].

The resulting family of EOSs is constrained by low-energy nuclear theory as well as general considerations on stability and causality. Finally, we enforce that each EOS reproduces a neutron

star with at least $1.9M_{\odot}$, which is a conservative estimate for the lower uncertainty bound for the two-solar-mass neutron star observations [98]. For each of the two families of EOSs, one for $n_{\text{tr}} = n_{\text{sat}}$ and one for $n_{\text{tr}} = 2n_{\text{sat}}$, we then randomly select 2000 EOSs that have a uniform prior in $R_{1.4}$.

2.3.2 Gravitational Wave Parameter Estimation

We use Bayesian methods to measure the tidal deformability of GW170817 and to infer the EOSs that are most consistent with the observations. Given time-series data from the Hanford, Livingston, and Virgo detectors $\vec{d} = \{\vec{d}_H(t), \vec{d}_L(t), \vec{d}_V(t)\}$ and a model waveform h , the probability that the binary has a set of parameter values $\vec{\vartheta}$ is

$$p(\vec{\vartheta}|\vec{d}(t), h) = \frac{p(\vec{d}(t)|\vec{\vartheta}, h)p(\vec{\vartheta}|h)}{p(\vec{d}(t)|h)}, \quad (2.1)$$

where $p(\vec{d}(t)|\vec{\vartheta}, h)$, $p(\vec{\vartheta}|h)$, and $p(\vec{d}(t)|h)$ are the likelihood, prior, and evidence, respectively. The I indicates additional assumed information, such as the field theory used to describe nuclear interactions. We assume that the detector noise is wide-sense stationary colored Gaussian noise with zero mean, and is independent between observatories. In that case, the likelihood is

$$p(\vec{d}(t)|\vec{\vartheta}, H) \propto \exp\left(-\frac{1}{2} \sum_{i=H,L,V} \langle \tilde{d}_i(f) - \tilde{h}_i(f, \vec{\vartheta}) | \tilde{d}_i(f) - \tilde{h}_i(f, \vec{\vartheta}) \rangle\right). \quad (2.2)$$

where the brackets $\langle \cdot, \cdot \rangle$ indicate an inner product that is weighted by the inverse power spectral density of the noise in each detector.

We use the gravitational wave data associated with the GWTC-1 release [4] from the Gravitational Wave Open Science Center (GWOSC) [226]. Specifically we use the 4096 s duration 16384 Hz sampled frame data for GW170817 from the list of GWTC-1 confident detections, which we downsample to 4096 Hz. These data contain a non-Gaussian noise transient in the L1 data, which we remove by subtracting the glitch model made available in LIGO document LIGO-T1700406. We include these glitch-subtracted data in our data release. Two hundred seconds of data spanning $[t_0 - 190 \text{ s}, t_0 + 10 \text{ s}]$ are filtered starting from 20 Hz, where $t_0 = 1187008882.443$ is an estimate of the geocentric GPS time of the merger obtained from the modeled searches that detected GW170817 [2]. The power spectral density of the noise is estimated using a variant of Welch’s method [227] on 1632 s of data that precedes the start of the analysis time.

To sample the posterior probability over the full parameter space we use MCMC [62, 63] and Nested Sampling stochastic samplers [64] in the `PyCBC Inference` framework [40]. The resulting probability-density function can be numerically marginalized to provide estimates of single parameters. Marginalizing $p(\vec{d}|\vec{\vartheta}, h)p(\vec{\vartheta}|h)$ over all parameters provides an estimate of the evidence $p(\vec{d}|h)$. Taking the ratio of evidences for different physical models $p(\vec{d}|h_B)/p(\vec{d}|h_A)$ provides the Bayes factor \mathcal{B} , which quantifies how much the data supports model B relative to model A . We assume that the binary consists of two compact objects with spins aligned with the orbital angular momentum, and that the binary has negligible eccentricity by the time it can be detected by the LIGO and Virgo interferometers. Under these assumptions, the observed gravitational wave

depends on 13 parameters: six “intrinsic” parameters – the mass $m_{1,2}$, dimensionless-spin magnitude $\chi_{1,2}$, and tidal deformability $\Lambda_{1,2}$ of each component star – and seven “extrinsic” parameters – the binary’s right ascension α , declination δ , luminosity distance d_L , inclination ι , coalescence time t_c , reference phase ϕ , and polarization ψ . We fix the sky location and luminosity distance in our analysis to $\alpha = 13^{\text{h}} 09^{\text{m}} 48.1^{\text{s}}$, $\delta = -23^{\circ} 22' 53.4''$ [3]; $d_L = 40.7 \text{ Mpc}$ [73]. The phase ϕ is analytically marginalized over using a prior uniform between 0 and 2π . We also use uniform priors on $\psi \in [0, 2\pi)$, $\cos \iota \in [-1, 1)$, and $t_c \in t_0 \pm 0.1 \text{ s}$. For the dimensionless spin components $\chi_{1,2}$ we use a prior uniform in $[-0.05, 0.05)$. This is consistent with the fastest-known pulsar in a double neutron star system [228], and was used in previous studies of GW170817 [2, 75, 193].

Observations of millisecond pulsars yield a large variance in possible neutron star masses, with the largest observed masses estimated to be $2.01 \pm 0.04 M_{\odot}$ [228] and $2.17_{-0.10}^{+0.11} M_{\odot}$ [201]. We therefore use a prior distribution uniform in $[1, 2) M_{\odot}$ for the detector frame component masses in our main analysis. Assuming the standard ΛCDM cosmology [229], this corresponds to $m_{1,2}/M_{\odot} \sim U(0.99, 1.98)$ in the source frame at 40.7 Mpc. Electromagnetic observations of double neutron star systems in the galaxy have yielded a best-fit neutron star mass distribution of $p(m_{\text{NS}}/M_{\odot}) \sim \mathcal{N}(\mu = 1.33, \sigma = 0.09)$ [71]. We repeated our analysis using this distribution as our prior on each component mass and we find that our results are insensitive to the choice of mass prior.

We directly sample over individual EOSs instead of $\Lambda_{1,2}$ or the combined dimensionless tidal deformability $\bar{\Lambda}$. For each of the 2000 EOSs for each model, we order the equations by the radius they yield for a $1.4 M_{\odot}$ neutron star, $R_{1.4 M_{\odot}}$. The EOSs are generated such that the distribution of $R_{1.4 M_{\odot}}$ is approximately uniform in the range supported. This results in the marginal prior on each star’s radius $R_{1,2}$ to also be approximately uniform for both of our mass priors, since the radii do not vary much over the mass ranges considered. We then sample over an EOS index $k_{\text{EOS}} \sim U[1, 2000]$. Using the index and the two component masses $m_{1,2}$, we calculate $\Lambda_{1,2}$, with which we generate a model gravitational wave $h(t, \vec{\vartheta})$ and measure the likelihood, Eq. (2.2). In this manner, we ensure that both component masses use exactly the same EOS, with all sampled EOSs being constrained by chiral EFT.

We use restricted TaylorF2 post-Newtonian waveforms [48–53] in our analysis. The effect of analyzing GW170817 using different waveforms was studied in Ref. [194] with unconstrained EOSs. To test the effect of using TaylorF2 waveforms in this study, we repeat the n_{sat} analysis with the uniform mass prior using PhenomDNRT [54–57]. We also tested whether increasing the sample rate to 8192 Hz had any effect using this waveform model. We found negligible differences in all three cases; we therefore only report results using the TaylorF2 model.

2.3.3 Constraints on Neutron Star Radii From Multimessenger Observations

Observations of the kilonova associated with GW170817 indicate that a large $\sim 0.02 - 0.08 M_{\odot}$ amount of mass was ejected, and that this ejecta must contain components with both large and small electron fraction [230]. These inferences are inconsistent with numerical simulations of binary neutron star mergers in which the remnant promptly (within milliseconds) collapses to form a black hole. These simulations generally find a low amount of ejected matter with only high electron fraction, at odds with the optical and near-infrared observations of GW170817. Therefore,

electromagnetic observations of GW170817 are inconsistent with a prompt collapse to a black hole.

Systematic numerical studies of binary neutron star mergers have found that the condition for prompt collapse depends primarily on the total binary mass in comparison to an EOS-dependent threshold mass [198, 199, 231]. (See [232] for possible effects of large mass ratios; however, such mass ratios are not expected if neutron stars are drawn from a distribution similar to the population of galactic binary neutron stars [213].) Bauswein et al. [198, 231] show that this threshold mass increases as a function of the neutron star radius and maximum mass, following

$$M_{\text{thresh}} \approx M_{\text{max}} \left(2.380 - 3.606 \frac{GM_{\text{max}}}{c^2 R_{1.6M_{\odot}}} \right) \pm 0.05 M_{\odot}. \quad (2.3)$$

We apply this condition to posterior samples for each EOS in our analysis to impose the requirement that the binary should not promptly collapse into a black hole upon merger. For each EOS in our sample we calculate the threshold mass using the above expression. To account for the systematic error in Eq. (2.3), a random draw from a normal distribution with a standard deviation of 0.05 is added to each threshold mass sample. We then discard samples from the posterior for which $M_{\text{total}} < M_{\text{thresh}}$. This rules out EOSs with low $R_{1.4M_{\odot}}$, as shown in Fig. 2.1. Bauswein et al. [197] first used similar methods to place a lower bound of $R_{1.6M_{\odot}} \geq 10.64\text{km}$. However, that study required EOS independent assumptions regarding causality to relate M_{max} to $R_{1.6M_{\odot}}$. Additionally, they imposed a more stringent constraint $M_{\text{total}} < M_{\text{thresh}} - 0.1M_{\odot}$ to obtain this value, and find instead $R_{1.6M_{\odot}} > 10.27\text{ km}$ for the more conservative assumption $M_{\text{total}} < M_{\text{thresh}}$ that we adopt here. Our results are consistent with these previous findings, but manage to place a slightly stronger lower limit on the radius (in the conservative case).

The electromagnetic observations of GW170817 are also inconsistent with a long-lived merger remnant. If even a small fraction of the remnant’s rotational energy is extracted through electromagnetic torques (as expected if the remnant neutron star develops even a modest external dipole magnetic field) this would deposit sufficient energy into the surrounding medium to be incompatible with energetic constraints from the kilonova and gamma-ray burst afterglow modelling [28]. A long-lived neutron star would also be in tension with the observed 1.7s delay between the gamma-ray burst and merger [233–235]. This requirement places an upper limit on M_{max} of roughly $\sim 2.2M_{\odot}$ [28, 233–235]. To err on the side of caution we here adopt a more conservative estimate $M_{\text{max}} < 2.3M_{\odot}$ [200]. We implement this constraint by discarding samples whose EOSs do not satisfy this requirement on M_{max} . As described in the main text, this has little affect on $R_{1.4M_{\odot}}$ because our EOSs allow for the most general behavior above n_{sat} or $2n_{\text{sat}}$ including phase transitions, such that the high-density EOS, which sets M_{max} , is effectively decoupled from the low-density region that determines $R_{1.4M_{\odot}}$.

2.3.4 Conditions for Neutron Star Tidal Disruption

Neutron star–black hole mergers have been studied extensively in the literature starting from the pioneering work of Lattimer and Schramm [236]. Despite this, an electromagnetic counterpart to such mergers has not yet been unambiguously detected. The most promising counterparts, optical/near-infrared kilonovae or a gamma-ray burst, depend on whether significant matter can be stripped off the neutron star prior to merger. The condition for the neutron star to be tidally disrupted before merger depends sensitively on the neutron star radius as well as the neutron star mass and black hole mass and spin [208, 237, 238]. Previous work has investigated this parameter space

identifying regions where electromagnetic counterparts may be expected and their observational signatures (e.g. [208, 239, 240]); however the unknown neutron star radius introduced an inherent uncertainty in such analyses. Our new constraint on $R_{1.4M_\odot}$ allows us to reduce the uncertainty in this four-parameter space and provide more precise predictions on whether electromagnetic counterparts may be expected for neutron star–black hole mergers given M_{BH} , M_{NS} , and χ_{BH} inferred from the gravitational wave signal.

Foucart et al. [212] presented a systematic numerical study of mass ejection from neutron star–black hole mergers and provided a fitting formula for the amount of mass remaining outside the black hole horizon shortly after merger and which could produce detectable electromagnetic emission, M_{det} ,

$$M_{\text{det}} \approx M_{\text{NS}} \left[\alpha \eta^{-1/3} \left(1 - 2 \frac{GM_{\text{NS}}}{c^2 R_{\text{NS}}} \right) - \beta \eta^{-1} \frac{R_{\text{ISCO}}}{R_{\text{NS}}} + \gamma \right]^\delta. \quad (2.4)$$

In the above, $(\alpha, \beta, \gamma, \delta) = (0.406, 0.139, 0.255, 1.761)$ are parameters fit to the numerical relativity simulations, η is the symmetric mass ratio, and $R_{\text{ISCO}}(\chi_{\text{BH}})$ is the radius of the innermost stable circular orbit (ISCO) of the black hole and depends on its spin parameter χ_{BH} [241]. In Fig. 2.3 we have shown curves along which $M_{\text{det}} = 0$ as a function of the black hole mass and spin, and for different neutron star masses. Above each curve (higher spin) the neutron star would cross the black hole ISCO before being tidally stripped of any matter, and a kilonova or gamma-ray burst counterpart would not be expected.

2.3.5 Prospects for Tighter Constraints On Neutron Star Radii

We explore the prospects for improving constraints on the neutron star radius and tidal deformability. We study the impact of a louder signal-to-noise ratio and the choice of waveform models used in the likelihood computation for such loud signals. We generate realizations of stationary Gaussian noise for the Advanced LIGO and Virgo detectors, colored by the power-spectral densities representative of the design sensitivity of the detectors [206]. A simulated signal with parameters representative of those for GW170817 is added to the noise. The EOS determining the structure of this system is the median from our $2n_{\text{sat}}$ analysis of GW170817. We place the source at a sky location such that an optimal contribution to the signal-to-noise ratio is obtained from the network of detectors. Specifically, the parameters of our simulated signal are $m_1 = 1.48 M_\odot$, $m_2 = 1.26 M_\odot$, $\chi_1 = -0.030$, $\chi_2 = -0.026$, $\Lambda_1 = 136$, $\Lambda_2 = 345$, $d_L = 40.7 \text{ Mpc}$, $\iota = 149^\circ$, $\psi = 273.8^\circ$, $t_c = 1187008882.4283648$, $\alpha = 16^{\text{h}} 15^{\text{m}} 4.9^{\text{s}}$, and $\delta = -32^\circ 52' 5.16''$. We use the PhenomDNRT model to construct the simulated signal. The resulting injected signal has a signal-to-noise ratio of ~ 100 . This represents the best possible scenario of observing GW170817 with the Advanced LIGO-Virgo detectors (keeping the luminosity distance unmodified). However, within the next decade the sensitivity of the LIGO detectors is expected to surpass the sensitivity we have assumed here [219]. It is therefore reasonable to expect that a binary neutron star will be detected at this signal-to-noise ratio within the next decade.

We perform a parameter estimation analysis on the simulated data using the same prior and settings as in the $2n_{\text{sat}}$ analysis described above. To study the effect of waveform systematics, which are significant at these signal-to-noise ratios, we do an analysis using the TaylorF2 waveform model, and compare to an analysis using the PhenomDNRT model. Fig. 2.1 shows a comparison of

the $R_{1.4M_{\odot}}$ and $\tilde{\Lambda}$ posterior probability densities obtained from the two analyses of the simulated data with that obtained from our gravitational wave only analysis of GW170817. Using TaylorF2, the measurements of $R_{1.4M_{\odot}}$ and $\tilde{\Lambda}$ improve by factors of 1.6 and 1.8 respectively, compared to GW170817. With PhenomDNRT, the measurements of $R_{1.4M_{\odot}}$ and $\tilde{\Lambda}$ are improved by factors of 2.9 and 3.2 relative to GW170817, respectively. This illustrates that at higher signal-to-noise ratio, parameter measurement accuracy is significantly improved with the use of better waveform models.

2.4 Data Availability

All data is available in the manuscript or the supplementary materials. Full posterior data samples are available at <https://github.com/sugwg/gw170817-eft-eos>. The gravitational wave data used in this work was obtained from the Gravitational Wave Open Science Center (GWOSC) at <https://www.gw-openscience.org>.

2.5 Code Availability

All software used in this analysis is open source and available from <https://github.com/gwastro/pycbc>.

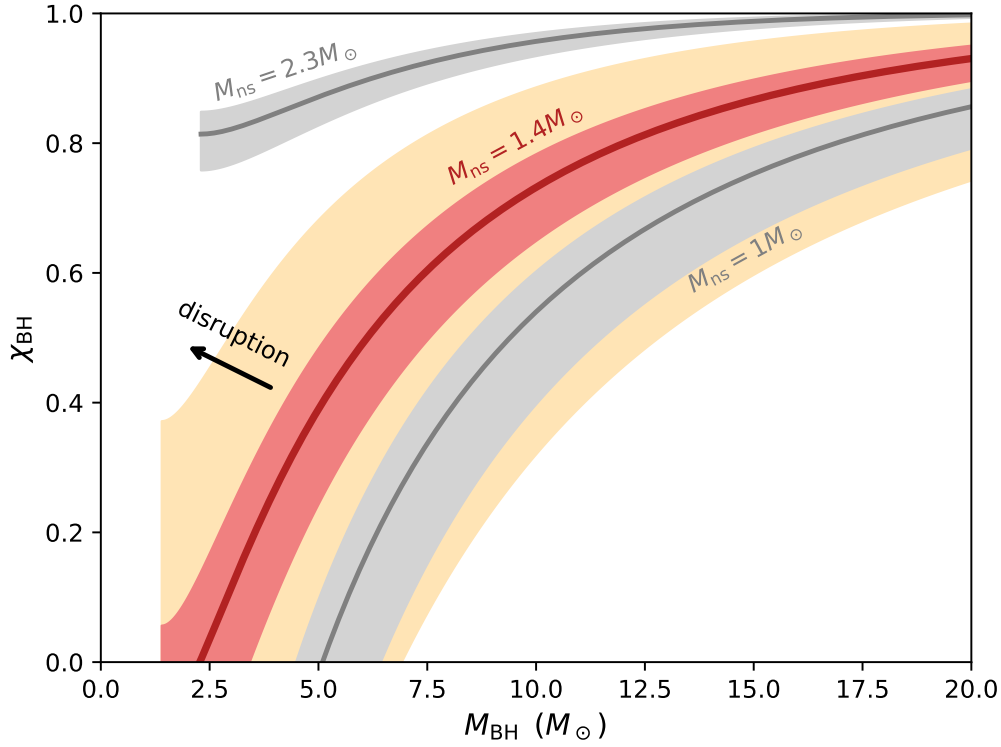


Figure 2.3: Parameter space of neutron star–black hole mergers delineating regions where the neutron star is tidally disrupted before merger (upper-left), from those in which the merger occurs without any mass ejection (lower-right). In the latter case, neither a gamma-ray burst nor a kilonova electromagnetic counterpart would be expected. Each curve shows the minimal black hole spin χ_{BH} required to disrupt a neutron star of a given mass (labeled) and as a function of the black hole mass M_{BH} , calculated following [212]. The criterion depends sensitively on the neutron star radius. Our finding of $R_{1.4M_{\odot}} = 11.0^{+0.9}_{-0.6}$ stringently constrains this parameter space and implies a narrow uncertainty width around each curve (shaded red/grey regions). For comparison, the $1.4 M_{\odot}$ curves for weakly-constrained neutron star radii, $9 \text{ km} < R_{1.4M_{\odot}} < 15 \text{ km}$, span the entire yellow-shaded region, providing only weak predictive power. Our new constraint on $R_{1.4M_{\odot}}$ implies that typical neutron stars cannot be disrupted by non-spinning black holes, except possibly for unusually low black hole mass. The grey curves show a rough bound on the parameter space of allowed neutron star masses, where $M_{\text{NS}} \leq M_{\text{max}} < 2.3 M_{\odot}$ as described in the text, and the lower limit $M_{\text{NS}} > 1 M_{\odot}$ is expected in standard astrophysical neutron star formation scenarios.

2.6 Acknowledgments

We thank Bruce Allen, Wolfgang Kastaun, James Lattimer, and Brian Metzger for valuable discussions.

Funding: This work was supported by U.S. National Science Foundation grants PHY-1430152 to the JINA Center for the Evolution of the Elements (SR), PHY-1707954 (DAB, SD); U.S. Department of Energy grant DE-FG02-00ER41132 (SR); NASA Hubble Fellowship grant #HST-HF2-51412.001-A awarded by the Space Telescope Science Institute, which is operated by the Association of Universities for Research in Astronomy, Inc., for NASA, under contract NAS5-26555 (BM); and the U.S. Department of Energy, Office of Science, Office of Nuclear Physics, under Contract DE-AC52-06NA25396, the Los Alamos National Laboratory (LANL) LDRD program, and the NUCLEI SciDAC program (IT). DAB, SD, and BM thank the Kavli Institute for Theoretical Physics (KITP) where portions of this work were completed. KITP is supported in part by the National Science Foundation under Grant No. NSF PHY-1748958. Computational resources have been provided by Los Alamos Open Supercomputing via the Institutional Computing (IC) program, by the National Energy Research Scientific Computing Center (NERSC), by the Jülich Supercomputing Center, by the ATLAS Cluster at the Albert Einstein Institute in Hannover, and by Syracuse University. GWOSC is a service of LIGO Laboratory, the LIGO Scientific Collaboration and the Virgo Collaboration. LIGO is funded by the National Science Foundation. Virgo is funded by the French Centre National de Recherche Scientifique (CNRS), the Italian Istituto Nazionale della Fisica Nucleare (INFN) and the Dutch Nikhef, with contributions by Polish and Hungarian institutes.

Authors contributions: Conceptualization, DAB, CDC, BK, BM, SR, IT; Data curation, DAB, CDC, SD, IT; Formal analysis, CDC, SMB, IT, SD; Funding acquisition: DAB, BK, BM, SR, IT; Methodology: DAB, CDC, SD, BK, BM, SR, IT; Project administration: DAB, BK, SR, IT; Resources: DAB, BK, IT; Software: DAB, SMB, CDC, SD, SK, BM, IT; Supervision: DAB, BK, SR; Validation: DAB, SMB, CDC, SD, IT; Visualization: SMB, CDC, BM; Writing—original draft: DAB, SMB, CDC, IT; Writing—review and editing: DAB, SMB, CDC, SD, BK, BM, SR, IT.

Competing interests: The authors declare no competing interests.

Observable	Analysis stage	n_{sat}	$2n_{\text{sat}}$
$R_{1.4}[\text{km}]$	Prior	12.1 ± 2.6	10.9 ± 1.4
	+GW	$10.5^{+1.8}_{-1.2}$	$10.5^{+1.3}_{-1.0}$
	+EM	$11.2^{+1.2}_{-0.8}$	$11.0^{+0.9}_{-0.6}$
$\tilde{\Lambda}$	Prior	330^{+1780}_{-300}	160^{+630}_{-130}
	+GW	180^{+340}_{-100}	190^{+210}_{-100}
	+EM	270^{+260}_{-100}	256^{+139}_{-75}
$M_{\text{max}} [\text{M}_{\odot}]$	Prior	$2.39^{+1.09}_{-0.48}$	$2.12^{+0.41}_{-0.21}$
	+GW	$2.01^{+0.33}_{-0.10}$	$2.01^{+0.34}_{-0.11}$
	+EM	$2.07^{+0.20}_{-0.14}$	$2.10^{+0.18}_{-0.17}$
$P_{\text{max}}[\text{MeV}/\text{fm}^3]$	Prior	517^{+512}_{-371}	644^{+437}_{-394}
	+GW	730^{+350}_{-380}	730^{+350}_{-440}
	+EM	600^{+380}_{-330}	570^{+320}_{-320}
$P_{4n_{\text{sat}}}[\text{MeV}/\text{fm}^3]$	Prior	170^{+182}_{-111}	158^{+142}_{-101}
	+GW	123^{+107}_{-70}	125^{+118}_{-68}
	+EM	154^{+58}_{-49}	161^{+58}_{-46}

Table 2.1: Summary of the radius of a $1.4M_{\odot}$ neutron star $R_{1.4M_{\odot}}$, the tidal deformability $\tilde{\Lambda}$, the maximum neutron star mass M_{max} , the maximum pressure explored in neutron stars P_{max} , and the pressure at four times nuclear saturation density $P_{4n_{\text{sat}}}$ at different stages in our analysis. We quote the prior values, values after applying gravitational wave (GW) constraints, and finally values when both constraints from electromagnetic (EM) observations are applied. Quoted values are the median plus/minus 95th and 5th percentiles.

2.7 Supplementary Material

2.7.1 Comparison to Previous Multimessenger Constraints

Recently, Radice and Dai [74] and Coughlin et al. [242] also performed multimessenger parameter estimation for GW170817. Radice and Dai [74] imposed a lower limit on the tidal deformability of the merging neutron stars based on arguments that the mass surrounding the remnant after merger (that can subsequently become unbound and contribute to the kilonova through secular disk winds [243–246]) is strongly correlated with $\tilde{\Lambda}$ [247]. Combining this lower limit with the gravitational wave data and translating their resulting constraints on $\tilde{\Lambda}$ into $R_{1.4M_{\odot}}$ using an EOS insensitive relation [193], they find $R = 12.2^{+1.0}_{-0.8} \pm 0.2$ km. Coughlin et al. [242] performed joint electromagnetic and gravitational wave parameter estimation, directly fitting the kilonova photometry using results from radiative transfer calculations [248] and numerical relativity simulations, along with modeling of the associated gamma-ray burst GRB170817A. Sampling in $\tilde{\Lambda}$ space and similarly translating their results into radius constraints using the EOS insensitive relation of De et al. [193], they obtained $R \in (11.1, 13.4) \pm 0.2$ km [242].

These earlier studies differ from our present work in several respects. First and foremost, we combine systematic nuclear theory with the gravitational wave and electromagnetic observations. We use theoretically motivated EOSs that comply with low-density nuclear experimental data and neutron star mass measurements while allowing for the most general behavior at large densities, and are therefore able to directly constrain the neutron star radius rather than the tidal deformability. This alleviates the need of assuming a universal relation between $\tilde{\Lambda}$ and $R_{1.4M_{\odot}}$, and allows us to explore the parameter space in the most self-consistent way. Furthermore, we have adopted conservative assumptions regarding the electromagnetic constraints, based on purely qualitative features of the electromagnetic counterparts. While quantitatively fitting these counterparts as in Coughlin et al. [242] provides a promising avenue for future investigation, the uncertainties associated with such modeling are still poorly constrained. In this respect, it is unsurprising that the lower limit on $R_{1.4M_{\odot}}$ we obtain here (and which is governed primarily by the electromagnetic constraint) is lower than in these previous studies as we have made conservative assumptions. As a final note, we point out that our results are also consistent with early suggestions for a small neutron star radius (≤ 12 km) as a possible way to explain the ‘blue’ kilonova component of GW170817 [249].

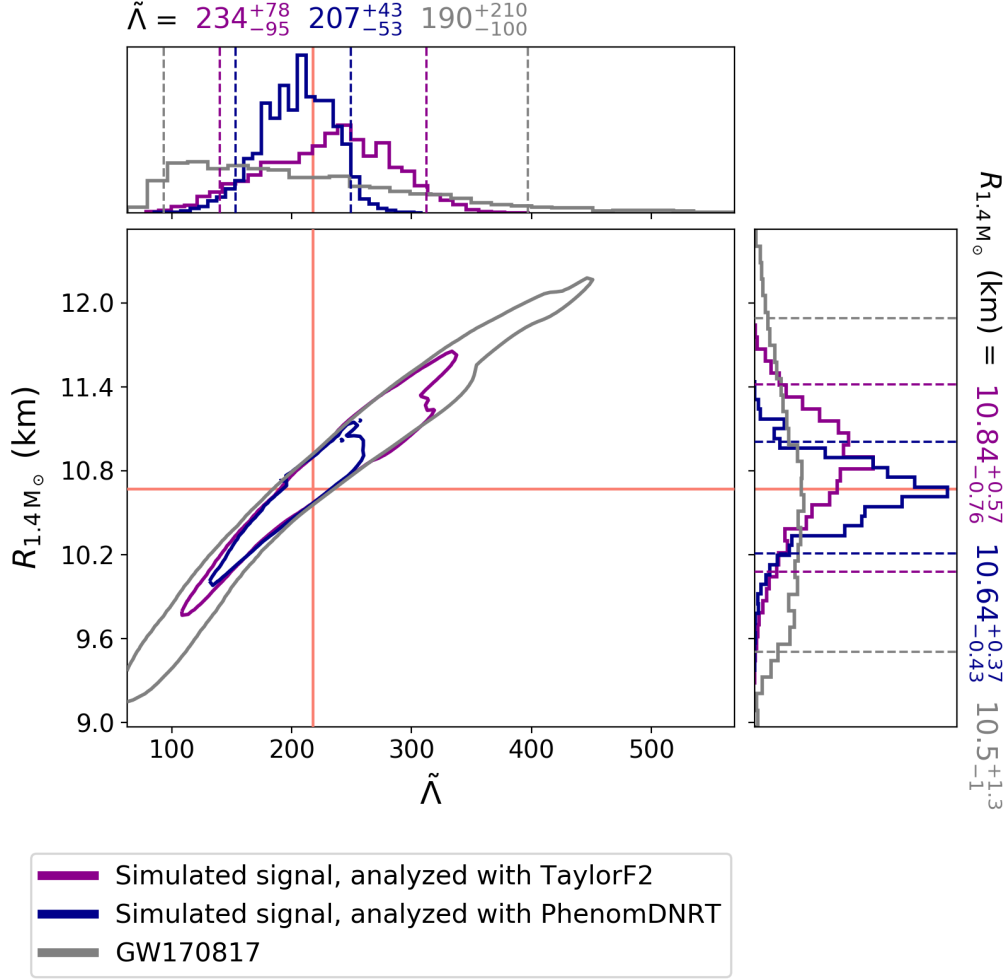


Figure 2.4: Posterior probability distribution of $R_{1.4M_\odot}$ and $\tilde{\Lambda}$ for a simulated GW170817-like signal at a signal-to-noise ratio of ~ 100 , compared to our gravitational wave only analysis of GW170817. Solid red lines show the parameters of the simulated signal. The top and side panels show 1D marginal posterior distributions for the parameters, with the dashed lines showing the 5th and 95th percentiles. The titles quote the median \pm the 95th and 5th percentile for each parameter. The contours show the 90% credible region of the 2D marginalized posterior. All of these analyses used the $2n_{\text{sat}}$ prior for the EOSs.

3 | Using Gravitational Waves to Distinguish Between Neutron Stars and Black Holes in Compact Binary Mergers

This chapter contains material published as Brown, Stephanie M., Capano, Collin D., Krishnan, Badri *Using Gravitational Waves to Distinguish Between Neutron Stars and Black Holes in Compact Binary Mergers*. *Astrophys J* (accepted 2022). <https://doi.org/10.48550/arXiv.2105.03485>

Abstract

In August 2017, the first detection of a binary neutron star merger, GW170817, made it possible to study neutron stars in compact binary systems using gravitational waves. Despite being the loudest gravitational wave event detected to date (in terms of signal-to-noise ratio), it was not possible to unequivocally determine that GW170817 was caused by the merger of two neutron stars instead of two black holes from the gravitational wave data alone. That distinction was primarily due to the accompanying electromagnetic counterpart. This raises the question: under what circumstances can gravitational wave data alone, in the absence of an electromagnetic signal, be used to distinguish between different types of mergers? Here, we study whether a neutron star-black hole binary merger can be distinguished from a binary black hole merger using gravitational wave data alone. We build on earlier results using chiral effective field theory to explore whether the data from LIGO and Virgo, LIGO A+, LIGO Voyager, the Einstein Telescope, or Cosmic Explorer could lead to such a distinction. The results suggest that the present LIGO-Virgo detector network will most likely be unable to distinguish between these systems even with the planned near-term upgrades. However, given an event with favorable parameters, third-generation instruments such as Cosmic Explorer will be capable of making this distinction. This result further strengthens the science case for third-generation detectors.

3.1 Introduction

Neutron stars are unique laboratories for studying ultra-dense, relativistic matter. Multimessenger observations of neutron star mergers provide unique opportunities to extract relevant physical information (such as compactness) from them. Measurements of neutron star compactnesses and radii are vital to constraining the EOS of ultra-dense matter [85]. In addition to gravitational wave

observations of the neutron star mergers GW170817 and GW190425 [2, 250], X-ray observations of accreting neutron stars [71, 72] have placed constraints on neutron star mass and radii. Of these, the recent results from NICER are especially promising [191, 192, 251].

The observation of GW170817 and its electromagnetic counterpart led to several important advances. The detection of the electromagnetic counterpart was possible because the LIGO-Virgo observation constrained the sky location of the event to 28 deg^2 . It was the detection of gamma-ray burst GRB170817A 1.7 seconds after GW170817 that provided the initial evidence that this event contained neutron star matter. Transient electromagnetic follow-ups [3, 73] further supported the neutron star hypothesis and provided more information about the binary. The combination of electromagnetic and gravitational wave observations led to new constraints on neutron star physics. For instance, analyses of GW170817 placed upper limits on the radius of a $1.4 M_\odot$ neutron star: $11.0^{+0.9}_{-0.6} \text{ km}$ [8], $12.2^{+1.0}_{-0.8} \pm 0.2 \text{ km}$ [74], $10.8^{+2.4}_{-1.9} \text{ km}$ [193]. The LIGO-Virgo Collaboration constrained the radii of the two components of GW170817 ($M_1 = (1.36, 1.58)M_\odot$, $M_2 = (1.18, 1.36)M_\odot$) to $11.9^{+1.4}_{-1.4} \text{ km}$ [75]. Later work constrained the properties of this event further $M_1 = 1.45^{+0.08}_{-0.06}$, $R_1 = 12.36^{+0.52}_{-0.38}$ and $M_2 = 1.28^{+0.05}_{-0.06}$, $R_2 = 12.32^{+0.66}_{-0.43}$ [76]. Combining gravitational wave observations GW170817 and GW190425 with NICER results led to constraints on the radius of a $1.4M_\odot$ of $12.33^{+0.76}_{-0.81} \text{ km}$ and $12.18^{+0.56}_{-0.79} \text{ km}$ [110].

Though GW170817 led to new constraints on the radii and tidal deformabilities of neutron stars, it alone was not sufficient to determine that the event was a binary neutron star rather than a binary black hole. The evidence that this was a binary neutron star merger came from observations of the electromagnetic counterpart. In future observations, we will likely not be in the fortuitous position of having a clear electromagnetic counterpart. To date, LIGO-Virgo has detected two neutron star-black hole binaries, neither of which had an electromagnetic counterpart [18]. Furthermore, if the mass of any of the binary components happen to lie within the mass gap, gravitational waves are the most promising avenue by which to determine whether the object is a black hole or a neutron star. This leads to the questions: under what conditions can a gravitational wave signal alone differentiate between a binary neutron star and a binary black hole? Can a neutron star-black hole binary be differentiated from a binary black hole by gravitational wave observations alone? This work addresses the second of these questions for current and future gravitational wave detectors. Current detectors may not be able to successfully differentiate between neutron star-black hole binaries and binary black holes, making future detectors vitally important. The importance of future detectors for studying neutron stars in binary neutron star mergers was shown in a recent paper [252].

In addition to the current LIGO-Virgo detectors, we consider LIGO A+, LIGO Voyager, the Einstein Telescope, and Cosmic Explorer. The plans for LIGO A+ aim to improve the detection range of binary neutron stars at $1.4 M_\odot$ by a factor of 1.9 [253]. These improvements to LIGO may occur as soon as three years from now. Further plans exist for LIGO Voyager, which will further increase detector sensitivity [254]. Power spectral density curves for the design sensitivity of these two detectors are publicly available [43] and are used in our analysis. Beyond LIGO A+ and LIGO Voyager, there are plans for third-generation (3G) detectors such as the Einstein Telescope (ET) and Cosmic Explorer. We consider the Einstein Telescope and both Cosmic Explorer's first run (CE1) expected to take place in the 2030s and its second run (CE2) which is planned for the 2040s. Cosmic Explorer is expected to vastly increase the number of neutron stars detected by expanding the redshift horizon for binary neutron star detections out to $z = 3.1$ in the first run. With predicted signal-to-noise ratios going up by an order of magnitude for nearby sources,

third-generation detectors will significantly improve our tidal deformability measurements [255].

We use standard Bayesian model selection tools in our analysis. The evidences are calculated using the dynamic nested sampling package `dynesty` [64, 65] accessed through the `PyCBC Inference Toolkit` [40]. In this analysis, we employ neutron star EOSs derived from chiral EFT, a theory that uses an effective description of nuclear matter in terms of nucleons and pions [91, 92, 94, 95]. The chiral EFT framework not only leads to EOSs consistent with all symmetries of the strong interactions and known experimental constraints, but it also provides reliable uncertainty estimates. We use the same subset of the EOSs employed successfully in [8] to improve constraints on neutron star radii.

We show that, at least for the proposed gravitational wave detectors within the next decade (namely LIGO A+ and LIGO Voyager), it is very unlikely that gravitational wave observations alone will be able to distinguish neutron star-black hole binaries from binary black holes. Third-generation gravitational wave detectors will be required for this purpose. Sec. 3.2 details our model selection procedure, Sec. 3.3 presents the main results, and Sec. 3.4 concludes with a discussion of the implication of these results.

3.2 Methods

Consider a network of gravitational wave detectors, and let $d_i(t)$ denote the gravitational wave strain time series data in the i^{th} detector as a function of time t . The collection of all time series data in the network will be denoted \vec{d} . The data is the sum of detector noise $n_i(t)$ and a possible astrophysical signal $h(t)$, which depends on certain parameters which we collectively denote $\vec{\vartheta}$:

$$d_i(t) = n_i(t) + h_i(t; \vec{\vartheta}). \quad (3.1)$$

The central goal of a Bayesian analysis is to calculate the posterior probability distributions $p(\vec{\vartheta}|\vec{d}(t))$ of the parameters $\vec{\vartheta}$. The basis of this is Bayes' Theorem

$$p(\vec{\vartheta}|\vec{d}(t), h) = \frac{p(\vec{d}(t)|\vec{\vartheta}, h)p(\vec{\vartheta}|h)}{p(\vec{d}(t)|h)}. \quad (3.2)$$

The fourteen parameters appearing in $\vec{\vartheta}$ are discussed below. The prior, $p(\vec{\vartheta}|h)$, represents the knowledge that we have about the parameters before considering the data. The likelihood function, $\mathcal{L} = p(\vec{d}(t)|\vec{\vartheta}, h)$, is the probability of obtaining the observation $\vec{d}(t)$ given a waveform h with parameters $\vec{\vartheta}$.

In order to obtain a posterior distribution on one or a few parameters, we marginalize over the other parameters by integrating $p(\vec{d}(t)|\vec{\vartheta}, h)p(\vec{\vartheta}|h)$. Marginalizing over all parameters yields the evidence. Comparing the evidence ($\mathcal{Z} = p(\vec{d}(t)|h)$) of two different models (H_A and H_B) gives the Bayes factor,

$$\mathcal{B} = \frac{p(\vec{d}(t)|H_A)}{p(\vec{d}(t)|H_B)}. \quad (3.3)$$

This number indicates how much the data supports one model over the other. When $\mathcal{B} > 1$, H_A is favored over H_B ; the larger \mathcal{B} is, the more H_A is favored. In this study, the Bayes factors express

how much A , the neutron star-black hole model, is favored over B , the binary black hole model. We measure evidences using the dynamic nested sampling package `dynesty` [64, 65]. To crosscheck our results, we analyze a subset of our signals using a parallel-tempered MCMC sampler called `emcee_pt` [62, 256]. The resulting posteriors were consistent with those generated by `dynesty`.

We generate simulated gravitational waves from neutron star-black hole binary (NSBH) mergers and add these to simulated Gaussian noise colored by the target detector configuration's power spectral density. Gravitational waves from neutron star-black hole mergers depend on multiple variables $\vec{\vartheta}$. The most relevant parameters for this work are the component masses $m_{1,2}$ and the dimensionless tidal deformabilities $\Lambda_{1,2}$, which are defined as

$$\Lambda_{1,2} = \frac{2k_2}{3} \left(\frac{c^2 R_{1,2}}{Gm_{1,2}} \right)^5. \quad (3.4)$$

Here $R_{1,2}$ are the radii of the individual stars, and k_2 is the tidal Love number, which is determined from the EOS and the mass. The leading order effect of $\Lambda_{1,2}$ on the waveform is through the combined tidal deformability parameter:

$$\tilde{\Lambda} = \frac{16(12q+1)\Lambda_1 + (12+q)q^4\Lambda_2}{13(1+q)^5}, \quad (3.5)$$

where we define the mass ratio $q = m_2/m_1 \geq 1$. The tidal deformability is the primary means to distinguish black holes from neutron stars using gravitational waves and infer the EOS of neutron stars. By definition, a black hole has zero tidal deformability, while larger values of Λ correspond to stiffer EOSs.

As the binary inspirals, merges, and then settles into a stable black hole, it emits gravitational waves. Gravitational waves have two polarizations, denoted as $h_{+, \times}$. The intrinsic parameters affect the phase evolution of the gravitational waves. Some parameters, such as the chirp mass and symmetric mass ratio, also affect the amplitude of the gravitational wave. The symmetric mass ratio ν and chirp mass \mathcal{M} are defined respectively as

$$\nu = \frac{m_1 m_2}{(m_1 + m_2)^2}, \quad \mathcal{M} = \mu^{3/5} M^{2/5}. \quad (3.6)$$

In the source frame, say one aligned with the source axis, $h_{+, \times}$ depend on the direction to the detector; equivalently, in a geocentric frame, $h_{+, \times}$ depend on the orientation of the source. Furthermore, the detectors do not detect h_+ and h_\times directly, they detect the gravitational wave strain:

$$h(t) = F_+(t; \alpha, \delta, \psi)h_+ + F_\times(t; \alpha, \delta, \psi)h_\times \quad (3.7)$$

where F_+ and F_\times are functions of the angles defining the location of the source. These angles are typically expressed as sky location (right ascension α , declination δ) and polarization angle ψ . Additionally, the amplitude depends on the inclination angle ι and the luminosity distance of the source. These extrinsic variables affect only the amplitude of the gravitational waveform. The last variable that defines the detected strain is the detection time t_c (which determines the detector position and orientation).

We employ the `PyCBC Inference Toolkit` [40] to generate the gravitational waveforms. This requires a specification of the parameters $\vec{\vartheta}$ and a waveform approximant. In the

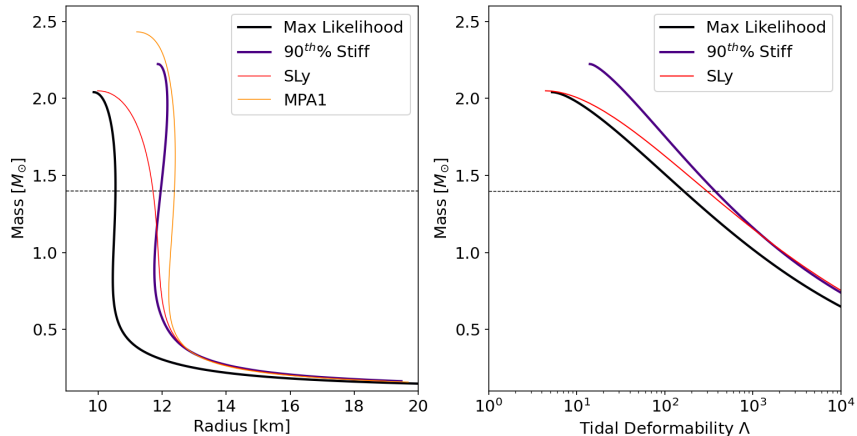


Figure 3.1: Mass-radius and mass-tidal deformability curves for the two EOSs used in this analysis compared to commonly used EOSs. The dashed horizontal line is at $1.4M_{\odot}$. The two equations used in this paper are labelled as ‘stiff’ and ‘maximum likelihood’. The stiff and maximum likelihood EOSs corresponds to $\Lambda = 369$ and $\Lambda = 162$ for a $1.4M_{\odot}$ neutron star respectively.

data analysis, colored Gaussian noise is added to the generated waveform using the detector power spectral density curve. We use a waveform approximant that combines inspiral, merger, and ring-down portions of the signal and has been calibrated to numerical relativity results (see e.g., [23, 257–260]). The bulk of the results presented in this work use the waveform approximant SEOB-NRv4_ROM_NRTidalv2_NSBH [59], which is tailored to neutron star-black hole systems. The waveform approximants IMRPhenomD_NRTidal [54, 56–58] and IMRPhenomNSBH [261] were considered as well; however, we found SEOBNRv4_ROM_NRTidalv2_NSBH to be the best choice for this analysis. We note here that neutron star-black hole systems present a considerable challenge for existing signal models and significant uncertainties remain. This is especially true at the high signal-to-noise ratios possible for third-generation detectors. For this reason, we compare the results for all three waveforms.

We set the neutron star mass to the standard $1.4M_{\odot}$ and vary the mass of the black hole between $(5, 10, 15, 20)M_{\odot}$ and the distance between $(40, 80)$ Mpc. For the neutron star, we choose two of the EOSs based on chiral EFT that were favored by parameter estimation in a previous work [8]. The first of these equations is the maximum likelihood EOS found therein. However, this EOS is quite soft and leads to small tidal deformabilities ($\Lambda = 162$ for a $1.4M_{\odot}$ neutron star). As neutron stars with large tidal deformabilities are easier to distinguish from black holes than those with small ones, we also consider a stiff EOS. The EOS is the stiffest EOS in the 90th percentile credible interval of [8] ($\Lambda = 369$ for a $1.4M_{\odot}$ neutron star).

For both the injection and the parameter estimation, the sky location is fixed to the reported sky location of GW170817 [3]:

$$\alpha = 13^{\text{h}} 09^{\text{m}} 48.1^{\text{s}}, \quad \delta = -23^{\circ} 22' 53.4'' . \quad (3.8)$$

For the injection, the polarization, inclination, and coalescence time are set to

$$\Psi = \pi, \quad tc = 1187008882.4434, \quad \iota = 0.35 . \quad (3.9)$$

The choice of sky location and inclination is arbitrary, and the effects of choice of sky location are discussed in Section 3.4. For the analysis with DYNESTY, we set up the parameter estimation to be as similar to the analysis for GW170817 as possible. As was done for GW170817 [8, 193], we fix the sky location and distance. While it is unlikely that the sky location of a detected neutron star-black hole system will be known to such accuracy, fixing the sky location in the analysis significantly reduces computation time and does not effect the resulting Bayes factors. To confirm this, we performed a series of parameter estimation runs where the sky location was a variable parameter and found the Bayes factors to be completely consistent. The variable parameters in our parameter estimation were the individual masses, spins, coalescence time, inclination, and polarization. The prior for the neutron star mass object was uniform on $[1, 2]M_{\odot}$ and for the black hole it was uniform on $[m_{BH} - 2, m_{BH} + 2]M_{\odot}$. The spin priors were both low spin $U[0.05, 0.05]$, which has been used in previous analyses of GW170817 (see e.g., [2, 8, 193]). We constrained the inclination ι and polarization ψ angles such that $\psi \in [0, 2\pi)$ rad and $\cos \iota \in U[-1, 1)$, and the coalescence time t_c was assumed to be uniform in the range $t_c \in t_0 \pm 0.1$ sec where t_0 is the trigger time.

The tidal deformability parameter estimation is what differs between our two models. To test the binary black hole hypothesis, the tidal deformability of both objects is set to 0 in the parameter estimation. We looked at two cases for the neutron star-black hole model parameter estimation. In one case, we sampled over the EOS for the neutron star mass object. The EOS has a uniform prior in radius at $1.4M_{\odot}$, and there are 2,000 equations in the prior. The equation selected by the sampler was then used to calculate the tidal deformability given m_1 and m_2 . In the other case, we set the EOS as a static variable in the parameter estimation. The reason for this is that, while the nuclear EOS is currently not well constrained, it is expected that experiments such as NICER will significantly improve our knowledge over the next decade. To take this into account, we consider the extreme case: the one in which the EOS is known exactly and is thus fixed in the parameter estimation.

3.3 Results

To determine if gravitational waves can distinguish between neutron star-black hole binaries and binary black holes, we look at the natural log of the Bayes factor ($\ln \mathcal{B}$) between two models. There is much debate on what constitutes evidence, strong evidence, decisive evidence, and so on. Commonly cited statistics papers such as [262] state that $\log_{10} \mathcal{B} \geq 2$ ($\ln \mathcal{B} \geq 5$) can be considered decisive evidence in favor of a model. However, this is questionable for gravitational wave model selection because of the high dimensionality, complexity and several degeneracies of the parameter space (which are not yet fully understood). Additionally, using different sampler settings and different noise realizations can lead to variations in $\ln \mathcal{B}$ of about ± 2 at the 1σ level when $\ln \mathcal{B} \approx 5$, and around ± 4 when $\ln \mathcal{B} \approx 10$. Taking account these uncertainties, we have decided to require a higher threshold thereby ensuring that our conclusions remain conservative regarding the capabilities of the gravitational wave detectors that we consider. We require

$$\ln \mathcal{B} \geq 10 \tag{3.10}$$

for decisive evidence.

The errors quoted in this paper are based on the standard deviation of $\ln \mathcal{B}$ across instances of the same injection parameters but with different noise realizations. Except for the specific case of $m_{BH} = 5M_{\odot}$, the errors for the current LIGO-Virgo detector network, LIGO A+, and LIGO Voyager are < 1 . For the Einstein Telescope and Cosmic Explorer 1, the errors are < 2.5 , and for Cosmic Explorer 2, the errors are < 4 . The errors in the case of $m_{BH} = 5M_{\odot}$ are larger (for details see Table 5.5.1). The maximum error for the current LIGO-Virgo detector network is ≈ 1.0 . This increases to 2.5 for LIGO A+, 4.7 for LIGO Voyager, ≈ 16 for Einstein Telescope, ≈ 19 for Cosmic Explorer 1, and ≈ 29 for Cosmic Explorer 2. The relative error decreases by nearly an order of magnitude as signal-to-noise ratio increases, from ~ 1 for aLIGO and Virgo to ~ 0.1 for Cosmic Explorer 2.

As mentioned earlier, we shall present results for a $1.4M_{\odot}$ neutron star with a black hole companion of mass (5, 10, 15, 20) M_{\odot} , and we shall take the distance to be 40 or 80Mpc. The neutron star EOS shall be either of the ones shown in Fig. 3.1. We shall consider the following detector networks:

- The current LIGO-Virgo network at design sensitivity in the zero-detuned high power configuration [42]
- The LIGO A+ upgrade [43]
- LIGO Voyager [43].
- The Einstein Telescope [43].
- The first observational run of the proposed 40 km Cosmic Explorer detector in the “compact binary” configuration [44].
- The second observational run of the proposed 40 km Cosmic Explorer detector, again in the “compact binary” configuration [44].

The results of our analysis for the various combinations of masses, distances and detector network are shown in Figs. 3.2 to 3.4 and in Tables 3.A.2-3.A.7

The Figs. 3.2 and 3.3 show the Bayes factors for the $5M_{\odot}$ and $10M_{\odot}$ black hole cases respectively. As expected, the $5M_{\odot}$ case leads to larger Bayes factors since the tidal effects on the neutron star are more significant. Nevertheless, for both cases, the important observation for our purposes is that the Bayes factors exceed our chosen threshold of Eq. (3.10) for the third-generation detectors (The Einstein Telescope and Cosmic Explorer). The Voyager results in Fig. 3.2 for the stiff EOS surpass the threshold slightly. However, the variation is seen to be large. Furthermore, this is not the case for the maximum likelihood EOS or for a 10 solar mass black hole companion. In a fine-tuned case, LIGO Voyager might be able to do this measurement. However, as it requires the event to be closer than any binary detected to date, to have a black hole companion that is smaller than any black hole observed by LIGO thus far, and to have a nuclear EOS that is rather optimistically stiff, it is unlikely. This same conclusion is evident in Fig. 3.4, which shows all the combinations that we have considered: $\ln \mathcal{B} > 10$ almost exclusively for the third-generation detectors.

The precise numerical values for the Bayes factors are found in Tables 3.A.2-3.A.7. Looking at Table 3.A.2, we see that for the current LIGO-Virgo detector network $|\ln \mathcal{B}| < 1.5$ in all cases.

For the upgraded detector LIGO A+, the range of Bayes factors is $[0.0, 4.8]$ for the variable EOS analysis and $[-0.2, 5.2]$ for the constant EOS analysis. From Table 3.A.3, we see that except for the $5M_{\odot}$ black hole companion and the 90th percentile stiff EOS all $|\ln \mathcal{B}| \leq 1.0$. We also see that the largest Bayes factor occurs, as expected, for the 90th percentile stiff EOS with a $5M_{\odot}$ black hole at 40Mpc. With the LIGO Voyager, we once again see the highest Bayes factor for the $5M_{\odot}$ black hole companion and the stiff EOS gravitational wave. In this case, we have 13.4 for the variable EOS case and 14.1 for the constant EOS case. Excluding these values, the range of $\ln \mathcal{B}$ is $[0.2, 2.6]$ for the variable EOS and $[-0.1, 2.9]$ for the constant EOS case.

The results using the third-generation detectors (the Einstein Telescope, Cosmic Explorer 1, and Cosmic Explorer 2) are more optimistic. We finally see multiple values above the threshold of 10, though in two cases, the 1σ error falls below the cut-off. Looking at Table 3.A.5, we see that for the Einstein Telescope, there are now three instances for both the variable and constant EOS cases that exceed our Bayes factor threshold. In all cases, this occurs for a black hole companion of mass $5M_{\odot}$. For the stiff EOS, we have $\ln \mathcal{B}$ of (81.8, 82.9) at 40Mpc and (17.4, 18.4) at 80Mpc for the (variable, constant) EOS cases. Additionally, for the maximum likelihood EOS, at 40Mpc, we have $\ln \mathcal{B}$ of (12.6, 13.4) for the variable and constant EOS, respectively. The results improve further when looking at Cosmic Explorer 1 and 2, particularly for the maximum likelihood EOS. We now see multiple results above the threshold at the 1σ level. For the stiff EOS we have $\ln \mathcal{B}$ of (130.9, 132.3) at 40Mpc and (29.2, 30.4) at 80Mpc for the (variable, constant) EOS cases. Additionally, for the maximum likelihood EOS, at 40Mpc, we have $\ln \mathcal{B}$ of (21.2, 22.2) for the variable and constant EOS, respectively. In Table 3.A.7, it can be seen that the results of Cosmic Explorer 2 are very similar to those of Cosmic Explorer 1. We have $\ln \mathcal{B} > 10$ for cases with a low black hole mass, for both EOSs, out to 80Mpc for both EOSs. For Cosmic Explorer 2 we see for the first time, the possibility of distinguishing a neutron star with a $10M_{\odot}$ black hole companion. Note, however, that this occurs only for the stiff EOS at 40Mpc.

Finally, we note that current waveform models for neutron star-black hole binaries have limitations in high signal-to-noise ratio and high mass ratio regimes such as the ones explored in this paper. Developing more accurate waveform models is important for analyzing real data. However, in our studies, we inject simulated signals in noise and recover them with the same signal model. Thus it is most important that the signal model capture the same qualitative features as the true signal. We considered two neutron star-black hole models, SEOBNRv4_ROM_NRTidalv2_NSBH and IMRPhenomNSBH, as well as the older IMRPhenomD_NRTidal model. Figure 3.5 compares the results from all three waveforms for the $m_{BH} = 5M_{\odot}$ case. For LIGO-Virgo and its upgrades, all three waveforms agree at the 2σ level. For the 3G detectors, however, IMRPhenomD_NRTidal gives significantly lower results than the two neutron star-black hole waveforms. We see that for all three waveforms, the results qualitatively agree: The Bayes factors for Einstein Telescope and the first and second runs of Cosmic Explorer remain comfortably above the threshold.

However, a closer look reveals that IMRPhenomNSBH is unsuitable for use with 3G detectors when $m_{BH} > 10M_{\odot}$. As the mass of the black hole companion increases, tidal effects decrease, and the gravitational waves emitted grow more similar to those of a binary black hole system. This means that the Bayes factor of the neutron star-black hole case over the binary black hole case should approach one for large black hole masses. This is indeed the behavior observed with SEOBNRv4_ROM_NRTidalv2_NSBH and IMRPhenomD_NRTidal. However, for IMRPhenomNSBH, we find that $\ln \mathcal{B}$ *increases* as the black hole companion mass increases from 10 to 20

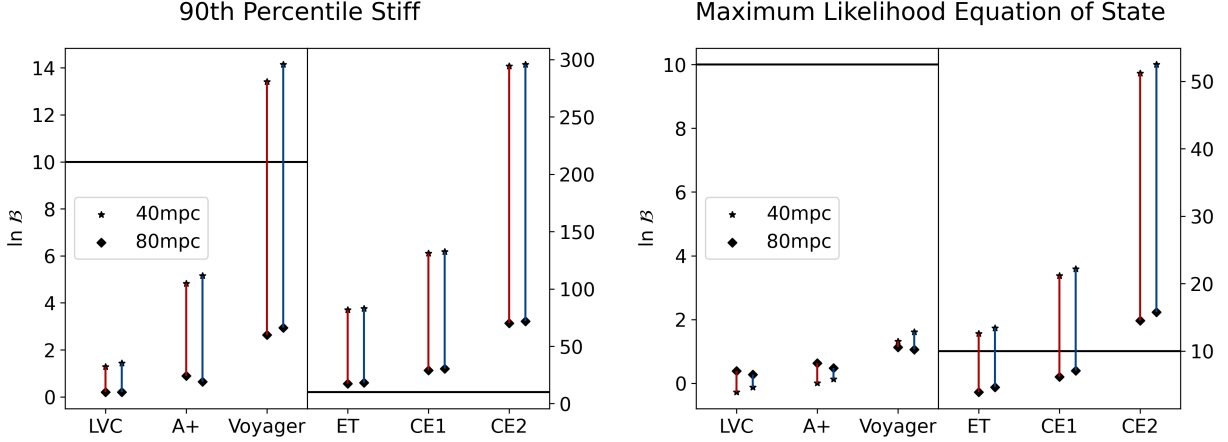


Figure 3.2: Natural Log Bayes factor for each detector with $m_{BH} = 5M_{\odot}$. The vertical line spans the range of Bayes factors for a given detector. The red line on the left indicates a variable EOS run, and the blue line on the right indicates a constant EOS. The horizontal black line corresponds to the $\ln \mathcal{B} = 10$ cut-off. As the 3G detectors have significantly high Bayes factors, the plots are split with different y -axis for current and third-generation detectors.

M_{\odot} (see Fig. 3.6). This is clearly unphysical behavior and deserves further explanation¹. Digging still deeper, the problem turns out to be the gravitational wave amplitude; IMRPhenomNSBH uses an older ansatz for the amplitude [263] (which was not originally intended for neutron star-black hole systems). Figure 3.7 compares the gravitational wave amplitude as a function of frequency for two different values of Λ , for the $m_{BH} = 20M_{\odot}$ case, for both approximants (along with the amplitude spectral density for the Cosmic Explorer 1 detector). We clearly see that while the SEOBNRv4_ROM_NRTidalv2_NSBH model shows no dependence of the amplitude on Λ , which is what we expect for these high mass configurations, the IMRPhenomNSBH model shows a large dependence on Λ for the post-merger signal which is clearly unphysical. This incorrect behavior explains the effect shown in Fig. 3.6. Due to this non-physical behavior, we choose to use SEOBNRv4_ROM_NRTidalv2_NSBH for our analysis.

3.4 Discussion

The results demonstrate that the current LIGO and Virgo detectors are not sufficient to differentiate between neutron star-black hole and binary black hole systems. In fact, the success of A+ and Voyager for this purpose is dubious. There were no cases for either LIGO-Virgo or LIGO A+ where the $\ln \mathcal{B}$ exceeded our threshold, and only a fine-tuned case for LIGO Voyager. However, it is important to note that the cases with the highest $\ln \mathcal{B}$ always occur with the stiff EOS, the $5M_{\odot}$ black hole companion, and at 40Mpc. This is not surprising. The stiff EOS was selected specifically for this property, and the signal-to-noise ratio at 40Mpc is higher than at 80Mpc.

It can be seen that the ability to differentiate between a neutron star-black hole system and a

¹We thank Jonathan Thompson for discussions on this issue.

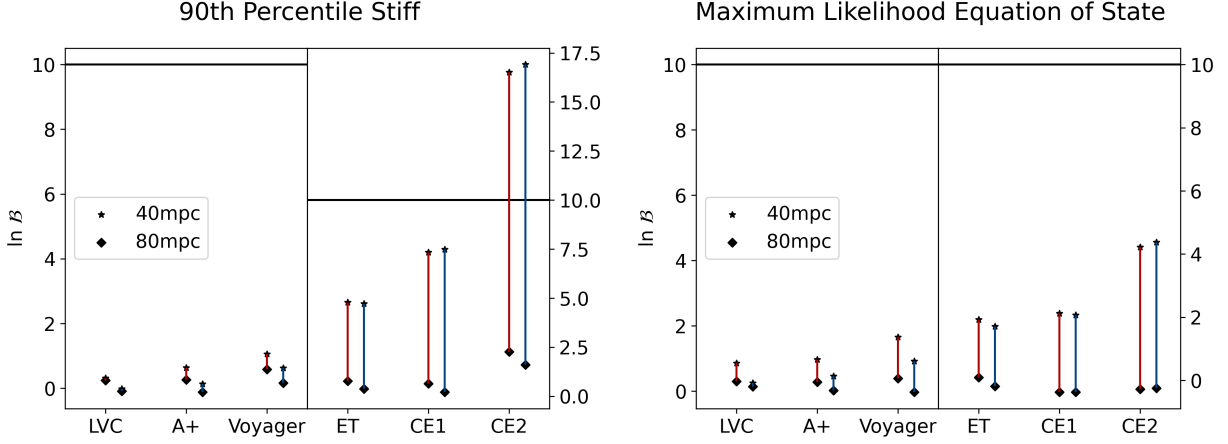


Figure 3.3: Natural Log Bayes factor for each detector with $m_{BH} = 10M_{\odot}$. The vertical line spans the range of Bayes factors for a given detector. The red line on the left indicates a variable EOS run, and the blue line on the right indicates a constant EOS. The horizontal black line corresponds to the $\ln \mathcal{B} = 10$ cut-off.

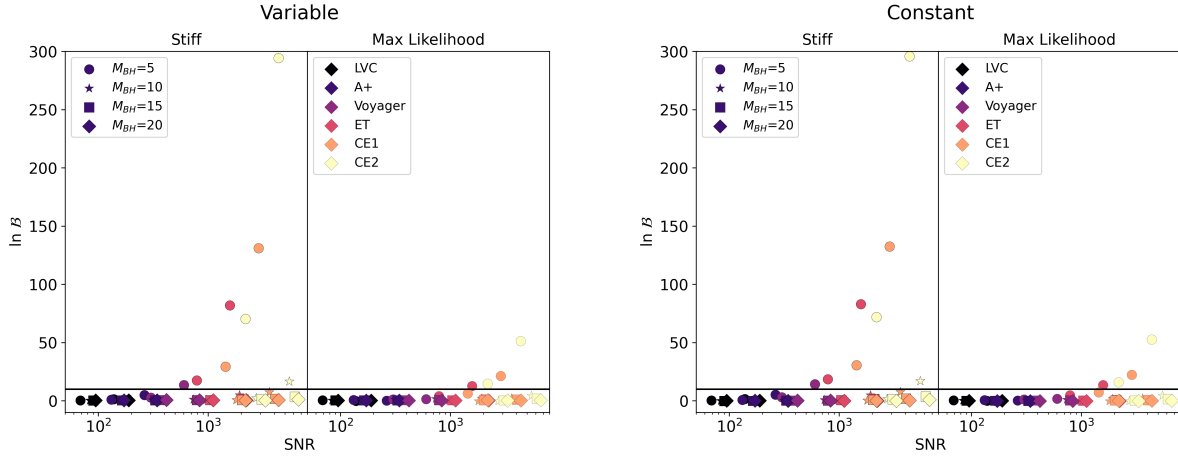


Figure 3.4: Natural Log Bayes factor for all combinations of parameters and detectors as a function of the signal-to-noise ratio. The right and left plots correspond to the constant and variable EOS cases. In each plot, the right panel shows the results for the maximum likelihood EOS and the left panel shows the stiff EOS. The marker color corresponds to the detector, and the marker shape indicates the mass of the black hole. The black horizontal line shows the cut-off of $\ln \mathcal{B} = 10$.

binary black hole system does not directly correspond to the signal-to-noise ratio. The highest $\ln \mathcal{B}$ occurs for $m_{BH} = 5M_{\odot}$, even though systems with $m_{BH} = 10, 15, \text{ and } 20M_{\odot}$ have higher signal-to-noise ratios. The tidal effects decrease as mass increases, and this effect is clearly of greater importance than the increase in signal strength. Detection of a neutron star-black hole system with a low mass ratio will almost certainly be required to give evidence of neutron star matter in the gravitational wave signal. Additionally, the nuclear EOS itself is an important factor

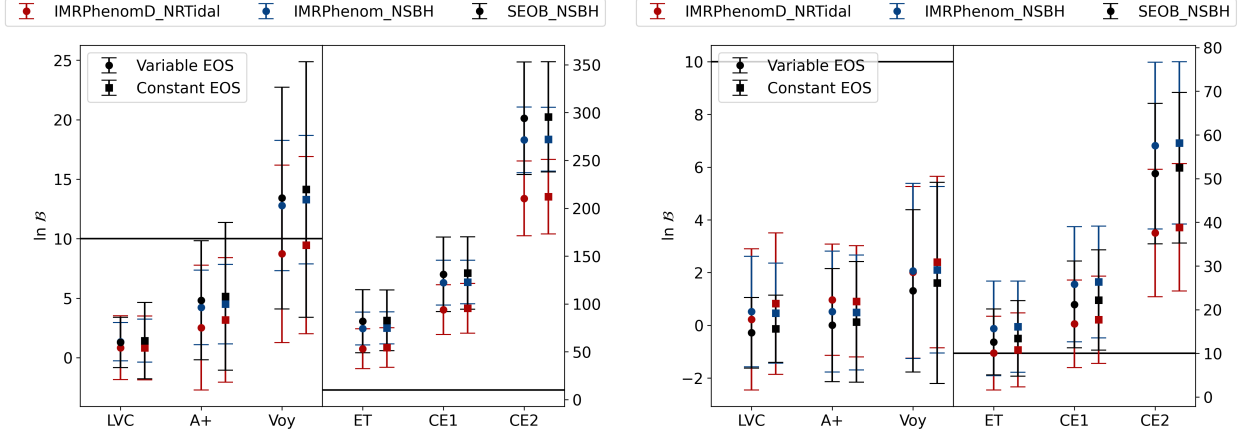


Figure 3.5: Comparison between the IMRPhenomD_NRTidal, IMRPhenomNSBH, and SEOB-NRv4_ROM_NRTidalv2_NSBH waveform approximants. For each detector, the variable EOS analysis is on the left (circle marker) and the constant EOS analysis is on the right (square marker). Each point corresponds to the average value of ten runs with different noise realizations, and the error bars are 2 standard deviations. The horizontal black line indicates the cut-off of $\ln \mathcal{B} = 10$.

in how soon we will and how likely we are to distinguish a neutron star-black hole system from a binary black hole system. Finally, in this analysis, we have made a particular choice of sky location and inclination angle of the source. This orientation, corresponding to GW170817, is a favorable one. As expected, repeating the simulations with randomly chosen sky-positions generally leads to smaller Bayes factors. However, even in this case, the Bayes factors for the Einstein Telescope, Cosmic Explorer 1 and Cosmic Explorer 2 remain comfortably above the threshold, while for Voyager, the results get closer to the threshold. Our basic conclusions therefore remain unchanged.

When looking at LIGO Voyager, we saw that in one case the results were close to our cut-off. Keep in mind, however, that this analysis was done with design sensitivity curves and this result occurs only for the fine-tuned case of a very close binary with a very small black hole that has a rather stiff EOS. Despite LIGO-Virgo’s recent detection of an object in the mass gap, $5M_{\odot}$ is still on the low end of what we expect for black hole masses. Looking at Fig. 3.3, it’s evident that, when the companion mass increases to even $10M_{\odot}$, the Bayes factor drops rapidly regardless of distance or EOS for all detectors. If the EOS is as soft as the analysis of GW170817 suggests, then LIGO Voyager will certainly be unable to distinguish neutron star-black hole systems from binary black holes regardless of how close or loud the signal is.

3G detectors will likely be required to obtain decisive evidence of neutron star-black hole system from gravitational wave data. We see here that the proposed designs for the Einstein Telescope and Cosmic Explorer may very well allow for these detections. Looking at Fig. 3.2 and Table 3.A.6, we see that regardless of the nuclear EOS, there are systems which have $\ln \mathcal{B} > 10$. Thus, if current analyses of GW170817 are accurate, we will be waiting until the Einstein Telescope or Cosmic Explorer for gravitational wave evidence of neutron star-black hole systems. Additionally, 3G detectors seem to be able to do this measurement at distances out 80Mpc (stiff EOS), which greatly expands the number of candidate systems. Even with very sensitive future detectors, the

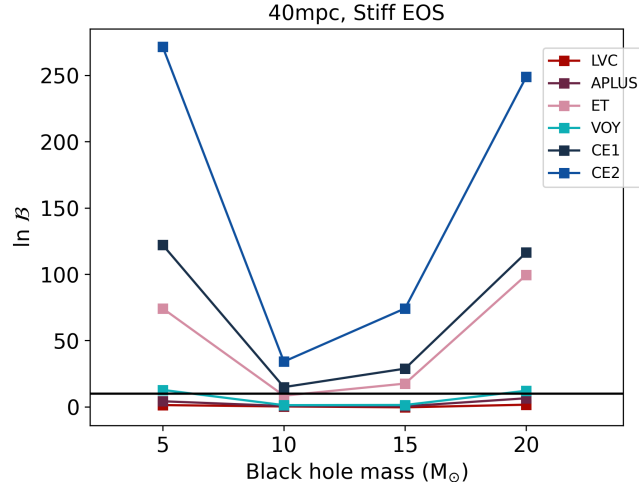


Figure 3.6: Natural Log Bayes factor plotted as a function of black hole mass for all six detectors considered using the IMRPhenomNSBH waveform approximant. All data points are at $d = 40\text{Mpc}$ and have a stiff EOS ($\Lambda = 369$).

ability to distinguish neutron star-black hole systems from binary black holes is very dependent on the mass of the black hole in the binary.

Acknowledgements

We thank Jonathon Thompson, Sumit Kumar, Sanjay Reddy, Ingo Tews, and Duncan Brown for their valuable discussions. Our computations used the ATLAS computing cluster at AEI Hannover [189] funded by the Max Planck Society and the State of Niedersachsen, Germany.

This research has made use of data, software, and/or web tools obtained from the LIGO Open Science Center (<https://losc.ligo.org>), a service of LIGO Laboratory, the LIGO Scientific Collaboration and the Virgo Collaboration. LIGO is funded by the U.S. National Science Foundation. Virgo is funded by the French Centre National de Recherche Scientifique (CNRS), the Italian Istituto Nazionale della Fisica Nucleare (INFN), and the Dutch Nikhef, with contributions by Polish and Hungarian institutes.

Appendix

3.A Data Tables

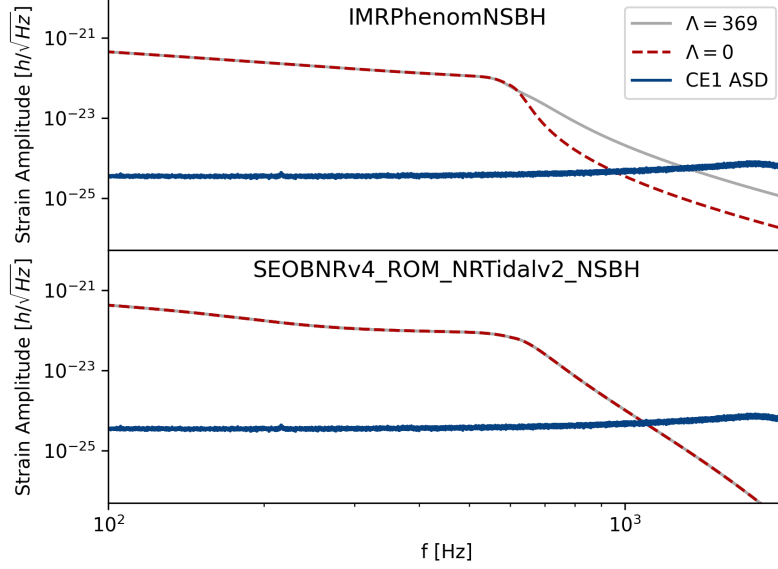


Figure 3.7: IMRPhenomNSBH and SEOBNRv4_ROM_NRTidalv2_NSBH waveform strain amplitude as a function of frequency plotted along with the Cosmic Explorer 1 amplitude spectral density. Both panels show waveforms with a black hole mass of $20M_{\odot}$. The red line corresponds to the $\Lambda = 0$ case (the waveform of a binary black hole) [59], and the grey line corresponds to a waveform with a stiff EOS ($\Lambda = 369$). The top panel shows unphysical dependence of the post-merger amplitude on Λ .

Table 3.A.1: Log Bayes Factor and standard deviation for selected cases.

$M_{BH}[M_{\odot}]$	$d[\text{Mpc}]$	EOS	LVC	A+	Voyager	ET	CE1	CE2
5	40	stiff	1.3 ± 1.0	4.8 ± 2.5	13.4 ± 4.7	81.8 ± 16.5	130.9 ± 19.0	294.4 ± 29.4
5	40	soft	-0.3 ± 0.7	0.0 ± 1.1	1.3 ± 1.5	12.6 ± 3.8	21.2 ± 5.0	51.2 ± 8.0
5	80	stiff	0.2 ± 0.5	0.9 ± 0.7	2.6 ± 1.2	17.4 ± 4.1	29.2 ± 5.6	70.2 ± 8.8
5	80	soft	0.4 ± 0.6	0.6 ± 0.9	1.1 ± 1.7	3.9 ± 1.8	6.2 ± 2.2	14.6 ± 3.3
10	40	stiff	0.3 ± 0.2	0.6 ± 0.4	1.1 ± 0.8	4.8 ± 2.3	7.3 ± 2.3	16.5 ± 3.8

Table 3.A.2: Neutron Star-Black Hole with LIGO-Virgo

Mass _{BH} [M _⊙]	Distance [Mpc]	SNR	90 th % Stiff		Maximum Likelihood	
			ln \mathcal{B} var	ln \mathcal{B} const	ln \mathcal{B} var	ln \mathcal{B} const
5	40	139	1.3	1.4	-0.3	-0.1
10	40	168	0.3	0.0	0.9	0.2
15	40	180	0.6	0.2	0.1	-0.2
20	40	190	0.3	0.0	0.3	0.1
5	80	69	0.2	0.2	0.4	0.3
10	80	84	0.2	-0.1	0.3	0.1
15	80	90	0.3	-0.2	0.3	0.0
20	80	95	0.3	0.0	0.2	0.0

Table 3.A.3: Neutron Star-Black Hole with LIGO A+

Mass _{BH} [M _⊙]	Distance [Mpc]	SNR	90 th % Stiff		Maximum Likelihood	
			ln \mathcal{B} var	ln \mathcal{B} const	ln \mathcal{B} var	ln \mathcal{B} const
5	40	264	4.8	5.2	0.0	0.1
10	40	316	0.6	0.1	1.0	0.5
15	40	329	0.5	0.1	0.3	-0.2
20	40	344	0.3	-0.2	0.4	-0.2
5	80	132	0.9	0.6	0.6	0.5
10	80	158	0.3	-0.1	0.3	0.0
15	80	164	0.4	-0.1	0.3	-0.1
20	80	172	0.3	0.0	0.3	-0.1

Table 3.A.4: Neutron Star-Black Hole with LIGO Voyager

Mass _{BH} [M _⊙]	Distance [Mpc]	SNR	90 th % Stiff		Maximum Likelihood	
			ln \mathcal{B} var	ln \mathcal{B} const	ln \mathcal{B} var	ln \mathcal{B} const
5	40	604	13.4	14.1	1.3	1.6
10	40	738	1.1	0.6	1.6	0.9
15	40	791	0.6	0.2	0.5	0.1
20	40	837	0.4	0.1	0.2	-0.1
5	80	302	2.6	2.9	1.1	1.1
10	80	369	0.6	0.2	0.4	0.0
15	80	396	0.6	0.2	0.4	0.2
20	80	419	0.6	0.1	0.2	-0.1

Table 3.A.5: Neutron Star-Black Hole with the Einstein Telescope

Mass _{BH} [M _⊙]	Distance [Mpc]	SNR	90 th % Stiff		Maximum Likelihood	
			ln \mathcal{B} var	ln \mathcal{B} const	ln \mathcal{B} var	ln \mathcal{B} const
5	40	1582	81.8	82.9	12.6	13.4
10	40	1935	4.8	4.7	1.9	1.7
15	40	2091	1.3	1.6	1.0	0.6
20	40	2233	0.4	0.0	0.3	-0.1
5	80	791	17.4	18.4	3.9	4.6
10	80	968	0.8	0.4	0.1	-0.2
15	80	1045	0.6	0.6	0.4	0.1
20	80	1116	0.4	-0.1	0.2	-0.1

Table 3.A.6: Neutron Star-Black Hole with Cosmic Explorer 1

Mass _{BH} [M _⊙]	Distance [Mpc]	SNR	90 th % Stiff		Maximum Likelihood	
			ln \mathcal{B} var	ln \mathcal{B} const	ln \mathcal{B} var	ln \mathcal{B} const
5	40	2888	130.9	132.3	21.2	22.2
10	40	3617	7.3	7.5	2.1	2.1
15	40	4055	1.8	1.9	1.0	0.5
20	40	4390	0.6	0.3	0.2	0.0
5	80	1444	29.2	30.4	6.2	7.1
10	80	1809	0.6	0.2	-0.4	-0.4
15	80	2028	0.8	0.8	0.5	0.2
20	80	2195	0.2	0.0	0.5	0.1

Table 3.A.7: Neutron Star-Black Hole with Cosmic Explorer 2

Mass _{BH} [M _⊙]	Distance [Mpc]	SNR	90 th % Stiff		Maximum Likelihood	
			ln \mathcal{B} var	ln \mathcal{B} const	ln \mathcal{B} var	ln \mathcal{B} const
5	40	4385	294.1	295.6	51.2	52.5
10	40	5491	16.5	16.9	4.2	4.4
15	40	6151	3.4	3.7	1.7	1.4
20	40	6655	1.1	0.8	0.4	0.1
5	80	2193	70.2	71.7	14.6	15.8
10	80	2745	2.3	1.6	-0.3	-0.2
15	80	3075	1.1	1.3	0.4	0.2
20	80	3328	0.3	-0.1	0.2	-0.1

4 | Tests of Gravitational Wave Birefringence With the Open Gravitational Wave Catalog

This chapter contains material published as Wang, Yifan Brown, Stephanie M., Shao, Lijing and Zhao, Wen *Tests of Gravitational-Wave Birefringence with the Open Gravitational-Wave Catalog* Phys Rev D (accepted 2022). <https://doi.org/10.48550/arXiv.2109.09718>

Abstract

We report the results of testing gravitational wave birefringence using the largest population of gravitational wave events currently available. Gravitational Wave birefringence, which can arise from the EFT extension of general relativity, occurs when the parity symmetry is broken, causing the left- and right-handed polarizations to propagate following different equations of motion. We perform Bayesian inference on the ninety-four events reported by the 4th-Open Gravitational-Wave Catalog (4-OGC) using a parity-violating waveform. We find no evidence for a violation of general relativity in the vast majority of events. However, the most massive event, GW190521, and the second most massive event, GW191109, show intriguing non-zero results for gravitational wave birefringence. We find that the probability of association between GW190521 and the possible electromagnetic counterpart reported by Zwicky Transient Facility (ZTF) is increased when assuming birefringence. Excluding GW190521 and GW191109, the parity-violating energy scale is constrained to $M_{\text{PV}} > 0.05\text{GeV}$ at 90% credible interval, which is an improvement over previous results from twelve events by a factor of five. We discuss the implications of our results on modified gravity and possible alternative explanations such as waveform systematics. More detections of massive binary black hole mergers from the upcoming LIGO/Virgo/KAGRA run will shed light on the true origin of the apparent birefringence.

4.1 Introduction

The advanced LIGO and Virgo [264, 265] detectors have completed three observation runs (O1-O3) and announced the detection of ninety confident gravitational wave events in the Gravitational-Wave Transient Catalog (GWTC) [4–7]. Additional compact binary coalescence events are reported by independent analysis [190, 266–270] of the public data [36]. The most recent version of Open Gravitational Wave Catalog, 4-OGC [190], used `PyCBC Inference Toolkit` [271]

to search the public data from all three observation runs and reported ninety-four events [268]. 4-OGC agrees with GWTC for all confident events with a probability of astrophysical origin $p_{\text{astro}} > 0.99$. The detection of gravitational waves has enabled numerous precise tests of general relativity in the strong, dynamical field [111–117] and high energy (sub-GeV) regimes [272]. All the tests to date have confirmed that gravitational wave data is consistent with the predictions of general relativity.

This work tests gravitational wave birefringence using the currently largest population of gravitational wave events from 4-OGC. Birefringence of gravitational waves emerges when the parity symmetry, which is the invariance of physical laws regarding the inversion of spatial coordinates, is broken between the left- and right-handed gravitational wave polarizations. While parity symmetry is conserved in general relativity, theories where parity is violated have been proposed such as Chern-Simons gravity [163, 165–168], Hořava-Lifshitz gravity [169–171], ghost-free scalar-tensor gravity [172], and the symmetric teleparallel equivalent of general relativity [164] to account for dark matter and dark energy. Parity violation also arises at high energy scales in quantum gravity theories such as loop quantum gravity and string theory [163].

We utilize an EFT extension of the linearized Einstein-Hilbert action to study how deviations from general relativity affect gravitational wave propagation. EFT is a flexible framework that includes all action terms that purposely preserve or violate certain symmetries. The leading order higher derivative modification of the linearized action comes from terms of mass dimension five that violate parity [160, 161]. Parity violation leads to an asymmetry in the propagation speeds and amplitudes of the left- and right-hand polarization of gravitational wave, which, in turn, leads to phase and amplitude birefringence, respectively. Given the relationship between parity violation and Lorentz violation [273], our tests have implications for constraining the standard model extension of gravity [274, 275], which is the most general EFT extension of linearized general relativity that violates Lorentz symmetry.

Tests of gravitational wave birefringence were first done in Ref. [276], where they checked for waveform peak splitting in the first-ever detected gravitational wave event, GW150914. Ref. [277] constrained birefringence using the gravitational wave propagation speed measured from the binary neutron star merger event GW170817 [2], and Refs. [115, 278–284] placed further constraints on birefringence using GWTC events.

We test for gravitational wave birefringence in ninety-four gravitational wave events and find no evidence of birefringence in ninety-two events. Intriguingly, we find two outliers, GW190521 and GW191109_010717 (hereafter GW191109), the most and second most massive binary black holes in 4-OGC [190, 285, 286], favor the birefringence waveform over the general relativity waveform with Bayes factors 11.0 and 22.9, respectively ($\ln \mathcal{B}_{\text{GR}}^{\text{nonGR}} = 2.4$ and 3.1). Excluding these two outliers, we place constraints on the cutoff energy scale $M_{\text{PV}} > 0.05 \text{ GeV}$, which is more stringent than Ref. [272] by a factor of five due to the larger data set and the more advanced waveform. The result can be mapped to the standard model extension coefficient $|\zeta^{(5)}| < 9 \times 10^{-16} \text{ m}$, which characterizes isotropic birefringence with mass dimension $d = 5$.

The nonzero results may be caused by non-Gaussian noise fluctuation, systematic errors in waveform templates, or physical effects that are outside the standard assumptions for quasi-circular binary black hole mergers, e.g., the presence of orbital eccentricity [287, 288], a hyperbolic encounter [289], or even entirely new physics [290]. We assess how the background noise affects the M_{pv} measurement for both GW190521 and GW191109 by injecting 100 general relativity signals into the detector noise around the observed coalescence time for each event. The results suggest

that our detection of general relativity deviation for GW190521 and GW191109 is not likely an artifact of the noise.

Lastly, we consider the possible electromagnetic counterpart of GW190521, which ZTF observed and comes from an active galactic nucleus [291, 292], by comparing the sky location posteriors for GW190521 with and without birefringence. Prior analyses of GW190521 do not strongly favor association with the EM counterpart. Ref. [293] reported the Bayes factor of $\ln B \gtrsim -4$ which disfavors a sky location fixed to that of the electromagnetic counterpart. However, if we assume gravitational wave birefringence, we find evidence in favor of the association with the electromagnetic counterpart with $\ln \mathcal{B}$ of 6.6.

4.2 Waveform Templates for Gravitational Wave Birefringence

We briefly overview the construction of waveform templates to test gravitational wave birefringence following Ref. [160]. From the perspective of EFT, the leading order modifications to the linearized Einstein-Hilbert action are terms with three derivatives and mass dimension five: $\epsilon^{ijk} \dot{h}_{il} \partial_j \dot{h}_{kl}$ and $\epsilon^{ijk} \partial^2 h_{il} \partial_j h_{kl}$ [160–162], where $i, j, \dots = 1, 2, 3$ refer to spatial coordinates, ∂_j denotes spatial derivatives, dot denotes derivatives with respect to time, ∂^2 is the Laplacian, ϵ^{ijk} is the antisymmetric symbol, and h_{ij} is the tensor perturbation of metric. Notably, both terms violate parity. Therefore, EFT suggests that the leading order modification to gravitational wave propagation arises from parity-violation. We do not consider the more complicated anisotropic gravitational wave birefringence, for which the effects can be found in Refs. [276, 284, 294]. Combining the above higher derivative terms with the linearized Einstein-Hilbert action gives

$$S = \frac{1}{16\pi G} \int dt d^3x a^3 \left[\frac{1}{4} \dot{h}_{ij}^2 - \frac{1}{4a^2} (\partial_k h_{ij})^2 + \frac{1}{4} \left(\frac{c_1}{a M_{\text{PV}}} \epsilon^{ijk} \dot{h}_{il} \partial_j \dot{h}_{kl} + \frac{c_2}{a^3 M_{\text{PV}}} \epsilon^{ijk} \partial^2 h_{il} \partial_j h_{kl} \right) \right], \quad (4.1)$$

where a is the cosmic scale factor, M_{PV} is the energy scale at which higher order modification starts to be relevant, and c_1 and c_2 are two undetermined functions of cosmic time; the speed of light and the reduced Planck's constant are set to $c = \hbar = 1$. Eq. (4.1) is the generic form of the action; c_1 , c_2 and M_{PV} can be mapped to the corresponding model parameters in a specific modified gravity theories [163–172], as explicitly demonstrated in Ref. [160].

The equation of motion for the gravitational wave circular polarization modes h_A , where $A = R$ or L for the right- and left-hand modes, is

$$h_A'' + (2 + \nu_A) \mathcal{H} h_A' + (1 + \mu_A) k^2 h_A = 0, \quad (4.2)$$

where \mathcal{H} is the conformal Hubble parameter, k is the wavenumber, and a prime denotes the derivative with respect to the cosmic conformal time τ , μ_A and ν_A are the phase and amplitude birefringence parameters. They have the exact forms

$$\begin{aligned} \nu_A &= -[\rho_A c_1 k / (a M_{\text{PV}})]' / \mathcal{H}, \\ \mu_A &= \rho_A (c_1 - c_2) k / (a M_{\text{PV}}), \end{aligned} \quad (4.3)$$

$\rho_A = \pm 1$ for left- and right-handed polarizations represents broken parity of gravitational waves during propagation.

We focus on velocity birefringence because the modification to gravitational wave strain from amplitude birefringence is negligible [160]. The general relativity solution can be found by setting $\mu_A = \nu_A = 0$ in Eq. (4.2).

Solving Eq. (4.2) gives the left- and right-handed circular polarization modes with parity violation. They are related to the general relativity waveform by

$$h_L^{\text{PV}}(f) = h_L^{\text{GR}}(f)e^{-i\delta\Psi(f)} \quad \& \quad h_R^{\text{PV}}(f) = h_R^{\text{GR}}(f)e^{i\delta\Psi(f)}. \quad (4.4)$$

The plus (h_+) and cross (h_\times) modes of gravitational wave are given by $h_+ = (h_L + h_R)/\sqrt{2}$ and $h_\times = (h_L - h_R)/(\sqrt{2}i)$.

For binary black holes, we use the IMRPhenomXPHM [45] general relativity waveform approximant, which includes sub-dominant harmonics and effects of precession; the IMRPhenomD_NRTidal [54, 56–58] and IMRPhenomNSBH [261], waveforms, which account for tidal deformability, are used for binary neutron stars and neutron-star–black-hole mergers respectively.

The phase modification to the general relativity waveform takes the following form

$$\delta\Psi(f) = \frac{(\pi f)^2}{M_{\text{PV}}} \int_0^z \frac{(c_1 - c_2)(1 + z')dz'}{H_0 \sqrt{\Omega_M(1 + z')^3 + \Omega_\Lambda}}, \quad (4.5)$$

where H_0 is the Hubble constant, z is the cosmic redshift, the frequency term f^2 corresponds to a modification at 5.5 post-Newtonian order, Ω_M is the matter density, and Ω_Λ is the dark energy density. We adopt a Λ CDM Cosmology with parameters $\Omega_M = 0.3075$, $\Omega_\Lambda = 0.691$, and $H_0 = 67.8 \text{ km s}^{-1} \text{ Mpc}^{-1}$ [229] to convert luminosity distance to redshift for Eq. (4.5). As most gravitational wave detections are from the local Universe, we make the simplifying assumption that c_1, c_2 are constants and $c_1 - c_2$ is of order unity. This is done by attributing its order of magnitude to M_{PV} . Also note that we do not consider the special case where $c_1 = c_2$ exactly, and thus $\mu_A = 0$, in this work. This is the case for dynamical Chern-Simons gravity [295–297] and the constraints on amplitude birefringence in this case can be found in Refs. [115, 281].

4.3 Bayesian Inference

We use Bayesian parameter estimation and model selection to test gravitational wave birefringence. Given data $d(t)$, which is a sum of the detector noise $n(t)$ and a possible gravitational wave signal $h(t, \vec{\vartheta})$ characterized by parameters $\vec{\vartheta}$, Bayes theorem states that

$$P(\vec{\vartheta}|d, h) = \frac{P(d|\vec{\vartheta}, h)P(\vec{\vartheta}|h)}{P(d|h)}, \quad (4.6)$$

where $P(\vec{\vartheta}|d, h)$ is the posterior probability distribution for parameters $\vec{\vartheta}$, $P(\vec{\vartheta}|h)$ is the prior distribution containing any a priori information, $P(d|\vec{\vartheta}, h)$ is the likelihood for obtaining the data given model parameters, $P(d|h)$ is a normalization factor called evidence, and h is the hypothesis for modeling the data. This work considers two competing hypotheses: \mathcal{H}_{GR} where GWs are

accurately described by general relativity and $\mathcal{H}_{\text{nonGR}}$ where GWs have birefringence and are described by Eq. (4.4). The Bayes factor, or the ratio of the evidences of two hypotheses,

$$\mathcal{B}_{\text{GR}}^{\text{nonGR}} = \frac{P(d|\mathcal{H}_{\text{nonGR}})}{P(d|\mathcal{H}_{\text{GR}})}, \quad (4.7)$$

quantifies the degree that data favor one hypothesis over another.

Using `PyCBC Inference` [40], we numerically sample over all gravitational wave intrinsic (mass $m_{1,2}$, spin $\vec{s}_{1,2}$, and, in the case of neutron stars, tidal deformability $\Lambda_{1,2}$) and extrinsic parameters (luminosity distance d_L , inclination angle ι , polarization angle Ψ , right ascension α , declination δ , coalescence time t_c , and phase ϕ_c) as well as the parity violation parameter M_{PV}^{-1} for \mathcal{H}_1 . The priors for the intrinsic and extrinsic parameters are the same as those in the 4-OGC [268] which are uniform for mass, spin amplitude, polarization, coalescence phase, and time. The distance prior is uniform in comoving volume. The spin orientation, sky location, and spatial orientation priors are isotropic. The prior for M_{PV}^{-1} is uniform in $[0, 200]\text{GeV}^{-1}$ except for the two outlier events which use $[0, 1000]$.

Assuming M_{PV}^{-1} is a universal quantity, the M_{PV}^{-1} posteriors from the individual gravitational wave events can be combined to obtain an overall constraint,

$$p(M_{\text{PV}}^{-1}|\{d_i\}, H_{\text{nonGR}}) \propto \prod_{i=1}^N p(M_{\text{PV}}^{-1}|d_i, H_{\text{nonGR}}), \quad (4.8)$$

where d_i denotes data of the i -th gravitational wave event.

4.4 Results

We find that ninety-two out of ninety-four events are consistent with general relativity; the M_{PV}^{-1} posteriors are shown in Fig. 4.4.1, with the most constraining events individually indicated in the legend. In general, the tightest constraints are all from events with relatively low mass ($\sim 10 M_{\odot}$) binary black hole mergers e.g., GW190707_093326 has component masses of $12.9M_{\odot}$ and $7.7M_{\odot}$ [268]. This result is unsurprising because the birefringence effect is more significant at higher frequencies, where low mass binaries spend more time (see Eq. (4.5)).

The overall constraint is obtained by multiplying the posterior distributions of the individual events together using Eq. (4.8). We find the 90% upper limit of M_{PV}^{-1} to be 19 GeV^{-1} , which corresponds to $M_{\text{PV}} > 0.05\text{GeV}$. This result is more stringent than previous results, based on twelve gravitational wave events, by a factor of five [272]. Note that Ref. [272] used $h = 1$ not $\hbar = 1$. Taking this into account, their result is $M_{\text{PV}} > 0.01\text{GeV}$. This improvement is due to the increased number of events analyzed and the use of improved gravitational wave waveforms [45] with longer duration and higher harmonic modes.

The limit on M_{PV} can be easily mapped to bounds on the standard model extension coefficients that describe isotropic birefringence of gravitational waves at mass dimension $d = 5$, via $|\zeta^{(5)}| \sim \frac{1}{4}M_{\text{PV}}^{-1}$ [276, 298]. For $M_{\text{PV}} > 0.05 \text{ GeV}$, one gets $|\zeta^{(5)}| < 9 \times 10^{-16} \text{ m}$, which is comparable to limits from Refs. [278, 282].

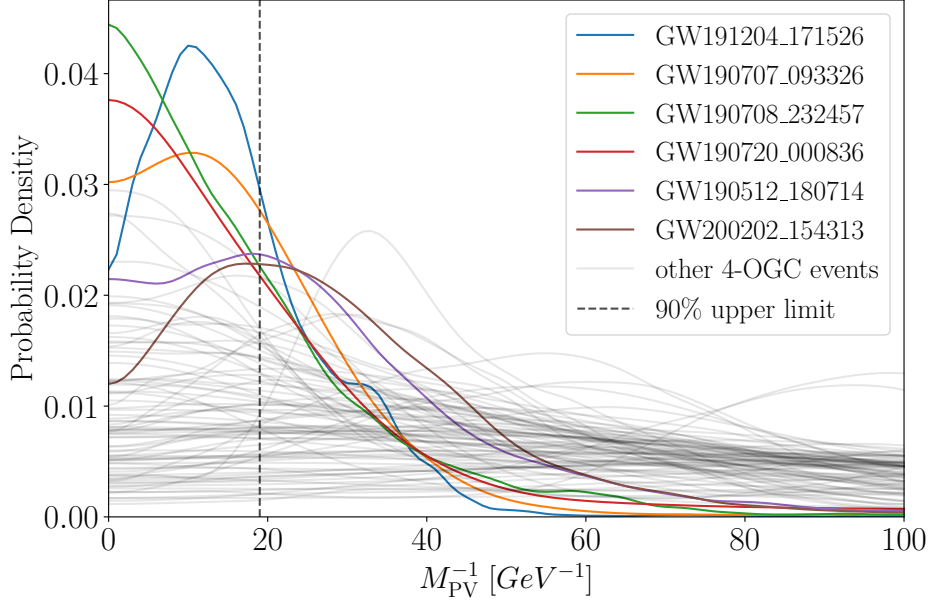


Figure 4.4.1: The M_{PV}^{-1} posterior distributions for all 4-OGC events except GW190521 and GW191109. The legend indicates the events that give the tightest constraints. The vertical dashed line denotes the 90% upper limit for M_{PV}^{-1} from combined results.

4.4.1 GW190521 and GW191109

We find non-zero results for birefringence in GW190521 and GW191109 with $M_{\text{PV}}^{-1} = 400_{-230}^{+460} \text{ GeV}^{-1}$ and $220_{-100}^{+150} \text{ GeV}^{-1}$ (90% credible interval). Furthermore, the Bayes factors support the non-general relativity hypothesis: $\mathcal{B}_{\text{GR}}^{\text{nonGR}} = 11.0$ and 22.9 , respectively ($\ln \mathcal{B}_{\text{GR}}^{\text{nonGR}} = 2.4$ and 3.1). The M_{PV}^{-1} , source frame chirp mass $\mathcal{M}^{\text{src}} = (m_1 m_2)^{3/5} / (m_1 + m_2)^{1/5}$, and mass ratio $q = m_1 / m_2$, posteriors are shown in Fig. 4.4.2. $m_{1/2}$ are the heavier/lighter binary component masses. Intriguingly, GW190521 and GW191109 are the most and second most massive events found in 4-OGC.

To investigate any systematics causing the apparent deviation from general relativity, we perform two more birefringence tests for the outlier events using a different phenomenological template model IMRPhenomPv3HM [46] and a numerical relativity surrogate model NRSur7dq4 [47]. We find consistent support for non-zero M_{PV}^{-1} in the posteriors for these runs. We further check the data quality around GW190521 and GW191109 by calculating the background noise power spectral density variation (see [299] for definition), which measures the noise non-stationarity. For GW190521, the power spectral density variation in a one-hour interval around the event only deviates from Gaussian stationary noise by $\lesssim 0.1$ (except for a glitch in LIGO Hanford 400s after the event), showing no significant deviation from other ordinary times. However, the LIGO detector data for GW191109 contains non-Gaussian and non-stationary transient noise artifacts or glitches [7]. Due to this, we performed our analysis using data with the glitch removed released by LIGO/Virgo [7].

To further quantify whether detector noise could be the cause of the observed non-zero result, we simulate 100 general relativity signals with parameters drawn from the GW190521 and

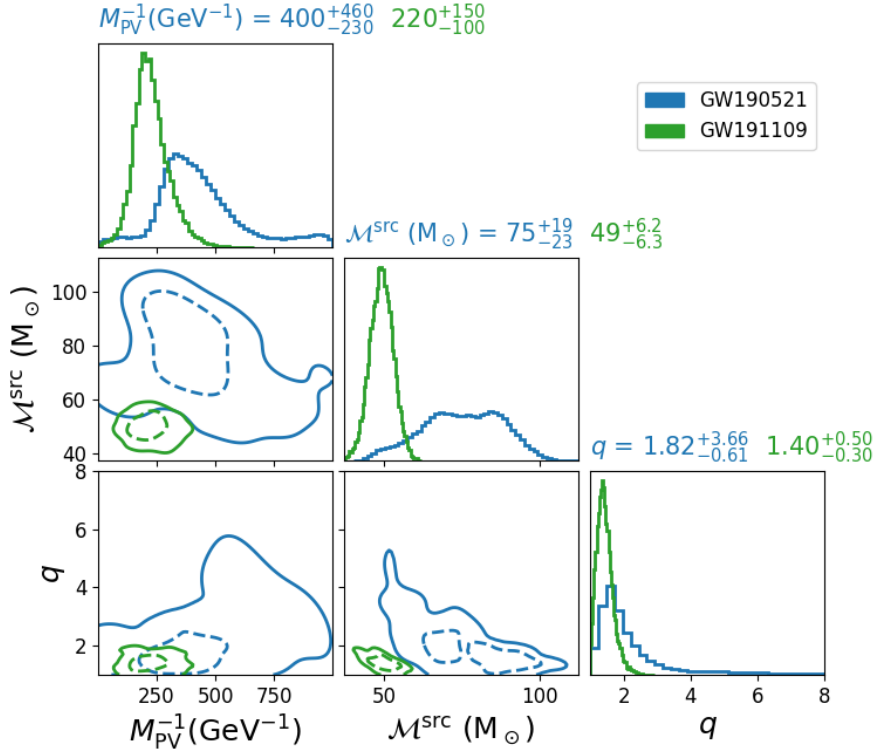


Figure 4.4.2: Chirp mass, mass ratio, and M_{PV}^{-1} posterior distributions for GW190521 and GW191109. The dashed (solid) two-dimensional contours denote the 50% (90%) credible intervals. The diagonal plots are the one-dimensional marginalization for the posterior.

GW191109 posteriors [190] and inject them into the LIGO/Virgo detector noise nearby the GW190521 and GW191109 triggers, respectively (see the appendix for technical details). We find only 1(4) events, out of 100 injections, have $\ln B_{GR}^{nonGR}$ larger than what we found for GW190521(GW191109). We thus conclude that the false alarm rate for detecting birefringence is 1(4) in 100 observations.

Lastly, we consider the possible electromagnetic counterpart for GW190521 reported by the ZTF [291, 292]. Interestingly, we find that including birefringence significantly improves the chance of association. Fig. 4.4.3 shows the right ascension (α), declination (δ), and luminosity distance posteriors from the birefringence analysis. The red lines mark the independent measurements by ZTF ($\alpha = 3.36$ rad, $\delta = 0.61$ rad, and redshift=0.438). The Bayes factor supports coincidence with $\ln \mathcal{B}_{overlap} = 6.6$ in favor of the association. The general relativity analyses did not favor association. For instance, Ref. [293] reports $\ln \mathcal{B}_{overlap} \sim -4.4$.

4.5 Discussion and Conclusion

We test for gravitational wave propagation birefringence using state-of-the-art waveform templates and 4-OGC, the most extensive gravitational wave catalog currently available. Combining the results from all of the events except the outliers GW190521 and GW191109, we constrain the

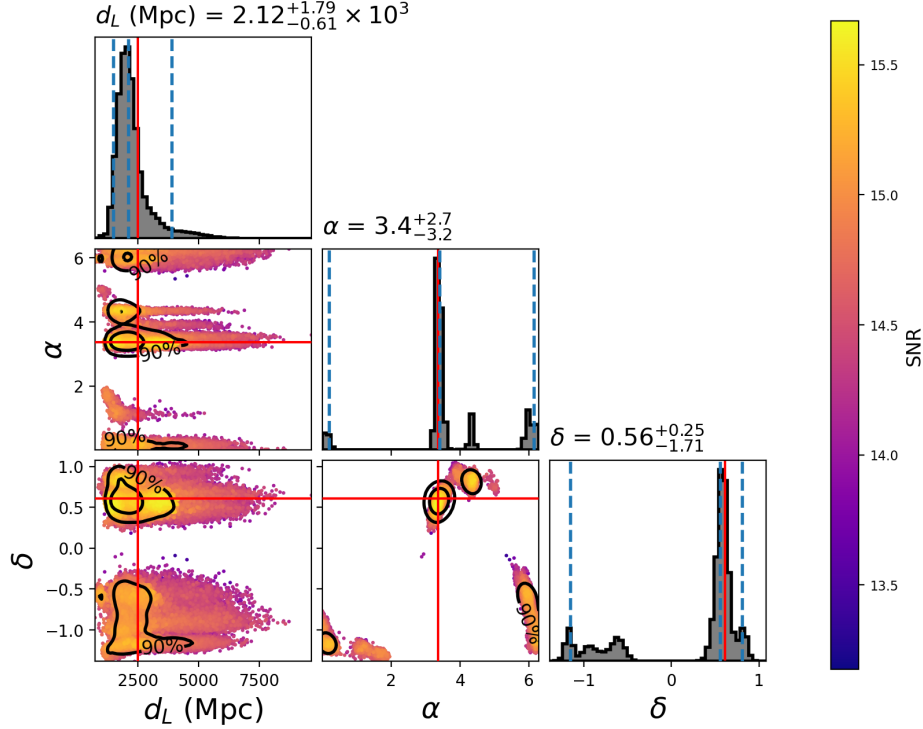


Figure 4.4.3: Posterior distributions for luminosity distance d_L , right ascension α , and declination δ for GW190521 assuming birefringence. The median values and 90% credible interval are denoted with dotted vertical lines; the vertical color bar shows the signal-to-noise-ratio. The red lines mark the sky location of a possible EM flare associated with GW190521.

lower energy scale cutoff to $M_{PV} > 0.05$ GeV, which is an improvement over previous constraints by a factor of 5. The constraint on M_{PV} allows us to limit the standard model extension isotropic birefringence parameter with mass dimension $d = 5$ to $|\zeta^{(5)}| < 9 \times 10^{-16}$ m. These results show that gravitational wave astronomy is a promising future avenue by which to study gravity at high energies.

We surprisingly find evidence in support of gravitational wave birefringence for GW190521 and GW191109, which happen to be the most and second most massive events in 4-OGC. Furthermore, we find that including birefringences increases the likelihood of association between GW190521 and its possible electromagnetic counterpart.

We find no disparity between three state-of-the-art waveform approximants and no significant issues with the data quality for GW190521. While there is a glitch in the GW191109 data, it was removed by LIGO/ Virgo, and our analysis suggests the noise fluctuation is unlikely to have caused the non-zero M_{PV}^{-1} result.

However, it is well documented that GW190521 is an exceptional event that may not fit well into the simple quasi-circular binary black hole merger picture. For instance, Refs. [287, 288] show that GW190521 is consistent with the merger of a binary black hole system with eccentric orbit, Ref. [289] gives a Bayes factor that highly favors a hyperbolic encounter over a quasi-circular merger, and Ref. [290] shows that GW190521 could be genuinely new physics, such as a proca star collision. The accuracy of current general relativity waveform approximants is limited at the

merger stage. This is quite relevant for GW190521 and GW110919 as most of the data is in the merger band. Our work provides further evidence for non-standard physical effects in gravitational wave data, which the available general relativity waveform approximants cannot currently account for. Even if the apparent deviation from general relativity is from new physics, our gravitational wave birefringence model can not provide a universal explanation. A possible extension might include a parity violation that depends on the masses of the binary.

As the advanced LIGO and Virgo detectors are upgraded and the KAGRA detector joins the network, we expect more high mass detections similar to GW190521 and GW191109, which may provide further insight into the physics behind the observed behavior of these outliers.

We release all posterior files and the scripts necessary to reproduce this work in <https://github.com/gwastro/4ogc-birefringence>.

Acknowledgements

YFW and SMB acknowledge the Max Planck Gesellschaft and thank the computing team from AEI Hannover for their significant technical support. LS was supported by the National Natural Science Foundation of China (11975027, 11991053), the National SKA Program of China (2020SKA0120300), the Young Elite Scientists Sponsorship Program by the China Association for Science and Technology (2018QNRC001), and the Max Planck Partner Group Program funded by the Max Planck Society.

This research has made use of data from the Gravitational Wave Open Science Center (<https://www.gwopenscience.org>), a service of LIGO Laboratory, the LIGO Scientific Collaboration and the Virgo Collaboration. LIGO is funded by the U.S. National Science Foundation. Virgo is funded by the French Centre National de Recherche Scientifique (CNRS), the Italian Istituto Nazionale della Fisica Nucleare (INFN) and the Dutch Nikhef, with contributions by Polish and Hungarian institutes.

Appendix

4.A Investigation of Data Quality Systematics by General Relativity Injection

We investigate the data quality to determine if non-stationary or non-Gaussian noise could be responsible for the apparent deviation from general relativity for GW190521 and GW191109. We generate 100 general relativity waveforms with the IMRPhenomXPHM [45] template and inject them into the LIGO and Virgo data near the coalescence times of GW190521 and GW191109. The waveform source parameters (component masses and spins, sky location, source orbital orientation, gravitational wave polarization angle, and coalescence phase) are sampled from the GW190521 and GW191109 posteriors released by 4-OGC [190]. For GW190521, the waveforms are injected into the time interval $[-20, 20]$ seconds around the trigger time of GW190521. However, we exclude the region $[-4, 4]$ seconds around the trigger time, where the event is predominant over the

noise. Both LIGO detectors contain transient noise artifacts at the merger time of GW191109 [7]. We have analyzed GW191109 using a deglitched version of data released by LIGO and Virgo [7]. However, a cleaned version of the data in the region of GW191109 is not readily available. To avoid the glitches, which were removed for the GW191109 analysis, we inject our signals into a segment of data [-100, -30] seconds from the trigger.

The injections are then analyzed the same as the actual event using the method presented in the main text. For the parameter estimation, all priors are the same as those used to analyze the GW190911 and GW190521 respectively.

The injections' M_{PV}^{-1} posteriors are shown in the first row of Fig. 4.A.1. For comparison, the figure also shows the GW190521 and GW191109 posteriors. We note that some results for GW191109-type injections have a spikey or multi-modal shape; we attribute this to the noisy data around GW191109.

We find that, in rare cases, the background noise fluctuation can produce non-zero peaks for M_{PV}^{-1} . To assess the significance of our non-zero M_{PV}^{-1} results for GW191109 and GW190521, we extract the Bayes factor from the posteriors using the Savage-Dickey density ratio; the second row of Fig. 4.A.1 shows the results. Using $\ln B_{\text{GR}}^{\text{nonGR}}$ as a statistic, only 1 in 100 and 4 in 100 simulations exceed the Bayes factor from GW190521 and GW191109, respectively. The false alarm rate or p-value to reject the null hypothesis that general relativity is correct is thus 1(4) out of 100 realizations.

We take the mean of M_{PV}^{-1} of all injections to determine the background distribution for the null hypothesis and note that the background is qualitatively different from the actual data results. Overall we do not find strong evidence that background noise artifacts caused the non-zero results for testing GR.

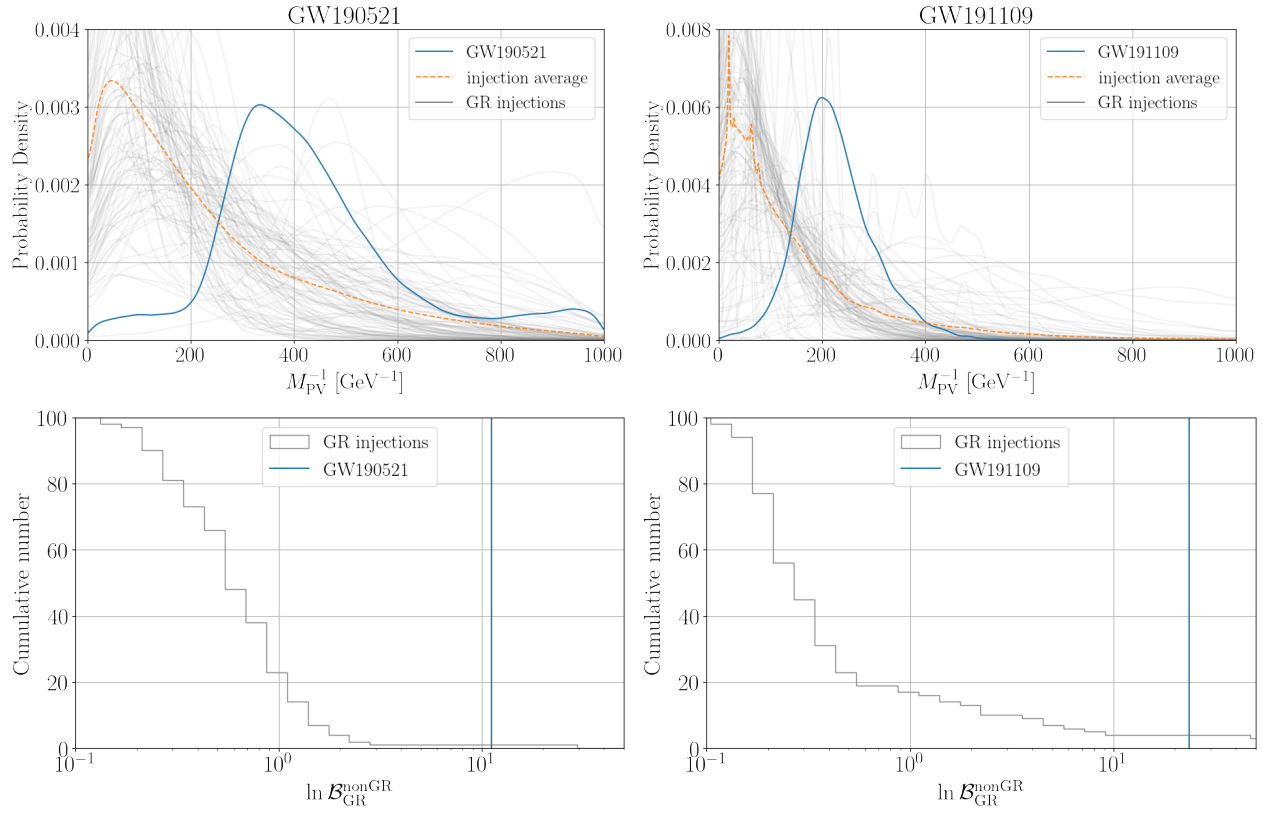


Figure 4.A.1: First row: the Bayesian posteriors of M_{PV}^{-1} for 100 general relativity injections that mimic GW190521 (left) and GW191109 (right). The posteriors for GW191109 and GW190521 are plotted for comparison. The average posterior of the 100 injections is shown. Second row: the cumulative distribution of $\ln \mathcal{B}_{\text{GR}}^{\text{nonGR}}$ for general relativity injections. The histogram shows the number of injections with $\ln \mathcal{B}_{\text{GR}}^{\text{nonGR}}$ equal or less than certain values. The Bayes factor for the real events is plotted as a comparison.

5 | Tidal Deformability of Neutron Stars in Scalar-Tensor Theory

The work contained in this chapter has not been submitted to or published in a peer reviewed journal. However, it contains material that is available on arXiv as a preprint: Brown, Stephanie M. *Tidal Deformability of Neutron Stars in Scalar-Tensor Theories of Gravity for Gravitational Wave Analysis*. arXiv:2210.14025 (2022).

Abstract

Gravitational waves from compact binary coalescence are valuable for testing theories of gravity in the strong field regime. By measuring neutron star tidal deformability in gravitational waves from binary neutron stars, stringent constraints were placed on the equation of state of matter at extreme densities. Tidal Love numbers in alternative theories of gravity may differ significantly from their general relativistic counterparts. Understanding exactly how the tidal Love numbers change will enable scientists to untangle effects from physics beyond general relativity from the uncertainty in the equation of state measurement. In this work, we explicitly calculate the fully relativistic $l \geq 2$ tidal love numbers for neutron stars in scalar-tensor theories of gravitation. We use several realistic equations of state to explore how the mass, radius, and tidal deformability relations differ from those of general relativity. We find that tidal Love numbers and tidal deformabilities can differ significantly from those in general relativity in certain regimes. The electric tidal deformability can differ by $\sim 350\%$, and the magnetic tidal deformability differs by $\sim 200\%$. These deviations occur at large compactnesses ($C = M/r > 0.2$) and vary slightly depending on the equation of state. This difference suggests that using the tidal Love numbers from general relativity could lead to significant errors in tests of general relativity using the gravitational waves from binary neutron star and neutron-star–black-hole mergers.

5.1 Introduction and Motivation

Compact objects such as neutron stars and black holes are essential for testing general relativity in the strong field regime. Gravitational waves emitted by compact objects by LIGO-Virgo have improved our understanding of gravity in the strong field regime. The LIGO/Virgo collaboration has detected almost one-hundred compact binary coalescences to date: two binary neutron star mergers, two neutron star-black hole mergers, and more than eighty binary black hole mergers [4, 5, 7]. An independent analysis of the available data found even more events [190, 267, 268]. Analysis

of these events has already placed limits on possible deviations from general relativity [10, 111, 112, 117, 272]. Recently, waveforms for various alternate theories of gravity have been developed and applied to parameter estimation. These waveforms allow for stringent tests of various theories of gravity and more general tests for physics beyond general relativity, such as scalar and tensor propagation modes [114, 115, 300].

Neutron stars are also unique laboratories for studying nuclear physics at ultra-high densities. Information about neutron star matter is encoded in gravitational waves from binary neutron star and neutron star-black hole mergers. Neutron stars contain vital information needed to understand phases of matter encountered in Quantum Chromodynamics. The tidal deformability encodes information about the nuclear EOS in gravitational waves. Studies of binary neutron star merger GW170817 have improved our knowledge of the nuclear EOS [8, 74, 75, 110]. Despite this, the nuclear EOS is still unknown. Studying neutron stars in alternative theories of gravity is challenging because deviations in neutron star properties caused by non general relativistic effects are of the same order of magnitude as the uncertainty in the EOS. Understanding how the mass-radius-tidal deformability relationships deviate from general relativity is essential to untangling these differences.

Tidal deformability connects gravitational waves and the nuclear EOS. Tidal deformabilities and the associated tidal Love numbers relate an applied external tidal field to the induced internal multipole moment, measuring the magnitude of deformation under a given tidal force. Love numbers were initially defined in Newtonian gravity [104, 105] and then expanded to general relativity by Flanagan and Hinderer [102, 103]. The concept was further expanded and made more concrete in several follow-up papers, including Binnington and Poisson [108] and Damour and Nagar [107].

This work focuses on scalar-tensor theory, one of the most natural and best studied alternate theories of gravity. The theory was initially motivated partly by Mach’s principle [173] and partly in an attempt to expand general relativity to five dimensions [301]. However, it is still of interest today. Scalar degrees of freedom are critical for string theory, superstring theory, and other supergravity theories [174]. Therefore scalar-tensor theories can sometimes be used as a phenomenological proxy for more complex extensions of general relativity. Furthermore, scalar fields have been proposed as an alternative solution to the dark energy problem [302–304].

Scalar-tensor theories add a massless scalar field (φ) to the standard general relativity metric ($g_{\mu\nu}$). The metric and the scalar field are coupled into an ‘effective metric’ $\tilde{g}_{\mu\nu} = A^2(\varphi)g_{\mu\nu}$. The earliest versions of this theory were presented more than half a century ago by Jordan, Fierz, and Brans and Dicke [173, 176, 301]. In the simplest scalar-tensor theory, known as JFBD (Jordan, Fierz, and Brans and Dicke), the scalar field is coupled to the metric by the coupling function $A(\varphi) = e^{\alpha\varphi}$. Solar system experiments have placed stringent constraints on the value of α . These constraints also significantly limit the strong-field behavior. Damour and Esposito-Ferèse discovered the ‘spontaneous scalarization’ effect, which allows large deviations from general relativity in the strong field regime without violating the strict solar system constraints. Damour and Esposito-Ferèse defined $A(\varphi) = e^{\beta\varphi^2/2}$ and found that scalarization occurs for $\beta \lesssim -4.5$ [187]. A follow-up study showed that scalarization occurs for $\beta \lesssim -4.35$ [188].

In this work, we calculate the tidal Love numbers of neutron stars in scalar-tensor theories of gravity, focusing on the spontaneous scalarization case. Sec. 5.2 presents the equilibrium configuration for neutron stars in scalar-tensor theory. Sec. 5.3 discusses the first order linear time-independent perturbations upon which the tidal deformabilities depend. Sec. 5.4 details the method for deriving the various tidal Love numbers. Sec. 5.5 presents the results and demonstrates

how the Love Numbers in scalar-tensor theories differ from those in general relativity. The paper concludes with Sec. 5.6, which discusses the results.

5.2 Neutron Stars in Scalar-Tensor Theory

Scalar-tensor theories are a straightforward alternative to general relativity. They depend on both a metric tensor ($g_{\mu\nu}$) and a massless scalar field (φ) and are typically expressed in one of two conformal frames: the Einstein frame and the Jordan frame. Historically, there has been much debate over the correct choice of frame [181], but it is now agreed that experiments measure Jordan frame quantities even though the field equations simplify in the Einstein frame [124, 172, 182–184].

In the Jordan frame, the action is

$$S = \frac{1}{16\pi G} \int \sqrt{-\tilde{g}} \left(\phi \tilde{R} - \frac{\omega(\phi)}{\phi} \tilde{g}^{\mu\nu} \partial_\mu \phi \partial_\nu \phi + 2\lambda(\phi) \right) d^4x + S_m[\Psi_m, \tilde{g}_{\mu\nu}] . \quad (5.1)$$

where the tilde denotes Jordan frame quantities, ϕ is the Jordan frame scalar field, $\tilde{g}_{\mu\nu}$ is metric, \tilde{R} is the Ricci scalar, $\omega(\phi)$ is a function of the scalar field that characterizes a specific scalar-tensor theory, and $\lambda(\phi)$ is the scalar potential. S_m denotes the action of the matter, which is a function of the matter fields Ψ_m and the Jordan metric $\tilde{g}_{\mu\nu}$. Due to the $\phi \tilde{R}$ term, the gravitational constant G becomes a function of the scalar field $\tilde{G} = G(\phi)$. Throughout this work, we will continue to denote Jordan frame quantities with a tilde.

The Jordan frame is the physical frame, but the field equations are typically expressed in the Einstein frame, where the metric and scalar decouple. A conformal transformation relates the two frames:

$$\tilde{g}_{\mu\nu} = A^2(\varphi) g_{\mu\nu} . \quad (5.2)$$

Using this transformation, the action can be re-written in a way that resembles the Einstein-Hilbert action:

$$S = \frac{1}{16\pi G_*} \int \sqrt{-g} (R - 2g^{\mu\nu} \partial_\mu \varphi \partial_\nu \varphi - 2\lambda(\phi)) d^4x + S_m[\Psi_m, A^2(\varphi) g_{\mu\nu}] \quad (5.3)$$

where all quantities are related to the Einstein metric $g_{\mu\nu}$. R is the scalar curvature, G_* is the bare gravitational coupling constant which is set to 1, along with c , from here on. This paper will focus on the $\lambda(\phi) = 0$ case.

Much of the work presented here is applicable for any $A(\varphi)$, but when necessary, the spontaneous scalarization coupling function [187] is used:

$$A(\varphi) = e^{\frac{1}{2}\beta\varphi^2} . \quad (5.4)$$

The modified field equations, derived from the Einstein frame action have the form

$$G_{\mu\nu} = 8\pi G_* T_{\mu\nu} + T_{\mu\nu}^{(\varphi)} \quad (5.5a)$$

$$\square_g \varphi = -4\pi G_* \alpha(\varphi) T , \quad (5.5b)$$

where $\alpha(\varphi) \equiv d \ln A(\varphi)/d\varphi$ and $T_{\mu\nu}^{(\varphi)}$ can be considered the stress-energy of the massless scalar field and has the form

$$T_{\mu\nu}^{(\varphi)} \equiv 2\partial_\mu\varphi\partial_\nu\varphi - g_{\mu\nu}g^{\alpha\beta}\partial_\alpha\varphi\partial_\beta\varphi. \quad (5.6)$$

$T_{\mu\nu}$ is the stress-energy tensor in the Einstein frame, and T is the contracted stress-energy tensor $T = T^\mu_\mu = g^{\mu\nu}T_{\mu\nu}$. $T_{\mu\nu}$ is related to the Jordan frame stress-energy tensor ($\tilde{T}_{\mu\nu}$) in the following manner

$$T^{\mu\nu} \equiv \frac{2}{\sqrt{|g|}} \frac{\delta S_m}{\delta g_{\mu\nu}} = A^6(\varphi)\tilde{T}^{\mu\nu}. \quad (5.7)$$

Note setting $\alpha(\varphi)$ to zero, retrieves the general relativity field equations.

We model neutron stars as static, spherically symmetric, non-rotating objects and assume that neutron star matter can be described as a perfect fluid. The stress-energy tensor for a perfect fluid is defined in the physical frame

$$\tilde{T}_{\mu\nu} = (\tilde{\rho} + \tilde{p})\tilde{u}_\mu\tilde{u}_\nu - \tilde{p}\tilde{g}_{\mu\nu} \quad (5.8)$$

where \tilde{u}_μ is the four-velocity of the fluid and $\tilde{\rho}$ and \tilde{p} are the energy density and pressure in the Jordan frame. We assume that \tilde{p} and $\tilde{\rho}$ are related by some barotropic EOS so that

$$\delta\tilde{\rho} = \frac{d\tilde{p}}{d\tilde{\rho}}\delta\tilde{p}. \quad (5.9)$$

where $\delta\tilde{p}$ and $\delta\tilde{\rho}$ are the Eulerian fluid perturbations. As the star is static, only the t component of the four-velocity is non-zero:

$$u^\mu = (e^{\nu/2}, 0, 0, 0) \quad (5.10)$$

Conservation of energy and momentum is defined in the physical or Jordan frame i.e., $\tilde{\nabla}_\mu\tilde{T}^\mu_\nu = 0$. Transforming to the Einstein Frame gives

$$\nabla_\nu T^\nu_\mu = \alpha(\varphi)T\nabla_\mu\varphi. \quad (5.11)$$

The metric for a static, spherically symmetric, self-gravitating object is

$$ds^2 = g_{\alpha\beta}dx^\alpha dx^\beta = -e^\nu dt^2 + e^\lambda dr^2 + r^2(d\theta^2 + \sin^2\theta d\phi^2) \quad (5.12)$$

where ν and λ are functions of r and $e^{-\lambda} = 1 - 2\mu(r)/r$.

The modified TOV or structure equations, which can be derived from the field equations and the equation for conservation of energy, have the form

$$\frac{d\mu}{dr} = 4\pi G_* r^2 A^4(\varphi)\tilde{\rho} + \frac{1}{2}r(r - 2\mu)\psi^2 \quad (5.13a)$$

$$\frac{d\nu}{dr} = 8\pi G_* \frac{r^2 A^4(\varphi)\tilde{p}}{r - 2\mu} + r\psi^2 + \frac{2\mu}{r(r - 2\mu)} \quad (5.13b)$$

$$\frac{d\varphi}{dr} = \psi \quad (5.13c)$$

$$\frac{d\psi}{dr} = 4\pi G_* \frac{r A^4(\varphi)}{r - 2\mu} [\alpha(\varphi)(\tilde{\rho} - 3\tilde{p}) + r\psi(\tilde{\rho} - \tilde{p})] - \frac{2(r - \mu)}{r(r - 2\mu)}\psi \quad (5.13d)$$

$$\frac{d\tilde{p}}{dr} = -(\tilde{\rho} + \tilde{p}) \left[4\pi G_* \frac{r^2 A^4(\varphi)\tilde{p}}{r - 2\mu} + \frac{1}{2}r\psi^2 + \frac{\mu}{r(r - 2\mu)} + \alpha(\varphi)\psi \right] \quad (5.13e)$$

where μ is the mass function. $\psi = \partial_r\varphi$ is used throughout this paper for improved readability.

5.3 Stationary Perturbations

In this section, we compute the linear, time-independent scalar and spacetime perturbations following the method initially laid out by [305]. The complete system of time-dependent perturbations in scalar-tensor theory was calculated in [306], and the perturbation equations in this section have been cross checked with the extant results.

We use the Regge-Wheeler gauge [307], which separates the metric perturbation $h_{\mu\nu}$ into its even and odd parity components $h_{\mu\nu} = h_{\mu\nu}^+ + h_{\mu\nu}^-$. [306] demonstrates that the metric in both frames can be written in the Regge-Wheeler gauge using the proper redefinition of the metric components between frames.

For this analysis, as we are interested in time-independent perturbations, all functions ($H_0, H_2, K, h_0,$ and h_1) are functions of r only. Furthermore, the tr term H_1 typically present in the Regge-Wheeler gauge vanishes.

The Einstein metric can be written in the following way:

$$h_{\mu\nu} = h_{\mu\nu}^+ + h_{\mu\nu}^- \quad (5.14)$$

where

$$h_{\mu\nu}^+ = \sum_{\ell=2}^{\infty} \sum_{m=-\ell}^{\ell} \begin{bmatrix} e^\nu H_{0,\ell m} & 0 & 0 & 0 \\ 0 & e^\lambda H_{2,\ell m} & 0 & 0 \\ 0 & 0 & r^2 K_{\ell m} & 0 \\ 0 & 0 & 0 & K_{\ell m} r^2 \sin^2 \theta \end{bmatrix} Y_{\ell m}(\theta, \phi) \quad (5.15)$$

and

$$h_{\mu\nu}^- = \sum_{\ell=2}^{\infty} \sum_{m=-\ell}^{\ell} \begin{bmatrix} 0 & 0 & -h_{0,\ell m} \sin^{-1} \theta \partial_\phi & h_{0,\ell m} \sin \theta \partial_\theta \\ 0 & 0 & -h_{1,\ell m} \sin^{-1} \theta \partial_\phi & h_{1,\ell m} \sin \theta \partial_\theta \\ sym & sym & 0 & 0 \\ sym & sym & 0 & 0 \end{bmatrix} Y_{\ell m}(\theta, \phi) \quad (5.16)$$

where $Y_{\ell m}(\theta, \phi)$ is the spherical harmonic function for l, m , and *sym* indicates that the metric is symmetric.

The explicit form of the conformal transformation between the Jordan and Einstein frame perturbation ($\tilde{h}_{\mu\nu} \rightarrow h_{\mu\nu}$) is needed to determine the Jordan frame tidal deformability. The conformal transformation is obtained by perturbing Eq. (5.2) and substituting in the Regge-Wheeler metric [306]. This gives

$$h_{\mu\nu} = \frac{1}{A^2(\varphi)} \tilde{h}_{\mu\nu} - \frac{2}{A(\varphi)} g_{\mu\nu} \delta A. \quad (5.17)$$

where δA is the variation of the conformal factor; it is a function of the scalar field perturbation $\delta\varphi = \delta\varphi(r)$. The relationship between δA and $\delta\varphi$ depends on the functional form of the conformal factor. In the case of spontaneous scalarization $\delta A = \beta A \varphi \delta\varphi$. The explicit relationships between the individual metric perturbations are

$$\tilde{H}_0 = A^2(\varphi) H_0 - 2A \delta A \quad (5.18a)$$

$$\tilde{H}_2 = A^2(\varphi) H_2 + 2A \delta A \quad (5.18b)$$

$$\tilde{K} = A^2(\varphi) K + 2A \delta A \quad (5.18c)$$

$$\tilde{h}_{0,1} = A^2(\varphi)h_{0,1} \quad (5.18d)$$

We dropped the ℓm subscripts from $H_0, H_2, K, h_0,$ and h_1 for readability and will continue to do so throughout this work.

The complete set of perturbation equations needed to calculate the tidal deformability are laid out in Appendix 5.B.

In general relativity, the full system of time-independent perturbed equations can be reduced to one differential equation for each parity: one for the even parity tensor perturbation (H) and one for the odd parity tensor perturbation (h). Scalar-tensor theories have an additional equation for the scalar field, which is of even parity. The metric and the scalar field are decoupled in the Einstein frame; therefore, the equations for H and $\delta\varphi$ decouple. The Jordan frame perturbation \tilde{H} depends on both H and $\delta\varphi$.

5.4 Neutron Star Tidal Deformability

We derive and compute the scalar-tensor tidal Love numbers and tidal deformabilities using the method developed by [102] and extended in [107, 108].

Tidal deformabilities (e.g., λ) relate an applied external tidal field ($\mathcal{E}_{ij\dots k}$) to the induced multipole moment ($Q_{ij\dots k}$). To linear order in $\mathcal{E}_{ij\dots k}$, the tidal deformability is a proportionality constant between the two [102] i.e.,

$$Q_{ij\dots k} = -\lambda\mathcal{E}_{ij\dots k} . \quad (5.19)$$

Both $\mathcal{E}_{ij\dots\ell}$ and $Q_{ij\dots\ell}$ can be decomposed into tensor harmonics

$$\mathcal{E}_{ij\dots k} = \sum_{m=-\ell}^{\ell} \mathcal{E}_m Y_{ij\dots k}^{\ell m}(\theta, \phi) \quad (5.20)$$

$$Q_{ij\dots k} = \sum_{m=-\ell}^{\ell} Q_m Y_{ij\dots k}^{\ell m}(\theta, \phi) \quad (5.21)$$

where $Y_{ij\dots k}^{\ell m}(\theta, \phi)$ are the even parity tensor spherical harmonics defined by [106]. This means that the tensor relation in Eq. (5.19) can be expressed as a scalar relation

$$Q_m = -\lambda\mathcal{E}_m . \quad (5.22)$$

To calculate λ it is sufficient to calculate one non-vanishing \mathcal{E}_m [102].

The external tidal field and the induced multipole moment affect space-time in and around the neutron star. Outside the star, the large r behavior of the metric can be written in terms of \mathcal{E}_{ij} and Q_{ij} [102, 109]. For example, the metric expansion for a spherically symmetric star of mass M in a quadrupolar tidal field \mathcal{E}_{ij} for large r is

$$g_{tt} = g_{tt}^0 + h_{tt} = -\left(1 - \frac{2\mu}{r}\right) + \frac{3Q_{ij}n^i n^j}{r^3} + \mathcal{O}(r^{-4}) - \mathcal{E}_{ij}n^i n^j r^2 + \mathcal{O}(r^3) \quad (5.23)$$

where n^i is the unit radial vector. The scalar tidal deformability is defined analogously to Eq. (5.19) except that it relates an applied scalar field to an induced multipole moment of the scalar field.

5.4.1 Electric Type Love Numbers

In general relativity, the electric or even parity Love numbers are calculated from the $g_{tt} = g_{tt}^{(0)} + h_{tt}$ component of the metric and are based on a single, second order linear differential equation for $H = H_0 = H_2$. However, in scalar-tensor theory, there are two types of even parity perturbations: scalar and tensor. The even parity metric tidal Love numbers k_ℓ define how the body responds to a change in the *metric*. The scalar tidal Love numbers κ_ℓ define how the body responds to a change in the applied *scalar field*. As the scalar field and the metric are not coupled in the Einstein frame, a change in the matter field does not induce a scalar perturbation, and vice-versa¹. The perturbation equations for the tidal Love number calculation must be derived carefully to first order in either the scalar perturbation or the metric perturbation but not both. This approach differs from previous approaches in [121] and [124].

There are two master equations: one second order linear differential equation for the tensor perturbation $H = H_0 = H_2$, which comes from the perturbation of the field equation Eq. (5.5a), and one for the scalar perturbation $\delta\varphi$ which comes from the scalar wave equation Eq. (5.5b).

While the differential equation for φ can be derived directly from the scalar wave equation (see Eq. (5.89)), the differential equation for H is derived from the a system of equations Eqs. (5.83) to (5.88) and is obtained by the following steps (which have been widely used in general relativity [102, 107, 108]):

- Eq. (5.83) $\longrightarrow H_0 = H_2 \equiv H$
- Eq. (5.84) $\longrightarrow K_r = H_r + \nu_r H$
- Eq. (5.85) $\longrightarrow K'' = H'' + \nu_r H' + \nu_{rr} H$
- Eq. (5.87) $\longrightarrow \delta p = \frac{1}{2}(p + \rho)H$
- Eq. (5.88) $\longrightarrow H'' + c_1 H' + c_2 H = 0$

This gives

$$H'' + \left(\frac{2}{r} + \frac{1}{2}(\nu_r - \lambda_r) \right) H' - \left(e^\lambda \frac{l(l+1)}{r^2} + \left(\frac{2\mu}{r(r-2\mu)} + r\psi^2 \right)^2 \right) H = 0 \quad (5.24)$$

$$\delta\varphi'' + \left(\frac{2}{r} + \frac{1}{2}(\nu_r - \lambda_r) \right) \delta\varphi' + e^\lambda \left(-\frac{l(l+1)}{r^2} \delta\varphi + 16A^3\pi\alpha(3p - \rho)\delta A + 4A^4\pi(3p - \rho)\delta\alpha \right) = 0. \quad (5.25)$$

where a prime (') denotes derivative with respect to r and λ refers to the metric function and not the tidal deformability. In the case of spontaneous scalarization, Eq. (5.25) becomes

$$\delta\varphi'' + \left(\frac{2}{r} + \frac{1}{2}(\nu_r - \lambda_r) \right) \delta\varphi' + e^\lambda \left(-\frac{l(l+1)}{r^2} + 4A^4\pi\alpha(3p - \rho)(1 + 4\alpha\varphi) \right) \delta\varphi = 0. \quad (5.26)$$

External to the star, Eqs. (5.24) and (5.26), reduce to

$$H'' + \frac{2(r - \mu)}{r(r - 2\mu)} H' - \left(e^\lambda \frac{l(l+1)}{r^2} + \left(\frac{2\mu}{r(r - 2\mu)} + r\psi^2 \right)^2 \right) H = 0 \quad (5.27a)$$

¹We thank Gast3n Creci for his insights on this matter.

$$\delta\varphi'' + \frac{2(r-\mu)}{r(r-2\mu)}\delta\varphi' - \left(e^\lambda \frac{l(l+1)}{r^2}\right)\delta\varphi = 0. \quad (5.27b)$$

Eq. (5.27a) depends on the ψ , and so is coupled to the scalar wave equation (Eq. (5.5b)). As long as $\psi > 0$, there is no analytical solution to Eq. (5.27a). Only approximate solutions exist at the surface of the star ($\tilde{p} = 0$) because $\psi \neq 0$. Since φ asymptotically approaches a constant value φ_∞ , the derivative ψ vanishes at large r . In this regime, Eq. (5.27a) has an exact solution. The solutions to Eqs. (5.27a) and (5.27b) are

$$H = c_1 Q_\ell^2 \left(\frac{r}{\mu} - 1\right) + c_2 P_\ell^2 \left(\frac{r}{\mu} - 1\right) \quad (5.28a)$$

$$\delta\varphi = d_1 Q_\ell \left(\frac{r}{\mu} - 1\right) + d_2 P_\ell \left(\frac{r}{\mu} - 1\right), \quad (5.28b)$$

where P_ℓ^m and Q_ℓ^m are associated Legendre functions of the first and second kind.

In order to determine c_1, c_2, d_1 , and d_2 , we match the asymptotic behavior of the two solutions i.e.

$$H = \frac{8}{5}c_1 \left(\frac{r}{\mu}\right)^{-3} + \mathcal{O}\left(\left(\frac{r}{\mu}\right)^{-4}\right) + 3c_2 \left(\frac{r}{\mu}\right)^2 + \mathcal{O}\left(\frac{r}{\mu}\right) \quad (5.29a)$$

$$\delta\varphi = \frac{2}{15}d_1 \left(\frac{r}{\mu}\right)^{-3} + \mathcal{O}\left(\left(\frac{r}{\mu}\right)^{-4}\right) + \frac{3}{2}d_2 \left(\frac{r}{\mu}\right)^2 + \mathcal{O}\left(\frac{r}{\mu}\right) \quad (5.29b)$$

to the expansion of and the scalar field and the g_{tt} component of the metric (Eq. (5.23)) respectively.

This gives us c_1, c_2, d_1 , and d_2 in terms of the tensor tidal deformability λ and the scalar tidal deformability λ_s respectively. For example, in the $\ell = 2$ case, we have

$$c_1 = \frac{15}{8} \frac{1}{\mu^3} \lambda \mathcal{E}, \quad c_2 = \frac{1}{3} \mu^2 \mathcal{E} \quad (5.30)$$

$$d_1 = \frac{45}{2} \frac{1}{\mu^3} \lambda \mathcal{E}, \quad d_2 = \frac{2}{3} \mu^2 \mathcal{E}. \quad (5.31)$$

By requiring continuity of the logarithmic derivatives

$$y = \frac{rH'}{H} \quad \& \quad w = \frac{r\delta\varphi'}{\varphi} \quad (5.32)$$

and thus of $H, \delta\varphi$, and their derivatives at the surface of the star, it is possible to determine λ and λ_s in terms of μ, r , and either y or w respectively. This is done by substituting ?? and Eq. (5.28a) or ?? and Eq. (5.28b) into Eq. (5.32) and solving for λ or $\lambda^{(\varphi)}$.

The tidal Love numbers are connected to the tidal deformabilities by the following equations

$$k_\ell = \frac{(2\ell-1)!!}{2} \lambda R^{-(2\ell+1)} \quad \& \quad \kappa_\ell = \frac{(2\ell-1)!!}{2} \lambda_s R^{-(2\ell+1)} \quad (5.33)$$

While this approach is sufficient to *define* λ , difficulty arises in numerically calculating λ and k_ℓ because Eq. (5.28a) is only a solution to Eq. (5.27a) in the large r limit. It is not a solution near the surface of the star where numerical matching is typically done. In this region, an exact solution

does not exist. While there is not an exact solution, an approximate series solution to Eq. (5.27a) can be constructed order by order in powers of r/μ . The leading order behavior of H is

$$H \approx a_\ell \left(\frac{r}{\mu}\right)^\ell + a_{-(\ell+1)} \left(\frac{r}{\mu}\right)^{-(\ell+1)} \quad (5.34)$$

However, the leading order solution alone is not accurate enough for our purposes. The solution to Eq. (5.27a) is a linear superposition of the growing and diminishing solution with two coefficients a_ℓ and $a_{-(\ell+1)}$ which are determined by the boundary conditions.

To create a more accurate solution, we construct two series solutions by adding higher order terms, one growing and one diminishing. From here higher order terms are added to construct a solution with the form

$$H \approx a_\ell \left(\left(\frac{r}{\mu}\right)^\ell + \alpha_1^+ \left(\frac{r}{\mu}\right)^{\ell-1} + \alpha_2^+ \left(\frac{r}{\mu}\right)^{\ell-2} + \dots + \alpha_n^+ \left(\frac{r}{\mu}\right)^{\ell-n} \right) \quad (5.35)$$

$$+ a_{-(\ell+1)} \left(\left(\frac{r}{\mu}\right)^{-(\ell+1)} + \alpha_1^- \left(\frac{r}{\mu}\right)^{-(\ell+2)} + \alpha_2^- \left(\frac{r}{\mu}\right)^{-(\ell+3)} + \dots + \alpha_n^- \left(\frac{r}{\mu}\right)^{-(\ell+1+n)} \right)$$

For numerical purposes, the series is truncated at order $n = 13$. This ensures the series has converged within 0.5%.

Note that H has only two degrees of freedom ($a_\ell, a_{-(\ell+1)}$). All other constants, α^+ and α^- , are functions of these two. The constants are determined by substituting one series solution, either growing or decaying, into Eq. (5.27a) and solving for the coefficients order by order.

Lastly, by matching a_ℓ and $a_{-(\ell+1)}$ to Eq. (5.23) and then substituting Eq. (5.35) into Eq. (5.32), the approximate tidal deformability λ can be derived in the same method described above.

5.4.2 Magnetic Type Love numbers

The odd parity or magnetic Love numbers j_ℓ and their associated tidal deformabilities σ_l are functions of the odd parity metric perturbation $h_{\mu\nu}^-(h_0, h_1)$. The odd parity metric perturbations h_0 and h_1 (Eq. (5.16)) are coupled only to the explicit fluid velocity perturbation $U(r)Y_{\ell m}$:

$$\delta u^\mu = [4\pi e^{-\nu/2} r^2 A^4 (\rho + p)]^{-1} \left(0, 0, \partial_\phi Y_{\ell m}(\theta, \phi), \partial_\theta Y_{\ell m}(\theta, \phi) \right) \sin^{-1} \theta U(r) . \quad (5.36)$$

The odd parity metric perturbations can be constrained by three equations, which come from the $t\phi$, $r\phi$, and $\theta\phi$ components of the perturbation equations (see Eqs. (5.90) to (5.92)). There are multiple approaches to the magnetic Love number in the literature, but two are worthy of note [308]. The earliest two publications on magnetic tidal deformabilities [107, 108] have approaches that are fundamentally different and whose results do not agree. The first approach developed by Binnington and Poisson [108] assumes a *strictly static* fluid i.e., $h_{0t} = h_{1t} = U = 0$. The second approach from Damour and Nagar [107] assumes an *irrotational* fluid. Instead of initially setting $h_{0t} = h_{1t} = U = 0$, this approach calculates the full Regge-Wheeler equation and then takes the static limit ($\omega \rightarrow 0$). Note that these approaches seem equivalent at a surface level but do not lead to the same answer because the irrotational approach picks up a non-vanishing term from the fluid velocity perturbation. This chapter lays out both approaches and clarifies the subtle differences between them.

Static Approach

In this section, we apply the static method derived in [108] to scalar-tensor theory; we assume that the perturbations are strictly static i.e., $h_{0t} = h_{1t} = U = 0$ and consider the odd parity perturbation equations Eqs. (5.90) to (5.92). Under this assumption, Eq. (5.91) becomes

$$h_1 = 0, \quad (5.37)$$

and Eq. (5.92) becomes independent of h_0 and constrains only h_1 .

The final remaining equation, Eq. (5.90), yields a second order differential equation for h_0 .

$$\begin{aligned} e^{-\lambda} h_0'' - \left[4\pi r A^4(\varphi)(p + \rho) + e^{-\lambda} r \psi^2 \right] h_0' \\ - \left[\frac{l(l+1)}{r^2} - \frac{4\mu}{r^3} + 8\pi A^4(\varphi)(p + \rho) - 2e^{-\lambda} \psi^2 \right] h_0 = 0, \end{aligned} \quad (5.38)$$

where the prime (') denotes a derivative with respect to r . This equation is consistent with Eq. B7 in [306].

In the region exterior to the star, $\mu(r) = \mu$ and $\tilde{p} = \tilde{\rho} = 0$ and Eq. (5.38) takes on a simpler form.

$$e^{-\lambda} h_0'' - \left[\frac{l(l+1)}{r^2} - \frac{4\mu(r)}{r^3} - 2e^{-\lambda} \psi^2 \right] h_0 = 0 \quad (5.39)$$

This equation differs from the general relativity equation by the factor of $-2e^{-\lambda} \psi^2$ [108]. Eq. (5.39) is now coupled to the scalar wave equation (Eq. (5.5)) and no longer has an exact solution. This differs result from the $f(R)$ results [121]. In $f(R)$ theories φ approaches zero as $r \rightarrow \infty$, whereas in the theories considered here φ approaches a constant, non-zero value. Rather than matching solutions at the surface, [121] matches the numerical solution to an analytical solution at some r_{match} , beyond which the ψ term can be neglected. r_{match} is defined by the Compton wavelength of the scalar field.

Since Eq. (5.39) is true for all $r > r_s$, including the large r regime where $r \gg r_s$ and $\psi \rightarrow 0$, there is an exact solution in the large r limit. This is sufficient to define the tidal Love numbers. However, as was the case with the electric tidal deformability, there is no analytical solution at the surface of the star. This solution can be approximated following the method laid out in Sec. 5.4.1 or a method similar to that used in the $f(R)$ case.

Furthermore, the irrotational approach is considered more physically relevant than the strictly static approach. As the irrotational case is more realistic and has an analytical solution, we will focus on the irrotational approach [308–310].

Irrotational Approach

In the *irrotational* approach, which was initially presented in [107], it is assumed that the perturbations have a standard $e^{-i\omega t}$ time dependence i.e. $h_i(r, t) = h_i(r) e^{-i\omega t}$.

Previous authors [107, 311–313] have noted that Eq. (5.92) can be solved for h_0 in terms of h_1 unless one assumes that $h_{0t} = 0$ (for that case see Sec. 5.4.2).

Under this assumption, Eq. (5.92) can be rewritten as

$$h_{0t} = e^{(\nu-\lambda)/2} (\Psi r)' \quad (5.40)$$

where Ψ is defined such that

$$h_1 = e^{(\lambda-\nu)/2}\Psi r . \quad (5.41)$$

Assuming that $h_0(r, t) = h_0(r)e^{-i\omega t}$, Eq. (5.40) can be used to define h_0 :

$$h_0 = \frac{i}{\omega} e^{(\nu-\lambda)/2} (\Psi r)' . \quad (5.42)$$

It is evident from this equation that h_0 is not well defined in the $\omega \rightarrow 0$ limit [308]. Substituting Eq. (5.42) and Eq. (5.41) into Eq. (5.90) gives the following master equation:

$$\Psi'' + \frac{e^\lambda}{r^2} [2m + 4\pi r^3 A^4(p - e)] \Psi' + e^\lambda \left[e^{-\nu} \omega^2 + \frac{6m}{r^3} - \frac{l(l+1)}{r^2} + 4\pi A^4(p - \rho) \right] = 0 . \quad (5.43)$$

This agrees with Equation 40 in [306].

Since it is assumed that the neutron star is static, we are interested in the $\omega \rightarrow 0$ limit. The master equation becomes

$$\Psi'' + \frac{e^\lambda}{r^2} [2m + 4\pi r^3 A^4(p - e)] \Psi' + e^\lambda \left[\frac{6m}{r^3} - \frac{l(l+1)}{r^2} + 4\pi A^4(p - \rho) \right] = 0 . \quad (5.44)$$

Outside of the star, this equation simplifies further:

$$\Psi'' + e^\lambda \frac{2m}{r^2} \Psi' + e^\lambda \left[\frac{6m}{r^3} - \frac{l(l+1)}{r^2} \right] = 0 . \quad (5.45)$$

Interestingly, this equation, unlike the static master equation (Eq. (5.38)), does not depend explicitly in φ or ψ . Therefore external to the star, the solution to Eq. (5.44) is known and identical to the general relativity solution. All non-general relativistic effects arise from matching the internal and external solutions at the surface of the star.

We briefly demonstrate the difference in the static and irrotational solutions in scalar-tensor theory. The method presented in [308] is applied to the scalar-tensor problem.

Using the axial component of the stress-energy tensor conservation equation (Eq. (5.11)) and assuming $\omega \neq 0$, one finds that

$$U(r) = -4\pi A^3(\rho + p)e^{-\nu} h_0 . \quad (5.46)$$

Substituting Eq. (5.46) into Eq. (5.90) and then taking the $\omega \rightarrow 0$ limit, the following differential equation for h_0 is obtained

$$\begin{aligned} e^{-\lambda} h_0'' - \left[4\pi A^4(\varphi)(p + \rho)r + e^{-\lambda} r \psi^2 \right] h_0' \\ - \left[\frac{l(l+1)}{r^2} - \frac{4m}{r^3} - 8\pi A^4(\varphi)(p + \rho) - 2e^{-\lambda} \varphi_r^2 \right] h_0 = 0 . \end{aligned} \quad (5.47)$$

There is a sign change in the $8\pi A^4(\varphi)(p + \rho)$ term between Eq. (5.38) and Eq. (5.47). The difference occurs because $U(r) = 0$ for the static approach and $U(r) \neq 0$ in the irrotational case. So while there is irrotational fluid motion in one case, the other has a completely static fluid. As a result of this difference, the irrotational tidal Love numbers are negative while the static Love numbers are positive.

Returning to the main goal of this work, calculating j_ℓ and σ_ℓ , we use the similarity between the irrotational master equation and its general relativity counterpart to define the solution. Eq. (5.45) has an exact solution of the form

$$\psi^{ext}(R) = b_p \psi_p(R) + b_q \psi_q(R) = b_p R^{l+1} - \frac{b_q}{4} R^3 \partial_R \left[(R)^{-4} F\left(l-1, l+2; 2l+2; \frac{2M}{r}\right) \right] \quad (5.48)$$

where $R = r/\mu$ and F is a hypergeometric function. For $l = 2$, F is expressible in terms of simple functions.

b_q and b_p are determined by the boundary conditions at the surface of the star. Since both ψ and ψ' are required to be continuous at the surface of the star, the logarithmic derivative $y^{odd} = r\psi'/\psi$ must also be continuous at the surface of the star.

j_ℓ and σ_ℓ are therefore defined to be

$$j_\ell \equiv -C^{2\ell+1} \frac{\psi'_p(R_s) - C y^{odd} \psi_p(R_s)}{\psi'_q(R_s) - C y^{odd} \psi_q(R_s)} \quad (5.49)$$

and

$$\sigma_\ell = \frac{\ell-1}{4(l+2)} \frac{j_\ell}{(2\ell-1)!!} C^{2\ell+1}, \quad (5.50)$$

where $R_s = r_s/\mu$ and C is the compactness.

j_ℓ and σ_ℓ are, at a glance, identical to their general relativity counterparts, but the scalar-tensor and general relativity values differ because all non-general relativistic effects are contained in the value of y_s^{odd} calculated by integrating Eq. (5.44) along with the modified TOV equations (Eq. (5.13)) inside the star.

5.5 Results

5.5.1 Electric Love Numbers

This section presents the electric tidal Love numbers and the associated tidal deformabilities and compare them to the general relativity results. There are two degrees of freedom needed to define a specific case of spontaneous scalarization: β and φ_∞ . β is constrained by binary pulsar experiments to $\beta < -5$ at the 1σ level [314]. In this work we use several values of β to demonstrate the results: $\beta = -4.5, -5, -5.5, -6$. Generally, we compare only the $\beta = -4.5$ and $\beta = -6$. This gives us two sets of results, one conservative and one optimistic. The value of the scalar field at infinity, φ_∞ , is tightly constrained by the Cassini experiment [315]. That experiment directly constrains the Brans-Dicke parameter ω_{BD} to be $> 4 \times 10^4$. The value of the scalar field at infinity is related to the Brans-Dicke parameter by the equation

$$\varphi_\infty = \frac{2}{|\beta|} \sqrt{\frac{\pi}{3 + 2\omega_{BD}}}. \quad (5.51)$$

This constrains φ_∞ to $< 2.7 \times 10^{-3}$ and $< 2.0 \times 10^{-3}$ for $\beta = -4.5$ and $\beta = -6$ respectively. We use $\varphi_\infty = 10^{-3}$ for all results presented. Changing φ_∞ to 2.0×10^{-3} increases the deviation

from general relativity. Conversely, changing φ_∞ to 10^{-4} decreases the deviation from general relativity. These differences grow with increasing compactness and are less than 1% for the values considered.

Using Eq. (5.28a) and Eq. (5.33), it is possible to define the tidal Love number in the large r limit. The scalar tidal Love number can be similarly calculated.

The $\ell = 2$ tidal Love numbers are defined as follows

$$k_2 = \left(8(2C - 1)^2 C^5 (2 + 2C(y - 1) - y) \right) \times \quad (5.52a)$$

$$\left[5(2C(6 + C^2(26 - 22y) - 3y + 4C^4(1 + y) + 3C(-8 + 5y) \right.$$

$$\left. + C^3(6y - 4)) - 3(1 - 2C)^2(2 + 2C(y - 1) - y) \ln[1 - 2C] \right]^{-1}$$

$$\kappa_2 = \left(4C^5(2C - 1)(2C^2w - 6Cw + 3w + 6C - 6) \right) \times \quad (5.52b)$$

$$\left[45(2C(C(12 - 9w) + 3(-2 + w) + C^2(-2 + 6w)) \right.$$

$$\left. + (-1 + 2C)(-6 + 6C + 3w - 6Cw + 2C^2w) \ln[1 - 2C] \right]^{-1},$$

where $y = rH'/H$ and $w = r\delta\varphi'/\delta\varphi$.

y is traditionally evaluated at the star's surface for numerical applications. However, Eq. (5.52a) is not valid when $r = r_s$. Close to the star $\psi \neq 0$, and the solution to Eq. (5.27a) can only be approximated. After constructing a series solution that is accurate to better than 0.5% for even the largest values of ψ considered (see Sec. 5.4.1), we compared values from the exact solution (Eq. (5.52a)) evaluated at the surface to the values of k_2 calculated from the approximate solution. The tidal deformabilities agreed to better than 3% for all values of β explored. The percent difference between the approximate and the exact values is strongly dependent on the compactness, and increases with increasing compactness. In the cases where $\beta \leq -5$, the difference between the series and exact approaches remains less than the differences between scalar-tensor theory and general relativity for the entire parameter space. For the case when $\beta = -4.5$, the difference between approximate and exact solutions exceeds the difference between general relativity and scalar-tensor theory for $C \approx 0.25$, with the exact number depending on the EOS.

Figure 5.5.1 shows how the electric tidal Love numbers and tidal deformabilities differ in scalar-tensor theory and general relativity. Three different equations of state are considered: FPS, SLy, and MS1. These equations of state cover a wide range of stiffness and support a maximum mass of $> 1.8M_\odot$. FPS and SLy are both within constraints from analyses of GW170817 [2, 8]. However, as NICER results favor stiffer equations of state, we include MS1 [110, 191, 192, 251].

Fig. 5.5.1 plots the physical or Jordan frame values, which are related to their Einstein frame counterparts by Eqs. (5.109) and (5.110).

$\tilde{\lambda}_2$ and \tilde{k}_2 are plotted against the neutron star's compactness, in this case defined as the **TOV mass** over the Jordan frame radius.

It is clear that the spontaneous scalarization effect can lead to significant deviations from the general relativity tidal deformabilities. It is also clear that the deviations are strongly dependent on the objects compactness and the coupling constant. For the case where $\beta = -6$, the tidal Love number differs at most by $\sim 20 - 25\%$ and the tidal deformability differs by $\sim 350\%$. The peak occurs around $\tilde{C} \approx 0.29$, with the exact value varying by EOS. In the more conservative case where $\beta = -4.5$, this reduces to $\sim 5\%$ and $\sim 20\%$ for the tidal Love number and tidal deformability, respectively, and the peak occurs around $\tilde{C} \approx 0.23$.

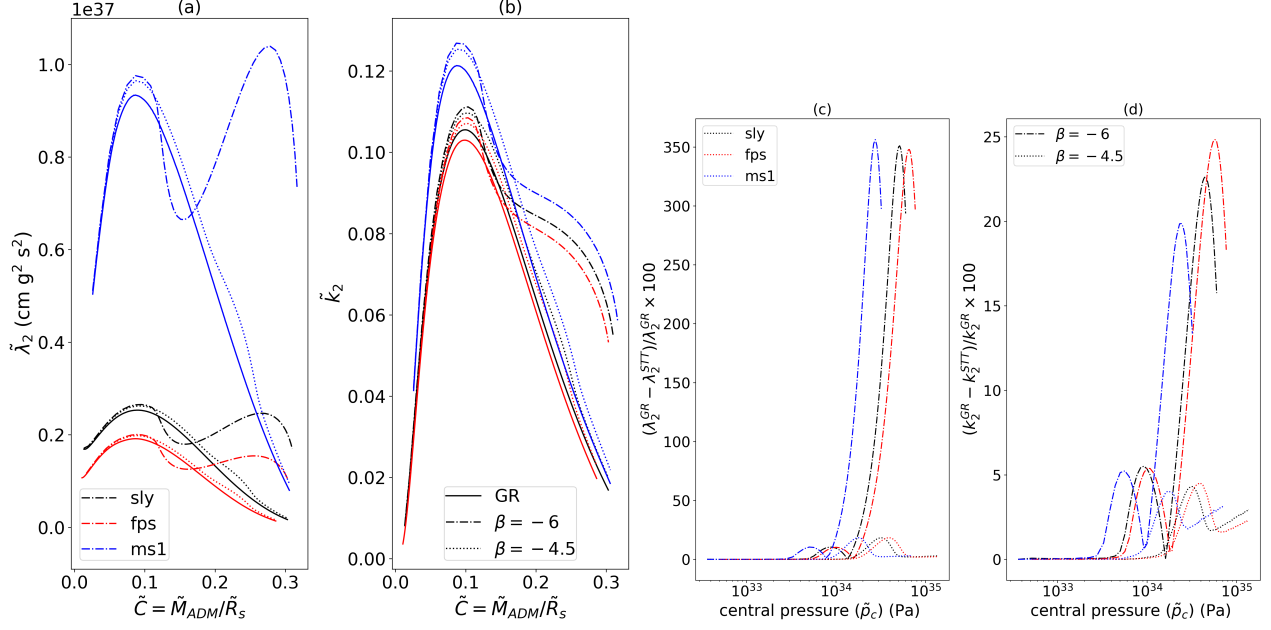


Figure 5.5.1: Panel (a) shows the $\ell = 2$ Jordan frame tidal deformability as a function of compactness, (b) shows the tidal Love number again as a function of compactness, (c) shows the percent difference between the tidal deformability in scalar-tensor theory and general relativity as a function of the pressure at the center of the star, and (d) shows the percent difference between the tidal Love numbers in scalar-tensor theory and general relativity as a function of the pressure at the center of the star. The value of the scalar field at infinity φ_∞ for all cases presented here is 10^{-3} . Three realistic nuclear equations of state (SLy, FPS, and MS1) are shown in black, blue, and red respectively. In both figures the results for $\beta = -6$ and $\beta = -4.5$ are shown with dash-dot and dotted linestyles. The purple line in (c) and (d) indicate the percent different between the analytical and approximate approaches to calculating the tidal Love number and tidal deformability.

The tidal deformability curve for scalar-tensor theories has a different shape than those in general relativity: a second peak appears. This peak is very small for the weak coupling case, but for more negative coupling constants, there second peak is clear. This second peak is caused by the spontaneous scalarization effect, which causes large deviations from general relativity in conditions with strong gravitational fields [187, 316].

As the difference between scalar-tensor theory and general relativity is much greater than the difference between the two methods of calculating k_ℓ , we consider Eq. (5.52a) evaluated at the surface of the star to be sufficiently accurate for gravitational wave parameter estimation with current detectors.

We show the Jordan frame $\ell = 2$ scalar tidal Love numbers and tidal deformabilities in Fig. 5.5.2. Scalar Tidal Love numbers will effect scalar gravitational wave emission [317]. We find that scalar tidal deformabilities are much smaller than electric tidal deformability, around two orders of magnitudes smaller even for strongly scalarized cases. Additionally, the scalar tidal deformabilites and tidal Love numbers depend strongly on the coupling constant, with strong scalarization leading to negative scalar tidal love numbers.

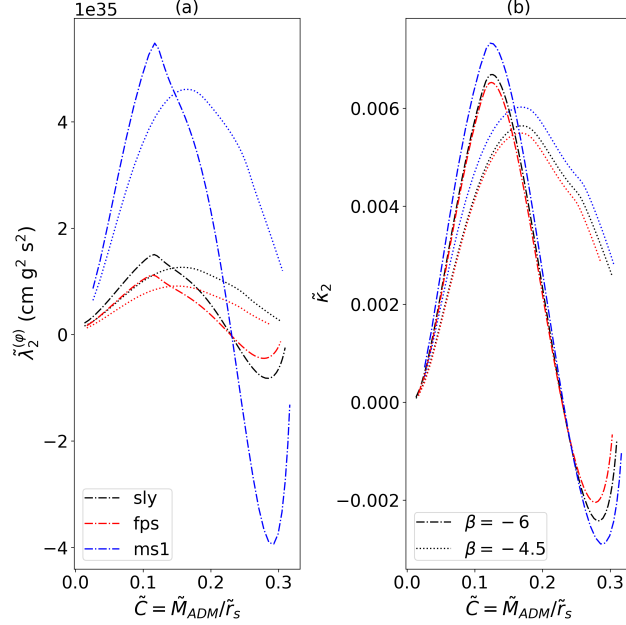


Figure 5.5.2: Panel (a) shows the $\ell = 2$ Jordan frame scalar tidal deformability as a function of compactness, (b) shows the scalar tidal Love number again as a function of compactness. The value of the scalar field at infinity φ_∞ for all cases presented here is 10^{-3} . In both figures the results for $\beta = -6$ and $\beta = 4.5$ are shown. Three realistic nuclear equations of state (SLy, FPS, and MS1) are shown in black, blue, and red respectively. In both figures the results for $\beta = -6$ and $\beta = -4.5$ are shown with dash-dot and dotted linestyles.

The $\ell = 3, 4$ tidal Love numbers are in Appendix 5.D.

5.5.2 Magnetic Love Numbers

This section presents the magnetic tidal Love number and the associated tidal deformabilities in scalar-tensor theory and compare them to the general relativity results.

The exact equations for the magnetic tidal Love numbers j_ℓ and tidal deformabilities σ_ℓ can be determined by substituting Eq. (5.48) into Eq. (5.49) and Eq. (5.50).

The explicit equation for the $\ell = 2$ or quadrupolar tidal Love number is

$$j_2 = (96C^5(2C - 1)(y - 3)) \times \quad (5.53)$$

$$\left[5(2C(12(y + 1)C^4 + 2(y - 3)C^3 + 2(y - 3)C^2 + 3(y - 3)C - 3y + 9) \right.$$

$$\left. + 3(2C - 1)(y - 3) \ln(1 - 2C)) \right]^{-1}$$

where $C = \mu/r_s$ is the Einstein frame compactness and $y = y^{odd}(r_s) = r_s \Psi'/\Psi$ is the logarithmic derivative at the surface.

Fig. 5.5.3 shows the Jordan frame $l = 2$ love numbers and tidal deformabilities and the difference between the general relativity and scalar-tensor tidal effects. The Jordan frame values are related to their Einstein frame counterparts by Eq. (5.101a) and Eq. (5.101b). The conformal transformations are derived in Appendix 5.C.

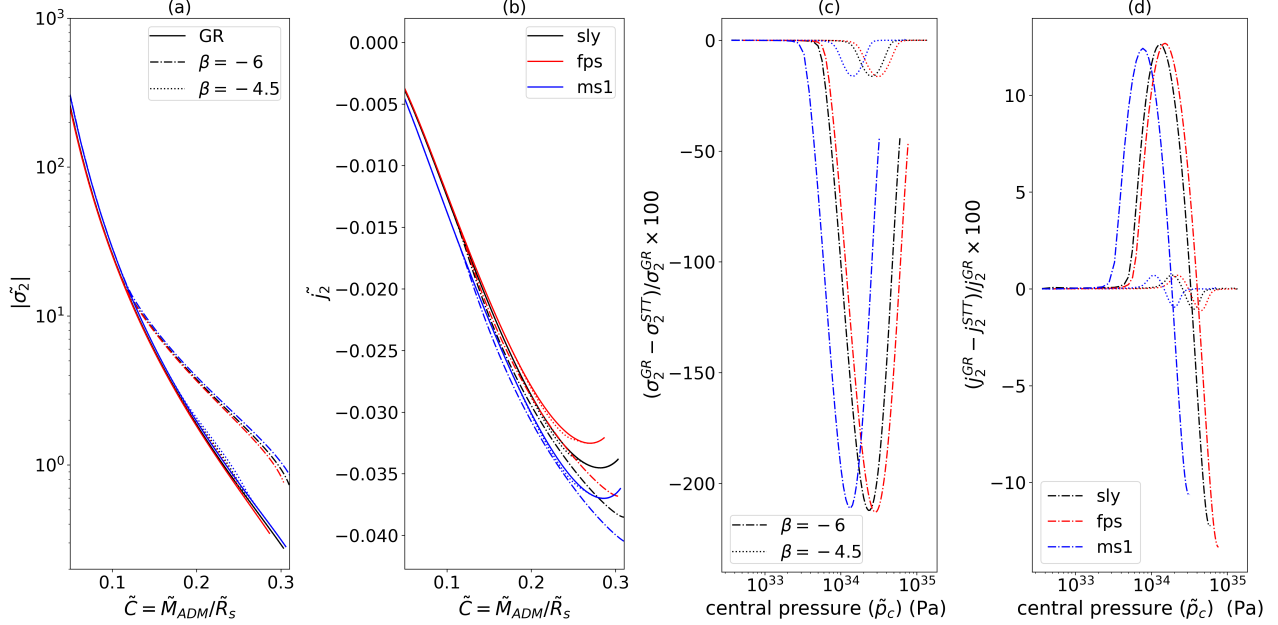


Figure 5.5.3: Panel (a) shows the absolute value of the magnetic $\ell = 2$ Jordan frame tidal deformability as a function of the neutron star compactness, (b) shows the tidal Love number again as a function of the neutron star compactness, (c) shows the percent difference between the percent difference between the tidal deformability in scalar-tensor theory and general relativity as a function of the pressure at the center of the star, and (d) shows the percent difference between the tidal Love numbers in scalar-tensor theory and general relativity as a function of the pressure at the center of the star. The value of the scalar field at infinity φ_∞ for all cases presented here is 10^{-3} . Three realistic nuclear equations of state (SLy, FPS, and MS1) are shown in black, blue, and red respectively. In both figures the results for $\beta = -6$ and $\beta = -4.5$ are shown with dash-dot and dotted linestyles.

It is clear that tidal Love numbers and tidal deformabilities differ between general relativity and scalar-tensor theory. For the optimistic case where $\beta = -6$, the tidal Love number has a maximum deviation of $\pm 12\%$ and the tidal deformability has a maximum deviation of $\sim 200\%$. This maximum deviation occurs at $\tilde{C} \approx 0.22$. In the more conservative case where $\beta = -4.5$, we find that the peak occurs at $\tilde{C} \approx 0.18$ and the deviation changes to $\sim 1\%$ and $\sim 15\%$ respectively.

In general relativity empirical relationships between the $\ell = 2$ dimensionless magnetic and electric tidal deformabilities have been found [318]. The dimensionless magnetic tidal deformability Σ_2 and the dimensionless electric tidal deformability Λ_2 have a quasi EOS independent relationship:

$$\ln(-\Sigma_2) = \sum_{n=0}^5 a_n (\ln \Lambda_2)^n. \quad (5.54)$$

We find that the scalar-tensor tidal deformabilities can be fit to a similar relationship, with the coefficients depending on the value of β . Regardless of equation of state, $R^2 > 0.999$ for all cases

There does not appear to be a similar relationship between the scalar deformability and the

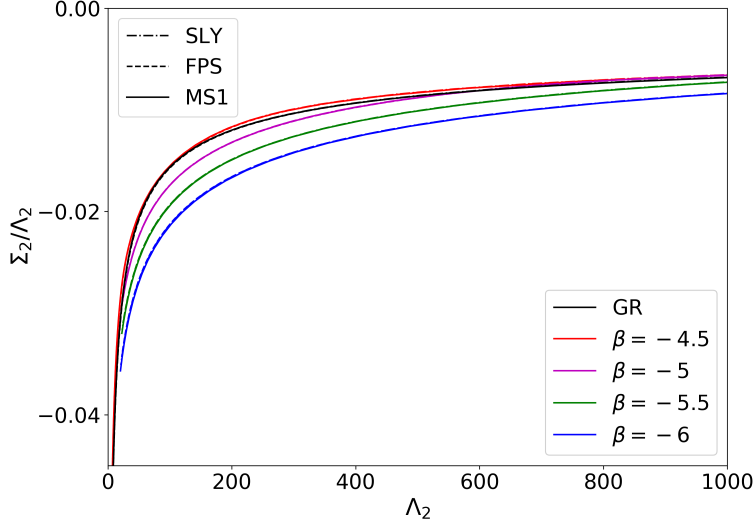


Figure 5.5.4: Quasiuniversal relations between the dimensionless magnetic tidal deformability Σ_2 and the dimensionless electric quadrupolar tidal deformability Λ_2 . Only the irrotational magnetic tidal deformability is shown in this figure. Three equations of state (SLY, FPS, and MS1) are shown in different linestyles, but they are indistinguishable. In both figures the results for general relativity, $\beta = -4.5$, and $\beta = -6$ are shown in black, red, and blue respectively.

Table 5.5.1: Fit Coefficients

Theory	a_0	a_1	a_2	a_3	a_4	a_5
GR	-1.99	4.51×10^{-1}	1.60×10^{-2}	6.51×10^{-4}	-1.07×10^{-4}	3.74×10^{-6}
$\beta = -4.5$	1.25	-3.46	1.76	-3.65×10^{-1}	3.66×10^{-2}	-1.41×10^{-3}
$\beta = -5$	-2.82	1.05	-2.10×10^{-1}	6.26×10^{-2}	-9.18×10^{-3}	4.93×10^{-4}
$\beta = -5.5$	-2.88	1.34	-3.53×10^{-1}	8.90×10^{-2}	-1.06×10^{-2}	4.64×10^{-4}
$\beta = -6$	-3.42	1.72	-4.11×10^{-1}	8.28×10^{-2}	-8.35×10^{-3}	3.20×10^{-4}

electric tidal deformability. The scalar tidal deformability depends very strongly on β and $\Lambda^{(\varphi)}/\Lambda$ can take on very different shapes. It may be possible to construct a relationship between the scalar deformability and the electric tidal deformability for a specific β but there is no general relationship.

5.6 Discussion

This work presents the electric, magnetic, and scalar tidal Love numbers and tidal deformabilities. We find that the electric and magnetic tidal effects may differ significantly from their general relativistic counterparts (~ 350 and ~ 200 for electric and magnetic respectively). These large deviations occur at larger compactnesses (~ 2) and are caused by the spontaneous scalarization effect. The exact deviation and the compactness where this maximum deviation occurs are EOS dependent.

This paper approaches tidal effects through the lens of gravitational wave parameter estimation. The mass-radius-tidal deformability relationships explored in this paper can be applied directly to

GW parameter estimation of GWs from binary neutron star and neutron star-black hole systems. The $\ell = 2$ electric tidal deformability is the leading order tidal effect for gravitational waves. Given that this number can vary by ~ 350 between scalar-tensor theory and general relativity, it may be necessary to take modified tidal effects into account when doing tests of general relativity using gravitational waves from systems with neutron stars.

We present an analytical expression for the magnetic tidal Love numbers in scalar-tensor theory for the first time. The results establish that the magnetic Love numbers are only implicitly dependent on the scalar field and have an analytical solution. This is in agreement with Ref. [306], which shows that the time-dependent perturbation equation is only implicitly dependent on the scalar field. However this was discussed only in the context of perturbations and not of tidal Love numbers.

The magnetic Love numbers in this paper can be compared to their $f(R)$ counterparts because $f(R)$ theory and scalar-tensor theory are mathematically similar. When calculating tidal Love numbers a difference arises in part due to the behavior of the scalar field at infinity. In $f(R)$ theory, the scalar field and its derivative go to zero at infinity, and the tidal deformability can be evaluated at some distance away from the neutron star where both the scalar field and its derivative are sufficiently small. This is different from the scalar-tensor theories considered in this paper where the scalar field asymptotically approaches a constant. Additionally, the coupling function differs between theories with $A(\varphi) \propto e^{\alpha\varphi}$ in $f(R)$. Despite this, the perturbation equations inside the star should agree when the correct substitutions for $A(\varphi)$ and $\alpha(\varphi)$ have been made because they are mathematically similar. However, our perturbation equation differs from Eq. (23) in [121]. Comparing the tidal Love numbers themselves, shown in Fig. 5.5.3, with the results from [121], it is clear that the qualitative features seem to agree, with the deviation from general relativity increasing with compactness. However, the difference between general relativity and scalar-tensor theory are smaller than those between general relativity and $f(R)$, at least for physically allowed values of β and φ_∞ .

This paper also includes the even parity tidal Love numbers and tidal deformabilities. The $\ell = 2$ electric tidal Love numbers in scalar-tensor theory were initially presented in [124] in the context of the so-called ‘‘I-Love-Q’’ relations. The methods in this paper differ significantly from those in Ref. [124].

There are both metric and scalar perturbations in the even parity case, and the relationship between them is not trivial. In the Einstein Frame, the metric tensor and the scalar field are not coupled. As a change in the metric should not affect the scalar-field and vice-versa, it is important to construct two independent first-order perturbation equations. One for the metric perturbation and one for the scalar. This differs from the approach in [124], where the two even parity equations are coupled. It is unsurprising, then, that Eqs. (5.24) and (5.25) are different from the equations presented in [124]. The resulting tidal Love numbers must also differ. The definition for the scalar tidal Love number in this paper also differs from that in [124]. [124] does not include a source term in their definition of the scalar tidal Love number and we do. This is because they are considering the perturbation in the scalar field produced by a change in the metric rather than by a change in the scalar field. This paper also includes the $\ell = 3, 4$ even parity Love numbers and tidal deformabilities in Sec. 5.D, which have not been presented before.

The results demonstrate that tidal Love numbers and tidal deformabilities can differ significantly between scalar-tensor theory and general relativity. This is consistent with other results in the literature, which show that tidal Love numbers in $f(R)$ theory and scalar-Gauss-Bonnet

gravity [121, 122] also differ significantly from their general relativistic counterparts. As gravitational waves emitted by neutron stars depend on the tidal deformability, it is essential to take the changes in the mass, radius, and tidal deformability into account when studying gravitational waves from neutron stars in theories beyond general relativity. The deviations from general relativity in the gravitational waves are smaller than or similar to the uncertainty in the tidal deformability measurement. By taking the modified tidal deformability into account, the small deviations from general relativity in the waveform can be more accurately determined.

Appendix

5.A Numerical Methods

This section lays out the numerical techniques used to calculate the mass, radius, and tidal deformability relations shown in Sec. 5.5, Figs. 5.5.1 to 5.5.3

First, the structure equations presented in Sec. 5.2 are solved numerically using Scipy’s `solve_ivp` with the ‘DOP853’ option, which is an eighth order Runge-Kutta method. To validate the results, the ‘DOP853’ results are compared to those from the older `odeint` solver and `solve_ivp`’s ‘RK45’ option, which is a Runge-Kutta solver that uses a fifth order accurate formula but calculates the accuracy using the fourth order method [319]. Next, the perturbation equations are added to the TOV solver, and the tidal deformabilities and Love numbers are calculated from Eqs. (5.49), (5.52a) and (5.52b).

As discussed in Sec. 5.2, in scalar-tensor theories, the structure equations can be expressed either in the Jordan Frame or the Einstein Frame. The code takes advantage of the relative simplicity of the Einstein frame structure equations to numerically construct the neutron star model. The Jordan frame quantities are calculated at the end of the code, using the Einstein frame values and the conformal transformations in Appendix 5.C.

5.A.1 Background Configuration

For numerical integration, the equations need to be posed as first order ordinary differential equations of the form

$$y'_i(x) = f(x, y_i, y_i) . \quad (5.55)$$

where $x = r$ is the independent variable and $y = M, \nu, \varphi, \psi$, and p are the dependent variables.

It is important to consider that the values of r, M, ν, ψ , and p may vary greatly in magnitude, which can lead to numerical errors and instabilities. Codes often use scale factors to mitigate the numerical errors. In [320] it is claimed that by choosing $\rho = \rho_0 \hat{\rho}$, $p = \rho_0 \hat{p}$, $M = r_0 \hat{M}$, and $r = r_0 \hat{r}$ the form of the modified TOV equations remains unchanged so long as $\rho_0 r_0^2 = 1$. However, this is not the case.

This code uses a new set of scale factors. Specifically, we scale only $\tilde{\rho}$ and \tilde{p} and not M or r . With $\rho = \tilde{\rho}_0 \hat{\rho}$ and $p = \tilde{p}_0 \hat{p}$, we are able to lay out the structure equations used in the code:

$$\frac{d\mu}{dr} = 4\pi G_* r^2 A^4(\varphi) \tilde{\rho}_0 \hat{\rho} + \frac{1}{2} r (r - 2\mu) \psi^2 \quad (5.56a)$$

$$\frac{d\nu}{dr} = 8\pi G_* \frac{r^2 A^4(\varphi) \tilde{p}_0 \hat{p}}{r - 2\mu} + r\psi^2 + \frac{2\mu}{r(r - 2\mu)} \quad (5.56b)$$

$$\frac{d\varphi}{dr} = \psi \quad (5.56c)$$

$$\frac{d\psi}{dr} = 4\pi G_* \frac{r A^4(\varphi)}{r - 2\mu} [\alpha(\varphi)(\tilde{\rho}_0 \hat{\rho} - 3\tilde{p}_0 \hat{p}) + r\psi(\tilde{\rho}_0 \hat{\rho} - \tilde{p}_0 \hat{p})] - \frac{2(r - \mu)}{r(r - 2\mu)} \psi \quad (5.56d)$$

$$\frac{d\hat{p}}{dr} = -\frac{1}{\tilde{p}_0} (\tilde{\rho}_0 \hat{\rho} + \tilde{p}_0 \hat{p}) \left[4\pi G_* \frac{r^2 A^4(\varphi) \tilde{p}_0 \hat{p}}{r - 2\mu} + \frac{1}{2} r\psi^2 + \frac{\mu}{r(r - 2\mu)} + \alpha(\varphi)\psi \right] \quad (5.56e)$$

In order to solve these equations, the numerical solver requires initial conditions. In this case, the initial conditions are defined near the center of the star ($r \approx 0$). Due to numerical instabilities at $r = 0$, the code starts at some small, but finite radius (e.g. $r_0 = 10^{-5}$ m). We used a convergence test to ensure that r_0 was sufficiently small and would not effect the final results.

We know that

$$\mu(r = 0) = 0 \quad (5.57a)$$

$$\nu(r = 0) = 0 \quad (5.57b)$$

$$\psi(r = 0) = 0 \quad (5.57c)$$

and the initial pressure p varies. However, the scalar field is defined at infinity $\varphi(\infty) = \varphi_0$ and not at $r = 0$. The shooting method is employed to convert the boundary value problem into a initial value problem.

The process begins with an initial guess for $\varphi(r = 0) = \varphi_c$. The system of equations is then integrated outward to the star's surface, which is defined to be where the pressure vanishes ($\tilde{p} = 0$). The code then calculates the value of the scalar field at infinity φ_∞ using the relationship between φ_s , the value of φ at the surface, and φ_∞ . The connection between φ_s and φ_∞ can be found by solving the scalar wave equation outside of the star and matching the interior and exterior solutions:

$$\varphi_\infty = \varphi_s + \frac{2\psi_s}{\sqrt{\nu_s'^2 + 4\psi_s^2}} \operatorname{arctanh} \left(\frac{\sqrt{\nu_s'^2 + 4\psi_s^2}}{\nu_s' + 2/r_s} \right), \quad (5.58)$$

where subscript s indicates values evaluated at the surface and the prime ($'$) denotes derivative with respect to r .

The code then compares the calculated value of the scalar field at infinity φ_∞ to the actual value of the scalar field at infinity φ_0 . The parameter $\Delta\varphi = \varphi_\infty - \varphi_0$ is calculated, and if $\Delta\varphi$ is greater than some tolerance (here $\Delta\varphi \leq 10^{-5}$), then the value of φ_c is updated and the process is repeated. The process is repeated until the φ_∞ agrees with φ_0 within some tolerance. For a more in depth discussion on the shooting method see, for instance, [321].

In order to solve the TOV equations, it is necessary to provide an EOS $\tilde{p}(\tilde{\rho})$ which relates the Jordan frame pressure and density. In this work, we consider a variety of EOSs. All EOSs are defined in the physical frame. In order to include realistic EOSs, our code takes in EOS data from external data files. The code obtains the density at any point by taking the given pressure and the data from the file and interpolating.

The Sly [322], FPS [323], and MS1 [324] EOS are considered because they are commonly used in literature and useful for comparison with previous results [85, 325].

5.A.2 Tidal Deformability

The definitions of the tidal deformabilities were derived in Sec. 5.5, now we focus on calculating them. First, we must integrate the perturbation equations for H , Ψ , and $\delta\varphi$ along with the scalar-tensor TOV equations. The initial value problem solver requires that we recast the second order differential equations Eqs. (5.24), (5.26) and (5.44) into first order differential equations. There are two ways to do this. One, any second order differential equation can be recast as a system of two first order differential equations. Two, a single first order differential equation for the logarithmic derivative (e.g. $y = rH'/H$) can be obtained from the original equation. Both approaches are valid. As the definitions of the tidal deformabilities and tidal love numbers Eqs. (5.49), (5.52a) and (5.52b) depend on the logarithmic derivative, we recast Eqs. (5.24), (5.26) and (5.44) into first order differential equations for the logarithmic derivative. These equations now have form:

$$\frac{dy(r)}{dr} = -\frac{1}{r} \left(y^2(r) + y(r)F(r) + r^2Q(r) \right) \quad (5.59)$$

For the magnetic perturbations

$$F(r) = \left(1 - \frac{2\mu}{r} \right)^{-1} \left(\frac{2\mu}{r} + 4\pi A^4(\varphi)r^2(\tilde{p} - \tilde{\rho}) \right) - 1 \quad (5.60a)$$

$$r^2Q(r) = \left(1 - \frac{2\mu}{r} \right)^{-1} \left(\frac{\ell(\ell+1)\mu}{r} + 4\pi A^4(\varphi)r^2(\tilde{p} - \tilde{\rho}) - 6 \right) \quad (5.60b)$$

For even parity tensor perturbations

$$F(r) = \left(1 - \frac{2\mu}{r} \right)^{-1} (1 + 4\pi A^4(\varphi)r^2(\tilde{p} - \tilde{\rho})) \quad (5.61a)$$

$$r^2Q(r) = \left(1 - \frac{2\mu}{r} \right)^{-1} \left(-\ell(\ell+1) + \frac{4\pi A^4(\varphi)r^2(\tilde{p} + \tilde{\rho})}{d\rho/dp} + 4\pi A^4(\varphi)r^2(9\tilde{p} + 5\tilde{\rho}) \right) - \left(\left(1 - \frac{2\mu}{r} \right)^{-1} (2\mu + 8\pi A^4(\varphi)r^3\tilde{p}) + r^3\psi^2 \right)^2 \quad (5.61b)$$

For the scalar perturbations

$$F(r) = \left(1 - \frac{2\mu}{r} \right)^{-1} (1 + 4\pi A^4(\varphi)r^2(\tilde{p} - \tilde{\rho})) \quad (5.62a)$$

$$r^2Q(r) = \left(1 - \frac{2\mu}{r} \right)^{-1} (4\pi A^4(\varphi)r^2(1 + 4\varphi\alpha(\varphi))\beta(3\tilde{p} - \tilde{\rho}) - \ell(\ell+1)) \quad (5.62b)$$

The initial conditions are

$$y_{even}(r=0) = 2 \quad (5.63a)$$

$$y_{scalar}(r=0) = 2 \quad (5.63b)$$

$$y_{odd}(r=0) = 3 \quad (5.63c)$$

The values of y_{odd} , y_{even} , and y_{scalar} at the surface are then determined, and the Love numbers can be calculated. Lastly, the Jordan frame values are calculated using then conformal transformation derived in appendix 5.C.

5.B Perturbation Equations

5.B.1 Perturbed Energy-Momentum Tensor

In this section of the appendix, the exact forms of the fluid stress-energy tensor perturbations are given. Subscripts are used to denote derivatives.

The pressure and density perturbations are defined in the physical frame to be $\delta\tilde{p}(r)Y_{\ell m}$ and $\delta\tilde{\rho}(r)Y_{\ell m}$. The fluid velocity and its perturbations are also written in the Jordan frame. In the case of static tides, the fluid velocity perturbation is generally a function only of the metric perturbations and does not have explicit velocity perturbations. Furthermore, as the tides are static, the total perturbed four velocity has the form:

$$\hat{u}^\mu = u^\mu + \delta u^\mu = (\hat{u}^0, 0, 0, 0) \quad (5.64)$$

where the tilde has been dropped for readability. The time component of \hat{u}^μ differs from u^μ because the perturbed metric differs from the unperturbed metric.

The even parity velocity perturbations are

$$\delta\tilde{u}^t = -\frac{1}{2A}e^{-\nu/2}H_0Y_{\ell m} \quad (5.65a)$$

$$\delta\tilde{u}^i = 0, \quad i = 1, 2, 3 \quad (5.65b)$$

While time independent perturbations do not depend explicitly on fluid velocity perturbations, the time-dependent equations do. The two methods presented in Sec. 5.4.2 differ in the way that the fluid velocity term $U(r)$ is treated. In both cases, the explicit dependence vanishes, but their results differ because of how they treat this term. The time-dependent odd parity velocity perturbations are

$$\delta\tilde{u}^\phi = \frac{e^{\nu/2}U(r)e^{-i\omega t}}{4\pi A^4(\varphi)(\tilde{p} + \tilde{\rho})} \csc\theta\partial_\theta Y_{\ell m} \quad (5.66a)$$

$$\delta\tilde{u}^\nu = 0, \quad \nu = 0, 1, 2 \quad (5.66b)$$

The components of \hat{u}_μ are calculated by lowering the contravariant four-velocity \hat{u}^μ with the total metric $g_{\mu\nu} = (g_{\mu\nu}^0 + h_{\mu\nu})$.

Additionally the perturbed matter stress-energy tensor depends on the the Eulerian fluid perturbations: $\delta\tilde{\rho}(r)Y_{\ell m}$ and $\delta\tilde{p}(r)Y_{\ell m}$ respectively. We assume a barotropic EOS, and so

$$\delta\tilde{\rho} = \frac{\partial\tilde{\rho}}{\partial\tilde{p}}\delta\tilde{p}. \quad (5.67)$$

Using these definitions and assuming that by symmetry $\partial_\phi Y_{\ell m} = 0$, the non-zero components of the perturbed matter stress-energy tensor are as follows:

$$\delta T_t^t = - (4A^3(\varphi)\tilde{\rho}\delta A + A^4(\varphi)\delta\tilde{\rho}) Y_{\ell m} \quad (5.68)$$

$$\delta T_\phi^t = - \left(A^4(\varphi)\tilde{\rho}h_0 + \frac{A(\varphi)}{4\pi}e^\nu U \right) \sin\theta\partial_\theta Y_\ell \quad (5.69)$$

$$\delta T_r^r = (4A^3(\varphi)\tilde{\rho}\delta A + A^4(\varphi)\delta\tilde{\rho}) Y_{\ell m} \quad (5.70)$$

$$\delta T_\phi^r = A^4(\varphi)\tilde{\rho} h_1 \sin\theta \partial_\theta Y_{\ell m} \quad (5.71)$$

$$\delta T_\theta^\theta = (4A^3(\varphi)\tilde{\rho}\delta A + A^4(\varphi)\delta\tilde{\rho}) Y_{\ell m} \quad (5.72)$$

$$\delta T_t^\phi = - \left(A^4(\varphi)\tilde{\rho}h_0 + \frac{A(\varphi)}{4\pi} e^\nu U \right) \sin\theta \partial_\theta Y_\ell \quad (5.73)$$

$$\delta T_r^\phi = A^4(\varphi)\tilde{\rho} h_1 \sin\theta \partial_\theta Y_{\ell m} \quad (5.74)$$

$$\delta T_\phi^\phi = (4A^3(\varphi)\tilde{\rho}\delta A + A^4(\varphi)\delta\tilde{\rho}) Y_{\ell m} \quad (5.75)$$

The nonzero components of the perturbed energy momentum tensor for the scalar field $T_{\mu\nu}^{(\varphi)}$ have the following form

$$\delta T_{00}^{(\varphi)} = -2e^{\nu-\lambda}[H\psi^2 - \psi\delta\varphi']Y_{\ell m} \quad (5.76)$$

$$\delta T_{03}^{(\varphi)} = -e^\lambda\psi^2 h_0 \sin\theta \partial_\theta Y_{\ell m} \quad (5.77)$$

$$\delta T_{11}^{(\varphi)} = 2\psi\delta\varphi'Y_{\ell m} \quad (5.78)$$

$$\delta T_{12}^{(\varphi)} = 2\psi\delta\varphi\partial_\theta Y_{\ell m} \quad (5.79)$$

$$\delta T_{13}^{(\varphi)} = -e^{-\lambda}\psi^2 h_1 \sin\theta \partial_\theta Y_{\ell m} \quad (5.80)$$

$$\delta T_{22}^{(\varphi)} = r^2 e^{-\lambda}[(H - K)\psi^2 - 2\psi\delta\varphi']Y_{\ell m} \quad (5.81)$$

$$\delta T_{33}^{(\varphi)} = r^2 e^{-\lambda}[(H - K)\psi^2 - 2\psi\delta\varphi']\sin^2\theta Y_{\ell m} \quad (5.82)$$

5.B.2 Equations for Even Parity

The following equations are derived from the even parity metric perturbation equations. The first six come from perturbing the Einstein equation: Eq. (5.5).

- Eq 5.83 is $\delta G_2^2 - \delta G_3^3 = 8\pi G_*(\delta T_2^2 - \delta T_3^3) + (\delta T_2^{(\varphi)2} - \delta T_3^{(\varphi)3})$
- Eq 5.84 is $\delta G_1^2 = 8\pi G_*\delta T_1^2 + \delta T_1^{(\varphi)2}$
- Eq 5.85 is $\partial_r \left(\delta G_1^2 = 8\pi G_*\delta T_1^2 + \delta T_1^{(\varphi)2} \right)$
- Eq 5.86 is $\delta G_1^1 = 8\pi G_*\delta T_1^1 + \delta T_1^{(\varphi)1}$
- Eq 5.87 is $\delta G_2^2 + \delta G_3^3 = 8\pi G_*(\delta T_2^2 + \delta T_3^3) + (\delta T_2^{(\varphi)2} + \delta T_3^{(\varphi)3})$
- Eq 5.88 is $\delta G_0^0 - \delta G_1^1 = 8\pi G_*(\delta T_0^0 - \delta T_1^1) + (\delta T_0^{(\varphi)0} - \delta T_1^{(\varphi)1})$.

$$H_0 = H_2 \quad (5.83)$$

$$K' = H_{0,r} + \nu' H_0 - 4\psi\delta\varphi \quad (5.84)$$

$$K'' = H_0'' + \nu'' H_0 + \nu' H_{0,r} - 4\psi'\delta\varphi - 4\psi\delta\varphi' \quad (5.85)$$

$$(l(l+1) + 2)K = (l(l+1) - 2e^{-\lambda}(1 + r\nu' - r^2\psi^2)) H_0 - 2e^{-\lambda}rH_{0r} \\ + e^{-\lambda}r(2 + r\nu')K' - 16\pi A^4(\varphi)r^2\delta\tilde{p} \quad (5.86)$$

$$16\pi A^4(\varphi)r^2\delta\tilde{p} = e^{-\lambda} \left(\frac{-4 + r\lambda' - 3r\nu'}{2r} \right) H_{0r} + e^{-\lambda} \left(\frac{4 - r\lambda' + r\nu'}{2r} \right) K' \\ - e^{-\lambda}H_{0rr} + e^{-\lambda}K'' - e^{-\lambda} \left(\frac{4r\psi^2 - (\lambda' - \nu')(2 + r\nu') + 2r\nu''}{2r} \right) \quad (5.87)$$

$$e^{-\lambda}K'' - e^{-\lambda} \left(\frac{-4 + r(\lambda' + \nu')}{2r} \right) K' + \left(\frac{e^{-\lambda}r(\lambda' + \nu' - 2r\psi^2) - l(l+1)}{r^2} \right) H_0 \\ = -8\pi A^4(\varphi) \left(1 + \frac{d\rho}{dp} \right) \delta p \quad (5.88)$$

The equation for the scalar perturbation $\delta\varphi$ is derived by perturbing scalar wave equation Eq. (5.89).

$$\delta\varphi'' = \left(\frac{-4 + r\lambda' - r\nu'}{2r} \right) \delta\varphi' + e^\lambda \frac{l(l+1)}{r^2} \delta\varphi + 16\pi A^3(\varphi)e^\lambda \alpha(\tilde{\rho} - 3\tilde{p})\delta A + 4\pi A^4(\varphi)e^\lambda(\tilde{\rho} - 3\tilde{p})\delta\alpha \quad (5.89)$$

5.B.3 Equations for Odd Parity

The static and irrotational methods used in this paper differ in their treatment of time derivatives. Even though the tidal Love numbers themselves are time-independent, we present the time-dependent equations in this section.

Combining the $\delta G_{\mu\nu}$ with the matter stress-energy tensor and scalar stress-energy tensor terms results in the following three equations:

- Equation 5.90 is $\delta G_{t\phi} = 8\pi\delta T_{t\phi} + T_{t\phi}^{(\varphi)}$
- Equation 5.91 is $\delta G_{r\phi} = 8\pi\delta T_{r\phi} + T_{r\phi}^{(\varphi)}$
- Equation 5.92 is $\delta G_{\theta\phi} = 8\pi\delta T_{\theta\phi} + T_{\theta\phi}^{(\varphi)}$

$$e^{-\lambda}(h_{0rr} - h_{1rt}) - \frac{2e^{-\lambda}}{r}h_{1t} + \left[4\pi r A^4(\varphi)(p + \rho) + e^{-\lambda}r\psi^2\right](h_{1t} - h_{0r}) \quad (5.90)$$

$$- \frac{1}{r^3} \left[l(l+1)r - 4m + 8\pi A^4(\varphi)(p + \rho)r^3 - 2r^3 e^{-\lambda}\psi^2 \right] h_0 - 4A(\varphi)e^\nu U = 0$$

$$e^{-\nu}(h_{0rt} - h_{1tt}) - 2\frac{e^{-\nu}}{r}h_{0t} - \left[\frac{l(l+1) - 2}{r^2} \right] h_1 = 0 \quad (5.91)$$

$$e^{-\nu}h_{0t} - \frac{1}{r^2} \left[2m - 4\pi r^3 A^4(\varphi)(\rho - p) \right] h_1 - e^{-\lambda}h_{1r} = 0 \quad (5.92)$$

5.C Conformal Transformations

The tidal Love numbers in this paper were derived in the Einstein frame; however, as experiments measure Jordan frame quantities, it is necessary to obtain the Jordan frame quantities using a conformal transformation. We assume here that the Jordan frame metric $\tilde{g}_{\mu\nu}$ is related to the Einstein frame metric $g_{\mu\nu}$ by a conformal factor $A(\varphi)$:

$$\tilde{g}_{\mu\nu} = A^2(\varphi)g_{\mu\nu} , \quad (5.93)$$

where $A(\varphi) = e^{\frac{1}{2}\beta\varphi^2}$. By construction, the Einstein frame metric is asymptotically flat. This implies that

$$\tilde{g}_{\mu\nu} \rightarrow A^2(\varphi)\eta_{\mu\nu} . \quad (5.94)$$

where $\eta_{\mu\nu} = \text{diag}(-1, 1, 1, 1)$ is the Minkowski metric. As the Jordan frame metric is also asymptotically flat or Minkowskian, the \tilde{r} and \tilde{t} components must be related to their Einstein frame counterparts in the following way: $\tilde{r} = A(\varphi)r$ and $\tilde{t} = A(\varphi)t$. Furthermore, the effective gravitational constant \tilde{G} is no longer a constant in the Jordan frame and is not necessarily equal to the bare gravitational constant G which appears in the Einstein frame equations. The relationship between the two is known [182]:

$$\tilde{G} = e^{\beta\varphi_\infty^2} \left[G + \frac{\beta\varphi_\infty^2}{4\pi} \right] . \quad (5.95)$$

We need the conformal transformations for the perturbations between the two frames to transform the tidal Love numbers and tidal deformabilities from the Einstein frame to the Jordan frame. These are presented in Sec. 5.3.

5.C.1 Magnetic

The odd parity perturbation in the Einstein frame h_0 is related to the odd parity perturbation in the Jordan frame by

$$\tilde{h}_0 = A^2(\varphi)h_0 . \quad (5.96)$$

From the definition of Ψ (Eq. (5.41)), it is straightforward to show that it transforms as

$$\tilde{\Psi}(\tilde{r}) = A^2(\varphi)\Psi(r) . \quad (5.97)$$

To properly define the magnetic tidal deformability in the Jordan frame, $\tilde{\Psi}$ must have the same leading order behavior as Ψ i.e.

$$\tilde{\Psi}^{ext}(\tilde{R}) = \tilde{b}_p \tilde{R}^{\ell+1} + \tilde{b}_q \tilde{R}^{-\ell} \quad (5.98)$$

where $\tilde{R} = \tilde{r}/\tilde{\mu} = A^2(\varphi)r/\mu$. Eqs. (5.97) and (5.98), can be used to relate $\tilde{b}_{q,p}$ to their Einstein frame counterparts:

$$\tilde{b}_p = A^{-4}(\varphi)b_p \quad \& \quad \tilde{b}_q = A^6(\varphi)b_q . \quad (5.99)$$

The Jordan frame tidal Love number \tilde{j}_ℓ is defined to be

$$\tilde{j}_\ell = \tilde{C}^{2\ell+1} \frac{\tilde{b}_q}{\tilde{b}_p} . \quad (5.100)$$

From Eqs. (5.99) and (5.100) it follows that

$$\tilde{j}_\ell = j_\ell \quad (5.101a)$$

$$\tilde{\sigma}_\ell = (A^2(\varphi_\infty))^{2\ell+1} \sigma_\ell \quad (5.101b)$$

5.C.2 Electric

To transform the scalar Love number between frames, it is only necessary to know the relationship between the scalar field in the Einstein (φ) and Jordan frames (ϕ)

$$\phi = e^{-\beta\varphi^2} . \quad (5.102)$$

By perturbing this equation, the relationship between the Jordan frame tidal deformability λ_ϕ and it's Einstein frame counterpart λ_φ can be derived:

$$\lambda_\phi = (A^2(\varphi_\infty))^{2\ell+1} \lambda_\varphi . \quad (5.103)$$

The tidal Love numbers are related by

$$\kappa_\phi = \kappa_\varphi . \quad (5.104)$$

In the case of the even parity tensor tidal Love number, the transformation between frames is more complex due to mixing of the scalar and tensor perturbations. The relationship between the even parity metric perturbations in the two frames is constrained by the choice of gauge. Taking equation relating the time-time component of the metric perturbation in the Jordan frame \tilde{H} to the Einstein frame metric perturbation H and the Einstein frame scalar perturbation $\delta\varphi$ from Sec. 5.3, we have

$$\tilde{H} = A^2(\varphi)H - 2A(\varphi)\delta A . \quad (5.105)$$

In the spontaneous scalarization case, this becomes

$$\tilde{H} = A^2(\varphi)(H - 2\beta\varphi\delta\varphi) . \quad (5.106)$$

Combining this with the leading order behavior of the perturbations, which are known to be

$$\begin{aligned} H &= -\mathcal{E}_{ij}r^2 + \mathcal{O}(r) + \frac{3Q_{ij}}{r^3} + \mathcal{O}(r^{-4}) \\ &= -\mathcal{E}_{ij}r^2 + \mathcal{O}(r) - \frac{3\lambda\mathcal{E}_{ij}}{r^3} + \mathcal{O}(r^{-4}) \end{aligned} \quad (5.107)$$

it is possible to define the Jordan frame tidal deformability $\tilde{\lambda}_J$:

$$\tilde{\lambda}_J = \frac{A^{2\ell+1}(\varphi_\infty)(\lambda_E\mathcal{E}_{ij}^E - 2\beta\varphi_\infty\lambda_\varphi\mathcal{E}_{ij}^\varphi)}{\mathcal{E}_{ij}^E - 2\beta\varphi_\infty\mathcal{E}_{ij}^\varphi} \quad (5.108)$$

where E denotes Einstein frame tensor quantities and φ denotes Einstein frame scalar quantities. From this equation, it is clear that the Jordan frame tidal deformability is related linearly to the even parity scalar and tensor tidal deformabilities. The exact relationship is

$$\tilde{\lambda}_J = A^{2\ell+1}(\varphi_\infty)(\lambda_E + \lambda^{(\varphi)}) . \quad (5.109)$$

Finally, we determine the tidal Love numbers to have the following relationship

$$\tilde{k}_\ell = k_\ell + \kappa_\ell \quad (5.110)$$

5.D Higher Order Love numbers

Using Eq. (5.28a), Eq. (5.28b), and the methods presented in Sec. 5.4.1, we determine the equations for the $\ell = 3, 4$ tidal Love numbers and tidal deformabilities at large r .

The $\ell = 3, 4$ even parity tensor tidal Love numbers are defined as

$$\begin{aligned} k_3 &= 8(1 - 2C)^2 C^7 (-3 - 3C(-2 + y) + 2C^2(-1 + y) + y) \times \\ &\quad \left[7(2C(15(-3 + y) + 4C^5(1 + y) - 45C(-5 + 2y) - 20C^3(-9 + 7y) + 2C^4(-2 + 9y) + \right. \\ &\quad \left. 5C^2(-72 + 37y)) + 15(1 - 2C)^2(-3 - 3C(-2 + y) + 2C^2(-1 + y) + y) \ln(1 - 2C) \right]^{-1} \end{aligned} \quad (5.111)$$

$$\begin{aligned} k_4 &= 32(1 - 2C)^2 C^9 (-7(-4 + y) + 28C(-3 + y) - 34C^2(-2 + y) \\ &\quad + 12C^3(-1 + y)) \times \left[147(2C(C^2(5360 - 1910y) + C^4(1284 - 996y) - 105(-4 + y) \right. \\ &\quad + 8C^6(1 + y) + 105C(-24 + 7y) + 40C^3(-116 + 55y) + C^5(-8 + 68y)) \\ &\quad \left. + 15(1 - 2C)^2(-7(-4 + y) + 28C(-3 + y) - 34C^2(-2 + y) + 12C^3(-1 + y)) \ln(1 - 2C) \right]^{-1} \end{aligned} \quad (5.112)$$

and the scalar tidal Love numbers are

$$\begin{aligned} \kappa_3 &= 12C^7(-1 + 2C)(-5(-3 + w) + 15C(-2 + w) - 12C^2(-1 + w) + 2C^3w) \times \\ &\quad \left[175(-2C(C^2(96 - 71w) - 15(-3 + w) + 15C(-9 + 4w) + C^3(-6 + 22w)) \right. \\ &\quad \left. + 3(-1 + 2C)(-5(-3 + w) + 15C(-2 + w) - 12C^2(-1 + w) + 2C^3w) \ln(1 - 2C) \right]^{-1} \end{aligned} \quad (5.113)$$

$$\begin{aligned}
\kappa_4 = & (64C^9(-1 + 2C)(35(-4 + w) - 140C(-3 + w) + 180C^2(-2 + w) \\
& - 80C^3(-1 + w) + 8C^4w)) \times \left[3675(-2C(105(-4 + w) - 190C^3(-4 + 3w) - \right. \\
& 105C(-16 + 5w) + 4C^4(-6 + 25w) + 10C^2(-206 + 89w)) + 3(-1 + 2C)(35(-4 + w) - \\
& \left. 140C(-3 + w) + 180C^2(-2 + w) - 80C^3(-1 + w) + 8C^4w) \ln(1 - 2C) \right]^{-1}.
\end{aligned} \tag{5.114}$$

6 | Conclusion and Outlook

The work presented in this thesis expands our understanding of neutron stars, nuclear matter, and general relativity, explores the capabilities of both current and future gravitational wave detectors, and forms a foundation for future studies of alternate theories of gravity.

Neutron stars are arguably the most fascinating astrophysical objects in the modern, multi-messenger era as they emit gravitational waves, neutrinos, and electromagnetic radiation at different stages of their lives. GW170817 and its electromagnetic counterpart have been the subject of numerous studies for this reason. This work starts by exploring what multi-messenger information from GW170817 and its electromagnetic counterpart can teach us about neutron stars and nuclear matter. Chapter 2 presents a novel, genuinely multi-messenger approach to studying GW170817 that combines gravitational wave data, electromagnetic data, and state-of-the-art nuclear theory. We improved the measurement of neutron star radii by a factor of approximately two and provided new constraints on neutron star tidal deformability. The radius constraint also enabled us to predict the future behavior of neutron star-black hole mergers.

There are only two observed binary neutron star mergers thus far, but more will be detected as current detectors are upgraded and new detectors come online. By applying the multi-messenger approach from this paper to future events we will improve our knowledge of neutron stars. Even if a binary neutron star merger has no electromagnetic counterpart, as was the case with GW190425 [250], applying the parameter estimation method from Chapter 2 will allow scientists to constrain neutron star properties better than previous methods.

LIGO-Virgo announced the detection of two neutron star/black hole systems (GW200105_162426 and GW200115_042309) for the first time in 2021 [18]. As was predicted in Chapter 2, neither one of these mergers has an electromagnetic companion, and they can only be studied with gravitational waves. Early research established that the gravitational wave data alone could not prove that the smaller objects in these two mergers were neutron stars. Even GW170817 did not have sufficient gravitational wave evidence to prove that the event was a binary neutron star merger rather than a binary black hole merger. This leads to a question: under what circumstances can we tell a neutron star from a black hole? That is one of the main questions explored in this thesis and the focus of Chapter 3.

We show that distinguishing neutron stars from black holes is difficult using a gravitational waves. We apply the parameter estimation method developed in Chapter 2 and find that there is little chance of our current detectors or their upgrades being able to distinguish a neutron star-black hole merger from a binary black hole merger. Distinguishing these two types of systems will almost certainly require third-generation detectors, and events like GW190814 with objects in the mass gap will remain a mystery until then. These results demonstrate the importance of the Einstein Telescope and Cosmic Explorer 1 and 2.

We acknowledge that all current studies of future detectors, including the one in this thesis, are limited by the existing waveform approximants. Therefore, we look forward to improvements in gravitational waveform modeling and being able to study the capabilities of third-generation detectors more accurately.

While studying neutron stars is fascinating and an important scientific goal, it is only one of the many uses of gravitational wave data. LIGO data is also useful for tests of general relativity in the strong-field regime. The literature contains many tests of general relativity using gravitational wave data [111–117]. However, the birefringence phenomenon has been largely overlooked. Birefringence occurs when the left- and right-hand gravitational wave polarization modes differ. It arises from the effective field theory extension of general relativity.

In this thesis, we test for birefringence on the most up-to-date gravitational wave catalog [190]. 4-OGC includes two neutron star-black hole mergers, two binary neutron star mergers, and more than eighty binary black hole mergers. While the overwhelming majority of events are consistent with general relativity, there is evidence of birefringence in the two most massive events: GW190521 and GW191109_010717. GW190521 has been the subject of numerous studies, suggesting that GW190521 could be as straightforward as an elliptical binary or as exotic as a proca star merger. While the findings presented in this thesis do not conclusively prove the existence of birefringence or other physics beyond general relativity; they indicate that further studies of high mass events are critical and lend strength to the idea that there is something outside the standard binary black hole merger model in the data. We must rely on future events to learn more. As the catalog of compact binary mergers grows, we will continue to explore the data, testing for birefringence and other interesting phenomena such as the presence of scalar or vector modes.

There are many ways to test general relativity using gravitational waves, and some of these use data from neutron star mergers. However, the exact properties that make neutron stars interesting make them tricky subjects for tests of general relativity. The nuclear equation of state affects the gravitational wave strain through the tidal deformability. Current tests of general relativity, including the one presented in Chapter 4, use general relativistic tidal deformabilities.

It is necessary to understand how tidal effects differ between general relativity and alternative theories because the uncertainty of the tidal deformability measurement is considerable. The uncertainty is the same as or larger than any expected deviation from general relativity. Therefore, analyses that neglect to include changes in the tidal effects may fail to identify deviations from general relativity because the deviations are hidden by the tidal uncertainties.

We derive the magnetic and electric tidal $\ell \geq 2$ Love numbers of neutron stars in scalar-tensor theory in Chapter 5 of this work and expand the limited research on tidal Love numbers beyond general relativity. The results indicate that analyses using incorrect Love numbers may have significant bias or error because tidal deformabilities can differ significantly between general relativity and alternative theories such as scalar-tensor theory.

The altered relationships between mass, radius, and tidal deformability computed in this work are designed to be used in gravitational wave parameter estimation. We plan to apply these results to GW170817 data and perform Bayesian parameter estimation and model selection. The goal of such a study is to demonstrate how the modified tidal deformabilities can effect the results of Bayesian analysis. This research is limited to scalar-tensor theory at this point in time, but the lesson holds for other alternative theories: modified tidal effects cannot be neglected.

This thesis demonstrates the value of gravitational wave data and deepens our understanding of nuclear physics and general relativity. There are currently only seven years of gravitational

wave data available, and our knowledge will improve as more data accumulates and detectors are upgraded and built. This thesis provides the groundwork for future studies and demonstrates that future detectors and observations are essential for studying neutron stars and general relativity. The work contained herein is part of the beginning of a long and exciting journey towards understanding our universe through the lens of gravitational waves.

Bibliography

- [1] B. P. Abbott et al. (LIGO Scientific, Virgo), “Observation of gravitational waves from a binary black hole merger”, *Phys. Rev. Lett.* **116**, 061102 (2016).
- [2] B. P. Abbott et al. (LIGO Scientific, Virgo), “GW170817: observation of gravitational waves from a binary neutron star inspiral”, *Physical Review Letters* **119**, 161101 (2017).
- [3] M. Soares-Santos et al., “The electromagnetic counterpart of the binary neutron star merger LIGO/Virgo GW170817. I. Discovery of the optical counterpart using the dark energy camera”, *The Astrophysical Journal* **848**, L16 (2017).
- [4] B. P. Abbott et al. (LIGO Scientific, Virgo), “GWTC-1: A Gravitational-Wave Transient Catalog of compact binary mergers observed by LIGO and Virgo during the first and second observing runs”, *Physical Review X* **9**, 10.1103/physrevx.9.031040 (2019).
- [5] B. P. Abbott et al. (LIGO Scientific, Virgo), “GWTC-2: Compact binary coalescences observed by LIGO and Virgo during the first half of the third observing run”, *Physical Review X* **11**, 10.1103/physrevx.11.021053 (2021).
- [6] R. Abbott et al., “GWTC-2.1: Deep extended catalog of compact binary coalescences observed by LIGO and Virgo during the first half of the third observing run”, arXiv e-prints, 10.48550/ARXIV.2108.01045 (2021).
- [7] R. Abbott et al. (LIGO Scientific, Virgo, KAGRA), “GWTC-3: Compact binary coalescences observed by LIGO and Virgo during the second part of the third observing run”, arXiv e-prints, 10.48550/ARXIV.2111.03606 (2021).
- [8] C. D. Capano et al., “Stringent constraints on neutron-star radii from multimessenger observations and nuclear theory”, *Nature Astron.* **4**, 625 (2020).
- [9] S. M. Brown, C. D. Capano, and B. Krishnan, “Using gravitational waves to distinguish between neutron stars and black holes in compact binary mergers”, *The Astrophysical Journal*, accepted, 10.48550/ARXIV.2105.03485 (2022).
- [10] Y.-F. Wang, S. M. Brown, L. Shao, and W. Zhao, “Tests of gravitational-wave birefringence with the Open Gravitational-Wave Catalog”, *Phys. Rev. D* **106**, 084005 (2022).
- [11] J. Wheeler and K. Ford, *Geons, Black Holes, and Quantum Foam: A Life in Physics* (Macmillan Publishers Limited. All rights reserved, 1998).
- [12] R. M. Wald, *General Relativity* (Chicago Univ. Pr., Chicago, USA, 1984).
- [13] J. B. Hartle, *Gravity: An Introduction to Einstein’s General Relativity* (Cambridge University Press, 2021).

- [14] K. Schwarzschild, “On the gravitational field of a mass point according to Einstein’s theory”, *Sitzungsber. Preuss. Akad. Wiss. Berlin (Math. Phys.)* **1916**, 189 (1916).
- [15] R. P. Kerr, “Gravitational field of a spinning mass as an example of algebraically special metrics”, *Phys. Rev. Lett.* **11**, 237 (1963).
- [16] A. Einstein, “Naherungsweise Integration der Feldgleichungen der Gravitation”, *Sitzungsberichte der physikalisch-mathematischen Klasse*, 688 (1916).
- [17] N. Andersson et al., “The transient gravitational-wave sky”, *Classical and Quantum Gravity* **30**, 193002 (2013).
- [18] R. Abbott et al. (LIGO Scientific Collaboration and Virgo Collaboration), “Observation of gravitational waves from two neutron star–black hole coalescences”, *The Astrophysical Journal Letters* **915**, L5 (2021).
- [19] L. Blanchet, “Analyzing gravitational waves with general relativity”, *Comptes Rendus Physique* **20**, Prizes of the French Academy of Sciences 2018, 507 (2019).
- [20] L. Blanchet, “Gravitational radiation from post-Newtonian sources and inspiralling compact binaries”, *Living Reviews in Relativity* **17**, 10.12942/lrr-2014-2 (2014).
- [21] C. M. Will, “On the unreasonable effectiveness of the post-Newtonian approximation in gravitational physics”, *Proceedings of the National Academy of Sciences* **108**, 5938 (2011).
- [22] L. Blanchet, B. R. Iyer, C. M. Will, and A. G. Wiseman, “Gravitational waveforms from inspiralling compact binaries to second-post-Newtonian order”, *Classical and Quantum Gravity* **13**, 575 (1996).
- [23] A. Buonanno and T. Damour, “Effective one-body approach to general relativistic two-body dynamics”, *Phys. Rev. D* **59**, 084006 (1999).
- [24] N. T. Bishop and L. Rezzolla, “Extraction of gravitational waves in numerical relativity”, *Living Reviews in Relativity* **19**, 10.1007/s41114-016-0001-9 (2016).
- [25] S. Bernuzzi, T. Dietrich, and A. Nagar, “Modeling the complete gravitational wave spectrum of neutron star mergers”, *Phys. Rev. Lett.* **115**, 091101 (2015).
- [26] M. Alcubierre, *Introduction to 3+1 Numerical Relativity* (Oxford University Press, Apr. 2008).
- [27] A. L. Piro, B. Giacomazzo, and R. Perna, “The fate of neutron star binary mergers”, *The Astrophysical Journal* **844**, L19 (2017).
- [28] B. Margalit and B. D. Metzger, “Constraining the maximum mass of neutron stars from multi-messenger observations of GW170817”, *The Astrophysical Journal* **850**, L19 (2017).
- [29] E. Berti, V. Cardoso, and A. O. Starinets, “Quasinormal modes of black holes and black branes”, *Classical and Quantum Gravity* **26**, 163001 (2009).
- [30] S. A. Teukolsky, “Rotating black holes: separable wave equations for gravitational and electromagnetic perturbations”, *Phys. Rev. Lett.* **29**, 1114 (1972).
- [31] B. Schutz, *A First Course in General Relativity* (Cambridge University Press, 2022).
- [32] The KAGRA Collaboration, “KAGRA: 2.5 generation interferometric gravitational wave detector”, *Nature* **3**, 35 (2018).

- [33] J. Aasi et al. (LIGO Scientific), “Advanced LIGO”, *Classical and Quantum Gravity* **32**, 074001 (2015).
- [34] F. Acernese et al. (Virgo), “Advanced Virgo: a second-generation interferometric gravitational wave detector”, *Classical and Quantum Gravity* **32**, 024001 (2014).
- [35] E. Gibney, “European detector spots its first gravitational wave”, *Nature*, [10 . 1038 / nature . 2017 . 22690](https://doi.org/10.1038/nature.2017.22690) (2017).
- [36] B. P. Abbott et al. (LIGO Scientific, Virgo), “Open data from the first and second observing runs of advanced LIGO and advanced Virgo”, *SoftwareX* **13**, 100658 (2021).
- [37] B. F. Schutz and M. Tinto, “Antenna patterns of interferometric detectors of gravitational waves – I. Linearly polarized waves”, *Monthly Notices of the Royal Astronomical Society* **224**, 131 (1987).
- [38] A. Gelman et al., *Bayesian Data Analysis* (Chapman and Hall/CRC, 2013).
- [39] J. Veitch et al., “Parameter estimation for compact binaries with ground-based gravitational-wave observations using the LALInference software library”, *Phys. Rev. D* **91**, [10 . 1103 / PhysRevD . 91 . 042003](https://doi.org/10.1103/PhysRevD.91.042003) (2015).
- [40] C. M. Biwer et al., “PyCBC Inference: a python-based parameter estimation toolkit for compact binary coalescence signals”, *Publications of the Astronomical Society of the Pacific* **131**, 024503 (2019).
- [41] M. Bayes and M. Price, “An essay towards solving a problem in the Doctrine of Chances. by the late Rev. Mr. Bayes, F. R. S. communicated by Mr. Price, in a letter to John Canton, A. M. F. R. S.”, *Philosophical Transactions (1683-1775)* **53**, 370 (1763).
- [42] LIGO Scientific Collaboration, *LIGO Algorithm Library - LALSuite*, free software (GPL), 2018.
- [43] M. Evans, R. Sturani, S. Vitale, and E. Hall, *Unofficial sensitivity curves (asd) for aLIGO, KAGRA, Virgo, Voyager, Cosmic Explorer and ET*, tech. rep. T1500293-v12, <https://dcc.ligo.org/LIGO-T1500293-v12/public> (LIGO Scientific Collaboration, Jan. 2020).
- [44] V. Srivastava et al., *Sensitivity curves for the Cosmic Explorer trade study*, CE-T2000007-v2, <https://dcc.cosmicexplorer.org/CE-T2000007-v2> (Cosmic Explorer, Mar. 2020).
- [45] G. Pratten et al., “Computationally efficient models for the dominant and subdominant harmonic modes of precessing binary black holes”, *Phys. Rev. D* **103**, 104056 (2021).
- [46] S. Khan, F. Ohme, K. Chatziioannou, and M. Hannam, “Including higher order multipoles in gravitational-wave models for precessing binary black holes”, *Phys. Rev. D* **101**, 024056 (2020).
- [47] V. Varma et al., “Surrogate models for precessing binary black hole simulations with unequal masses”, *Phys. Rev. Research* **1**, 033015 (2019).
- [48] B. S. Sathyaprakash and S. V. Dhurandhar, “Choice of filters for the detection of gravitational waves from coalescing binaries”, *Phys. Rev. D* **44**, 3819 (1991).

- [49] A. Buonanno et al., “Comparison of post-Newtonian templates for compact binary inspiral signals in gravitational-wave detectors”, *Phys. Rev. D* **80**, 084043 (2009).
- [50] B. Mikóczi, M. Vasúth, and L. Á. Gergely, “Self-interaction spin effects in inspiralling compact binaries”, *Phys. Rev. D* **71**, 10.1103/physrevd.71.124043 (2005).
- [51] K. G. Arun, A. Buonanno, G. Faye, and E. Ochsner, “Higher-order spin effects in the amplitude and phase of gravitational waveforms emitted by inspiraling compact binaries: ready-to-use gravitational waveforms”, *Phys. Rev. D* **79**, 104023 (2009).
- [52] A. Bohé, S. Marsat, and L. Blanchet, “Next-to-next-to-leading order spin–orbit effects in the gravitational wave flux and orbital phasing of compact binaries”, *Classical and Quantum Gravity* **30**, 135009 (2013).
- [53] J. Vines, É. É. Flanagan, and T. Hinderer, “Post-1-Newtonian tidal effects in the gravitational waveform from binary inspirals”, *Phys. Rev. D* **83**, 10.1103/physrevd.83.084051 (2011).
- [54] T. Dietrich, S. Bernuzzi, and W. Tichy, “Closed-form tidal approximants for binary neutron star gravitational waveforms constructed from high-resolution numerical relativity simulations”, *Phys. Rev. D* **96**, 121501 (2017).
- [55] T. Dietrich et al., “Improving the NRTidal model for binary neutron star systems”, *Phys. Rev. D* **100**, 044003 (2019).
- [56] S. Husa et al., “Frequency-domain gravitational waves from nonprecessing black-hole binaries. I. New numerical waveforms and anatomy of the signal”, *Phys. Rev. D* **93**, 044006 (2016).
- [57] S. Khan et al., “Frequency-domain gravitational waves from nonprecessing black-hole binaries. II. A phenomenological model for the advanced detector era”, *Phys. Rev. D* **93**, 044007 (2016).
- [58] T. Dietrich et al., “Matter imprints in waveform models for neutron star binaries: tidal and self-spin effects”, *Phys. Rev. D* **99**, 024029 (2019).
- [59] A. Matas et al., “Aligned-spin neutron-star–black-hole waveform model based on the effective-one-body approach and numerical-relativity simulations”, *Phys. Rev. D* **102**, 10.1103/physrevd.102.043023 (2020).
- [60] C. F. Gauss, *Theoria motvs corporvm coelestivm in sectionibvs conicis solem ambientivm* (Hambvrgi, Svmtibvs F. Perthes et I. H. Besser, 1809).
- [61] L. A. Wainstein, V. D. Zubakov, and R. A. Silverman, *Extraction of Signals From Noise* (Englewood Cliffs, 1962).
- [62] W. D. Vousden, W. M. Farr, and I. Mandel, “Dynamic temperature selection for parallel tempering in Markov chain Monte Carlo simulations”, *Monthly Notices of the Royal Astronomical Society* **455**, 1919 (2015).
- [63] D. Foreman-Mackey, D. W. Hogg, D. Lang, and J. Goodman, “Emcee: the mcmc hammer”, *Publications of the Astronomical Society of the Pacific* **125**, 306 (2013).

- [64] J. S. Speagle, “Dynesty: a dynamic nested sampling package for estimating Bayesian posteriors and evidences”, *Monthly Notices of the Royal Astronomical Society* **493**, 3132 (2020).
- [65] S. Kuposov et al., *Joshspeagle/dynesty: v1.2.3*, version v1.2.3, <https://doi.org/10.5281/zenodo.6609296>, June 2022.
- [66] J. Skilling, “Nested sampling for general Bayesian computation”, *Bayesian Analysis* **1**, 833 (2006).
- [67] W. Baade and F. Zwicky, “Remarks on super-novae and cosmic rays”, *Phys. Rev.* **46**, 76 (1934).
- [68] J. Chadwick, “Possible existence of a neutron”, *Nature* **129**, 312 (1932).
- [69] A. a. Hewish, “Observation of a rapidly pulsating radio source”, *Nature* **217**, 709 (1968).
- [70] J. Lattimer and M. Prakash, “Neutron star observations: Prognosis for equation of state constraints”, *Physics Reports* **442**, 109 (2007).
- [71] F. Özel and P. Freire, “Masses, radii, and the equation of state of neutron stars”, *Annual Review of Astronomy and Astrophysics* **54**, 401 (2016).
- [72] A. L. Watts et al., “Colloquium: Measuring the neutron star equation of state using X-Ray timing”, *Reviews of Modern Physics* **88**, 10.1103/revmodphys.88.021001 (2016).
- [73] M. Cantiello et al., “A precise distance to the host galaxy of the binary neutron star merger GW170817 using surface brightness fluctuations”, *The Astrophysical Journal* **854**, L31 (2018).
- [74] D. Radice and L. Dai, “Multimessenger parameter estimation of GW170817”, *The European Physical Journal A* **55**, 10.1140/epja/i2019-12716-4 (2019).
- [75] B. P. Abbott et al., “GW170817: Measurements of neutron star radii and equation of state”, *Physical Review Letters* **121**, 10.1103/physrevlett.121.161101 (2018).
- [76] M. Fasano, T. Abdelsalhin, A. Maselli, and V. Ferrari, “Constraining the neutron star equation of state using multiband independent measurements of radii and tidal deformabilities”, *Physical Review Letters* **123**, 10.1103/physrevlett.123.141101 (2019).
- [77] G. Burgio, H.-J. Schulze, I. Vidaña, and J.-B. Wei, “Neutron stars and the nuclear equation of state”, *Progress in Particle and Nuclear Physics* **120**, 103879 (2021).
- [78] A. Y. Potekhin, J. A. Pons, and D. Page, “Neutron stars—cooling and transport”, *Space Science Reviews* **191**, 239 (2015).
- [79] S. Tsuruta et al., “Thermal Evolution of Hyperon-Mixed Neutron Stars”, *The Astrophysical Journal* **691**, 621 (2009).
- [80] D. Page and S. Reddy, “Dense matter in compact stars: Theoretical developments and observational constraints”, *Annual Review of Nuclear and Particle Science* **56**, 327 (2006).
- [81] D. Page, U. Geppert, and F. Weber, “The cooling of compact stars”, *Nuclear Physics A* **777**, 497 (2006).
- [82] D. Yakovlev and C. Pethick, “Neutron star cooling”, *Annual Review of Astronomy and Astrophysics* **42**, 169 (2004).

- [83] D. Yakovlev, “Neutrino emission from neutron stars”, *Physics Reports* **354**, 1 (2001).
- [84] D. G. Yakovlev, K. P. Levenfish, and Y. A. Shibano, “Cooling of neutron stars and superfluidity in their cores”, *Physics-Uspekhi* **42**, 737 (1999).
- [85] J. M. Lattimer and M. Prakash, “Neutron star structure and the equation of state”, *The Astrophysical Journal* **550**, 426 (2001).
- [86] G. Baym, H. A. Bethe, and C. J. Pethick, “Neutron star matter”, *Nuclear Physics A* **175**, 225 (1971).
- [87] D. G. Ravenhall, C. J. Pethick, and J. R. Wilson, “Structure of matter below nuclear saturation density”, *Phys. Rev. Lett.* **50**, 2066 (1983).
- [88] K. Oyamatsu, “Nuclear shapes in the inner crust of a neutron star”, *Nuclear Physics A* **561**, 431 (1993).
- [89] P. Haensel, A. Y. Potekhin, and D. G. Yakovlev, eds., *Neutron Stars I* (Springer New York, New York, NY, 2007).
- [90] R. W. Romani, D. Kandel, A. V. Filippenko, et al., “PSR J0952-0607: The fastest and heaviest known galactic neutron star”, *The Astrophysical Journal Letters* **934**, L17 (2022).
- [91] S. Weinberg, “Nuclear forces from chiral lagrangians”, *Physics Letters B* **251**, 288 (1990).
- [92] S. Weinberg, “Effective chiral lagrangians for nucleon-pion interactions and nuclear forces”, *Nuclear Physics B* **363**, 3 (1991).
- [93] U. van Kolck, “Few-nucleon forces from chiral lagrangians”, *Phys. Rev. C* **49**, 2932 (1994).
- [94] E. Epelbaum, H. W. Hammer, and U. G. Meißner, “Modern theory of nuclear forces”, *Reviews of Modern Physics* **81**, 1773 (2009).
- [95] R. Machleidt and D. Entem, “Chiral effective field theory and nuclear forces”, *Physics Reports* **503**, 1 (2011).
- [96] I. Tews, J. Margueron, and S. Reddy, “Critical examination of constraints on the equation of state of dense matter obtained from GW170817”, *Physical Review C* **98**, 10 . 1103 / physrevc . 98 . 045804 (2018).
- [97] K. Hebeler, J. M. Lattimer, C. J. Pethick, and A. Schwenk, “Constraints on neutron star radii based on chiral effective field theory interactions”, *Physical Review Letters* **105**, 10 . 1103 / physrevlett . 105 . 161102 (2010).
- [98] J. Antoniadis et al., “A massive pulsar in a compact relativistic binary”, *Science* **340**, 10 . 1126 / science . 1233232 (2013).
- [99] R. C. Tolman, “Static solutions of Einstein’s field equations for spheres of fluid”, *Phys. Rev.* **55**, 364 (1939).
- [100] J. R. Oppenheimer and G. M. Volkoff, “On massive neutron cores”, *Phys. Rev.* **55**, 374 (1939).
- [101] C. W. Misner, K. S. Thorne, and J. A. Wheeler, *Gravitation* (W. H. Freeman, San Francisco, 1973).
- [102] T. Hinderer, “Tidal Love numbers of neutron stars”, *The Astrophysical Journal* **677**, 1216 (2008).

- [103] È. È. Flanagan and T. Hinderer, “Constraining neutron-star tidal Love numbers with gravitational-wave detectors”, *Phys. Rev. D* **77**, 10.1103/physrevd.77.021502 (2008).
- [104] A. E. H. Love, “The yielding of the earth to disturbing forces”, *Proceedings of the Royal Society of London. Series A, Containing Papers of a Mathematical and Physical Character* **82**, 73 (1909).
- [105] T. Shida, “On the body tides of the earth, a proposal for the international geodetic association”, *Proceedings of the Tokyo Mathematico-Physical Society. 2nd Series* **6**, 242 (1912).
- [106] K. S. Thorne, “Multipole expansions of gravitational radiation”, *Rev. Mod. Phys.* **52**, 299 (1980).
- [107] T. Damour and A. Nagar, “Relativistic tidal properties of neutron stars”, *Phys. Rev. D* **80**, 10.1103/physrevd.80.084035 (2009).
- [108] T. Binnington and E. Poisson, “Relativistic theory of tidal Love numbers”, *Phys. Rev. D* **80**, 10.1103/physrevd.80.084018 (2009).
- [109] K. S. Thorne, “Tidal stabilization of rigidly rotating, fully relativistic neutron stars”, *Phys. Rev. D* **58**, 10.1103/physrevd.58.124031 (1998).
- [110] G. Raaijmakers et al., “Constraints on the dense matter equation of state and neutron star properties from NICER’s mass–radius estimate of PSR J0740+6620 and multimessenger observations”, *The Astrophysical Journal Letters* **918**, L29 (2021).
- [111] R. Abbott et al. (LIGO Scientific, Virgo), “Tests of general relativity with binary black holes from the second LIGO-Virgo Gravitational-Wave Transient Catalog”, *Phys. Rev. D* **103**, 122002 (2021).
- [112] B. P. Abbott et al. (LIGO Scientific, Virgo), “Tests of general relativity with the binary black hole signals from the LIGO-Virgo catalog GWTC-1”, *Phys. Rev. D* **100**, 10.1103/physrevd.100.104036 (2019).
- [113] B. P. Abbott et al. (LIGO Scientific, Virgo), “Tests of general relativity with GW150914”, *Phys. Rev. Lett.* **116**, [Erratum: *Phys. Rev. Lett.* 121,no.12,129902(2018)], 221101 (2016).
- [114] K. Chatziioannou, M. Isi, C.-J. Haster, and T. B. Littenberg, “Morphology-independent test of the mixed polarization content of transient gravitational wave signals”, *Phys. Rev. D* **104**, 044005 (2021).
- [115] R. Nair, S. Perkins, H. O. Silva, and N. Yunes, “Fundamental physics implications for higher-curvature theories from binary black hole signals in the LIGO-Virgo catalog GWTC-1”, *Phys. Rev. Lett.* **123**, 191101 (2019).
- [116] R. Abbott, H. Abe, F. Acernese, K. Ackley, et al. (LIGO Scientific, Virgo), “Tests of general relativity with GWTC-3”, *arXiv e-prints*, 10.48550/ARXIV.2112.06861 (2021).
- [117] A. K. Mehta et al., “Tests of general relativity with gravitational-wave observations using a flexible–theory-independent method”, *arXiv e-prints*, arXiv:2203.13937 (2022).
- [118] B. P. Abbott et al. (LIGO Scientific, Virgo), “Tests of general relativity with GW170817”, *Physical Review Letters* **123**, 10.1103/physrevlett.123.011102 (2019).

- [119] Y. Hagihara et al., “Constraining extra gravitational wave polarizations with advanced LIGO, advanced Virgo, and KAGRA and upper bounds from GW170817”, *Phys. Rev. D* **100**, 064010 (2019).
- [120] H. Takeda, S. Morisaki, and A. Nishizawa, “Pure polarization test of GW170814 and GW170817 using waveforms consistent with modified theories of gravity”, *Phys. Rev. D* **103**, 10.1103/physrevd.103.064037 (2021).
- [121] S. S. Yazadjiev, D. D. Doneva, and K. D. Kokkotas, “Tidal Love numbers of neutron stars in $f(R)$ gravity”, *The European Physical Journal C* **78**, 10.1140/epjc/s10052-018-6285-z (2018).
- [122] A. Saffer and K. Yagi, “Tidal deformabilities of neutron stars in scalar-gauss-bonnet gravity and their applications to multimessenger tests of gravity”, *Phys. Rev. D* **104**, 10.1103/physrevd.104.124052 (2021).
- [123] S. Ajith, K. Yagi, and N. Yunes, “I-Love-Q in Hořava-Lifshitz gravity”, 10.48550/ARXIV.2207.05858 (2022).
- [124] P. Pani and E. Berti, “Slowly rotating neutron stars in scalar-tensor theories”, *Phys. Rev. D* **90**, 10.1103/physrevd.90.024025 (2014).
- [125] J. S. Farnes, “A unifying theory of dark energy and dark matter: Negative masses and matter creation within a modified Λ CDM”, *Astronomy & Astrophysics* **620**, 20 (2018).
- [126] B. K. William Thomson, *Baltimore Lectures on Molecular Dynamics and the Wave Theory of Light* (Cambridge University Press, Cambridge, UK, 1904).
- [127] J. C. Kapteyn, “First attempt at a theory of the arrangement and motion of the sidereal system”, *Astrophysical Journal* **55**, 302 (1922).
- [128] J. H. Oort, “The force exerted by the stellar system in the direction perpendicular to the galactic plane and some related problems”, *Bulletin of the Astronomical Institutes of the Netherlands* **6**, 249 (1932).
- [129] V. C. Rubin and W. K. J. Ford, “Rotation of the andromeda nebula from a spectroscopic survey of emission regions”, *The Astrophysical Journal* **159**, 397 (1970).
- [130] V. C. Rubin, W. K. J. Ford, and N. Thonnard, “Rotational properties of 21 sc galaxies with a large range of luminosities and radii, from NGC 4605 ($R = 4\text{kpc}$) to UGC 2885 ($R = 122\text{kpc}$).”, *The Astrophysical Journal* **238**, 471 (1980).
- [131] R. Massey, T. Kitching, and J. Richard, “The dark matter of gravitational lensing”, *Reports on Progress in Physics* **73**, 086901 (2010).
- [132] G. Adhikari et al., “Strong constraints from cosine-100 on the dama dark matter results using the same sodium iodide target”, *Science Advances* **7**, eabk2699 (2021).
- [133] F. Chadha-Day, J. Ellis, and D. J. E. Marsh, *Axion dark matter: What is it and why now?*, 2021.
- [134] G. Bertone, D. Hooper, and J. Silk, “Particle dark matter: Evidence, candidates and constraints”, *Physics Reports* **405**, 279 (2005).
- [135] P. Tisserand et al., “Limits on the MACHO content of the galactic halo from the EROS-2 survey of the Magellanic Clouds”, *Astronomy & Astrophysics* **469**, 387 (2007).

- [136] C. Alcock et al. (MACHO Collaboration), “The MACHO project: Microlensing results from 5.7 years of large magellanic cloud observations”, *The Astrophysical Journal* **542**, 281 (2000).
- [137] R. B. Tully, O. de Marseille, and J. R. Fisher, “A new method of determining distances to galaxies”, in *Bulletin of the american astronomical society*, Vol. 7 (June 1975), p. 426.
- [138] S. S. McGaugh, J. M. Schombert, G. D. Bothun, and W. J. G. de Blok, “The baryonic Tully-Fisher relation”, *The Astrophysical Journal* **533**, L99 (2000).
- [139] M. Milgrom, “A modification of the Newtonian dynamics as a possible alternative to the hidden mass hypothesis.”, *The Astrophysical Journal* **270**, 365 (1983).
- [140] J. D. Bekenstein, “Relativistic gravitation theory for the modified Newtonian dynamics paradigm”, *Phys. Rev. D* **70**, 083509 (2004).
- [141] E. Verlinde, “On the origin of gravity and the laws of Newton”, *Journal of High Energy Physics* **2011**, 10.1007/jhep04(2011)029 (2011).
- [142] S. Perlmutter et al., “Measurements of Ω_M and Λ from 42 high-redshift supernovae”, *The Astrophysical Journal* **517**, 565 (1999).
- [143] A. Einstein, “Kosmologische Betrachtungen zur allgemeinen Relativitätstheorie”, *Sitzungsberichte der Königlich Preußischen Akademie der Wissenschaften* (Berlin, 142 (1917).
- [144] P. J. E. Peebles and B. Ratra, “The cosmological constant and dark energy”, *Rev. Mod. Phys.* **75**, 559 (2003).
- [145] B. Ratra and P. J. E. Peebles, “Cosmological consequences of a rolling homogeneous scalar field”, *Phys. Rev. D* **37**, 3406 (1988).
- [146] M. Doran, M. Lilley, J. Schwindt, and C. Wetterich, “Quintessence and the separation of cosmic microwave background peaks”, *The Astrophysical Journal* **559**, 501 (2001).
- [147] C. Wetterich, “Cosmology and the fate of dilatation symmetry”, *Nuclear Physics B* **302**, 668 (1988).
- [148] T. Kaluza, “Zum Unitätsproblem der Physik”, *Sitzungsberichte der Königlich Preußischen Akademie der Wissenschaften* (Berlin, 966 (1921).
- [149] O. Klein, “Quantentheorie und fünfdimensionale Relativitätstheorie”, *Zeitschrift für Physik* **37**, 895 (1926).
- [150] P. Jordan, “Formation of the stars and development of the universe”, *Nature* **164**, 637 (1949).
- [151] D. Wallace, *The quantization of gravity - an introduction*, 2000.
- [152] A. Friedmann, “Über die Krümmung des Raumes”, *Zeitschrift für Physik* **10**, 377 (1922).
- [153] G. Lemaître, “Expansion of the universe, A homogeneous universe of constant mass and increasing radius accounting for the radial velocity of extra-galactic nebulae”, *Monthly Notices of the Royal Astronomical Society* **91**, 483 (1931).
- [154] G. Lemaître, “L’Univers en expansion”, *Annales de la Société Scientifique de Bruxelles* **53**, 51 (1933).

- [155] H. P. Robertson, “Kinematics and World-Structure”, *The Astrophysical Journal* **82**, 284 (1935).
- [156] H. P. Robertson, “Kinematics and World-Structure II.”, *The Astrophysical Journal* **83**, 187 (1936).
- [157] H. P. Robertson, “Kinematics and World-Structure III.”, *The Astrophysical Journal* **83**, 257 (1936).
- [158] A. G. Walker, “On Milne’s theory of world-structure”, *Proceedings of the London Mathematical Society* **42**, 90 (1937).
- [159] L. Bergström and A. Goobar, *Cosmology and Particle Astrophysics* (Springer, Jan. 2004).
- [160] W. Zhao, T. Zhu, J. Qiao, and A. Wang, “Waveform of gravitational waves in the general parity-violating gravities”, *Phys. Rev. D* **101**, 024002 (2020).
- [161] P. Creminelli, J. Gleyzes, J. Noreña, and F. Vernizzi, “Resilience of the standard predictions for primordial tensor modes”, *Phys. Rev. Lett.* **113**, 231301, 231301 (2014).
- [162] X. Gao and X.-Y. Hong, “Propagation of gravitational waves in a cosmological background”, *Phys. Rev. D* **101**, 064057 (2020).
- [163] N. Yunes, K. G. Arun, E. Berti, and C. M. Will, “Post-Circular Expansion of Eccentric Binary Inspirals: Fourier-Domain Waveforms in the Stationary Phase Approximation”, *Phys. Rev. D* **80**, [Erratum: *Phys. Rev. D* **89**, no.10, 109901(2014)], 084001 (2009).
- [164] A. Conroy and T. Koivisto, “Parity-violating gravity and GW170817 in non-riemannian cosmology”, *Journal of Cosmology and Astroparticle Physics* **2019**, 016 (2019).
- [165] D. Yoshida and J. Soda, “Exploring the string axiverse and parity violation in gravity with gravitational waves”, *Int. J. Mod. Phys. D* **27**, 1850096 (2018).
- [166] C.-S. Chu, J. Soda, and D. Yoshida, “Gravitational Waves in Axion Dark Matter”, *Universe* **6**, 89 (2020).
- [167] S. Jung, T. Kim, J. Soda, and Y. Urakawa, “Constraining the gravitational coupling of axion dark matter at LIGO”, *Phys. Rev. D* **102**, 055013 (2020).
- [168] K. Kamada, J. Kume, and Y. Yamada, “Chiral gravitational effect in time-dependent backgrounds”, *JHEP* **05**, 292 (2021).
- [169] P. Hořava, “Quantum gravity at a Lifshitz point”, *Phys. Rev. D* **79**, 084008 (2009).
- [170] A. Wang, Q. Wu, W. Zhao, and T. Zhu, “Polarizing primordial gravitational waves by parity violation”, *Phys. Rev. D* **87**, 103512 (2013).
- [171] T. Takahashi and J. Soda, “Chiral Primordial Gravitational Waves from a Lifshitz Point”, *Phys. Rev. Lett.* **102**, 231301 (2009).
- [172] M. Crisostomi, K. Noui, C. Charmousis, and D. Langlois, “Beyond Lovelock gravity: higher derivative metric theories”, *Phys. Rev. D* **97**, 044034 (2018).
- [173] C. Brans and R. H. Dicke, “Mach’s principle and a relativistic theory of gravitation”, *Physical Review* **124**, 925 (1961).
- [174] Y. Fujii and K.-i. Maeda, *The Scalar-Tensor Theory of Gravitation*, Cambridge Monographs on Mathematical Physics (Cambridge University Press, 2003).

- [175] P. Jordan, “Zum gegenwärtigen stand der diracschen kosmologischen hypothesen”, *Zeitschrift für Physik* **157**, 112 (1959).
- [176] M. Fierz, “Über die physikalische deutung der erweiterten gravitationstheorie p. jordans”, *Helvetica Physica Acta* **29**, 128 (1956).
- [177] P. G. Bergmann, “Comments on the scalar-tensor theory”, *International Journal of Theoretical Physics*, **1**, 25 (1968).
- [178] J. Nordtvedt Kenneth, “Post-Newtonian metric for a general class of scalar-tensor gravitational theories”, *The Astrophysical Journal* **161**, 1059 (1970).
- [179] R. V. Wagoner, “Scalar-tensor theory and gravitational waves”, *Phys. Rev. D* **1**, 3209 (1970).
- [180] T. Damour and G. Esposito-Farèse, “Tensor-multi-scalar theories of gravitation”, *Classical and Quantum Gravity* **9**, 2093 (1992).
- [181] N. Deruelle and M. Sasaki, in *Springer proceedings in physics* (Springer Berlin Heidelberg, 2011), pp. 247–260.
- [182] C. Palenzuela, E. Barausse, M. Ponce, and L. Lehner, “Dynamical scalarization of neutron stars in scalar-tensor gravity theories”, *Phys. Rev. D* **89**, 044024 (2014).
- [183] D. D. Doneva, S. S. Yazadjiev, N. Stergioulas, and K. D. Kokkotas, “Rapidly rotating neutron stars in scalar-tensor theories of gravity”, *Phys. Rev. D* **88**, 084060 (2013).
- [184] E. Barausse, C. Palenzuela, M. Ponce, and L. Lehner, “Neutron-star mergers in scalar-tensor theories of gravity”, *Phys. Rev. D* **87**, 10.1103/physrevd.87.081506 (2013).
- [185] C. M. Will, *Theory and Experiment in Gravitational Physics* (Cambridge University Press, 1993).
- [186] I. I. Shapiro, “Solar system tests of general relativity: Recent results and present plans”, in *General Relativity and Gravitation*, 1989, edited by N. Ashby, D. F. Bartlett, and W. Wyss (Jan. 1990), p. 313.
- [187] T. Damour and G. Esposito-Farèse, “Nonperturbative strong-field effects in tensor-scalar theories of gravitation”, *Phys. Rev. Lett.* **70**, 2220 (1993).
- [188] T. Harada, “Neutron stars in scalar-tensor theories of gravity and catastrophe theory”, *Phys. Rev. D* **57**, 4802 (1998).
- [189] AEI, *The Atlas Computing Cluster*, <https://www.aei.mpg.de/43564/atlas-computing-cluster>, 2017.
- [190] A. H. Nitz et al., “4-OGC: Catalog of gravitational waves from compact-binary mergers”, *arXiv e-prints*, 10.48550/ARXIV.2112.06878 (2021).
- [191] S. Bogdanov et al., “Constraining the neutron star mass–radius relation and dense matter equation of state with NICER. I. The millisecond pulsar X-Ray data set”, *The Astrophysical Journal* **887**, L25 (2019).
- [192] S. Bogdanov et al., “Constraining the neutron star mass–radius relation and dense matter equation of state with NICER. II. Emission from hot spots on a rapidly rotating neutron star”, *The Astrophysical Journal* **887**, L26 (2019).

- [193] S. De et al., “Tidal deformabilities and radii of neutron stars from the observation of GW170817”, *Physical Review Letters* **121**, 091102 (2018).
- [194] B. P. Abbott et al. (LIGO Scientific, Virgo), “Properties of the binary neutron star merger GW170817”, *Phys. Rev.* **X9**, 011001 (2019).
- [195] J. Carlson et al., “QuantumMonte Carlo methods for nuclear physics”, *Reviews of Modern Physics* **87**, 1067 (2015).
- [196] I. Tews, J. Carlson, S. Gandolfi, and S. Reddy, “Constraining the speed of sound inside neutron stars with chiral effective field theory interactions and observations”, *The Astrophysical Journal* **860**, 149 (2018).
- [197] A. Bauswein, O. Just, H.-T. Janka, and N. Stergioulas, “Neutron-star radius constraints from GW170817 and future detections”, *The Astrophysical Journal* **850**, L34 (2017).
- [198] A. Bauswein, T. W. Baumgarte, and H.-T. Janka, “Prompt merger collapse and the maximum mass of neutron stars”, *Physical Review Letters* **111**, 10.1103/physrevlett.111.131101 (2013).
- [199] S. Köppel, L. Bovard, and L. Rezzolla, “A general-relativistic determination of the threshold mass to prompt collapse in binary neutron star mergers”, *The Astrophysical Journal* **872**, L16 (2019).
- [200] M. Shibata, E. Zhou, K. Kiuchi, and S. Fujibayashi, “Constraint on the maximum mass of neutron stars using GW170817 event”, *Phys. Rev. D* **100**, 10.1103/physrevd.100.023015 (2019).
- [201] H. T. Cromartie et al., “Relativistic Shapiro delay measurements of an extremely massive millisecond pulsar”, *Nature Astronomy* **4**, 72 (2019).
- [202] P. Bedaque and A. W. Steiner, “Sound velocity bound and neutron stars”, *Physical Review Letters* **114**, 10.1103/physrevlett.114.031103 (2015).
- [203] J. M. Lattimer and M. Prakash, “What a two solar mass neutron star really means”, in *From nuclei to stars* (World Scientific Publishing Co, 2011), pp. 275–304.
- [204] M. Hannam et al., “When can gravitational-wave observations distinguish between black holes and neutron stars?”, *The Astrophysical Journal* **766**, L14 (2013).
- [205] B. P. Abbott et al. (LIGO Scientific, Virgo), “Model comparison from LIGO–Virgo data on GW170817’s binary components and consequences for the merger remnant”, *Classical and Quantum Gravity* **37**, 045006 (2020).
- [206] L. S. Collaboration, *Advanced LIGO anticipated sensitivity curves*, tech. rep. T0900288-v3 (LIGO Scientific Collaboration, Dec. 2010).
- [207] T. Hinderer et al., “Distinguishing the nature of comparable-mass neutron star binary systems with multimessenger observations: GW170817 case study”, *Phys. Rev. D* **100**, 10.1103/physrevd.100.063021 (2019).
- [208] F. Foucart, “Black-hole–neutron-star mergers: Disk mass predictions”, *Phys. Rev. D* **86**, 10.1103/physrevd.86.124007 (2012).

- [209] A. Bauswein, S. Goriely, and H.-T. Janka, “Systematics of dynamical mass ejection, nucleosynthesis, and radioactively powered electromagnetic signals from neutron-star mergers”, *The Astrophysical Journal* **773**, 78 (2013).
- [210] K. Hotokezaka et al., “Mass ejection from the merger of binary neutron stars”, *Phys. Rev. D* **87**, 10.1103/physrevd.87.024001 (2013).
- [211] The LIGO Scientific Collaboration and Virgo Collaboration, *GCN CIRCULAR:LIGO/Virgo s190814bv: update on sky-localization and source-classification*, tech. rep. 25333 (LIGO Scientific Collaboration, Aug. 2019).
- [212] F. Foucart, T. Hinderer, and S. Nissanke, “Remnant baryon mass in neutron star-black hole mergers: predictions for binary neutron star mimickers and rapidly spinning black holes”, *Phys. Rev. D* **98**, 10.1103/physrevd.98.081501 (2018).
- [213] B. Margalit and B. D. Metzger, “The multi-messenger matrix: the future of neutron star merger constraints on the nuclear equation of state”, *The Astrophysical Journal* **880**, L15 (2019).
- [214] R. Wijnands, N. Degenaar, and D. Page, “Cooling of accretion-heated neutron stars”, *Journal of Astrophysics and Astronomy* **38**, 10.1007/s12036-017-9466-5 (2017).
- [215] E. F. Brown and A. Cumming, “Mapping crustal heating with the cooling lightcurves of quasi-persistent transients”, *The Astrophysical Journal* **698**, 1020 (2009).
- [216] W. Lewin, ed., *Compact Stellar X-Ray Sources*, Cambridge Astrophysics (Cambridge University Press, 2006).
- [217] K. Barkett et al., “Gravitational waveforms for neutron star binaries from binary black hole simulations”, *Phys. Rev. D* **93**, 10.1103/physrevd.93.044064 (2016).
- [218] T. Narikawa et al., “Reanalysis of the binary neutron star mergers GW170817 and GW190425 using numerical-relativity calibrated waveform models”, *Physical Review Research* **2**, 10.1103/physrevresearch.2.043039 (2020).
- [219] B. P. Abbott (LIGO Scientific, Virgo, KAGRA), “Prospects for observing and localizing gravitational-wave transients with advanced LIGO, advanced Virgo and KAGRA”, *Living Reviews in Relativity* **23**, 10.1007/s41114-020-00026-9 (2020).
- [220] J. A. Melendez, S. Wesolowski, and R. J. Furnstahl, “Bayesian truncation errors in chiral effective field theory: nucleon-nucleon observables”, *Physical Review C* **96**, 10.1103/physrevc.96.024003 (2017).
- [221] J. E. Lynn et al., “Chiral three-nucleon interactions in light nuclei, neutron- α scattering, and neutron matter”, *Physical Review Letters* **116**, 10.1103/physrevlett.116.062501 (2016).
- [222] D. Lonardonì et al., “Properties of nuclei up to $A = 16$ using local chiral interactions”, *Physical Review Letters* **120**, 10.1103/physrevlett.120.122502 (2018).
- [223] J. Lynn, I. Tews, S. Gandolfi, and A. Lovato, “Quantum Monte Carlo methods in nuclear physics: recent advances”, *Annual Review of Nuclear and Particle Science* **69**, 279 (2019).
- [224] I. Tews, “Spectrum of shear modes in the neutron-star crust: estimating the nuclear-physics uncertainties”, *Physical Review C* **95**, 10.1103/physrevc.95.015803 (2017).

- [225] I. Tews, J. Margueron, and S. Reddy, “Confronting gravitational-wave observations with modern nuclear physics constraints”, *The European Physical Journal A* **55**, 10.1140/epja/i2019-12774-6 (2019).
- [226] M. Vallisneri et al., “The LIGO open science center”, *Journal of Physics: Conference Series* **610**, 012021 (2015).
- [227] B. Allen et al., “FINDCHIRP: an algorithm for detection of gravitational waves from inspiraling compact binaries”, *Phys. Rev. D* **85**, 10.1103/physrevd.85.122006 (2012).
- [228] M. Burgay et al., “An increased estimate of the merger rate of double neutron stars from observations of a highly relativistic system”, *Nature* **426**, 531 (2003).
- [229] Planck Collaboration, “Planck 2015 results. XIII. Cosmological parameters”, *Astronomy & Astrophysics* **594**, A13 (2016).
- [230] V. A. Villar et al., “The combined ultraviolet, optical, and near-infrared light curves of the kilonova associated with the binary neutron star merger GW170817: Unified data set, analytic models, and physical implications”, *The Astrophysical Journal* **851**, L21 (2017).
- [231] A. Bauswein and N. Stergioulas, “Semi-analytic derivation of the threshold mass for prompt collapse in binary neutron-star mergers”, *Monthly Notices of the Royal Astronomical Society* **471**, 4956 (2017).
- [232] K. Kiuchi, K. Kyutoku, M. Shibata, and K. Taniguchi, “Revisiting the lower bound on tidal deformability derived by AT 2017gfo”, *The Astrophysical Journal* **876**, L31 (2019).
- [233] M. Shibata et al., “Modeling GW170817 based on numerical relativity and its implications”, *Phys. Rev. D* **96**, 10.1103/physrevd.96.123012 (2017).
- [234] L. Rezzolla, E. R. Most, and L. R. Weih, “Using gravitational-wave observations and quasi-universal relations to constrain the maximum mass of neutron stars”, *The Astrophysical Journal* **852**, L25 (2018).
- [235] M. Ruiz, S. L. Shapiro, and A. Tsokaros, “GW170817, general relativistic magnetohydrodynamic simulations, and the neutron star maximum mass”, *Phys. Rev. D* **97**, 10.1103/physrevd.97.021501 (2018).
- [236] J. M. Lattimer and D. N. Schramm, “Black-Hole-Neutron-Star Collisions”, *ApJL* **192**, L145 (1974).
- [237] M. Shibata and K. Taniguchi, “Merger of black hole and neutron star in general relativity: Tidal disruption, torus mass, and gravitational waves”, *Phys. Rev. D* **77**, 10.1103/physrevd.77.084015 (2008).
- [238] K. Kyutoku et al., “Dynamical mass ejection from black hole-neutron star binaries”, *Phys. Rev. D* **92**, 10.1103/physrevd.92.044028 (2015).
- [239] F. Pannarale and F. Ohme, “Prospects for joint gravitational-wave and electromagnetic observations of neutron-star–black-hole coalescing binaries”, *The Astrophysical Journal* **791**, L7 (2014).
- [240] C. Barbieri et al., “Electromagnetic counterparts of black hole-neutron star mergers: Dependence on the neutron star properties”, *The European Physical Journal A* **56**, 10.1140/epja/s10050-019-00013-x (2020).

- [241] J. M. Bardeen, W. H. Press, and S. A. Teukolsky, “Rotating black holes: Locally nonrotating frames, energy extraction, and scalar synchrotron radiation”, *ApJL* **178**, 347 (1972).
- [242] M. W. Coughlin, T. Dietrich, B. Margalit, and B. D. Metzger, “Multimessenger Bayesian parameter inference of a binary neutron star merger”, *Monthly Notices of the Royal Astronomical Society: Letters* **489**, L91 (2019).
- [243] B. D. Metzger, A. L. Piro, and E. Quataert, “Time-dependent models of accretion discs formed from compact object mergers”, *Monthly Notices of the Royal Astronomical Society*, [10.1111/j.1365-2966.2008.13789.x](https://doi.org/10.1111/j.1365-2966.2008.13789.x) (2008).
- [244] R. Fernández and B. D. Metzger, “Delayed outflows from black hole accretion tori following neutron star binary coalescence”, *Monthly Notices of the Royal Astronomical Society* **435**, 502 (2013).
- [245] D. M. Siegel and B. D. Metzger, “Three-dimensional general-relativistic magnetohydrodynamic simulations of remnant accretion disks from neutron star mergers: Outflows and r -process nucleosynthesis”, *Phys. Rev. Lett.* **119**, 231102 (2017).
- [246] R. Fernández et al., “Long-term GRMHD simulations of neutron star merger accretion discs: implications for electromagnetic counterparts”, *Monthly Notices of the Royal Astronomical Society* **482**, 3373 (2018).
- [247] D. Radice, A. Perego, F. Zappa, and S. Bernuzzi, “GW170817: Joint constraint on the neutron star equation of state from multimessenger observations”, *The Astrophysical Journal* **852**, L29 (2018).
- [248] D. Kasen et al., “Origin of the heavy elements in binary neutron-star mergers from a gravitational-wave event”, *Nature* **551**, 80 (2017).
- [249] M. Nicholl et al., “The electromagnetic counterpart of the binary neutron star merger LIGO/Virgo GW170817. III. Optical and UV spectra of a blue kilonova from fast polar ejecta”, *The Astrophysical Journal* **848**, L18 (2017).
- [250] B. P. Abbott et al., “GW190425: Observation of a compact binary coalescence with total mass $\sim 3.4 M_{\odot}$ ”, *The Astrophysical Journal* **892**, L3 (2020).
- [251] G. Raaijmakers et al., “Constraining the dense matter equation of state with joint analysis of NICER and LIGO/Virgo measurements”, *The Astrophysical Journal* **893**, L21 (2020).
- [252] C. Pacilio, A. Maselli, M. Fasano, and P. Pani, “Ranking Love numbers for the neutron star equation of state: The need for third-generation detectors”, *Physical Review Letters* **128**, [10.1103/physrevlett.128.101101](https://doi.org/10.1103/physrevlett.128.101101) (2022).
- [253] L. Barsotti, L. McCuller, M. Evans, and F. Fritschel, *The A+ design curve*, tech. rep. T1500293-v12, <https://dcc.ligo.org/LIGO-T1800042/public> (LIGO Scientific Collaboration, Oct. 2018).
- [254] D. McClelland et al., *The LSC-Virgo white paper on instrument science (2016-2017 edition)*, tech. rep. LIGO-T1600119-v4, <https://dcc.ligo.org/LIGO-T1600119/public> (LIGO Scientific Collaboration, Oct. 2016).
- [255] D. Reitze et al., “Cosmic Explorer: The U.S. contribution to gravitational-wave astronomy beyond LIGO”, (2019).

- [256] D. Foreman-Mackey, D. W. Hogg, D. Lang, and J. Goodman, “emcee: The MCMC Hammer”, *Publ. Astron. Soc. Pac.* **125**, 306 (2013).
- [257] P. Ajith et al., “A template bank for gravitational waveforms from coalescing binary black holes: Non-spinning binaries”, *Phys. Rev. D.* **77**, 104017 (2008).
- [258] T. Damour and A. Nagar, “Effective one body description of tidal effects in inspiralling compact binaries”, *Phys. Rev. D* **81**, 084016 (2010).
- [259] F. Pannarale, E. Berti, K. Kyutoku, and M. Shibata, “Nonspinning black hole-neutron star mergers: A model for the amplitude of gravitational waveforms”, *Phys. Rev. D* **88**, 084011 (2013).
- [260] B. D. Lackey et al., “Extracting equation of state parameters from black hole-neutron star mergers: Aligned-spin black holes and a preliminary waveform model”, *Phys. Rev. D* **89**, 043009 (2014).
- [261] J. E. Thompson et al., “Modeling the gravitational wave signature of neutron star black hole coalescences”, *Phys. Rev. D* **101**, 124059 (2020).
- [262] R. E. Kass and A. E. Raftery, “Bayes factors”, *Journal of the American Statistical Association* **90**, 773 (1995).
- [263] L. Santamaria et al., “Matching post-Newtonian and numerical relativity waveforms: systematic errors and a new phenomenological model for non-precessing black hole binaries”, *Phys. Rev. D* **82**, 064016 (2010).
- [264] J. Aasi et al. (LIGO Scientific), “Advanced LIGO”, *Class. Quant. Grav.* **32**, 074001 (2015).
- [265] F. Acernese et al. (Virgo Collaboration), “Advanced Virgo: a second-generation interferometric gravitational wave detector”, *Class. Quantum Grav.* **32**, 024001 (2015).
- [266] A. H. Nitz et al., “1-OGC: The first open gravitational-wave catalog of binary mergers from analysis of public advanced LIGO data”, *The Astrophysical Journal* **872**, 195 (2019).
- [267] A. H. Nitz et al., “2-OGC: Open gravitational-wave catalog of binary mergers from analysis of public advanced LIGO and virgo data”, *The Astrophysical Journal* **891**, 123 (2020).
- [268] A. H. Nitz et al., “3-OGC: Catalog of gravitational waves from compact-binary mergers”, *The Astrophysical Journal* **922**, 76 (2021).
- [269] T. Venumadhav et al., “New binary black hole mergers in the second observing run of Advanced LIGO and Advanced Virgo”, *Phys. Rev. D* **101**, 083030 (2020).
- [270] S. Olsen et al., “New binary black hole mergers in the LIGO-Virgo O3a data”, *Phys. Rev. D* **106**, 10.1103/physrevd.106.043009 (2022).
- [271] A. H. Nitz et al., *PyCBC Software*, <https://github.com/gwastro/pycbc>, 2018.
- [272] Y. Wang, R. Niu, T. Zhu, and W. Zhao, “Gravitational wave implications for the parity symmetry of gravity in the high energy region”, *The Astrophysical Journal* **908**, 58 (2021).
- [273] O. W. Greenberg, “CPT violation implies violation of Lorentz invariance”, *Phys. Rev. Lett.* **89**, 231602 (2002).
- [274] V. Kostelecky, “Gravity, Lorentz violation, and the standard model”, *Phys. Rev. D* **69**, 105009 (2004).

- [275] J. D. Tasson, “The standard-model extension and gravitational tests”, *Symmetry* **8**, 111 (2016).
- [276] V. A. Kostelecký and M. Mewes, “Testing local Lorentz invariance with gravitational waves”, *Physics Letters B* **757**, 510 (2016).
- [277] A. Nishizawa and T. Kobayashi, “Parity-violating gravity and GW170817”, *Phys. Rev. D* **98**, 124018 (2018).
- [278] L. Shao, “Combined search for anisotropic birefringence in the Gravitational-Wave Transient Catalog GWTC-1”, *Phys. Rev. D* **101**, 104019 (2020).
- [279] S. Wang and Z.-C. Zhao, “Tests of CPT invariance in gravitational waves with LIGO-Virgo catalog GWTC-1”, *Eur. Phys. J. C* **80**, 1032 (2020).
- [280] K. Yamada and T. Tanaka, “Parametrized test of parity-violating gravity using GWTC-1 events”, *PTEP* **2020**, 093E01 (2020).
- [281] M. Okounkova, W. M. Farr, M. Isi, and L. C. Stein, “Constraining gravitational wave amplitude birefringence and Chern-Simons gravity with GWTC-2”, arXiv e-prints, 10.48550/ARXIV.2101.11153 (2021).
- [282] Z. Wang, L. Shao, and C. Liu, “New limits on the Lorentz/CPT symmetry through fifty gravitational-wave events”, *Astrophys. J.* **921**, 158 (2021).
- [283] Z.-C. Zhao, Z. Cao, and S. Wang, “Search for the birefringence of gravitational waves with the third observing run of Advanced LIGO-Virgo”, arXiv e-prints, 10.3847/1538-4357/ac62d3 (2022).
- [284] R. Niu, T. Zhu, and W. Zhao, “Constraining anisotropy birefringence dispersion in gravitational wave propagation with GWTC-3”, arXiv e-prints, 10.48550/ARXIV.2202.05092 (2022).
- [285] R. Abbott et al. (LIGO Scientific, Virgo), “GW190521: A binary black hole merger with a total mass of $150 M_{\odot}$ ”, *Phys. Rev. Lett.* **125**, 101102 (2020).
- [286] R. Abbott et al. (LIGO Scientific, Virgo), “Properties and astrophysical implications of the $150 M_{\odot}$ binary black hole merger GW190521”, *Astrophys. J. Lett.* **900**, L13 (2020).
- [287] I. M. Romero-Shaw, P. D. Lasky, E. Thrane, and J. C. Bustillo, “GW190521: Orbital eccentricity and signatures of dynamical formation in a binary black hole merger signal”, *Astrophys. J. Lett.* **903**, L5 (2020).
- [288] V. Gayathri et al., “GW190521 as a highly eccentric black hole merger”, arXiv e-prints, 10.48550/ARXIV.2009.05461 (2020).
- [289] R. Gamba et al., “GW190521: A dynamical capture of two black holes”, arXiv e-prints, 10.48550/ARXIV.2106.05575 (2021).
- [290] J. C. Bustillo et al., “GW190521 as a merger of proca stars: a potential new vector boson of 8.7×10^{-13} eV”, *Phys. Rev. Lett.* **126**, 081101 (2021).
- [291] M. J. Graham et al., “Candidate electromagnetic counterpart to the binary black hole merger Gravitational Wave Event S190521g”, *Phys. Rev. Lett.* **124**, 251102 (2020).

- [292] G. Ashton, K. Ackley, I. M. Hernandez, and B. Piotrkowski, “Current observations are insufficient to confidently associate the binary black hole merger GW190521 with AGN J124942.3 + 344929”, *Class. Quant. Grav.* **38**, 235004 (2021).
- [293] A. H. Nitz and C. D. Capano, “GW190521 may be an intermediate-mass ratio inspiral”, *The Astrophysical Journal* **907**, L9 (2021).
- [294] K. O’Neal-Ault et al., “Analysis of birefringence and dispersion effects from spacetime-symmetry breaking in gravitational waves”, *Universe* **7**, 380 (2021).
- [295] N. Yunes, R. O’Shaughnessy, B. J. Owen, and S. Alexander, “Testing gravitational parity violation with coincident gravitational waves and short gamma-ray bursts”, *Phys. Rev. D* **82**, 064017 (2010).
- [296] K. Yagi and H. Yang, “Probing gravitational parity violation with gravitational waves from stellar-mass black hole binaries”, *Phys. Rev. D* **97**, 104018 (2018).
- [297] S. H. Alexander and N. Yunes, “Gravitational wave probes of parity violation in compact binary coalescences”, *Phys. Rev. D* **97**, 064033 (2018).
- [298] M. Mewes, “Signals for Lorentz violation in gravitational waves”, *Phys. Rev. D* **99**, 104062 (2019).
- [299] S. Mozzon et al., “Dynamic normalization for compact binary coalescence searches in non-stationary noise”, *Class. Quant. Grav.* **37**, 215014 (2020).
- [300] S. Mirshekari and C. M. Will, “Compact binary systems in scalar-tensor gravity: Equations of motion to 2.5 post-Newtonian order”, *Phys. Rev. D* **87**, 10.1103/physrevd.87.084070 (2013).
- [301] P. Jordan, *Schwerkraft und Weltall* (Friedrich Vieweg und Sohn, Braunschweig, 1955).
- [302] J. Garcı-Bellido and M. Quiros, “Extended inflation in scalar-tensor theories of gravity”, *Phys. Lett. B* **243**, 45 (1990).
- [303] B. Boisseau, G. Esposito-Fare se, D. Polarski, and A. A. Starobinsky, “Reconstruction of a scalar-tensor theory of gravity in an accelerating universe”, *Physical Review Letters* **85**, 2236 (2000).
- [304] T. Clifton, P. G. Ferreira, A. Padilla, and C. Skordis, “Modified gravity and cosmology”, *Physics Reports* **513**, *Modified Gravity and Cosmology*, 1 (2012).
- [305] K. S. Thorne and A. Campolattaro, “Non-radial pulsation of general-relativistic stellar models. I. Analytic analysis for $L \geq 2$ ”, *The Astrophysical Journal* **149**, 591 (1967).
- [306] H. Sotani and K. D. Kokkotas, “Stellar oscillations in scalar-tensor theory of gravity”, *Phys. Rev. D* **71**, 10.1103/physrevd.71.124038 (2005).
- [307] T. Regge and J. A. Wheeler, “Stability of a Schwarzschild singularity”, *Phys. Rev.* **108**, 1063 (1957).
- [308] P. Pani, L. Gualtieri, T. Abdelsalhin, and X. Jimenez-Forteza, “Magnetic tidal Love numbers clarified”, *Phys. Rev. D* **98**, 10.1103/physrevd.98.124023 (2018).
- [309] P. Landry and E. Poisson, “Gravitomagnetic response of an irrotational body to an applied tidal field”, *Physical Review D* **91**, 10.1103/physrevd.91.104026 (2015).

- [310] S. L. Shapiro, “Gravitomagnetic induction during the coalescence of compact binaries”, *Phys. Rev. Lett.* **77**, 4487 (1996).
- [311] C. T. Cunningham, R. H. Price, and V. Moncrief, “Radiation from collapsing relativistic stars. I. Linearized odd-parity radiation.”, *The Astrophysical Journal* **224**, 643 (1978).
- [312] Z. Andrade and R. H. Price, “Excitation of the odd parity quasinormal modes of compact objects”, *Phys. Rev. D* **60**, 10.1103/physrevd.60.104037 (1999).
- [313] Y. Kojima, “Equations governing the nonradial oscillations of a slowly rotating relativistic star”, *Phys. Rev. D* **46**, 4289 (1992).
- [314] P. C. C. Freire et al., “The relativistic pulsar–white dwarf binary PSR J1738+0333 – II. The most stringent test of scalar–tensor gravity”, *Monthly Notices of the Royal Astronomical Society* **423**, 3328 (2012).
- [315] B. Bertotti, L. Iess, and P. Tortora, “A test of general relativity using radio links with the Cassini spacecraft”, *Nature* **425**, 374 (2003).
- [316] T. Damour and G. Esposito-Farèse, “Tensor-scalar gravity and binary-pulsar experiments”, *Phys. Rev. D* **54**, 1474 (1996).
- [317] L. Bernard, “Dipolar tidal effects in scalar-tensor theories”, *Phys. Rev. D* **101**, 10.1103/physrevd.101.021501 (2020).
- [318] X. J. Forteza, T. Abdelsalhin, P. Pani, and L. Gualtieri, “Impact of high-order tidal terms on binary neutron-star waveforms”, *Phys. Rev. D* **98**, 10.1103/physrevd.98.124014 (2018).
- [319] P. Virtanen et al., “SciPy 1.0: Fundamental Algorithms for Scientific Computing in Python”, *Nature Methods* **17**, 261 (2020).
- [320] D. Manolidis, “Neutron star models in alternative theories of gravity”, PhD thesis (Washington University in St. Louis, Sept. 2014).
- [321] W. H. Press, S. A. Teukolsky, W. T. Vetterling, and B. P. Flannery, *Numerical Recipes 3rd Edition: The Art of Scientific Computing*, 3rd ed. (Cambridge University Press, USA, 2007).
- [322] F. Douchin and P. Haensel, “A unified equation of state of dense matter and neutron star structure”, *Astronomy & Astrophysics* **380**, 151 (2001).
- [323] B. Friedman and V. R. Pandharipande, “Hot and cold, nuclear and neutron matter”, *Nucl. Phys. A* **361**, 502 (1981).
- [324] H. Müller and B. D. Serot, “Relativistic mean-field theory and the high-density nuclear equation of state”, *Nuclear Physics A* **606**, 508 (1996).
- [325] J. S. Read, B. D. Lackey, B. J. Owen, and J. L. Friedman, “Constraints on a phenomenologically parametrized neutron-star equation of state”, *Phys. Rev. D* **79**, 124032 (2009).

7 | Acknowledgements

There are a great number of people to whom I owe thanks for their support, advice, and aid during the process of writing this thesis. I would like to thank everyone who helped me along this path.

First, I would like to thank Badri Krishnan, my supervisor, for accepting me as student and guiding me through the last four years. Thank you for all that you have taught me.

Thanks to all my coauthors for their patience and for all the knowledge shared with me. I have learned something from each and everyone of you, and for that, I am grateful. Research is a collaborative effort, and much of the work presented here wouldn't exist without you. I am also grateful to all my fellow researchers in the observational cosmology and relativity group. Your scientific input and friendship have shaped my experience. Special thanks to Sumit, Xisco, Pierre, and Sayak, who helped me when they were under no obligation to do so. I would also like to thank the ATLAS computing team without whom this research would have gone exactly nowhere. I also owe thanks to Gaston Creci for sharing his insights into the scalar-tensor tidal Love number problem.

I would like to offer special thanks to Dr. Mike Kilburn and Dr. Zachary Constan for their passion and dedication to scientific outreach, for introducing me to physics, and for igniting in me a passion for astrophysics that will never fade. You changed the course of my life, and I owe you more than I can say.

I want to thank my friends, who are like family to me and have kept me sane during the Covid pandemic, which coincided completely with the research and writing of this thesis. Thanks to Ella and EJ who are always ready to listen, to offer advice and support, and to make sure I actually rest occasionally. Thanks to Jade, Lionel, Hayley, and David who made a new city a friendly place. Thanks to Renata Kopečná for the solidarity, the jokes, and the company. I am also deeply grateful to Dr. Nathan Smith, Dr. Renata Kopečná, and Olivia Vilella for taking the time to read parts of this thesis and give me feedback.

I would also like to thank my family. First, I offer thanks to those who are no longer here. To my nana, Nancy Hammond, whose staunch feminism and legal work improved legal protections for women studying in universities and who never once doubted that a woman could succeed anywhere a man could: I hope you rest easier knowing that your hard work paved the way for women like me to chase their dreams. To my father, Jim Brown, who never quite understood my goals but supported me anyway: I told you I could do it; I just wish you were here to see it. Last, but very certainly not least, I would like to thank my mother, Dr. Wendy Keilholtz. I would not have made it this far without you. I have been chasing the goal of finishing this thesis for half my life, and I could never have made it without the dedication and tenacity you instilled in me and all the support that you gave me.

(And of course, thanks to Magnus and Maximus for the 24/7 'help' and support)

Curriculum Vitae Stephanie Brown

NEUTRON STARS · GRAVITATIONAL WAVES · ALTERNATE THEORIES OF GRAVITATION

✉ stephanie.brown@aei.mpg.de ☎ +49 0160 919 6543 ⓘ Stephanie (Alex) Brown

Education

- Sep. 2018 – present Ph.D. in Physics Leibniz Universität Hannover
Max Planck Institute for Gravitational Physics, DE
“Using Gravitational Waves to Study Neutron Stars in General Relativity and Alternative Theories of Gravity”
Advisor: Badri Krishnan
- Jun. 2014 – May 2018 B.S. in Astronomy and Astrophysics (with honors) Pennsylvania State University, USA
“Temperature simulation and calculation for the antimatter Experiment: Gravity, Interferometry, and Spectroscopy.”
Advisors: Miguel Mostafa

Research Experience

- Oct. 2018 – present Doctoral Researcher Max Planck Institute for Gravitational Physics, DE
Supervisor: Badri Krishnan
- Utilizing Bayesian statistics and data analysis techniques to study properties of nuclear matter by analyzing gravitational wave signals
 - Calculating tidal deformability by applying perturbation theory in scalar tensor theories of gravitation
 - Integrating theoretical calculations into existing python based frameworks for analyzing gravitational waves
- Jan. 2017 – May 2017 Undergraduate Research Assistant Pennsylvania State University, USA
Supervisor: B. S. Sathyaprakash Institute for Gravitation and the Cosmos
- Apply computational methods to develop Mathematica programs to determine the gravitational wave pattern of stellar mass compact object binaries with high spin.
- May 2017 – Aug. 2017 Summer Student Max Planck Institute for Gravitational Physics, DE
Supervisor: Badri Krishnan

- Determining geodesics and quasinormal modes for black holes with a Vaidya metric and a linear mass function in order to compare apparent and event horizons.

Jun. 2016 – Dec. 2016 Undergraduate Research Assistant AEGIS Collaboration, CERN, CH
Supervisor: Ingmari Tietje

- Develop a ROOT based simulation of the temperature measurement to be taken in the AEGIS beam line.
- Working AEGIS beam control shift: communicating with beam control and other experiments, monitoring beam status, real time analysis and trouble shooting of the system, determining and controlling experimental variables

Sep. 2014 – May 2016 Undergraduate Research Assistant Pennsylvania State University, USA
Supervisor: Michael Eracleous

- Work on candidate supermassive binary black hole systems and line-emitting accretion disks in active galactic nuclei.

Jun. 2015 – Aug. 2015 Summer Student AEGIS Collaboration, CERN, CH
Supervisor: Julian Fesel

- Work with mathematical descriptions of C_2^- in a penning trap with a magnetic mirror for sympathetic cooling of antiprotons used for gravity tests

Teaching Experience

Oct. 2020 – Feb. 2021 Teaching Assistant Leibniz Universität Hannover, DE

- Teach students fundamental data analysis techniques employed in gravitational wave data analysis
- Guide students through developing their own data analysis codes
- Evaluate student work and provide feedback

Apr. 2020 – Sept. 2020 Teaching Assistant Leibniz Universität Hannover, DE

- Evaluate student work and provide feedback

Invited Talks

1. **Brown, S. M.** *Tidal Deformability of Neutron Stars in Scalar Tensor Theories of Gravity* Institute for Theoretical Physics, Utrecht University. October 2022. Utrecht, NL

Conference Talks

1. **Brown, S. M.**, Krishnan, B. *Tidal Deformability of Neutron Stars in Scalar Tensor Theories of Gravity* 23rd International Conference on General Relativity and Gravitation; July 2022; Beijing, China. *Online*.
2. **Brown, S. M.**, Krishnan, B. *Tidal Deformability of Neutron Stars in Scalar Tensor Theories of Gravitation* American Physical Society April Meeting 2022; April 2022; New York City, New York, USA
3. **Brown, S. M.** *When neutron stars collide: cataclysms in space* November der Wissenschaft 2021; November 2021; Max Planck Institute for Gravitational Physics, Hannover, DE. *Online*.
4. **Brown, S. M.**, Capano, C.D., Krishnan, B. *Using gravitational waves to distinguish between neutron stars and black holes in binaries* Physikerinnentagung 2020; November 2020; Universität Hamburg, Hamburg, DE. *Online*.
5. Capano, C.D., Tews, I., **Brown, S. M.** *Measurement of the tidal deformabilities of GW170817 component neutron stars using Chiral-EFT equations of state* January 2020 American Astronomical Society 235th Meeting, Honolulu, Hawaii
6. **Brown, S. M.**, Capano C.D., Tews, I., et al *Measurement of the tidal deformabilities of GW170817 component neutron stars using Chiral-EFT equations of state.* GWPAW 2019, RESCEU; October 2019; The University of Tokyo, Tokyo, Japan. *Online*.
7. **Brown, S. M.**, Capano C.D., Tews, I., et al *Constraining Neutron Star Equations of State Using GW170817* YITP Longterm Workshop: Multimessenger Astrophysics in the Gravitational Wave Era; September 2019; Yukawa Institute for Theoretical Physics, Kyoto, Japan.
8. **Brown, S. M.** *Trapping and Cooling Antimatter for Gravity Research.* Schreyer Honors College: Scones and Scholarship; April 2016; University Park, PA, USA
9. **Brown, S. M.** *Antimatter Research at CERN.* Graduate Women in Science: Spring 2016 Girl Scout Workshop; April 2016; University Park, PA, USA
10. **Brown, S. M.** *Mathematical Descriptions of Axially Varying Penning Traps* August 2015. University of Michigan Research Experience, CERN
11. **Brown, S. M.** *Creating biofuels through electrocatalysis.* April 2014. Youth Inspiring Youth, Michigan State University Science Festival.

Workshops and Schools

July 2022	Summer School New Frontiers in Strong Gravity	Centro de Ciencias de Benasque Pedro Pascual, ES
Mar. 2022 – Apr. 2022	IMPRS Lectures Gravitational Wave Astronomy: Computational Physics	Max Planck Institute for Gravitational Physics, DE
May 2021 – Jun. 2021	IMPRS Lectures Gravitational Wave Astronomy: Astrophysics of Compact Objects	Max Planck Institute for Gravitational Physics, DE
Sept 2019	YTIP Longterm Workshop Multimessenger Astrophysics in the Gravitational Wave Era	Yukawa Institute for Theoretical Physics, JPN

Publications

1. Wang, Y. **Brown, S. M.**, Shao, L., Zhao, W. “Tests of Gravitational-Wave Birefringence with the Open Gravitational-Wave Catalog”. *Phys. Rev. D* 106, 084005 (2022)
2. **Brown, S. M.**, Capano, C. D., Krishnan, B. “Using gravitational waves to distinguish between neutron stars and black holes in compact binary mergers”. *The Astrophysical Journal*. *accepted 2022*
3. Capano, C. D., Tews, I., **Brown, S. M.**, Margalit, B. De, S., Kumar, S., Brown, D. A, Krishnan, B., Reddy, S. “Stringent Constraints on Neutron-Star Radii from Multimessenger Observations and Nuclear Theory.” *Nature Astronomy* (2020)
4. Runnoe, J. C., Eracleous, M., Pennell, A., Mathes, G., Boroson, T., Sigurdsson, S., Bogdanovic, T., Halpern, J. P., Liu, J., **Brown, S. M.**. “A Large Systematic Search for Close Supermassive Binary and Rapidly Recoiling Black Holes - III. Radial Velocity Variations.” *Monthly Notices of the Royal Astronomical Society* 468.2 (2017): 1683–1702.